ISSN 1997-308X
eISSN 2412-8767

ИЗВЕСТИЯ ВУЗОВ
ПОРОШКОВАЯ МЕТАЛЛУРГИЯ И ФУНКЦИОНАЛЬНЫЕ ПОКРЫТИЯ

POWDER METALLURGY AND FUNCTIONAL COATINGS

2024
Том 18 № 6
Vol. 18 No. 6
powder.misis.ru

ISSN 1997-308X
eISSN 2412-8767

POWDER METALLURGY AND FUNCTIONAL COATINGS

Scientific and Technical Journal

Founded in 2007
Six issues per year

2024

Том 18 № 6
Vol. 18 No. 6

ИЗВЕСТИЯ ВУЗОВ

ПОРОШКОВАЯ МЕТАЛЛУРГИЯ И ФУНКЦИОНАЛЬНЫЕ ПОКРЫТИЯ

Научно-технический журнал

Основан в 2007 г.
Выходит 6 раз в год

POWDER METALLURGY AND FUNCTIONAL COATINGS

SCIENTIFIC AND TECHNICAL JOURNAL
FOUNDED IN 2007
SIX ISSUES PER YEAR

http://powder.misis.ru

ISSN 1997-308X
eISSN 2412-8767

Founder:

National University of Science
and Technology "MISIS"
Address: 1 Bld, 4 Leninskiy Prosp., Moscow 119049, Russian Federation
http://www.misis.ru

Editor-in-Chief

Evgeny A. Levashov

Prof., Dr. Sci. (Eng.), Acad. of the RANS, NUST MISIS, Moscow, Russian Federation

Journal is included into the List of peer-reviewed scientific publications recommended by the Highest Attestation Commission of the Ministry of Education and Science of the Russian Federation for publishing the results of doctoral and candidate dissertations.
Abstracting/Indexing: Scopus, Russian Science Citation Index (RSCI), Ulrich's Periodicals Directory, VINITI Database (Abstract Journal).

Editorial Board

M. I. Alymov – Dr. Sci. (Eng.), Corresponding Member of the RAS, Merzhanov Institute of Structural Macrokinetics and Materials Sciences of the RAS, Chernogolovka, Russia
A. P. Amosov – Prof., Dr. Sci. (Phys.-Math.), Samara State Technical University, Samara, Russia
G. A. Bagliuk – Prof., Dr. Sci. (Eng.), Acad. of the NASU, IPMS NASU, Kiev, Ukraine
I. V. Blinkov – Prof., Dr. Sci. (Eng.), NUST MISIS, Moscow, Russia
M. V. Chukin – Prof., Dr. Sci. (Eng.), Magnitogorsk State Technical University, Magnitogorsk, Russia
H. Danninger – Prof., Dr. Sci., Vienna University of Technology, Vienna, Austria
B. Derin – Assoc. Prof., Dr. Sci. (Phil.), Istanbul Technical University, Maslak, Istanbul, Turkey
V. Yu. Dorofeyev – Prof., Dr. Sci. (Eng.), South-Russian State Polytechnical University (NPI), Novocherkassk, Russia
Yu. Estrin – Prof., Dr. Sci. (Nat.), Monash University, Clayton, Australia
A. Ph. Ilyushchanka – Prof., Dr. Sci. (Eng.), Acad. of the NAS of Belarus, State Research and Production Powder Metallurgy Association, Minsk, Belarus
Yu. R. Kolobov – Prof., Dr. Sci. (Phys.-Math.), Federal Research Center of Problems of Chemical Pfysics and Medicinal Chemistry of the RAS, Chernogolovka, Russia
V. S. Komlev – Prof., Dr. Sci. (Eng.), Corresponding Member of the RAS, Institute of Metallurgy of the RAS, Moscow, Russia
I. Konyashin – Prof., Dr. Sci. (Econ.), Element Six GmbH, Burghaun, Germany
Yu. M. Korolyov – Prof., Dr. Sci. (Eng.), Scientific and Technical Association "Powder Metallurgy", Moscow, Russia
D. Yu. Kovalev – Dr. Sci. (Phys.-Math.), Merzhanov Institute of Structural Macrokinetics and Materials Sciences of the RAS, Chernogolovka, Russia
S. A. Kulinich – Assoc. Prof., PhD (Chem.), Tokai University, Hiratsuka, Kanagawa, Japan
S. V. Kuzmin – Prof., Dr. Sci. (Eng.), Corresponding Member of the RAS, Volgograd State Technical University, Volgograd, Russia
V. P. Kuznetsov – Prof., Dr. Sci. (Eng.), Ural Federal University, Ekaterinburg, Russia
Yu. V. Levinsky – Prof., Dr. Sci. (Eng.) Merzhanov Institute of Structural Macrokinetics and Materials Sciences of the RAS, Chernogolovka, Russia
A. E. Ligachyov – Prof., Dr. Sci. (Phys.-Math.), Prokhorov General Physics Institute of the RAS, Moscow, Russia
V. Yu. Lopatin – Cand. Sci., NUST MISIS, Moscow, Russia
A. A. Lozovan – Prof., Dr. Sci (Eng.), Moscow Aviation Institute (NRU), Moscow, Russia
V. I. Lysak – Prof., Dr. Sci. (Eng.), Acad. of the RAS, Volgograd State Technical University, Volgograd, Russia
A. V. Makarov – Dr. Sci. (Eng.), Corresponding Member of the RAS, M.N. Mikheev Institute of Metal Physics of the Ural Branch of the RAS, Ural Federal University, Ekaterinburg, Russia
L. L. Mishnaevsky – Dr. Habil. (Eng.), Technical University of Denmark, Roskilde, Denmark
A. S. Mukasyan – Prof., Dr. Sci. (Phys.-Math.), University of Notre Dame, Notre Dame, USA
S. A. Oglezneva – Prof., Dr. Sci. (Eng.), Perm National Research Polytechnical University, Perm, Russia
R. Orrù – Prof., Dr. Sci. (Eng.), University of Cagliari, Cagliari, Italy
I. B. Panteleev – Prof., Dr. Sci. (Eng.), St. Petersburg State Technological Institute (Technical University), St. Petersburg, Russia
F. Peizhong – Prof., Dr. Sci., China University of Mining and Technology, Xuzhou, P.R. China
C. Pengwan – Prof., Dr. Sci., Beijing Institute of Technology, Beijing, P.R. China
M. I. Petrzhik – Dr. Sci. (Eng.), NUST MISIS, Moscow, Russia
Yu. S. Pogozhev – Assoc. Prof., Cand. Sci. (Eng.), NUST MISIS, Moscow, Russia
V. V. Polyakov – Prof., Dr. Sci. (Phys.-Math.), Altai State University, Barnaul, Russia
A. A. Popovich – Prof., Dr. Sci. (Eng.)., Corresp. Member of the RANS, St. Petersburg State Polytechnical University (National Research University), St. Petersburg, Russia
S. E. Porozova – Dr. Sci. (Eng.), Perm National Research Polytechnical University, Perm, Russia
A. A. Rempel – Prof., Dr. Sci. (Phys.-Math.), Acad. of the RAS, Institute of Metallurgy of the Ural Branch of the RAS, Ekaterinburg, Russia
F. Rustichelli – Prof., Dr. Sci. (Phys.), University of Marches, Ancona, Italy
S. D. Shlyapin – Prof., Dr. Sci. (Eng.), Moscow Aviation Institute (NRU), Moscow, Russia
D. V. Shtansky – Prof., Dr. Sci. (Phys.-Math.), NUST MISIS, Moscow, Russia
A. N. Timofeev – Dr. Sci. (Eng.), JSC "Komposite", Korolev, Russia
P. A. Vityaz' – Prof., Dr. Sci. (Eng.), Acad. of the NAS of Belarus, Minsk, Belarus
A. A. Zaitsev – Assoc. Prof., Cand. Sci. (Eng.), NUST MISIS, Moscow, Russia
Zheng YongTing – Prof., Dr. Sci., Harbin Institute of Technology, Harbin, P.R. China
F. Zhengyi – Prof., Dr. Sci., Wuhan University of Technology, Wuhan, P.R. China

Editorial Staff

Address: NUST MISIS,
1 Bld, 4 Leninskiy Prosp., Moscow 119049, Russian Federation

Phone: +7 (495) 638-45-35. *E-mail:* izv.vuz@misis.ru

Certificate of registration **No. FS77-27955** (12.04.2007)
Re-registration **PI No. FS77-79230** (25.09.2020)

PM & FC © NUST MISIS, Moscow, 2024

Articles are available under Creative Commons Attribution Non-Commercial No Derivatives

Leading Editor: O.V. Sosnina
Executive Editor: A.A. Kudinova
Layout Designer: V.V. Rasenets

Signed print 21.12.2024. Format 60×90 $^1/_8$
Offset paper No. 1. Digital printing. Quires 11.0
Order 21241. Free price
Printed in the printing house of the MISIS Publish House
1 Bld, 4 Leninskiy Prosp., Moscow 119049, Russian Federation
Phone/fax: +7 (499) 236-76-17

ИЗВЕСТИЯ ВУЗОВ ПОРОШКОВАЯ МЕТАЛЛУРГИЯ И ФУНКЦИОНАЛЬНЫЕ ПОКРЫТИЯ

НАУЧНО-ТЕХНИЧЕСКИЙ ЖУРНАЛ
ОСНОВАН В 2007 Г.
ВЫХОДИТ 6 РАЗ В ГОД

http://powder.misis.ru

ISSN 1997-308X
eISSN 2412-8767

Учредитель:

ФГАОУ ВО Национальный исследовательский технологический университет «МИСИС»
Адрес: 119049, Москва, Ленинский пр-т, 4, стр. 1
https://www.misis.ru

Главный редактор

Евгений Александрович Левашов
д.т.н., академик РАЕН, профессор, НИТУ МИСИС, г. Москва

Журнал включен в Перечень рецензируемых научных изданий, рекомендованных ВАК Минобрнауки РФ для публикации результатов диссертаций на соискание ученых степеней.
Журнал включен в базы данных: Scopus, Russian Science Citation Index (RSCI), Ulrich's Periodicals Directory, РИНЦ, БД/РЖ ВИНИТИ.

Редакционная коллегия

М. И. Алымов – д.т.н., чл.-корр. РАН, проф., ИСМАН, г. Черноголовка
А. П. Амосов – д.ф.-м.н., проф., СамГТУ, г. Самара
Г. А. Баглюк – д.т.н., акад. НАНУ, проф., ИПМ НАН Украины, г. Киев
И. В. Блинков – д.т.н., проф., НИТУ МИСИС, г. Москва
П. А. Витязь – д.т.н., акад. НАНБ, проф., НАН Беларуси, г. Минск
В. Ю. Дорофеев – д.т.н., проф., ЮРГПУ (НПИ), г. Новочеркасск
А. А. Зайцев – к.т.н., доц., НИТУ МИСИС, г. Москва
А. Ф. Ильющенко – д.т.н., акад. НАН Беларуси, проф., ГНПО ПМ НАН Беларуси, г. Минск
Д. Ю. Ковалев – д.ф.-м.н., ИСМАН, г. Черноголовка
Ю. Р. Колобов – д.ф.-м.н., проф., ФИЦ ПХФ и МХ РАН, г. Черноголовка
В. С. Комлев – д.т.н., чл.-корр. РАН, проф., ИМЕТ РАН, г. Москва
Ю. М. Королев – д.т.н., проф., НТА «Порошковая металлургия», г. Москва
В. П. Кузнецов – д.т.н., проф., УрФУ, г. Екатеринбург
С. В. Кузьмин – д.т.н., чл.-корр. РАН, проф., ВолгГТУ, г. Волгоград
Ю. В. Левинский – д.т.н., проф., ИСМАН, г. Черноголовка
А. Е. Лигачев – д.ф.-м.н., проф., ИОФ РАН, г. Москва
А. А. Лозован – д.т.н., проф., МАИ (НИУ), г. Москва
В. Ю. Лопатин – к.т.н., доц., НИТУ МИСИС, г. Москва
В. И. Лысак – д.т.н., акад. РАН, проф., ВолгГТУ, г. Волгоград
А. В. Макаров – д.т.н., чл.-корр. РАН, ИФМ УрО РАН, УрФУ, г. Екатеринбург
С. А. Оглезнева – д.т.н., проф., ПНИПУ, г. Пермь
И. Б. Пантелеев – д.т.н., проф., СПбГТИ (ТУ), г. Санкт-Петербург
М. И. Петржик – д.т.н., проф., НИТУ МИСИС, г. Москва
Ю. С. Погожев – к.т.н., доц., НИТУ МИСИС, г. Москва
В. В. Поляков – д.ф.-м.н., проф., АлтГУ, г. Барнаул
А. А. Попович – д.т.н., чл.-корр. РАЕН, проф., СПбГПУ, г. Санкт-Петербург
С. Е. Порозова – д.т.н., проф., ПНИПУ, г. Пермь
А. А. Ремпель – д.ф.-м.н., акад. РАН, проф., ИМЕТ УрО РАН, г. Екатеринбург
А. Н. Тимофеев – д.т.н., АО «Композит», г. Королев
М. В. Чукин – д.т.н., проф., МГТУ, г. Магнитогорск
С. Д. Шляпин – д.т.н., проф., МАИ (НИУ), г. Москва
Д. В. Штанский – д.ф.-м.н., проф., НИТУ МИСИС, г. Москва
H. Danninger – Dr. Sci., Prof., Vienna University of Technology, Vienna, Austria
B. Derin – Dr. Sci. (Phil.), Assoc. Prof., Istanbul Technical University, Maslak, Istanbul, Turkey
Yu. Estrin – Dr. Sci. (Nat.), Prof., Monash University, Clayton, Australia
I. Konyashin – Dr. Sci. (Econ.), Prof., Element Six GmbH, Burghaun, Germany
S. A. Kulinich – PhD (Chem.), Associate Prof., Tokai University, Hiratsuka, Kanagawa, Japan
L. L. Mishnaevsky – Dr. Habil. (Eng.), Technical University of Denmark, Roskilde, Denmark
A. S. Mukasyan – Dr. Sci. (Phys.-Math.), Prof., University of Notre Dame, Notre Dame, USA
R. Orrù – Dr. Sci. (Eng.), Prof., University of Cagliari, Cagliari, Italy
F. Peizhong – Dr. Sci., Prof., China University of Mining and Technology, Xuzhou, P.R. China
C. Pengwan – Dr. Sci., Prof., Beijing Institute of Technology, Beijing, P.R. China
F. Rustichelli – Dr. Sci. (Phys.), Prof., University of Marches, Ancona, Italy
Zheng YongTing – Dr. Sci., Prof., Harbin Institute of Technology, Harbin, P.R. China
F. Zhengyi – Dr. Sci., Prof., Wuhan University of Technology, Wuhan, P.R. China

Редакция журнала

Адрес: 119049, Москва,
Ленинский пр-т, 4, стр. 1. НИТУ МИСИС

Тел.: +7 (495) 638-45-35. ***Эл. почта:*** izv.vuz@misis.ru

Свидетельство о регистрации № **ФС77-27955** от 12.04.2007 г.
Перерегистрация 25.09.2020 г. **ПИ № ФС77-79230**

ПМ и ФП
ИЗВЕСТИЯ ВУЗОВ

© НИТУ МИСИС, Москва, 2024

Статьи доступны под лицензией Creative Commons Attribution Non-Commercial No Derivatives

Ведущий редактор: О.В. Соснина
Выпускающий редактор: А.А. Кудинова
Дизайн и верстка: В.В. Расенецъ

Подписано в печать 21.12.2024. Формат 60×90 $^1/_8$
Бум. офсетная № 1. Печать цифровая. Усл. печ. л. 11,0
Заказ 21241. Цена свободная
Отпечатано в типографии Издательского Дома МИСИС
119049, г. Москва, Ленинский пр-т, 4, стр. 1
Тел./факс: +7 (499) 236-76-17

Contents

Self-Propagating High-Temperature Synthesis

Bobozhanov A.R., Rogachev A.S.
Self-propagating high-temperature synthesis of high-entropy materials: A review 5

Jussupkaliyeva R.I., Bystrova I.M., Pomogailo S.I., Borshch V.N.
Synthesis of Co–Mn catalysts for deep oxidation of CO and propane based on natural opoka by low-temperature combustion 17

Amosov A.P., Titova Yu.V., Uvarova I.A., Belova G.S.
Azide self-propagating high-temperature synthesis of a highly dispersed AlN–SiC powder composition using polytetrafluoroethylene 28

Titova Yu.V., Yakubova A.F., Belova G.S.
Self-propagating high-temperature synthesis of highly dispersed Si_3N_4–TiC composition using sodium azide and various carbon sources 44

Porous Materials and Biomaterials

Shustov V.S., Zelensky V.A., Alymov M.I., Ankudinov A.B., Ustyukhin A.S.
The influence of porogen dispersion on the structure and permeability of highly porous material from nickel nanopowder 56

Sudarchikova M.A., Nasakina E.O., Davydova G.A., Valiullin L.R., Morozova Ya.A., Kottsov S.Yu., Prokofiev P.A., Konushkin S.V., Sergienko K.V., Sevostyanov M.A., Kolmakov A.G.
Influence of composition and surface roughness of titanium alloys on vital activity of mesenchymal stem cells 65

Materials and Coatings Fabricated Using the Additive Manufacturing Technologies

Zaytsev A.I., Sotov A.V., Abdrahmanova A.E., Popovich A.A.
Additive manufacturing of polymer-ceramic materials using fused deposition modeling (FDM) technology: A review 77

Содержание

Самораспространяющийся высокотемпературный синтез

Бобожанов А.Р., Рогачев А.С.
Самораспространяющийся высокотемпературный синтез высокоэнтропийных материалов: Обзор 5

Джусупкалиева Р.И., Быстрова И.М., Помогайло С.И., Борщ В.Н.
Синтез в процессе низкотемпературного горения на основе природной опоки Co–Mn-катализаторов глубокого окисления CO и пропана 17

Амосов А.П., Титова Ю.В., Уварова И.А., Белова Г.С.
Азидный самораспространяющийся высокотемпературный синтез высокодисперсной порошковой композиции AlN–SiC с применением политетрафторэтилена 28

Титова Ю.В., Якубова А.Ф., Белова Г.С.
Самораспространяющийся высокотемпературный синтез высокодисперсной композиции Si_3N_4–TiC с использованием азида натрия и различных источников углерода 44

Пористые материалы и биоматериалы

Шустов В.С., Зеленский В.А., Алымов М.И., Анкудинов А.Б., Устюхин А.С.
Влияние дисперсности порообразователя на структуру и проницаемость высокопористого материала из нанопорошка никеля 56

Сударчикова М.А., Насакина Е.О., Давыдова Г.А., Валиуллин Л.Р., Морозова Я.А., Котцов С.Ю., Прокофьев П.А., Конушкин С.В., Сергиенко К.В., Севостьянов М.А., Колмаков А.Г.
Влияние состава и шероховатости поверхности титановых сплавов на жизнедеятельность мезенхимальных стволовых клеток 65

Материалы и покрытия, получаемые методами аддитивных технологий

Зайцев А.И., Сотов А.В., Абдрахманова А.Э., Попович А.А.
Аддитивное производство полимер-керамических материалов методом послойного наплавления материала (FDM-технология): Обзор 77

Self-Propagating High-Temperature Synthesis
Самораспространяющийся высокотемпературный синтез

UDC 621.762

https://doi.org/10.17073/1997-308X-2024-6-5-16

Review article
Обзорная статья

Self-propagating high-temperature synthesis of high-entropy materials: A review

A. R. Bobozhanov✉**, A. S. Rogachev**

Merzhanov Institute of Structural Macrokinetics and Materials Science of the Russian Academy of Sciences
8 Academician Osip'yan Str., Chernogolovka, Moscow Region 142432, Russia

✉ bobozhanov.anis@mail.ru

Abstract. High-entropy alloys (HEAs) and compounds, first studied in 2004, represent a new class of materials with promising applications across various technologies and industries. Currently, they include metallic alloys based on disordered solid solutions, ceramic materials based on multicomponent oxides, borides, carbides, silicides, nitrides, and their combinations, as well as ceramic-metal composites. Among the methods for producing high-entropy materials, such as the crystallization of multicomponent melts, mechanical alloying in ball mills, and others, self-propagating high-temperature synthesis (SHS) holds a special place. This review presents the current state of research and development on high-temperature materials produced using the SHS method. It has been shown that the synthesis of metallic high-entropy alloys via SHS is only possible when thermally coupled reactions are employed. This is realized in metallothermic processes and in the synthesis of ceramic-metal composites from elements. The SHS of refractory high-entropy carbides, nitrides, borides, and other compounds can also be performed following the classical element-based synthesis approach. At the same time, the combination of SHS with pre-mechanical alloying of metallic components proves to be effective. For the consolidation of SHS-produced powder products, spark plasma sintering is most commonly used. Additionally, the method of solution combustion synthesis for producing high-entropy ceramics based on oxides is discussed. It has been demonstrated that SHS technology, combined with mechanical activation, mechanical alloying, electric spark plasma sintering, and hot pressing, allows for solving many practical problems in the production of a variety of ceramic, ceramic-metal, and metallic materials based on high-entropy phases.

Keywords: self-propagating high-temperature synthesis (SHS), high-entropy alloys (HEAs), high-entropy compounds, powder metallurgy, carbides, nitrides, oxides, borides

Acknowledgements: This work was carried out with the support of the Russian Science Foundation, Project № 20-13-00277П.

For citation: Bobozhanov A.R., Rogachev A.S. Self-propagating high-temperature synthesis of high-entropy materials: A review. *Powder Metallurgy and Functional Coatings*. 2024;18(6):5–16. https://doi.org/10.17073/1997-308X-2024-6-5-16

Самораспространяющийся высокотемпературный синтез высокоэнтропийных материалов: Обзор

А. Р. Бобожанов✉**, А. С. Рогачев**

Институт структурной макрокинетики и проблем материаловедения
им. А.Г. Мержанова Российской академии наук
Россия, 142432, Московская обл., г. Черноголовка, ул. Акад. Осипьяна, 8

✉ bobozhanov.anis@mail.ru

Аннотация. Высокоэнтропийные сплавы и соединения, первые исследования которых были опубликованы в 2004 г., представляют новый класс материалов, перспективных для использования во многих технологиях и производствах. В настоящее время они включают в себя металлические сплавы на основе разупорядоченных твердых растворов, керамические материалы на основе многокомпонентных оксидов, боридов, карбидов, силицидов, нитридов и их комбинаций, а также керамико-металлические композиты. Среди методов получения высокоэнтропийных материалов, таких как кристаллизация многокомпонентных расплавов, механическое сплавление в шаровых мельницах и др., особое место занимает самораспространяющийся высокотемпературный синтез (СВС). В обзоре представлено современное состояние исследований и разработок высокотемпературных материалов, получаемых с использованием метода СВС. Показано, что синтез металлических высокоэнтропийных сплавов методом СВС возможен только при использовании термически сопряженных реакций. Это реализуется в процессах металлотермического типа, а также в синтезе керамико-металлических композитов из элементов. Осуществление СВС тугоплавких высокоэнтропийных карбидов, нитридов, боридов и других соединений возможно и по классической схеме синтеза из элементов. При этом эффективным оказывается сочетание СВС с предварительным механическим сплавлением металлических компонентов. Для консолидации порошковых продуктов СВС чаще всего используется электроискровое плазменное спекание. Рассмотрен также метод синтеза горением растворов для получения высокоэнтропийной керамики на основе оксидов. Показано, что технология СВС в сочетании с механическим активированием, механосплавлением, электроискровым плазменным спеканием и горячим прессованием позволяет решать многие практические задачи получения разнообразных керамических, керамико-металлических и металлических материалов на основе высокоэнтропийных фаз.

Ключевые слова: самораспространяющийся высокотемпературный синтез (СВС), высокоэнтропийные сплавы (ВЭС), высокоэнтропийные соединения, порошковая металлургия, карбиды, нитриды, оксиды, бориды

Благодарности: Работа выполнена при поддержке Российского научного фонда, проект № 20-13-00277П.

Для цитирования: Бобожанов А.Р., Рогачев А.С. Самораспространяющийся высокотемпературный синтез высокоэнтропийных материалов (обзор). *Известия вузов. Порошковая металлургия и функциональные покрытия*. 2024;18(6):5–16. https://doi.org/10.17073/1997-308X-2024-6-5-16

Introduction

A new class of materials, known as “high-entropy,” encompasses metallic alloys based on disordered solid solutions, ceramic materials based on multicomponent oxides, borides, carbides, silicides, nitrides, and their combinations, as well as ceramic-metal composites. The history of their development spans only two decades – a very short period for metallurgy. The first publications on high-entropy alloys (HEAs) appeared in 2004 [1; 2]. These alloys represented single-phase solid solutions of five or more metals, taken in equal or comparable concentrations. This distinguishes HEAs from traditional alloys, in which the base is typically one metal (at most two), with other components added in small concentrations. Mixing five or more different types of atoms in the crystal structure of disordered solid solutions results in a sufficiently high configurational mixing entropy to stabilize the solid solution.

As is well known from thermodynamics, the stable state of a system corresponds to the minimum value of the Gibbs free energy:

$$G = H - TS, \tag{1}$$

where H is enthalpy, S is entropy (considering only the mixing entropy), and T is the absolute temperature in Kelvin. Thus, the stability of a phase at temperature T is ensured if any change in the structure of the phase leads to an increase in Gibbs free energy:

$$\Delta G = \Delta H - T\Delta S > 0. \tag{2}$$

For example, the decomposition of a disordered solid solution into ordered intermetallic phases (compounds) can be thermodynamically favorable due to a reduction in enthalpy ($\Delta H < 0$), but at the same time, the mixing entropy will decrease as more ordered phases are formed ($\Delta S < 0$), causing the second term in equation (2) to be positive ($-T\Delta S > 0$). The phase will remain stable only if the increase in free energy due to the formation of ordered phases is greater than the decrease due to the reduction in enthalpy. The stability condition from (2) can be rewritten as

$$\left|\Delta S\right| > \left|\frac{\Delta H}{T}\right|. \tag{3}$$

Here, the magnitudes of ΔS and ΔH are compared, as both quantities are negative in this case. Therefore, a sufficiently high mixing entropy is required to stabilize the phase. According to Boltzmann’s formula, the mixing entropy of N types of atoms (alloy components) in equal proportions can be approximated as

$$\Delta S = R\ln N, \tag{4}$$

where R is the universal gas constant. The more components there are in an equiatomic alloy, the higher the mixing entropy.

For five or more components

$$\Delta S \geq 1.61R = 13.4\ \text{J/(mol·K)}. \tag{5}$$

This is the condition of high entropy that gave these new alloys their name [2; 3]. It should be noted that the stabilizing role of entropy in the formation of multicomponent solid solutions is still not entirely clear. Therefore, in addition to the most common name “high-entropy alloys”, other terms are used in the scientific literature for this class of materials, such as complex concentrated alloys, multi-principal element alloys (MPEAs), and others. The rapid development of HEAs is reflected in thousands of publications, the results of which are analyzed in several reviews [4–11] and monographs [12–14].

Ten to fifteen years after the first publications on HEAs, research on high-entropy ceramics (HECs) began to emerge. Initially, these were multicomponent oxides [15], followed by carbides and nitrides [16–18], borides [19; 20], and other compounds. A common feature of these materials is the presence of five or more types of atoms in the lattice sites of the crystal structure, with smaller non-metal atoms occupying the interstitial spaces between the metallic atoms. Thus, HECs can be considered as solid solutions of several binary compounds. For example, carbides such as TiC, ZrC, HfC, NbC, and TaC can dissolve in each other to form the high-entropy carbide $TaNbHfTiZrC_5$.

The intense research and development in the field of HEAs and HECs can be explained by their exceptional properties, including high mechanical strength and toughness at both low (down to cryogenic) and high temperatures, wear resistance, heat resistance, and corrosion resistance, as well as unusual electrical and magnetic characteristics. Powder metallurgy methods, particularly mechanical alloying and self-propagating high-temperature synthesis (SHS), are highly promising for the production of HEAs and HECs. To date, there is no specialized review on the application of SHS for the synthesis of HEAs and HECs. Therefore, the goal of our work was to assess the current state of research on SHS of various high-entropy materials – HEAs, HECs, and their composites.

1. SHS of high-entropy metallic alloys

1.1. Thermally coupled reactions

For the SHS process to proceed, sufficient heat must be released during the reaction to sustain the propagation of the combustion wave. This requires a highly negative enthalpy change ΔH. For example, in the reaction Ni + Al = NiAl, the enthalpy is –118 kJ/mol, while in the reaction Ti + C = TiC, it is –209 kJ/mol. Clearly, this contradicts the stability condition (3) for the formation of a disordered solid solution. In [21], the following semi-empirical criterion for HEA formation was proposed:

$$\Omega = \frac{T_m \Delta S}{\Delta H} \geq 1.1, \qquad (6)$$

where T_m is the melting temperature of the alloy.

This leads to a constraint on the heat of the SHS reaction:

$$G = |\Delta H| \leq 0.91 T_m \Delta S \approx 20 \div 30 \text{ kJ/mol}. \qquad (7)$$

This value is an order of magnitude lower than typical SHS reaction enthalpies. Therefore, direct SHS from elemental metallic HEAs through a reaction such as $A + B + C + D + E = ABCDE$ becomes impossible for two reasons. First, the heat released during the mixing of metals, such as in the Cantor alloy CoCrFeNiMn, is insufficient to sustain a self-propagating reaction. Second, even if five metals are found that release enough heat upon mixing, a solid solution will not form due to the constraint presented in equation (7), and instead, several intermetallic phases will form.

This problem can be solved using the method of thermally coupled reactions proposed by A.G. Merzhanov [22], where two reactions participate in the SHS process – one weakly exothermic and the other strongly exothermic. The heat released from the first reaction provides additional heating for the second. Merzhanov referred to these as “thermally coupled” reactions. This scheme is well-suited for the synthesis of HEAs because the weakly exothermic process of forming a metallic solid solution becomes possible due to the additional heat from another SHS reaction, such as the formation of aluminum oxide, titanium carbide, or similar compounds. Currently, two approaches to thermally coupled synthesis of metallic HEAs can be distinguished, which can be termed the “metallothermic” and “cermet” approaches. Both of these methods are discussed further below.

1.2. Metallothermic synthesis of HEAs

The first results on the aluminothermic synthesis of HEAs with the composition $CoCrFeNiMnAl_x$ (where $x = 0.2 \div 2.0$) were obtained in 2016 [23]. For example, the chemical equation of the coupled reactions for the synthesis of equiatomic HEAs can be written as

$$0.33Co_3O_4 + 0.5Cr_2O_3 + 0.5Fe_2O_3 + NiO +$$
$$+ MnO_2 + 4.22Al = CoCrFeNiMnAl + 2.11Al_2O_3. \qquad (8)$$

In this case, the highly exothermic reaction is the oxidation of aluminum, which reduces all the oxides to form molten Al_2O_3. The heat released during this process is sufficient to melt all the reduced metals, which then mix to form a six-component metallic melt. The total heat release for this process is 480 kJ per mole of product, and the combustion temperature exceeds 2500 °C, which is higher than the melting points of all the components and products. Since the metallic and oxide melts do not mix and have different specific gravities, they separate under the influence of gravity. Centrifugal machines are used to accelerate this separation by artificially increasing gravitational force by several hundred times. As a result, the metallic melt accumulates at the bottom of the crucible, while the lighter aluminum oxide melt remains at the top. After cooling, two separate crystalline products are formed – a HEA ingot and solid aluminum oxide.

Using this method, HEAs such as $CuAlZrTiLi_x$ and $CuAlZrTi(LiCr)_x$, which have submicron microstructures and low specific gravities, have also been synthesized [24]. HEAs synthesized by the metallothermic method, like the Cantor alloy CoCrFeNiMn, can be applied in laser welding [25; 26] and friction stir welding [27]. The addition of carbon to the initial thermite powder mixture allowed the production of Cantor alloys strengthened by dispersions of $Me_{23}C_6$-type carbides [28].

HEAs such as $Co_xCrFeNiAl$ [29], $CoCrFeNiAl_xMo_y$ [30] and $CoCrFeNiAl_xCu_y$ [31] were also synthesized using the metallothermic process, but without the use of a centrifugal separator. The combustion occurred in a powder mixture of oxides and aluminum, with the bulk density placed in a copper crucible. The separation of the metallic melt and slag occurred under natural gravitational forces. This demonstrated the economic efficiency of this method for HEA production.

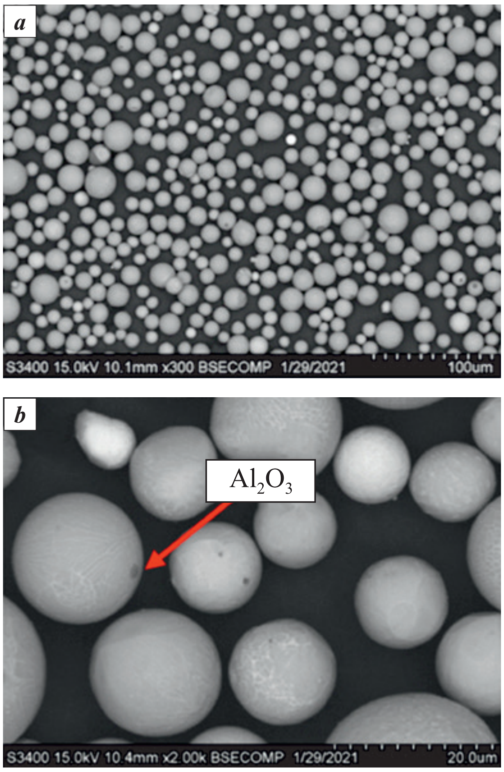

Fig. 1. Powder of heat-resistant NiAl–Cr–Co + 15 % Mo alloy obtained by metallothermic SHS followed by plasma spheroidization [32]

Рис. 1. Порошок жаропрочного сплава NiAl–Cr–Co + 15 % Mo, полученный методом металлотермического СВС с последующей плазменной сфероидизацией [32]

One promising application of metallothermically synthesized HEAs is the production of spherical-shaped powders for additive manufacturing technologies. SHS-produced ingots are crushed and ground in planetary mills, and the resulting narrow powder fractions are then spheroidized in an electric arc plasma torch. Using this method, heat-resistant alloys of NiAl–Cr–Co + 15 %Mo with an average particle size of 14.8 μm were produced [32]. The morphology of the resulting powder is shown in Fig. 1. Individual inclusions of aluminum oxide are observed on the surface of the particles (Fig. 1, *b*).

A four-component (medium-entropy) alloy AlTiVCr was recently obtained via metallothermy without centrifugal forces in steel crucibles [33]. The separation of the metallic melt and slag apparently occurred due to capillary forces, and the solidified alloy and oxide inclusions were then mechanically separated.

Finally, it is worth mentioning the work on the metallothermic synthesis of the AlCoCrFeNi HEA in graphite crucibles within a centrifugal machine [34]. Although the authors of this work claimed the method to be “new,” it essentially replicates the technology described in [23] a year earlier. Moreover, centrifugal SHS-metallothermy has been known for more than 30 years [35], and metallothermy in general for over 120 years [36].

In conclusion, it can be noted that the metallothermic synthesis of HEAs is currently the most developed among the methods for producing metallic HEAs using SHS processes.

1.3. SHS of high-entropy cermets

The production of ceramic-metal composites using the SHS method is also based on the aforementioned principle of thermally coupled SHS reactions. In this case, the highly exothermic reaction is typically synthesis from elements. Reactions between transition metals and carbon or boron are often used, for example:

$$Ti + C = TiC + 230\ \text{kJ/mol}, \tag{9}$$

$$Ti + 2B = TiB_2 + 290\ \text{kJ/mol}. \tag{10}$$

As mentioned earlier, the allowable heat for the formation of metallic HEAs is much lower than the heat of these chemical reactions, so the HEA components added to the exothermic mixture act as inert diluents. The SHS reaction scheme can be represented as:

$$(1-x)(\mathrm{Ti}+\mathrm{C})+x(\mathrm{Co}+\mathrm{Cr}+\mathrm{Fe}+$$
$$+\mathrm{Ni}+\mathrm{Mn})=(1-x)\mathrm{TiC}+x\mathrm{CoCrFeNiMn}. \quad (11)$$

The heat released during the reaction between titanium and carbon (9) is sufficient to raise the temperature above the melting points of all the metals. The melts of Co, Cr, Fe, Ni, and Mn combine and, after cooling, crystallize as an HEA. Instead of adding individual metals, pre-prepared HEA powder obtained by other methods (such as mechanical alloying) can be added to the reaction mixture:

$$(1-x)(\mathrm{Ti}+\mathrm{C})+x\mathrm{CoCrFeNiMn}=$$
$$=(1-x)\mathrm{TiC}+x\mathrm{CoCrFeNiMn}. \quad (12)$$

The addition of HEA, either as a mixture of metallic powders or as a pre-synthesized alloy, to the highly exothermic composition leads to a reduction in the combustion temperature. Fig. 2 shows the results of thermodynamic calculations of the adiabatic combustion temperature and experimental measurements of the combustion rate for compositions similar to (12), depending on the HEA content [37]. They indicate that combustion of such mixtures is possible with HEA content up to 40–50 wt. %, provided the combustion temperature remains above the melting points of the metals.

As a result of the SHS reaction, a solid framework of titanium carbide grains is formed, impregnated with a multicomponent metallic melt. Unlike in the metallothermic process, the ceramic and metallic phases do not separate, and upon cooling, a ceramic-metal composite (cermet) forms, consisting of TiC grains and a high-entropy metallic binder. An example of the microstructure and element distribution in such a cermet is shown in Fig. 3. Some features of the structure formation of these materials were studied in [38].

To consolidate ceramic-metal composites with a multicomponent binder based on the Cantor alloy, a method of hot SHS pressing was applied, where the workpiece is subjected to quasi-isostatic compression in a sand-filled mold immediately after the combustion wave passes through it [39]. This method, known as the technology for synthetic hard tool materials (STIM technology), had previously been developed for cermets with simpler binder compositions, such as TiC–Ni, TiC–Ni–Mo, TiC–Ni–Cr [35; 36; 40; 41].

The range of ceramic-metallic materials with HEA binders also includes:

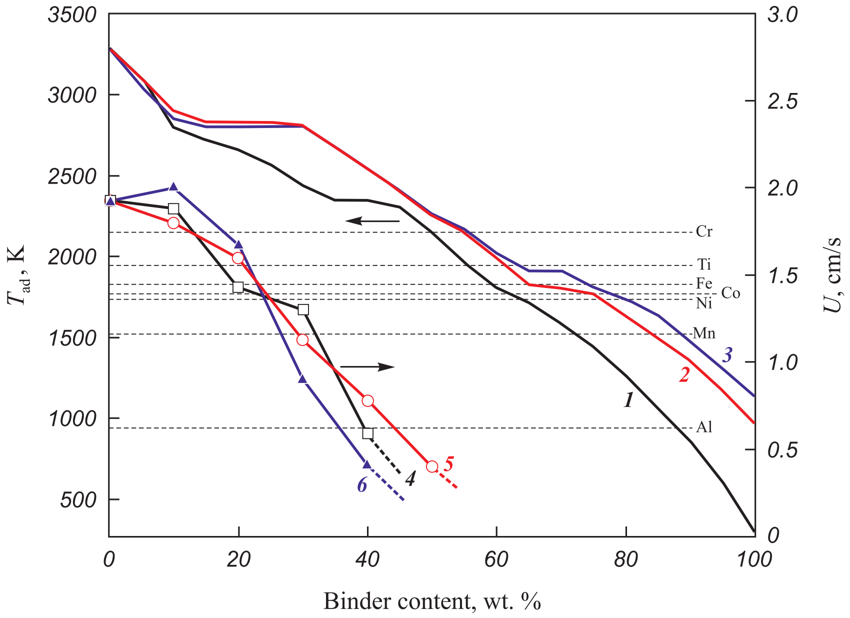

Fig. 2. Adiabatic combustion temperatures (thermodynamic calculation) and combustion rates (experiment) of Ti + C + HEA mixtures, depending on the composition and mass content of HEA: CoCrFeNiMn (***1***, ***4***); CoCrFeNiTi (***2***, ***5***); CoCrFeNiAl (***3***, ***6***) [37]
Dashed lines indicate the melting temperatures of the metals

Рис. 2. Адиабатические температуры горения (термодинамический расчет) и скорости горения (эксперимент) смесей Ti + C + ВЭС в зависимости от состава и массового содержания ВЭС: CoCrFeNiMn (***1***, ***4***); CoCrFeNiTi (***2***, ***5***); CoCrFeNiAl (***3***, ***6***) [37]
Штриховыми линиями показаны температуры плавления металлов

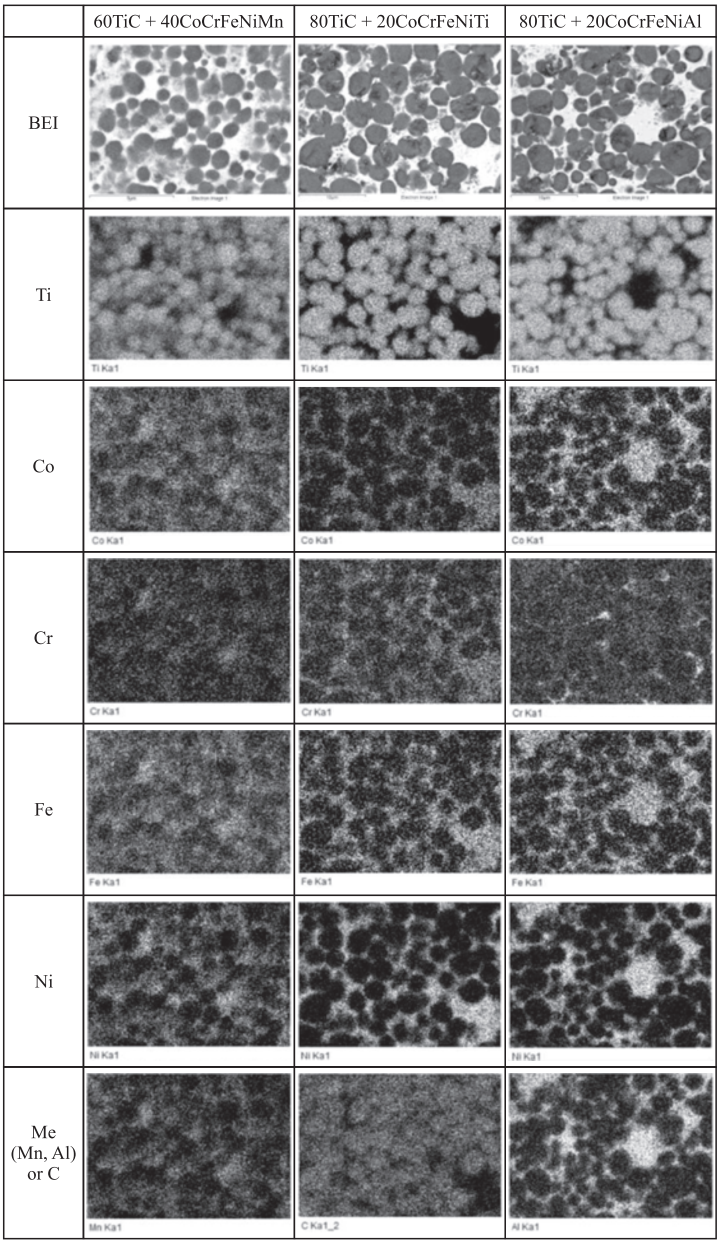

Fig. 3. Microstructure and elemental distribution in some SHS cermets with high-entropy binders [37]

Рис. 3. Микроструктура и распределение элементов в некоторых СВС-керметах с высокоэнтропийными связками [37]

- WC–CoCrFeNiMn [42],
- Ti(C,N)–CoCrFeNiAl [43; 44],
- TiB_2–CoCrFeNiTiAl [45; 46],
- TiB_2–CoCrFeNiAl [47],
- TiB_2–TiC–CoCrFeNiTiAl [48] and others.

The authors of [49] proposed considering such materials as a new class of cermets. However, in studies [42–48], pre-synthesized ceramic powders of carbides, borides, and carbonitrides were used, so SHS reactions did not occur. The material was formed during processes such as spark plasma sintering or hot pressing, where heating occurs not due to chemical reactions but from passing an electric current through the mold or the powder itself. There are few studies where such materials are produced without external heating, relying solely on the heat generated from the SHS reaction. However, thermodynamic calculations and initial experimental results indicate that these processes are entirely feasible, suggesting an expansion of research into high-entropy SHS cermets in the near future.

Recently, new types of high-entropy cermets have emerged. In these materials, the high-entropy phase is a multicomponent ceramic, while the binder consists of conventional metals or alloys. These materials will be discussed in the next section.

2. SHS of high-entropy ceramic phases

The crystalline structure of high-entropy ceramic phases consists of two sublattices: a cationic and an anionic one. In the cationic sublattice, there are metal cations of several types (no fewer than five), which are randomly distributed across the lattice sites. This random arrangement provides these compounds with high mixing entropy, which should stabilize the high-entropy ceramics (HECs) and prevent their decomposition into simpler phases. The anionic sublattice consists of atoms of a single type – oxygen, boron, carbon, or nitrogen. Depending on the type of anion, these materials are classified as high-entropy oxides, borides, carbides, or nitrides. It is theoretically possible to combine several anions in the anionic sublattice, such as in carbonitrides or oxycarbonitrides, but the realization of such HECs remains a task for the future. High-entropy ceramics can be considered as solid solutions of corresponding simple compound.

The dissolution of binary compounds into each other under external heating was used to produce the first HECs. Using this method, high-entropy diborides were synthesized [50]:

- $(Hf_{0.2}Zr_{0.2}Ta_{0.2}Mo_{0.2}Ti_{0.2})B_2$,
- $(Hf_{0.2}Zr_{0.2}Ta_{0.2}Nb_{0.2}Ti_{0.2})B_2$,
- $(Hf_{0.2}Zr_{0.2}Nb_{0.2}Mo_{0.2}Ti_{0.2})B_2$,
- $(Hf_{0.2}Mo_{0.2}Ta_{0.2}Nb_{0.2}Ti_{0.2})B_2$,
- $(Mo_{0.2}Zr_{0.2}Ta_{0.2}Nb_{0.2}Ti_{0.2})B_2$,
- $(Hf_{0.2}Zr_{0.2}Ta_{0.2}Cr_{0.2}Ti_{0.2})B_2$.

In this process, a mixture of simple diborides (e.g., TiB_2, ZrB_2, etc.) was processed for 6 h in a Spex 8000D shaker ball mill (SPEX SamplePrep LLC, USA) and then subjected to spark plasma sintering (SPS) for 5 min at a temperature of 2000 °C and a pressure of 30 MPa. The result was the formation of multicomponent hexagonal phases, some of which have ultra-high melting points. A similar method was used to obtain high-entropy carbides $(V_{0.2}Nb_{0.2}Ta_{0.2}Mo_{0.2}W_{0.2})C$ from a mixture of simple carbides, with milling time reduced to 2 h and SPS carried out at 2200 °C and 30 MPa for 10 min [51]. However, this approach is not applicable to SHS. As mentioned earlier, SHS of multicomponent ceramics from mixtures of pre-formed simple compounds is not possible due to insufficient heat from the reaction (with some oxide combinations being an exception). Therefore, to produce HECs via combustion or thermal explosion, mixtures of metallic and non-metallic reagents must be used, which react with significant heat release.

The exothermic SHS reaction can proceed in mixtures of metals with carbon or boron, during mechanical treatment in high-energy planetary ball mills and during SPS. Using this approach, carbides such as (HfTaTiNbZr)C, (HfTaTiNbMo)C and (TiZrHfTaNb)C were synthesized [52–54]. If the chemical reaction leading to the formation of new phases occurs due to heating during SPS, this process is called “reaction SPS” [55]. It can, in principle, be considered a type of SHS process, although there is insufficient data on the temperature conditions inside the molds to determine whether self-heating or the formation of self-propagating combustion waves occurs during mechanical alloying and SPS.

High-entropy carbides such as $TaZrHfNbTiC_5$ [56–59], $TaTiNbVWC_5$, and $TaNbVMoWC_5$ [58] were directly synthesized using SHS, revealing two key features.

1. Direct synthesis from a mixture of elemental metal and carbon powders often leads to the formation of a multiphase mixture of carbides. This is likely because each metal reacts with carbon separately in the combustion zone. For example, titanium melts at a relatively low temperature (1670 °C) and forms TiC particles before tantalum (3017 °C) melts and reacts with the remaining carbon. Once the simple carbide particles are formed, it becomes difficult to dissolve them into each other. Therefore, a three-stage process was proposed:

– a mixture of metallic powders is processed in planetary mills to form a powder of a high-entropy solid solution of metals;

– carbon (soot) is added to the solution, and additional processing in planetary mills is carried out;

– the resulting reaction mixture is used for SHS of carbides.

2. Some highly refractory HEC components (e.g., Mo, W, V) release little heat during their reaction with carbon, so it is advisable to conduct SHS in the thermal explosion mode, using additional heating of the samples to the point of self-ignition.

Through preliminary mechanical activation of metal mixtures in a planetary mill under an argon atmosphere, followed by SHS in a nitrogen atmosphere, the high-entropy nitride $(Hf_{0.25}Ti_{0.25}Cr_{0.25}(FeV)_{0.25})N$ was synthesized in [60], and by combining metallothermic synthesis and SHS from elements, the HEC Al_2O_3/(NbTaMoW)C was obtained [61].

Finally, a new trend of adding a metallic binder to HECs should be noted [62; 63]. Although such materials, belonging to the class of sintered hard alloys, have so far been produced by traditional powder metallurgy methods, the use of SHS (e.g., via STIM technology) appears to be a promising approach in this area.

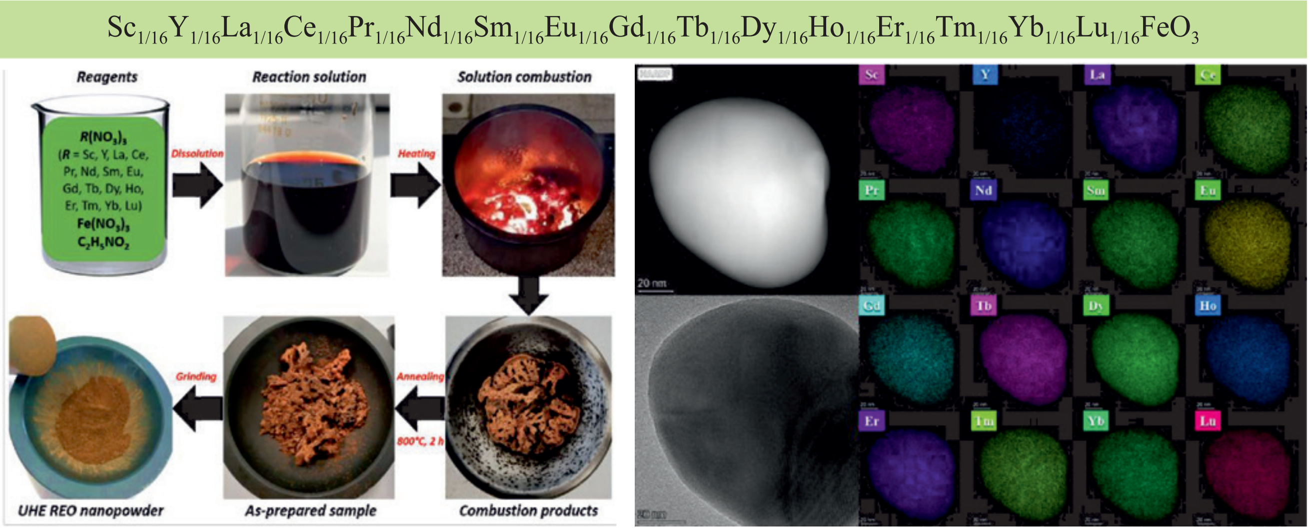
$Sc_{1/16}Y_{1/16}La_{1/16}Ce_{1/16}Pr_{1/16}Nd_{1/16}Sm_{1/16}Eu_{1/16}Gd_{1/16}Tb_{1/16}Dy_{1/16}Ho_{1/16}Er_{1/16}Tm_{1/16}Yb_{1/16}Lu_{1/16}FeO_3$

Fig. 4. Scheme of the solution combustion synthesis process and distribution of elements in the product nanoparticle [66]

Рис. 4. Схема процесса синтеза горением растворов и распределение элементов в наночастице продукта [66]

3. Synthesis of high-entropy phases by solution combustion

Solution Combustion Synthesis (SCS) is a variation of SHS that allows the production of nanopowders of oxides and other compounds, including multicomponent materials [64]. The process proceeds as follows: metal nitrates are dissolved in water along with an organic compound (such as glycine, urea, or citric acid). The solution is then heated to a relatively low temperature of 120–140 °C, causing the water to evaporate, after which the resulting gel ignites. The combustion product is a loose powder composed of particles ranging in size from 10 to 100 nm. Since all the components are mixed at the molecular level in the solution, they are also uniformly distributed in the nanoparticles of the product. This enables the combination of many elements in solid solutions and single-phase compounds. Using this method, high-entropy oxides such as $(Co_{0.2}Cu_{0.2}Mg_{0.2}Ni_{0.2}Zn_{0.2})O$ have been produced. Another example is a “record-breaking” ferrite in terms of the number of components [66], which exhibits valuable magnetic properties. The schematic of the SCS process and *X*-ray maps showing the homogeneous distribution of many elements in the nanoparticles of the product are presented in Fig. 4.

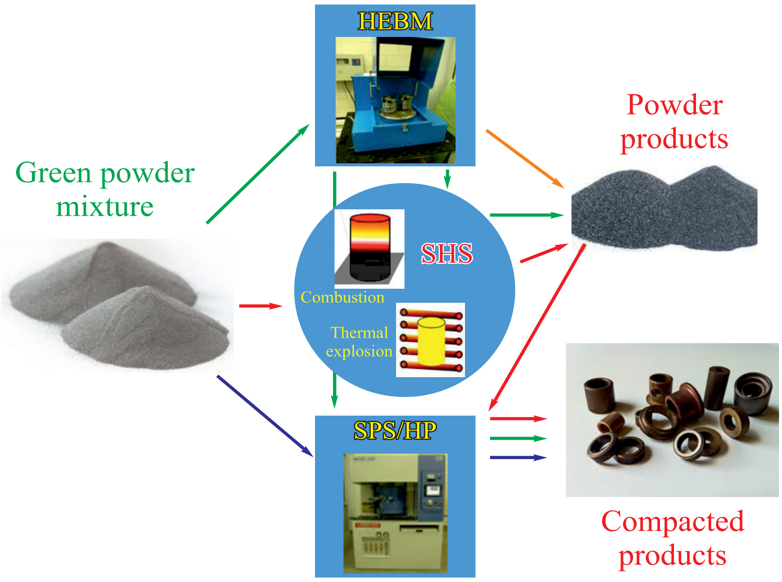

Fig. 5. Scheme of possible pathways for obtaining high-entropy materials using SHS

Рис. 5. Схема возможных маршрутов получения высокоэнтропийных материалов с использованием СВС

Conclusion

The SHS technology, in combination with mechanical activation, mechanical alloying, spark plasma sintering, and hot pressing, provides solutions to many practical challenges in the production of various ceramic, ceramic-metal, and metallic materials based on high-entropy phases. Possible technological pathways for producing such materials are illustrated in the diagram in Fig. 5. It seems highly likely that this scientific and technological field will experience rapid development in the coming years.

References / Список литературы

1. Cantor B., Chang I.T.H., Knight P., Vincent A.J.B. Microstructural development in equiatomic multicomponent alloys. *Materials Science and Engineering: A*. 2004;375-377: 213–218. https://doi.org/10.1016/j.msea.2003.10.257
2. Yeh J.-W., Chen S.-K., Lin S.J., Gan J.-Y., Chin T.-S., Shun T.-T., Tsau C.-H., Chang S.-Y. Nanostructured high-entropy alloys with multiple principal elements: Novel design concepts and outcomes. *Advanced Engineering Materials*. 2004;6(5):299–303. https://doi.org/10.1002/adem.200300567
3. Yeh J.-W. Recent progress in high-entropy alloys. *Annales De Chimie – Science des Materiaux*. 2006;31(6):633–648. https://doi.org/10.3166/ACSM.31.633-648
4. Zhang Y., Zuo T.T., Tang Z., Gao M.C., Dahmen K.A., Liaw P.K., Lu Z.P. Microstructures and properties of high-entropy alloys. *Progress in Materials Science*. 2014;61: 1–93. https://doi.org/10.1016/j.pmatsci.2013.10.001
5. Cantor B. Multicomponent and high entropy alloys. *Entropy*. 2014;16(9):4749–4768. https://doi.org/10.3390/e16094749
6. Alaneme K.K., Bodunrin M.O., Oke S.R. Processing, alloy composition and phase transition effect on the mechanical and corrosion properties of high entropy alloys: a review. *Journal of Materials Research and Technology*. 2016;5(4):384–393. http://doi.org/10.1016/j.jmrt.2016.03.004
7. Miracle D.B., Senkov O.N. A critical review of high entropy alloys and related concepts. *Acta Materialia*. 2017;122: 448–511. https://doi.org/10.1016/j.actamat.2016.08.081
8. Zhang W., Liaw P.K., Zhang Y. Science and technology in high-entropy alloys. *Science China Materials*. 2018;61(1): 2–22. https://doi.org/10.1007/s40843-017-9195-8
9. Rogachev A.S. Structure, stability, and properties of high-entropy alloys. *Physics Metals and Metallography*. 2020;121(8):733–764. https://doi.org/10.1134/S0031918X20080098
10. Cantor B. Multicomponent high-entropy Cantor alloys. *Progress in Materials Science*. 2021;120:1–36. https://doi.org/10.1016/j.pmatsci.2020.100754
11. Bridges D., Fieser D., Santiago J.J., Hu A. Novel frontiers in high-entropy alloys. *Metals*. 2023;13(7):1193. https://doi.org/10.3390/met13071193
12. Murty B.S., Yeh J.W., Ranganathan S., Bhattacharjee P.P. High-entropy alloys. 2nd ed. Amsterdam: Elsevier, 2019. 374 p. https://doi.org/10.1016/C2017-0-03317-7
13. Zhang Y. High-entropy materials. A brief introduction. Singapore: Springer Nature, 2019. 159 p. https://doi.org/10.1007/978-981-13-8526-1
14. Jamieson B., Liaw P.K. (Ed.). High-entropy materials: Theory, experiments, and applications. Switzerland AG: Springer Nature, 2021, 774 p. https://doi.org/10.1007/978-3-030-77641-1
15. Rost C.M., Sachet E., Borman T., Moballegh A., Dickey E.C., Hou D., Jones J.L., Curtarolo S., Jon-Paul M. Entropy-stabilized oxides. *Nature Communications*. 2015; 6(1):8485. https://doi.org/10.1038/ncomms9485
16. Dusza J., Švec P., Girman V., Sedlák R., Castle E.G., Csanádi T., Kovalčíková A., Reece M.J. Microstructure of (Hf–Ta–Zr–Nb)C high-entropy carbide at micro and nano/atomic level. *Journal of the European Ceramic Society*. 2018; 38(12):4303–4307. https://doi.org/10.1016/j.jeurceramsoc.2018.05.006
17. Castle E., Csanádi T., Grasso S., Dusza J., Reece M. Processing and properties of high-entropy ultra-high temperature carbides. *Scientific Reports*. 2018;8609(8):1–12. https://doi.org/10.1038/s41598-018-26827-1
18. Yang Y., Ma L., Gan G.-Y., Wang W., Tang B.-Y. Investigation of thermodynamic properties of high entropy (TaNbHfTiZr)C and (TaNbHfTiZr)N. *Journal of Alloys and Compounds*. 2019;788:1076–1083. https://doi.org/10.1016/j.jallcom.2022.164526
19. Gu J., Zou J., Sun S.-K., Wang H., Yu S.-Y., Zhang J., Wang W., Fu Z. Dense and pure high-entropy metal diboride ceramics sintered from self-synthesized powders via boro/carbothermal reduction approach. *Science China Materials*. 2019; 62(12):1898–1909. https://doi.org/10.1007/s40843-019-9469-4
20. Tallarita G., Licheri R., Garroni S., Orrù R., Cao G. Novel processing route for the fabrication of bulk high-entropy metal diborides. *Scripta Materialia*. 2019;158:100–104. https://doi.org/10.1016/j.scriptamat.2018.08.039
21. Yang X., Zhang Y. Prediction of high-entropy stabilized solid-solution in multi-component alloys. *Materials Chemistry and Physics*. 2012;132:233– 238. https://doi.org/10.1016/j.matchemphys.2011.11.021
22. Merzhanov A.G. Thermally coupled processes of self-propagating high-temperature synthesis. *Doklady Academii nauk*. 2010;433(5):1–4. (In Russ.).

    Мержанов А.Г. Термически сопряженные процессы самораспространяющегося высокотемпературного синтеза. *Доклады Академии наук*. 2010;433(5):1–4.
23. Sanin V.N., Yukhvid V.I., Ikornikov D.M., Andreev D.E., Sachkova N.V. SHS metallurgy of high-entropy transition metal alloys. *Doklady Physical Chemistry* 2016;470: 145–149. https://doi.org/10.1134/S001250161610002X

    Санин В.Н., Юхвид В.И., Икорников Д.М., Андреев Д.Е., Сачкова Н.Д, Алымов М.И. СВС-металлургия литых высокоэнтропийных сплавов на основе переходных металлов. *Доклады Академии наук*. 2016;470(4):421–426. https://doi.org/10.7868/S0869565216280124

24. Sanin V.N., Ikornikov D.M., Andreev D.E., Sachkova N.V., Yukhvid V.I. Synthesis of cast high entropy alloys with a low specific gravity by centrifugal metallothermic SHS-methods. *Advanced Materials & Technologies*. 2017;(3):24–33.
https://doi.org/10.17277/amt.2017.03.pp.024-033

25. Kashaev N., Ventzke V., Stepanov N., Shaysultanov D., Sanin V., Zherebtsov S. Laser beam welding of a CoCrFeNiMn-type high entropy alloy produced by self-propagating high-temperature synthesis. *Intermetallics*. 2018;96:63–71.
https://doi.org/10.1016/j.intermet.2018.02.014

26. Kashaev N., Ventzke V., Petrov N., Horstmann M., Zherebtsov S., Shaysultanov D., Sanin V., Stepanov N. Fatigue behaviour of a laser beam welded CoCrFeNiMn-type high entropy alloy. *Materials Science and Engineering: A*. 2019;766:138358.
https://doi.org/10.1016/j.msea.2019.138358

27. Shaysultanov D., Stepanov N., Malopheyev S., Vysotskiy I.V., Sanin V.V., Mironov S., Kaibyshev R., Salishchev G., Zherebtsov S. Friction stir welding of a carbon-doped CoCrFeNiMn high-entropy alloy. *Materials Characterization*. 2018;145:353–361.
https://doi.org/10.1016/j.matchar.2018.08.063

28. Klimova M., Shaysultanov D., Chernichenko R.S., Sanin V.N., Stepanov N., Zherebtsov S., Belyakov A.N. Recrystallized microstructures and mechanical properties of a C-containing CoCrFeNiMn-type high-entropy alloy. *Materials Science and Engineering: A*. 2019;740:201–210.
https://doi.org/10.1016/j.msea.2018.09.113

29. Kaya F., Yetiş M., Selimoğlu G. İ., Derin B. Influence of Co content on microstructure and hardness of $AlCo_xCrFeNi$ ($0 \le x \le 1$) high-entropy alloys produced by self-propagating high-temperature synthesis. *Engineering Science and Technology, an International Journal*. 2022;27:101003.
https://doi.org/10.1016/j.jestch.2021.05.007

30. Kaya F., Dizdar K.C., Aliakbarlu S., Selimoğlu G.İ., Derin B. Self-propagating high-temperature synthesis of Al_x-$CoCrFeNiMo_y$ high-entropy alloys: Thermochemical modelling, microstructural evaluation and high temperature oxidation behaviour. *Materials Chemistry and Physics*. 2024;318:129304.
https://doi.org/10.1016/j.matchemphys.2024.129304

31. Kaya F., Erşan A.A., Çayır E., Kirim T., Duygulu Ö., Selimoğlu G.İ., Derin B. Cost-effective synthesis and thermomechanical processing of $Al_xCoCrFeNiCu_y$ ($x\&y$ = 0.5, 1) high-entropy alloys. *Materials Chemistry and Physics*. 2024;311:128554.
https://doi.org/10.1016/j.matchemphys.2023.128554

32. Sanin V.V., Kaplansky Yu.Yu., Aheiev M.I., Levashov E.A., Petrzhik M.I., Bychkova M.Ya., Samokhin A.V., Fadeev A.A., Sanin V.N., Heat-resistant alloys NiAl–Cr–Co–X (X = La, Mo, Zr, Ta, Re) and fabrication of powders for additive manufacturing. *Materials*. 2021;14:3144. https://doi.org/10.3390/ma14123144

33. Dastjerdi Z., Sharifitabar M., Afarani M. S. Preparation of a hard AlTiVCr compositionally complex alloy by self-propagating high-temperature synthesis. *International Journal of Refractory Metals and Hard Materials*. 2024;122:106694.
https://doi.org/10.1016/j.ijrmhm.2024.106694

34. Li R.X., Liaw P.K., Zhang Y., Synthesis of $Al_xCoCrFeNi$ high-entropy alloys by high-gravity combustion from oxides. *Materials Science and Engineering: A*. 2017; 707:668–673. https://doi.org/10.1016/j.msea.2017.09.101

35. Borovinskaya I.P., Gromov A.A., Levashov E.A., Maksimov Yu.M., Mukasyan A.S., Rogachev A.S. (eds.). Concise encyclopedia of SHS. Elsevier, 2017. 438 p.
https://doi.org/10.1016/C2015-0-00439-7

36. Rogachev A.S., Mukasyan A.S. Combustion for material synthesis. 1st ed. CRC Press Taylor & Francis Group, 2014. 424 p. https://doi.org/10.1201/b17842

37. Rogachev A.S., Vadchenko S.G., Kochetov N.A., Kovalev D.Yu., Kovalev I.D., Shchukin A.S., Gryadunov A.N., Baras F., Politano O. Combustion synthesis of TiC-based ceramic-metal composites with high entropy alloy binder. *Journal of the European Ceramic Society*. 2020;40(7):2527–2532.
https://doi.org/10.1016/j.jeurceramicsos.2019.11.059

38. Vadchenko S.G., Vergunova Yu.S., Rogachev A.S., Kovalev I.D., Mukhina N.I. Formation of products upon ignition, combustion and melting of mixtures of high-entropy alloy FeNiCoCrCu with titanium and carbon. *Powder Metallurgy and Functional Coatings*. 2023;17(1):28–38.
https://doi.org/10.17073/1997-308X-2023-1-28-38

Вадченко С.Г., Вергунова Ю.С., Рогачев А.С., Ковалев И.Д., Мухина Н.И. Формирование продуктов при воспламенении, горении и плавлении смесей высокоэнтропийного сплава FeNiCoCrCu с титаном и углеродом. *Известия вузов. Порошковая металлургия и функциональные покрытия*. 2023;17(1):28–38.
https://doi.org/10.17073/1997-308X-2023-1-28-38

39. Rogachev A.S., Gryadunov A.N., Kochetov N.A., Shchukin A.S., Baras F., Politano O. High-entropy-alloy binder for TiC-based cemented carbide by SHS method. *International Journal of Self-Propagating High-Temperature Synthesis*. 2019;28:196–198.
https://doi.org/10.3103/S1061386219030117

40. Merzhanov A.G. Self-propagating high-temperature synthesis: Twenty years of research and findings. In: *Combustion and plasma synthesis of high-temperature materials*. Munir Z., Holt J.B. (Eds.). New York: VCH, 1990. P. 1–53.

41. Levashov E.A., Mukasyan A.S., Rogachev A.S., Shtansky D.V. Self-propagating high-temperature synthesis of advanced materials and coatings. *International Materials Reviews*. 2017;62(4):203–239.
https://doi.org/10.1080/09506608.2016.1243291

42. Velo I.L., Gotor F.J., Alcala M.D., Real C., Cordoba J.M. Fabrication and characterization of WC-HEA cemented carbide based on the CoCrFeNiMn high entropy alloy. *Journal of Alloys and Compounds*. 2018;746:1–8.
https://doi.org/10.1016/j.jallcom.2018.02.292

43. Zhu G., Liu Y., Ye J. Fabrication and properties of Ti(C,N)-based cermets with multi-component AlCoCrFeNi high-entropy alloys binder. *Materials Letters*. 2013;113:80–82.
http://dx.doi.org/10.1016/j.matlet.2013.08.087

44. Zhu G., Liu Y., Ye J. Early high-temperature oxidation behavior of Ti(C,N)-based cermets with multi-compo-

nent AlCoCrFeNi high-entropy alloy binder. *International Journal of Refractory Metals and Hard Materials*. 2014;44:35–41.
http://dx.doi.org/10.1016/j.ijrmhm.2014.01.005

45. Ji W., Zhang J., Wang W., Wang H., Zhang F., Wang Y., Fu Z. Fabrication and properties of TiB$_2$-based cermets by spark plasma sintering with CoCrFeNiTiAl high-entropy alloy as sintering aid. *Journal of the European Ceramic Society*. 2015;35(3):879–886.
http://dx.doi.org/10.1016/j.jeurceramsoc.2014.10.024

46. Fu Z., Koc R. Ultrafine TiB$_2$–TiNiFeCrCoAl high-entropy alloy composite with enhanced mechanical properties. *Materials Science and Engineering: A*. 2017;702:184–188.
http://dx.doi.org/10.1016/j.msea.2017.07.008

47. Zhang S., Sun Y., Ke B., Li Y., Ji W., Wang W., Fu Z., Preparation and characterization of TiB$_2$-(supra-nano-dual-phase) high-entropy alloy cermet by spark plasma sintering. *Metals*. 2018;58(8):1–10.
https://doi.org/10.3390/met8010058

48. Fu Z., Koc R. TiNiFeCrCoAl high-entropy alloys as novel metallic binders for TiB$_2$–TiC based composites. *Materials Science and Engineering A*. 2018;735:302–309.
https://doi.org/10.1016/j.msea.2018.08.058

49. De la Obra A.G., Avilés M.A., Torres Y., Chicardi E., Gotor F.J. A new family of cermets: Chemically complex but microstructurally simple. *International Journal of Refractory Metals and Hard Materials*. 2017;63:17–25.
http://dx.doi.org/10.1016/j.ijrmhm.2016.04.011

50. Gild J., Zhang Y., Harrington T., Jiang S., Hu T., Quinn M.C., Mellor W.M., Zhou N., Vecchio K., Luo J. High-entropy metal diborides: A new class of high-entropy materials and a new type of ultrahigh temperature ceramics. *Scientific Reports*. 2016;6(1):37946.
https://doi.org/10.1038/srep37946

51. Harrington T.J., Gild J., Sarker P., Toher C., Rost C.M., Dippo O.F., McElfresh C., Kaufmann K., Marin E., Borowski L., Hopkins P.E., Luo J., Curtarolo S., Brenner D.W., Vecchio K.S. Phase stability and mechanical properties of novel high entropy transition metal carbides. *Acta Materialia*. 2019;166:271–280.
https://doi.org/10.1016/j.actamat.2018.12.054

52. Moskovskikh D.O., Vorotilo S., Sedegov A.S., Kuskov K.V., Bardasova K.V., Kiryukhantsev-Korneev P.V., Zhukovskyi M., Mukasyan A.S. High-entropy (HfTaTiNbZr)C and (HfTaTiNbMo)C carbides fabricated through reactive high-energy ball milling and spark plasma sintering. *Ceramics International*. 2020;46:19008–19014.
https://doi.org/10.1016/j.ceramint.2020.04.230

53. Sedegov A.S., Bobojanov A.R., Vorotilo S., Kuskov K.V., Moscovskikh D.O. Synthesis, structure and properties of high entropy materials. *IOP Conference Series: Materials Science and Engineering*. 2021;1014(1):1–4.
https://doi.org/10.1088/1757-899X/1014/1/012049

54. Kovalev D.Yu., Kochetov N.A., Chuev I.I. Fabrication of high-entropy carbide (TiZrHfTaNb)C by high-energy ball milling. *Ceramics International*. 2021; 47(23):32626–32633.
https://doi.org/10.1016/j.ceramint.2021.08.158

55. Mukasyan A.S., Rogachev A.S., Moskovskikh D.O., Yermekova Zh.S. Reactive spark plasma sintering of exothermic systems: A Critical review. *Ceramic International*. 2022;48(3):2988–2998.
https://doi.org/10.1016/j.ceramint.2021.10.207

56. Kochetov N.A., Kovalev I.D. Synthesis and investigation of thermal stability of multicomponent carbide (TaZrHfNbTi)C$_5$. *Inorganic Materials*. 2021;57(1):8–13.
http://dx.doi.org/10.1134/S0020168520120109

Кочетов Н.А., Ковалев И.Д. Синтез и исследование термической стабильности многокомпонентного карбида (TaZrHfNbTi)C$_5$. *Неорганические материалы*. 2021;57(1):10–15.
https://doi.org/10.31857/S0002337X20120106

57. Vadchenko S.G., Sedegov A.S., Kovalev I.D. Thermal explosions in (Ti, Zr, Hf, Nb, Ta) carbon mixtures. *Powder Metallurgy and Functional Coatings*. 2023;17(3):14–21.
https://doi.org/10.17073/1997-308X-2023-3-14-21

Вадченко С.Г., Седегов А.С., Ковалев И.Д. Тепловой взрыв в смесях (Ti, Zr, Hf, Nb, Ta) с углеродом. *Известия вузов. Порошковая металлургия и функциональные покрытия*. 2023;17(3):14–21.
https://doi.org/10.17073/1997-308X-2023-3-14-21

58. Vergunova Yu.S., Vadchenko S.G., Kovalev I.D., Kovalev D.Yu., Rogachev A.S., Alymov M.I. Self-propagating high-temperature synthesis of high-entropy carbides in the gasless thermal explosion mode. *Doklady Physical Chemistry*. 2024;513(1):131–134.
https://doi.org/10.1134/S001250162360033X

59. Vadchenko S.G., Kovalev I.D., Mukhina N.I., Sedegov A.S., Rogachev A.S. Thermal Explosion in Ti + Zr + Hf + Nb + Ta + 5C system: effect of mechanical activation. *International Journal of Self-Propagating High-Temperature Synthesis*. 2022;31(4):207–213.
https://doi.org/10.3103/S1061386222040136

60. Evseev N., Matveev A., Belchicov I., Zhukov I. Self-propagating high-temperature synthesis of high-entropy ceramic composition (Hf$_{0.25}$Ti$_{0.25}$Cr$_{0.25}$(FeV)$_{0.25}$)N. *Materials Letters*. 2023;346:134562.
https://doi.org/10.1016/j.matlet.2023.134562

61. Liu D., Zhang H., You X., Jia J., Meng J. Low temperature synthesized high entropy carbide composites: A potential high temperature anti-wear material. *Ceramics International*. 2024;50(1):2111–2121.
https://doi.org/10.1016/j.ceramint.2023.10.320

62. Potschke J., Vornberger A., Gestrich T., Berger L.-M., Michaelis A., Influence of different binder metals in high entropy carbide based hardmetals. *Powder metallurgy*. 2022;65(5):373–381.
https://doi.org/10.1080/00325899.2022.2076311

63. Luo Si-Chun, Guo Wei-Ming, Lin Hua-Tay. High-entropy carbide-based ceramic cutting tools. *Journal American Ceramic Society*. 2023;106(2):933–940.
https://doi.org/10.1111/jace.18852

64. Patil K.C., Hedge M.S., Rattan T., Aruna S.T. Chemistry of nanocrystalline oxide materials: Combustion synthesis, properties and applications. New Jersey: World Scientific, 2008. 345 p. https://doi.org/10.1142/9789812793157

65. Aiqin Mao, Hou-Zheng Xiang, Zhan-Guo Zhang, Koji Kuramoto, Haiyun Yu, Songlin Ran. Solution combustion synthesis and magnetic property of rock-salt (Co$_{0.2}$Cu$_{0.2}$Mg$_{0.2}$Ni$_{0.2}$Zn$_{0.2}$)O high-entropy oxide nanocrystalline powder. *Journal of Magnetism and Magnetic Materials*. 2019;484:245–252. https://doi.org/10.1016/j.jmmm.2019.04.023

66. Bui L.M., Cam S.T., Buryanenko I.V., Semenov V.G., Nazarov D.V., Kazin P.E., Nevedomskiy V.N., Gerasimov E.Y., Popkov V.I. An ultra-high-entropy rare earth orthoferrite (UHE REO): solution combustion synthesis, structural features and ferrimagnetic behavior. *Dalton Transactions*. 2023;15:1–3. https://doi.org/10.1039/D2DT04103K

Information about the Authors

Anis R. Bobozhanov – Junior Researcher, Postgraduate Student of the Laboratory of Dynamics of Microheterogeneous Processes, Merzhanov Institute of Structural Macrokinetics and Problems of Materials Science of the Russian Academy of Sciences (ISMAN)
ORCID: 0009-0008-7021-7156
E-mail: bobozhanov.anis@mail.ru

Alexander S. Rogachev – Dr. Sci. (Phys.-Math.), Prof., Chief Researcher of the Laboratory of Dynamics of Microheterogeneous Processes, ISMAN
ORCID: 0000-0003-1554-0803
E-mail: rogachev@ism.ac.ru

Сведения об авторах

Анис Рахмонович Бобожанов – мл. науч. сотрудник, аспирант лаборатории динамики микрогетерогенных процессов, Институт структурной макрокинетики и проблем материаловедения им. А.Г. Мержанова Российской академии наук (ИСМАН)
ORCID: 0009-0008-7021-7156
E-mail: bobozhanov.anis@mail.ru

Александр Сергеевич Рогачев – д.ф.-м.н., проф., гл. науч. сотрудник лаборатории динамики микрогетерогенных процессов, ИСМАН
ORCID: 0000-0003-1554-0803
E-mail: rogachev@ism.ac.ru

Contribution of the Authors

A. R. Bobozhanov – search for references on the topic of the review, their analysis, writing.
A. S. Rogachev – task and concept of the work, analysis of literature sources, writing, editing.

Вклад авторов

А. Р. Бобожанов – поиск и анализ литературных источников по теме, написание текста статьи.
А. С. Рогачев – определение цели и концепции работы, анализ источников, написание и корректировка текста статьи.

Received 30.08.2024
Revised 11.09.2024
Accepted 16.09.2024

Статья поступила 30.08.2024 г.
Доработана 11.09.2024 г.
Принята к публикации 16.09.2024 г.

Self-Propagating High-Temperature Synthesis
Самораспространяющийся высокотемпературный синтез

UDC 66.09: 66.094.3.097: 66.097.5

https://doi.org/10.17073/1997-308X-2024-6-17-27

Research article
Научная статья

Synthesis of Co–Mn catalysts for deep oxidation of CO and propane based on natural opoka by low-temperature combustion

R. I. Jussupkaliyeva[1], I. M. Bystrova[2],
S. I. Pomogailo[2], V. N. Borshch[2]

[1] **Zhangir Khan West Kazakhstan Agrarian Technical University**
51 Zhangir Khan Str., Uralsk 090009, Republic of Kazakhstan
[2] **Merzhanov Institute of Structural Macrokinetics and Materials Science of the Russian Academy of Sciences**
8 Academician Osip'yan Str., Chernogolovka, Moscow Region 142432, Russia

pomogsvetlana@mail.ru

Abstract. Natural opoka from the Taskalin deposit in the Republic of Kazakhstan was used as a support for Co–Mn catalysts in the deep oxidation of CO and hydrocarbons. After preliminary preparation of the opoka samples by water washing (opoka *I*), calcination at 500 °C (opoka *II*), HCl treatment (opoka *III*), or combined HCl treatment and calcination at 500 °C (opoka *IV*), an active phase (AP) consisting of 5 wt. % Co + 5 wt. % Mn (based on metals) was applied via low-temperature combustion of a metal nitrates and urea mixture. The support and catalyst samples were analyzed using XRD and SEM/EDS, and their specific surface area was measured by the BET method. The primary phases identified in the support and catalyst compositions were various modifications of SiO_2, as well as Na-, Ca-, and Mg-aluminosilicates. Due to their low content, AP components in the form of cobalt oxyhydroxide and potassium manganite were detected only on two of the catalyst samples. According to SEM/EDS data, the original nanoscale honeycomb structures on the opoka surface were almost completely destroyed during opoka processing and after AP application. Elemental composition showed notable variability across different granules of both the support and the catalyst, likely due to the natural structural heterogeneity of opoka. It was established that as the complexity of opoka treatment increased, its specific surface area tripled, from 21.0 to 64.1 m^2/g. In contrast, the specific surface area of catalysts based on these opoka samples varied irregularly. Testing of the resulting catalysts in the deep oxidation of CO and propane over a temperature range of 150–540 °C revealed substantial activity, with the best performance observed in the catalyst based on water-washed opoka without further treatment. This sample achieved 100 % CO conversion at $T = 500$ °C and 97 % propane conversion at 540 °C. Thus, natural opoka with minimal processing can serve as an effective support for deep oxidation catalysts for CO and hydrocarbons.

Keywords: opoka, support, low-temperature combustion, Co–Mn catalysts, carbon monoxide, propane, deep oxidation

Acknowledgements: The work was carried out within the framework of the State Assignment of ISMAN and with the financial support of JSC Center for International Programs "Bolashak" of the Republic of Kazakhstan.

For citation: Jussupkaliyeva R.I., Bystrova I.M., Pomogailo S.I., Borshch V.N. Synthesis of Co–Mn catalysts for deep oxidation of CO and propane based on natural opoka by low-temperature combustion. *Powder Metallurgy and Functional Coatings*. 2024;18(6):17–27. https://doi.org/10.17073/1997-308X-2024-6-17-27

Синтез в процессе низкотемпературного горения на основе природной опоки Co–Mn-катализаторов глубокого окисления СО и пропана

Р. И. Джусупкалиева[1], И. М. Быстрова[2],
С. И. Помогайло[2] ✉, В. Н. Борщ[2]

[1] **Западно-Казахстанский аграрно-технический университет им. Жангир Хана**
Республика Казахстан, 090009, г. Уральск, ул. Жангир Хана, 51
[2] **Институт структурной макрокинетики и проблем материаловедения**
им. А.Г. Мержанова Российской академии наук
Россия, 142432, Московская обл, г. Черноголовка, ул. Акад. Осипьяна, 8

✉ pomogsvetlana@mail.ru

Аннотация. Природная опока Таскалинского месторождения Республики Казахстан использована как носитель Co–Mn-катализаторов глубокого окисления СО и углеводородов. После предварительной подготовки ее образцов путем промывки водой (опока *I*), прокалки при температуре 500 °С (опока *II*), обработки HCl (опока *III*) или обработки HCl и прокалки при 500 °С (опока *IV*) на них в процессе низкотемпературного горения смеси нитратов металлов и мочевины была нанесена активная фаза (АФ) состава 5 мас. % Co + 5 мас. % Mn в пересчете на металлы. Образцы носителя и катализатора исследовались методами РФА и SEM/EDS, измерена удельная поверхность по БЭТ. Показано, что основными фазами в составе носителей и катализаторов являются различные модификации SiO_2, а также Na-, Ca- и Mg-алюмосиликаты. Компоненты АФ вследствие их низкого содержания в виде оксогидроксида кобальта и манганита калия были обнаружены только на двух образцах катализаторов. Согласно данным SEM/EDS в ходе обработки опоки и после нанесения АФ исходные наноразмерные сотовые структуры на поверхности практически полностью разрушаются. Имеет место неравномерность элементного состава на поверхности разных гранул как носителя, так и катализатора, связанная, по-видимому, с неоднородностью природной структуры опоки. Установлено, что по мере усложнения обработки опоки ее удельная поверхность монотонно возрастает в 3 раза – с 21,0 до 64,1 $м^2$/г. С другой стороны, удельная поверхность катализаторов на основе этих образцов опоки изменяется нерегулярно. Испытания полученных катализаторов в процессе глубокого окисления СО и пропана в интервале температур от 150 до 540 °С выявили их достаточно высокую активность, причем наилучшие характеристики показал катализатор на основе промытой водой опоки без последующей обработки. На этом образце 100 %-ная конверсия СО была получена уже при $T = 500$ °С, а конверсия пропана при 540 °С достигла 97 %. Таким образом, природная опока с минимальной обработкой может служить эффективным носителем катализаторов глубокого окисления СО и углеводородов.

Ключевые слова: опока, носитель, низкотемпературное горение, Co–Mn-катализаторы, оксид углерода, пропан, глубокое окисление

Благодарности: Работа выполнена в рамках Госзадания ИСМАН и при финансовой поддержке АО Центр международных программ «Болашак» Республики Казахстан.

Для цитирования: Джусупкалиева Р.И., Быстрова И.М., Помогайло С.И., Борщ В.Н. Синтез в процессе низкотемпературного горения на основе природной опоки Co–Mn-катализаторов глубокого окисления СО и пропана. *Известия вузов. Порошковая металлургия и функциональные покрытия*. 2024;18(6):17–27. https://doi.org/10.17073/1997-308X-2024-6-17-27

Introduction

Supported catalysts represent the most widely used class of heterogeneous catalysts. Active phases (AP) are very often deposited on supports made of simple and complex oxides of elements from the main subgroups of the middle of the Periodic Table, such as γ-Al_2O_3, SiO_2 (typically in hydrated form as silica gel), amorphous and crystalline aluminosilicates, and their complexes with oxides of transition and rare-earth metals. Generally, synthetic materials with a fixed set of physicochemical properties are used. However, there remains significant interest in using natural high-porosity materials as supports due to their low cost and environmental friendliness. The primary challenge usually involves standardizing these natural materials since even within a single deposit, their composition and properties can vary considerably.

The literature documents the use of natural minerals such as bentonite clays (specifically montmorillonite), which are hydroxylated nanoscale-layered aluminosilicates, as acid-base catalysts [1], catalyst supports [2; 3], and photocatalysts [4; 5]. Of particular interest is their dehydrated modification – multilayered aluminosilicate nanotubes known as the natural mineral halloysite [6; 7]. Another popular catalyst support in various processes discussed in the literature is the highly porous silica rock, diatomite [8; 9]. Closely related to diatomite in composition and properties is opoka – a microporous, high-silica sedimentary rock containing up to 92–98 wt. %[1] SiO_2. It is widely used in construction as a thermal and sound insulation material, and due to its high adsorption, filtration, and ion-exchange properties, opoka is also employed as an adsorbent and filter filler [10–14]. However, there is no information in the literature regarding its use as a support for AP in catalysis.

Deep catalytic oxidation processes are essential for purifying anthropogenic gas emissions and have long been crucial from an environmental standpoint. Additionally, these processes are applied in flameless heat generators, catalytic burners, fuel cells, and gas composition monitoring systems within fire- and explosion-hazardous industries, among others. According to the literature, catalyst development for these applications is advancing rapidly. It is well established that the most effective catalysts for such reactions are those with AP containing noble metals, effective in both CO oxidation [15; 16] and the deep oxidation of hydrocarbons [17–19].

However, aside from their high cost, a major drawback of noble metal catalysts is their low resistance to catalytic poisons (see, for example, [20]). Consequently, a significant focus in the global literature is on developing and researching new catalytic systems based on non-noble transition and rare-earth elements, particularly in nanoscale forms. Among the most active elements in these systems, Co and Mn are often highlighted, both as supported catalysts on various substrates – such as sialon [21], the previously mentioned diatomite [8], γ-Al_2O_3 [22], silica gel modified with aluminum oxide [23], foamed silicalite-1 [24], and nanostructured CeO_2 [25] – and in monolithic complex oxide forms [26–29].

One of the promising methods for producing supported catalysts is the low-temperature combustion method, also known as self-propagating surface thermosynthesis [22; 23; 30; 31]. This method involves impregnating the support with a solution mixture of oxidizers (usually nitrates of active metals) and a reducer or fuel (a water-soluble organic compound), followed by drying and heating the sample to initiate the combustion reaction. This technique offers several advantages over traditional impregnation methods, including low energy consumption, short reaction time, the formation of highly dispersed (including nanoscale) oxide and/or metallic active phases on the pore surfaces of the support, and the absence of harmful gas emissions (typically only CO_2, nitrogen, and water vapor are released). The low combustion temperature (in our practice, ≤ 360 °C) minimizes the interaction between the AP and the support, preventing particle sintering of the resulting AP.

Previously, using this method, we produced Co-, Mn-, and Ni-containing catalysts on various supports [7; 22; 23], which demonstrated high activity in the deep oxidation of propane and CO.

The aim of this study is to synthesize and examine the physicochemical and catalytic properties of new 5 % Co – 5 % Mn catalyst samples, with the active phase deposited on pre-treated opoka from the Taskalin deposit in Kazakhstan [32] (referred to hereafter as 5Co5Mn/opoka *I–IV*). These catalysts were evaluated in the deep oxidation of propane and CO.

Before applying the AP, the natural opoka samples underwent several preliminary treatment procedures. A common step for all samples was washing to remove impurities of water-soluble salts and easily washable clay contaminants. The purpose of calcination at 500 °C was to burn off organic impurities in the air and to dehydrate the remaining clay impurities. Treatment with HCl solution was performed to remove oxide impurities, complex oxides, and carbonates containing transition metals, primarily iron, as well as alkaline earth metal carbonates. These procedures were applied to different samples to assess the impact of each treatment step.

Research methodology

Before use, all opoka samples were ground to a particle size of 0.1–0.3 mm, washed several times with distilled water, and dried in an oven at 90 °C. The first part (opoka *I*) was set aside without further treatment, the second (opoka *II*) was additionally calcined at 500 °C, the third (opoka *III*) was washed with a 10 % HCl solution and then rinsed with distilled water, while the fourth (opoka *IV*) was also washed with a 10 % HCl solution, rinsed with distilled water, and then calcined at 500 °C.

The prepared supports, each weighing 5 g, were impregnated with a solution mixture of metal nitrates ($Co(NO_3)\cdot 6H_2O + Mn(NO_3)_2\cdot 6H_2O$) and urea, with concentration ratios calculated to yield the pure metals. The sample was dried at 90 °C and placed in a flat-bottomed quartz tube reactor, sealed with a dust collection system and purged with argon. The heater at the bottom of the reactor was turned on, and its power remained constant throughout the process. Temperature was monitored by a thermocouple placed in the sample layer at the center of the reactor. After the reaction and cooling, the sample in the argon-filled reactor was

---

[1] All percentages are by weight (wt. %) unless otherwise indicated.

stabilized with a 5 % H_2O_2 solution to prevent spontaneous ignition of any highly dispersed metallic phases in the active phase. The sample was then washed with distilled water and dried at 90 °C. Particles smaller than 0.1 mm were removed from the resulting catalyst. The setup and synthesis procedure were previously described in detail [22; 23].

X-ray diffraction analysis (XRD) of the samples was conducted using a DRON-3M diffractometer (Russia) with FeK_α radiation.

The morphology and elemental composition of the catalyst surfaces were examined with a high-resolution field-emission scanning electron microscope, the Zeiss Ultra Plus, based on the Ultra 55 platform (Carl Zeiss, Germany), equipped with an INCA Energy 350 XT microanalysis system from Oxford Instruments. The specific surface area was measured through nitrogen physical adsorption by the BET method on an apparatus designed according to GOST 23401-90.

The obtained samples were tested on a catalytic setup with a flow-through quartz reactor containing a fixed bed of catalyst (1 cm^3 of 0.1–0.3 mm fraction). Analysis of the initial gas mixture and reaction products from deep oxidation was conducted using a 5-component gas analyzer, Avtotest 02.03P, with zero-class accuracy (Meta, Russia). The initial gas mixture had the following composition by vol. %: propane – 0.15, CO – 0.6, O_2 – 1.6, nitrogen – up to 100 %. The gas flow rate was 120,000 h^{-1}. Experiments were carried out within a temperature range from 150 to 540 °C in 50 °C intervals. CO and propane conversions during deep oxidation were calculated using the formula

$$X_{R.T} = \frac{C_{R,0} - C_{R,T}}{C_{R,0}} 100\ \%,$$

where $C_{R,0}$ and $C_{R,T}$ are the concentrations of the reactant (CO or propane) in the initial gas mixture and at the reactor outlet at temperature T, respectively, vol. %.

Results and discussion

Fig. 1 shows thermograms of the catalyst synthesis process on opoka samples prepared as described above. The self-ignition temperatures (T_S) at the start of the combustion wave and the maximum temperatures ($T_{\max}$) within the combustion wave were recorded. As shown, the T_S values for samples on opokas *I* and *II* are nearly identical, though the $T_{\max}$ on opoka *II* is noticeably higher. The highest self-ignition (192 °C) and combustion (322 °C) temperatures were recorded during synthesis on sample *III*. Secondary peaks at lower temperatures, likely corresponding to the afterburning wave, were observed on opokas *I–III*. This phenomenon was also noted in our previous synthesis of a similar AP-based catalyst on γ-Al_2O_3 [22]. Synthesis on opoka *IV* proceeded in a low-intensity mode, with minimal T_S and $T_{\max}$.

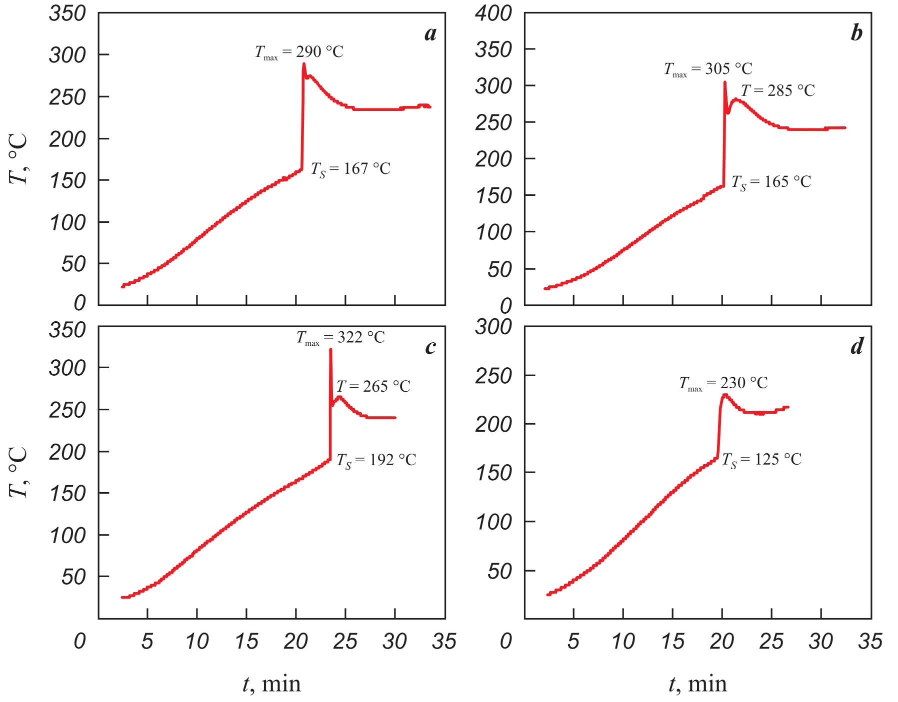

Fig. 1. Thermograms of the synthesis process for catalysts 5Co5Mn/opoka *I* (***a***), *II* (***b***), *III* (***c***), and *IV* (***d***)

Рис. 1. Термограммы процесса синтеза катализаторов 5Co5Mn/опока *I* (***a***), *II* (***b***), *III* (***c***), *IV* (***d***)

XRD patterns of the prepared supports and their corresponding catalysts are shown in Figs. 2 and 3. Notably, opoka samples *I* and *II* contain complex oxide impurity phases of iron and magnesium, which disappear after HCl treatment (see Fig. 2). The primary phases present are various modifications of SiO_2, along with Na-, Ca-, and Mg-aluminosilicates, with a significant portion of amorphous phases also observed.

As shown in Fig. 3, Co- and Mn-containing APs appeared only on two catalyst samples – those based on opokas *I* and *III*, and separately: in sample *I*, likely as trivalent Co oxyhydroxide, and in opoka *III* as potassium manganite. This likely results from the low AP component content, which is near the detection limit of the XRD analysis. Aluminosilicate phases were preserved only in samples based on opokas *I* and *II*, while in samples with supports *III* and *IV*, the amount of silica phase modifications increased.

The morphology and surface elemental composition of supports *II* and *IV*, as well as the catalyst based on opoka *II*, were studied using SEM/EDS. The results are shown in Figs. 4–6.

It can be noted that a characteristic feature of the support granule surfaces, both before (Fig. 4) and after (Fig. 5) acid washing, is the presence of nanoscale honeycomb structures with wall thicknesses of ≤ 50 nm, which are clearly visible in Fig. 4. After HCl treatment and calcination, the honeycomb walls appear to melt and thicken noticeably (Fig. 5), though only the application of AP almost completely destroys these formations (Fig. 6). Only isolated elements of the honeycomb structures remain. Notably, as the sample treatment procedures become more complex (opoka *I* → opoka *II* → opoka *III* → opoka *IV*, followed by AP application), the morphology of the support and catalyst granule surfaces takes on an increasingly fragmented, amorphous appearance.

Elemental microanalysis data show significant variability in the element content across individual granules of both the supports and the catalyst. This applies not only to impurity elements but also to the primary structural elements (Si, Al). This variability may be related to the structural heterogeneity of natural minerals, as noted above. Some samples show detectable

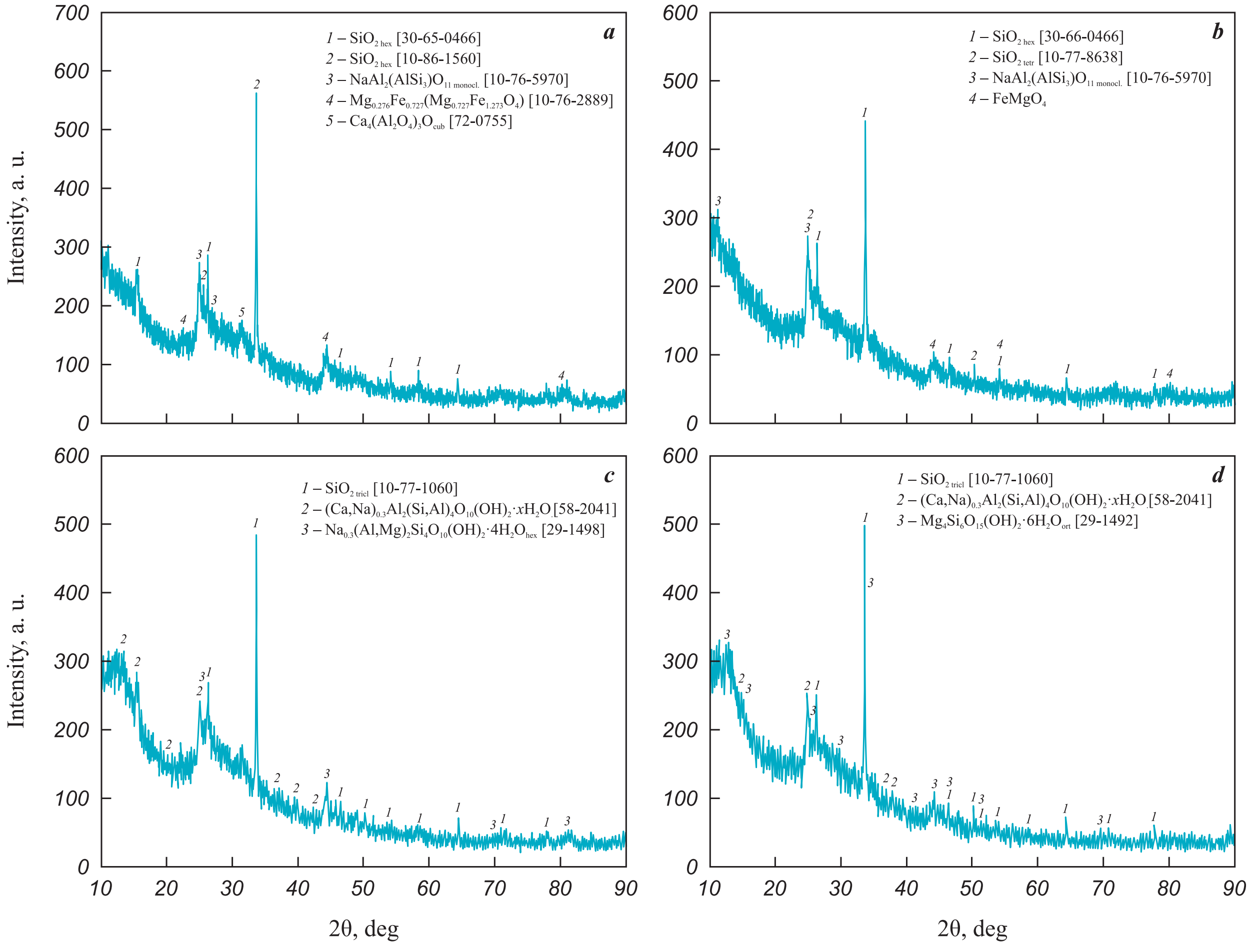

Fig. 2. XRD patterns of support samples opoka *I* (***a***), *II* (***b***), *III* (***c***), and *IV* (***d***)

Рис. 2. Рентгенограммы образцов носителя опок *I* (***a***), *II* (***b***), *III* (***c***), *IV* (***d***)

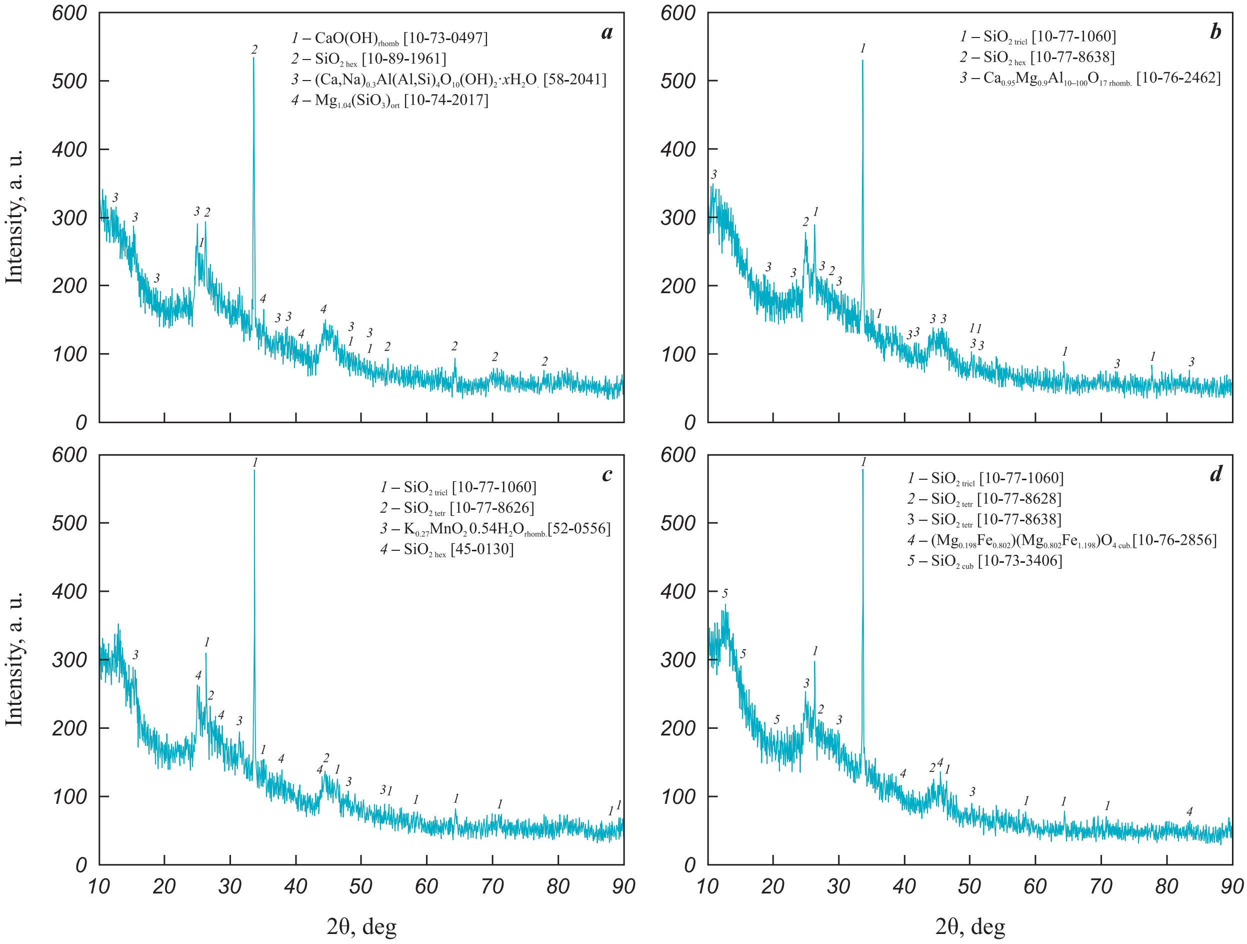

Fig. 3. XRD patterns of catalysts 5Co5Mn/opoka *I* (***a***), *II* (***b***), *III* (***c***), and *IV* (***d***)

Рис. 3. Результаты РФА образцов катализаторов 5Co5Mn/опока *I* (***a***), *II* (***b***), *III* (***c***), *IV* (***d***)

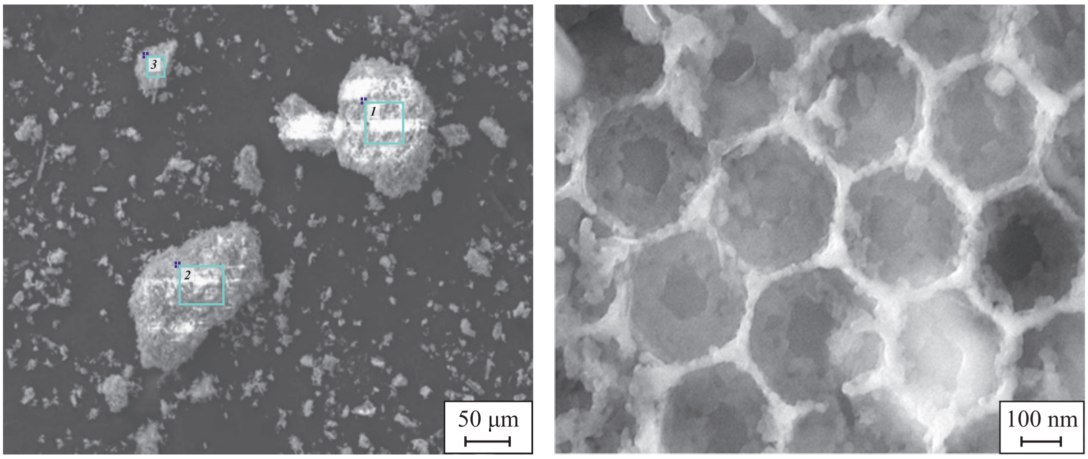

Area	Element content, wt. %							
	O	Na	Mg	Al	Si	K	Ca	Fe
1	58.18	0.14	0.83	8.68	28.18	1.29	0.42	2.30
2	57.39	0.10	0.82	8.50	28.71	1.59	0.14	2.77
3	65.16	0	0.66	6.31	25.61	0.88	0.08	1.32
Average	60.24	0.08	0.77	7.83	27.50	1.25	0.21	2.13

Fig. 4. Surface morphology of opoka *II* sample (SEM) and elemental composition at marked points

Рис. 4. Морфология поверхности образца опоки *II* (СЭМ) и элементный состав в отмеченных областях

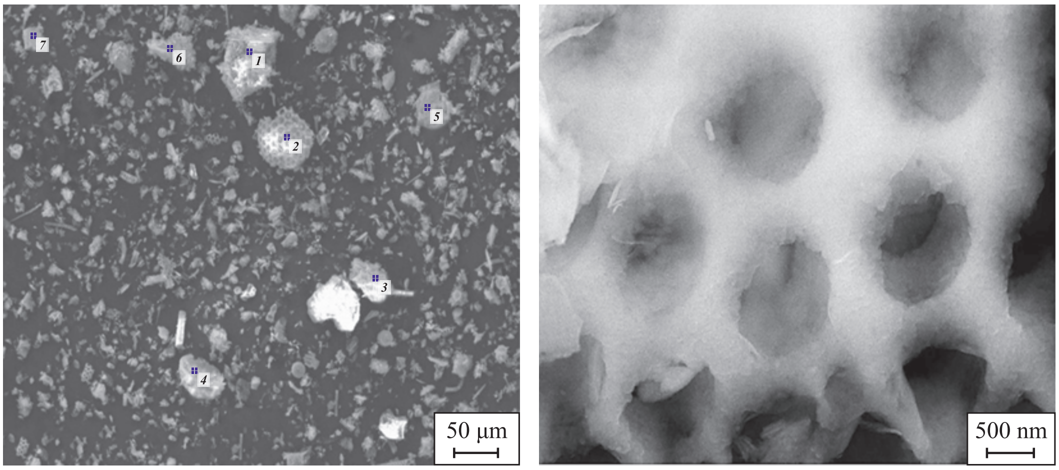

Point	Element content, wt. %						
	O	Mg	Al	Si	K	Ti	Fe
1	62.65	0.29	3.04	10.58	0.15	22.59	0.70
2	57.52	0.42	4.58	35.79	0.69	0.21	0.78
3	65.74	0.12	5.19	22.04	1.78	0.75	4.41
4	70.59	0.25	2.87	25.39	0.46	0.06	0.40
5	76.34	0.18	2.98	19.91	0.28	0.03	0.28
6	64.15	0.61	9.21	23.07	1.05	0.32	1.59
7	61.48	0.06	0.90	37.29	0.11	0	0.16
Average	65.50	0.28	4.11	24.87	0.64	3.42	1.19

Fig. 5. Surface morphology of opoka *IV* sample (SEM) and elemental composition at marked points

Рис. 5. Морфология поверхности образца опоки *IV* (СЭМ) и элементный состав в отмеченных точках

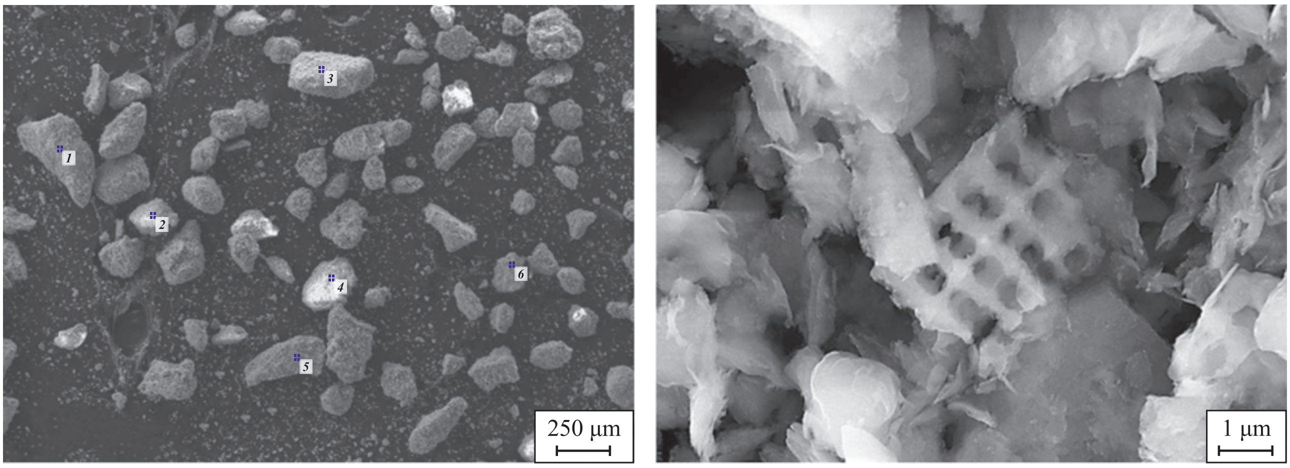

Point	Element content, wt. %								
	O	Mg	Al	Si	K	Ti	Mn	Fe	Co
1	64.39	0.50	4.56	26.05	0.34	0.07	1.50	0.84	1.73
2	38.39	0.99	0.35	35.77	1.86	0.57	5.55	3.39	5.12
3	14.66	0	21.22	3.54	0.19	0	17.19	21.98	21.23
4	5.05	0.83	3.66	47.53	1.61	3.20	16.08	5.90	16.15
5	36.58	0.74	7.40	30.93	1.63	0.17	9.03	4.46	9.05
6	55.00	0.89	7.40	24.52	0.79	0.23	4.38	1.63	5.14
Average	35.68	0.66	7.43	28.06	1.12	0.71	8.96	6.35	9.68

Fig. 6. Surface morphology of the 5Co5Mn/opoka *II* catalyst sample (SEM) and elemental composition at marked points

Рис. 6. Морфология поверхности образца катализатора 5Co5Mn/опока *II* (СЭМ) и элементный состав в отмеченных точках amounts of titanium, which does not appear in XRD, likely due to its low concentration, even if present in compound form. Conversely, magnesium, which constitutes a fraction of a percent on the surface, is consistently detected in the form of magnesium silicate on diffractograms, particularly for the opoka *IV* sample (see Fig. 2, *d*). The application of AP to the opoka *II* sample resulted in a noticeable reduction in oxygen content on its surface (compare the data in the Tables in Figs. 4 and 6), even considering that the surface was stabilized with a hydrogen peroxide solution after synthesis. It can be assumed that a portion of weakly bonded oxygen on the support surface reacted during the combustion process when the AP was applied. Significant variations in Co and Mn concentrations on the catalyst granule surfaces are also observed, both in absolute terms and in their relative ratios. This variability likely stems from the structural heterogeneity noted earlier, especially in the number of open pores, where the AP precursor solution penetrates through capillary action prior to synthesis.

The specific surface area (S_{sp}) of certain support and catalyst samples, determined by the BET method, is shown below, in m^2/g:

Opoka *I*	21.0
Opoka *II*	42.0
Opoka *IV*	64.1
5Co5Mn/opoka *I*	40.6
5Co5Mn/opoka *II*	29.5
5Co5Mn/opoka *IV*	62.8

A distinctive feature of the support treatment process is evident: as the treatment becomes more complex, the specific surface area of the samples increases, likely due to the exposure of an increasing number of fine pores. However, the application of the AP has varying effects on this value. As can be seen, the catalyst based on opoka *I* has twice the specific surface area S_{sp} of the initial support. Conversely, for the catalyst based on opoka *II*, this trend is reversed, while for the 5Co5Mn/opoka *IV* sample, there was almost no change. This may indicate differences in the dispersion of the AP formed during synthesis, depending on the surface morphology and, to some extent, the elemental composition of the different support samples.

A series of catalysts based on treated opoka was tested in the deep oxidation of propane and CO. The results are shown in Fig. 7. According to these data, the opoka-based catalysts demonstrated fairly high activity in both CO oxidation and propane deep oxidation. In the first case, 100 % CO conversion was achieved at 500 °C on the 5Co5Mn/opoka *I* catalyst (Fig. 7, *a*), with its activity being higher across the entire temperature range. In the second case, this same catalyst achieved a propane conversion of 97 % at 540 °C (Fig. 7, *b*). The sample based on opoka *IV* showed the lowest activity in these processes, despite having the highest specific surface area among the samples. It should be noted that for the 5Co5Mn/opoka *II* and 5Co5Mn/opoka *IV* samples, propane conversion in the high-temperature region (≥ 500 °C) exceeded CO conversion.

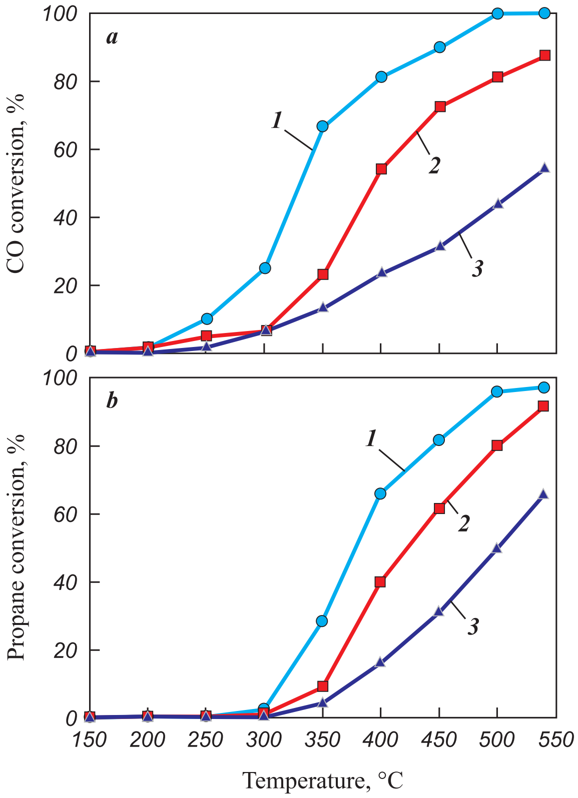

Fig. 7. Temperature dependences of CO (***a***) and propane (***b***) conversions on catalyst samples

1 – 5Co5Mn/opoka *I*, ***2*** – 5Co5Mn/opoka *II*, ***3*** – 5Co5Mn/opoka *IV*

Рис. 7. Зависимости конверсий CO (***a***) и пропана (***b***) от температуры на исследуемых образцах катализаторов

1 – 5Co5Mn/опока *I*, ***2*** – 5Co5Mn/опока *II*, ***3*** – 5Co5Mn/опока *IV*

Conclusion

For the first time, catalysts with a CoMn active phase (5 % + 5 % based on metals) on differently treated opoka were obtained using the low-temperature combustion method with mixtures of Co and Mn nitrates and urea. XRD analysis showed that, following acid treatment and subsequent calcination, iron-magnesium complex oxide impurities are removed from the opoka samples, with the main phases being various modifications of silica, along with Na-, Ca-, and Mg-aluminosilicates, and a significant proportion of amorphous phases.

SEM/EDS analysis of the morphology and surface elemental composition of the supports and catalyst revealed degradation of the initial nanoscale honeycomb structures as opoka processing became more complex, with further degradation upon AP application. A significant variability in elemental content among individual granules of both supports and catalysts was observed, likely due to the structural heterogeneity of this natural mineral.

The specific surface area of the support samples increased with more complex processing steps, but the surface area of the catalysts varied non-monotonically. Testing of several catalysts showed the activity order in the deep oxidation of both CO and propane as follows: 5Co5Mn/opoka *I* > 5Co5Mn/opoka *II* > 5Co5Mn/opoka *IV*, with CO conversion reaching 100 % at 500 °C and propane conversion reaching 97 % at 540 °C on the 5Co5Mn/opoka *I* sample. The sample based on opoka *IV* demonstrated the lowest activity in these processes, despite having the highest specific surface area among the catalysts studied (62.8 m^2/g).

Thus, natural opoka with minimal processing can serve as an effective support for deep oxidation catalysts for hydrocarbons and CO.

References / Список литературы

1. Gandhi D., Bandyopadhyay R., Soni B. Naturally occurring bentonite clay: Structural augmentation, characterization and application as catalyst. *Materials Today: Proceedings*. 2022;57(1):194–201.
https://doi.org/10.1016/j.matpr.2022.02.346
2. Borah D., Nath H., Saikia H. Modification of bentonite clay & its applications: A review. *Reviews in Inorganic Chemistry*. 2022;42(3):265–282.
https://doi.org/10.1515/revic-2021-0030
3. Vaculíková L.,Valovičová V., Plevová E., Napruszewska B.D., Duraczyńska D., Karcz R., Serwicka E.M. Synthesis, characterization and catalytic activity of cryptomelane/montmorillonite composites. *Applied Clay Science*. 2021;202(1):105977.
https://doi.org/10.1016/j.clay.2021.105977
4. Zhou D., Jiang D., Jing H., Yin C., Li C. Natural aluminosilicate nanoclay mineral for photocatalytic applications: Influence of the surface properties in photocatalysis. *Applied Clay Science*. 2024;249(1):107240.
https://doi.org/10.1016/j.clay.2023.107240
5. Feng J., Hu X., Yue P.L. Novel bentonite clay-based Fe-nanocomposite as a heterogeneous catalyst for photo-Fenton discoloration and mineralization of orange II. *Environmental Science & Technology*. 2004;38(1):269–275.
https://doi.org/10.1021/es034515c
6. Massaro M., Noto R., Riela S. Halloysite nanotubes: Smart nanomaterials in catalysis. *Catalysts*. 2022;12(2):149.
https://doi.org/10.3390/catal12020149
7. Borshch V.N., Bystrova I.M., Pugacheva E.V., Smirnova E.M., Stavitskaya A.V., Vinokurov V.A. Low-temperature combustion synthesis of halloysite-based catalysts for the deep oxidation of hydrocarbons and carbon monoxide and the methanation of carbon dioxide. *Kinetics and Catalysis*. 2022;63(6):775–786.
https://doi.org/10.1134/S0023158422060027

   Борщ В.Н., Быстрова И.М., Пугачева Е.В., Смирнова Е.М., Ставицкая А.В., Винокуров В.А. Синтез в режиме низкотемпературного горения катализаторов на основе галлуазита для глубокого окисления углеводородов, CO и метанирования CO_2. *Кинетика и катализ*. 2022;63(6):845–857.
https://doi.org/10.31857/S0453881122060028
8. Liu Q., Li M.., Wang S., Lv S., Han F., Xi Y., Cao Z., Ouyang J. Ultrathin 3D CoMn nanoflowers coupled diatomite for highly efficient catalytic oxidation of CO and propane. *Chemical Engineering Journal*. 2023;477:147102.
https://doi.org/10.1016/j.cej.2023.147102
9. Liang L., Miao C., Ke X., Peng Y., Chen G., Ouyang J. A superior strategy for CO_2 methanation under atmospheric pressure: Organic acid-assisted Co nanoparticles assembly on diatomite. *Fuel*. 2023;351:128931.
https://doi.org/10.1016/j.fuel.2023.128931
10. Mal’kova V.N. Method for obtaining a sorbent for cleaning solid surfaces and water from oil and liquid petroleum products: Patent 2642799. (RF). 2018. (In Russ.).

    Малькова В.Н. Способ получения сорбента для очистки твердых поверхностей и воды от нефти и жидких нефтепродуктов: Патент 2642799. (РФ). 2018.
11. Smol M., Włóka D. Use of natural sorbents in the processes of removing biogenic compounds from the aquatic environment. *Sustainability*. 2022;14:6432.
https://doi.org/10.3390/su14116432
12. Kotlyar V.D., Bratskiy D.I., Ustinov A.V. Material composition and pre-firing ceramic properties of clay flasks. *Inzhenernyi vestnik Dona*. 2010;4:47–59. (In Russ.).
http://www.ivdon.ru/magazine/archive/n4y2010/249

    Котляр В.Д., Братский Д.И., Устинов А.В. Вещественный состав и дообжиговые керамические свойства глинистых опок. *Инженерный вестник Дона*. 2010;4:47–59.
http://www.ivdon.ru/magazine/archive/n4y2010/249
13. Makarov D.V., Manakova N.K., Suvorova O.V. Production of rock-based foam-glass materials. *Glass and Ceramics*. 2023;79(9):411–417.
https://doi.org/10.1007/s10717-023-00522-8
14. Kurmangazhy G., Tazhibayeva S., Musabekov K., Sydykbayeva S., Zhakipbaev B. Magnetite-gaize composite stabilized with polyacrylic acid. *Chemical Bulletin of Kazakh National University*. 2020;98(3):12–17.
https://doi.org/10.15328/cb1160
15. Schilling C., Ziemba M., Hess C., Ganduglia-Pirovano M.V. Identification of single-atom active sites in CO oxidation over oxide-supported Au catalysts. *Journal of Catalysis*. 2020;383:264–272.
https://doi.org/10.1016/j.jcat.2020.01.022
16. Fan J., Hu S., Li C., Wang Y., Chen G. Effect of loading method on catalytic performance of Pt/CeO_2 system for CO oxidation. *Molecular Catalysis*. 2024;558:114013.
https://doi.org/10.1016/j.mcat.2024.114013

17. Auvray X., Lindholm A., Milh M., Olsson L. The addition of alkali and alkaline earth metals to Pd/Al$_2$O$_3$ to promote methane combustion. Effect of Pd and Ca loading. *Catalysis Today*. 2018;299:212–218.
https://doi.org/10.1016/j.cattod.2017.05.066

18. Zhang W-X., Zhao X., Xu L-Y., Xia S., Zhou Y-F., Chen C-L., He H-H., Luo M-F., Chen J. Unveiling the crucial active sites responsible for CO, n-heptane, and toluene oxidation over Pt/ZrO$_2$ catalyst. *Molecular Catalysis*. 2024;558:114015.
https://doi.org/10.1016/j.mcat.2024.114015

19. Shikina N.V., Yashnik S.A., Gavrilova A.A., Nikolaeva O.A., Dovlitova L.S., Ishchenko A.V., Ismagilov Z.R. Effect of the conditions of solution combustion synthesis on the properties of monolithic Pt–MnO$_x$ catalysts for deep oxidation of hydrocarbons. *Kinetics and Catalysis*. 2020;61(5):809–823.
https://doi.org/10.1134/S0023158420050110

20. Montenegro N.D., Epling W.S. Effects of SO$_2$ poisoning and regeneration on spinel containing CH$_4$ oxidation catalysts. *Applied Catalysis B: Environmental*. 2023;336: 122894. https://doi.org/10.1016/j.apcatb.2023.122894

21. Borshch V.N., Zhuk S.Ya., Vakin N.A., Smirnov K.L., Borovinskaya I.P., Merzhanov A.G. Sialons as a new class of supports for oxidation catalysts. *Doklady Physical Chemistry*. 2008;420(2)121–124.
https://doi.org/10.1016/10.1134/S0012501608060018

Борщ В.Н., Жук С.Я., Вакин Н.А., Смирнов К.Л., Боровинская И.П., Мержанов А.Г. Сиалоны как новый класс носителей катализаторов окисления. *Доклады Академии наук*. 2008;420(4):496–499.

22. Borshch V.N., Dement'eva I.M., Khomenko N.Yu. Supported polymetallic catalysts by self-propagating surface synthesis. *International Journal of Self-Propagating High-Temperature Synthesis*. 2019;28(1):45–49.
https://doi.org/10.3103/S1061386219010059

23. Borshch V.N., Bystrova I.M., Boyarchenko, O.D., Khomenko N.Yu., Belousova O.V. Low-temperature combustion synthesis and characterization of Co-containing catalysts based on modified silica gel. *International Journal of Self-Propagating High-Temperature Synthesis*. 2023;32(2):126–138.
https://doi.org/10.3103/S1061386223020024

24. Guan Y., Shen H., Guo X., Mao B., Yang Z., Zhou Y., Liang H., Fan X., Jiao Y., Zhang J. Structured hierarchical Mn–Co mixed oxides supported on silicalite-1 foam catalyst for catalytic combustion. *Chinese Journal of Chemical Engineering*. 2020;28:2319–2327.
https://doi.org/10.1016/j.cjche.2020.06.019

25. Liu Z., Li J., Wang R. CeO2 nanorods supported M–Co bimetallic oxides (M = Fe, Ni, Cu) for catalytic CO and C$_3$H$_8$ oxidation. *Journal of Colloid and Interface Science*. 2020;560:91–102.
https://doi.org/10.1016/j.jcis.2019.10.046

26. Zhang X., Ye J., Yuan J., Cai T., Xiao B., Liu Z., Zhao K., Yang L., He D. Excellent low-temperature catalytic performance of nanosheet Co–Mn oxides for total benzene oxidation. *Applied Catalysis A: General*. 2018;566:104–112.
https://doi.org/10.1016/j.apcata.2018.05.039

27. Feng C., Chen C., Xiong G., Yang D., Wang Z., Pan Y., Fei Z., Lu Y., Liu Y., Zhang R., Li X. Cr-doping regulates Mn$_3$O$_4$ spinel structure for efficient total oxidation of propane: Structural effects and reaction mechanism determination. *Applied Catalysis B: Environmental*. 2023;328:122528.
https://doi.org/10.1016/j.apcatb.2023.122528

28. Shen K., Wang C.-Y., Rai R.K., Stach E.A., Vohs J.M., Gorte R.J. Synthesis of thin-film CuMn$_2$O$_4$ for low-temperature CO oxidation. *Applied Catalysis A: General*. 2024;682:119823.
https://doi.org/10.1016/j.apcata.2024.119823

29. González-Cobos J., Mylonoyannis B., Chai G., Zhang W., Tian C., Kaddouri A., Gil S. Low-temperature gas-phase toluene catalytic combustion over modified CoCr$_2$O$_4$ spinel catalysts: Effect of Co/Cr content and calcination temperature. *Applied Catalysis A: General*. 2023;657:119162.
https://doi.org/10.1016/j.apcata.2023.119162

30. Zav'yalova U.F., Tret'yakov V.F., Burdeinaya T.N., Lunin V.V., Shitova N.B., Ryzhova N.D., Shmakov A.N., Nizovskii A.I., Tsyrul'nikov P.G. Self-propagating synthesis of supported oxide catalysts for deep oxidation of CO and hydrocarbons. *Kinetics and Catalysis*. 2005; 46(5):752–757.
https://doi.org/10.1007/s10975-005-0132-6

Завьялова У.Ф., Третьяков В.Ф., Бурдейная Т.Н., Лунин В.В., Шитова Н.Б., Рыжова Н.Д., Шмаков А.Н., Низовский А.И., Цырульников П.Г. Самораспространяющийся синтез нанесенных оксидных катализаторов окисления CO и углеводородов. *Кинетика и катализ*. 2005;46(5):795–800.

31. Kotolevich Y.S., Mamontov G.V., Vodyankina O.V., Petrova N.I., Smirnova N.S., Tsyryul'nikov P.G., Trenikhin M.V., Nizovskii A.I., Kalinkin A.V., Smirnov M.Y., Goncharov V.B. Catalytic Pd–Ag nanoparticles immobilized on fiber glass by surface self-propagating thermal synthesis. *International Journal of Self-Propagating High-Temperature Synthesis*. 2017;26(4):234–239.
https://doi.org/10.3103/S1061386217040045

32. Smirnov P.V., Zhakipbayev B.E., Staroselets D.A., Deryagina O.I., Batalin G.A., Gareev B.I., Vergunov A.V. Diatomites and opoka from Western Kazakhstan deposits: lithogeochemistry, structural and textural parameters, potential of use. *Izvestiya Tomskogo politekhnicheskogo universiteta. Inzhiniring georesursov*. 2023;334(7)187–201. (In Russ.).
https://doi.org/10.18799/24131830/2023/7/4046

Смирнов П.В., Жакипбаев Б.Е., Староселец Д.А., Дерягина О.И., Баталин Г.А., Гареев Б.И., Вергунов А.В.. Диатомиты и опоки месторождений Западного Казахстана: литология, структурно-текстурные параметры, потенциал использования. *Известия Томского политехнического университета. Инжиниринг георесурсов*. 2023;334(7)187–201.
https://doi.org/10.18799/24131830/2023/7/4046

Information about the Authors

Roza I. Jussupkaliyeva – Master Sci. (Tech.), Senior Lecturer at Zhangir Khan West Kazakhstan Agrarian Technical University
ORCID: 0000-0001-8916-0008
E-mail: rozaid2@mail.ru

Inna M. Bystrova – Junior Researcher, Laboratory of Catalytic Processes, Merzhanov Institute of Structural Macrokinetics and Materials Science, Russian Academy of Sciences (ISMAN)
ORCID: 0000-0003-3739-7390
E-mail: inna2019@ism.ac.ru

Svetlana I. Pomogailo – Cand. Sci. (Chem.), Senior Research Scientist, Laboratory of Catalytic Processes, ISMAN
ORCID: 0000-0001-8200-0706
E-mail: pomogsvetlana@mail.ru

Vyacheslav N. Borshch – Cand. Sci. (Chem.), Leading Researcher, Laboratory of Catalytic Processes, ISMAN
ORCID: 0000-0001-5827-4942
E-mail: borsch@ism.ac.ru

Сведения об авторах

Роза Ибраимовна Джусупкалиева – магистр технических наук, ст. преподаватель Индустриально-технологического института Западно-Казахстанского аграрно-технического университета им. Жангир хана
ORCID: 0000-0001-8916-0008
E-mail: rozaid2@mail.ru

Инна Михайловна Быстрова – мл. науч. сотрудник лаборатории каталитических процессов Института структурной макрокинетики и проблем материаловедения им. А.Г. Мержанова Российской академии наук (ИСМАН)
ORCID: 0000-0003-3739-7390
E-mail: inna2019@ism.ac.ru

Светлана Ибрагимовна Помогайло – к.х.н., ст. науч. сотрудник лаборатории каталитических процессов ИСМАН
ORCID: 0000-0001-8200-0706
E-mail: pomogsvetlana@mail.ru

Вячеслав Николаевич Борщ – к.х.н., вед. науч. сотрудник лаборатории каталитических процессов ИСМАН
ORCID: 0000-0001-5827-4942
E-mail: borsch@ism.ac.ru

Contribution of the Authors

R. I. Jussupkalieyva – defining the research goals and objectives, data collection, conducting experiments, analyzing the obtained data, and processing results.

I.M. Bystrova – conducting experiments, analyzing the obtained data, and participating in the discussion of results.
S.I. Pomogailo – participation in the discussion of results.
V.N. Borshch – developing the main concept, research supervision, organizing the work, and discussing the research results.

All authors contributed equally to writing the manuscript and share responsibility for identifying any instances of plagiarism, self-plagiarism, or other ethical issues.

Вклад авторов

Р. И. Джусупкалиева – определение целей и задач исследования, сбор данных для исследования, проведение экспериментов, анализ полученных первичных данных, обработка результатов.
И. М. Быстрова – проведение экспериментов, анализ полученных первичных данных, участие в обсуждении результатов.
С. И. Помогайло – участие в обсуждении результатов.
В. Н. Борщ – формирование основной концепции, руководство исследованием, организация работ, обсуждение результатов исследования.

Все авторы в равной степени участвовали в написании рукописи, и несут ответственность при обнаружении плагиата, самоплагиата или других неэтических проблем.

Received 13.08.2024
Revised 23.08.2024
Accepted 28.08.2024

Статья поступила 13.08.2024 г.
Доработана 23.08.2024 г.
Принята к публикации 28.08.2024 г.

Self-Propagating High-Temperature Synthesis
Самораспространяющийся высокотемпературный синтез

UDC 544.452 + 621.762.2 + 666.3

https://doi.org/10.17073/1997-308X-2024-6-28-43

Research article
Научная статья

Azide self-propagating high-temperature synthesis of a highly dispersed AlN–SiC powder composition using polytetrafluoroethylene

A. P. Amosov ✉, Yu. V. Titova, I. A. Uvarova, G. S. Belova

Samara State Technical University
244 Molodogvardeyskaya Str., Samara 443100, Russia

✉ egundor@yandex.ru

Abstract. Composite ceramics from aluminum nitride with silicon carbide (AlN–SiC) is promising for applications in both metallurgy and mechanical engineering as a refractory and structural material with enhanced properties, as well as in electronics and photonics as an advanced material for creating various high-performance devices. To fabricate products with optimal properties, compositions (mixtures) of highly dispersed AlN and SiC powders with particle sizes of less than 1 μm must be used. This study is dedicated to improving a simple, energy-efficient method of azide self-propagating high-temperature synthesis (SHS) for such powder compositions, using mixtures of sodium azide (NaN_3) powder and elemental powders of aluminum, silicon, and carbon with the addition of polytetrafluoroethylene (PTFE) powder as an activating and carbidizing additive. During the combustion of these mixtures in a bulk or pressed form in a reactor under 3 MPa of nitrogen gas pressure, the temperature, pressure, and yield of solid combustion products were evaluated. Scanning electron microscopy and *X*-ray phase analysis were employed to determine the microstructure and phase composition of the combustion products. The addition of PTFE helped to eliminate, in most cases, the drawbacks of the traditional azide SHS approach using halide salts such as $(NH_4)_2SiF_6$, AlF_3, and NH_4F. While maintaining the high dispersity of the synthesized AlN–SiC powder compositions, their phase composition, particularly in pressed charges, became significantly closer to the targeted theoretical composition, with a substantial increase in SiC phase content and the elimination of undesirable by-products such as silicon nitride and the water-insoluble cryolite salt Na_3AlF_6.

Keywords: aluminum nitride, silicon carbide, powder compositions, self-propagating high-temperature synthesis, sodium azide, polytetrafluoroethylene, combustion products, composition, structure

Acknowledgements: The work was supported by the Russian Science Foundation under grant No. 23-29-00680.

For citation: Amosov A.P., Titova Yu.V., Uvarova I.A., Belova G.S. Azide self-propagating high-temperature synthesis of a highly dispersed AlN–SiC powder composition using polytetrafluoroethylene. *Powder Metallurgy and Functional Coatings*. 2024;18(6):28–43. https://doi.org/10.17073/1997-308X-2024-6-28-43

Азидный самораспространяющийся высокотемпературный синтез высокодисперсной порошковой композиции AlN–SiC с применением политетрафторэтилена

А. П. Амосов, Ю. В. Титова, И. А. Уварова, Г. С. Белова

Самарский государственный технический университет
Россия, 443100, г. Самара, ул. Молодогвардейская, 244

egundor@yandex.ru

Аннотация. Композиционная керамика из нитрида алюминия с карбидом кремния (AlN–SiC) является перспективной для применения как в металлургии и машиностроении в качестве огнеупорного и конструкционного материала с повышенными свойствами, так и в электронике и фотонике в качестве нового материала для создания соответствующих разнообразных высокоэффективных устройств. Для изготовления из нее изделий с наилучшими свойствами необходимо использовать композиции (смеси) высокодисперсных порошков AlN и SiC с размером частиц менее 1 мкм. Настоящая работа посвящена усовершенствованию простого энергосберегающего метода азидного самораспространяющегося высокотемпературного синтеза (СВС) композиций таких порошков из смесей порошка азида натрия (NaN_3) и элементных порошков алюминия, кремния и углерода за счет применения активирующей и карбидизирующей добавки порошкового политетрафторэтилена (ПТФЭ). При сжигании этих смесей в насыпном или прессованном виде в реакторе с давлением газообразного азота 3 МПа оценивались температура и давление, а также выход твердых продуктов горения. С применением сканирующей электронной микроскопии и рентгенофазового анализа определялись микроструктура и фазовый состав продуктов горения. Применение добавки ПТФЭ позволило устранить в большинстве случаев недостатки традиционного подхода азидного СВС с использованием галоидных солей $(NH_4)_2SiF_6$, AlF_3 и NH_4F. При сохранении высокой дисперсности синтезированных композиций порошков AlN–SiC их фазовый состав, особенно в случае прессованных шихт, стал значительно ближе к задаваемому теоретическому составу, также существенно выросло содержание фазы SiC, исчезли нежелательные побочные фазы нитрида кремния и водонерастворимой соли криолита Na_3AlF_6.

Ключевые слова: нитрид алюминия, карбид кремния, композиции порошков, самораспространяющийся высокотемпературный синтез, азид натрия, политетрафторэтилен, продукты горения, состав, структура

Благодарности: Работа выполнена при поддержке Российского научного фонда в рамках гранта № 23-29-00680.

Для цитирования: Амосов А.П., Титова Ю.В., Уварова И.А., Белова Г.С. Азидный самораспространяющийся высокотемпературный синтез высокодисперсной порошковой композиции AlN–SiC с применением политетрафторэтилена. *Известия вузов. Порошковая металлургия и функциональные покрытия*. 2024;18(6):28–43. https://doi.org/10.17073/1997-308X-2024-6-28-43

Introduction

Aluminum nitride (AlN) is one of the foremost materials in technical ceramics [1]. It exhibits an exceptional combination of physical, electrical, and chemical properties: low density, high melting (or decomposition) temperature, thermal conductivity, electrical resistance, hardness, strength, wear resistance, and heat resistance, as well as resistance to thermal shock, acids, and molten metals, and stability at elevated temperatures in various gaseous environments. Owing to these characteristics, aluminum nitride has long found applications across diverse industrial sectors, particularly for high-temperature applications. It is widely used as a refractory material for lining tanks, electrolyzers, and containers in metallurgy and chemical engineering, as well as for producing protective sheaths for metallic thermocouples and manufacturing crucibles. AlN ceramics are among the most widely used electrical insulating materials. Furthermore, aluminum nitride is employed as a structural material for parts operating in aggressive environments and in cutting tools [2]. Intensive research to enhance its physical and mechanical properties continues [3].

However, due to the unique physical properties of AlN, its application in electronics and photonics has recently expanded rapidly [4; 5]. In electronics, this expansion is driven by its excellent heat dissipation capabilities in electronic devices, attributed to its uniquely high thermal conductivity combined with high electrical resistance and a coefficient of thermal expansion (CTE) close to that of silicon. This has led to a transition to aluminum nitride in nearly all areas of electronic component production, where the highly toxic beryllium oxide was traditionally used [4]. In photonics, AlN's wide bandgap, broad transparency window (covering the range from ultraviolet to mid-infrared), and significant second-order nonlinear optical effect have further broadened its utility. Additionally, AlN exhibits piezoelectric and pyroelectric effects, enabling its use in opto-mechanical devices and pyroelectric photodetectors, respectively [5]. However, in both these fields and in high-temperature structural applications, the use of aluminum nitride is constrained by its brittleness, specifically its relatively low fracture toughness and thermal shock resistance [6].

In this regard, significant attention is being drawn to the development of composite ceramics of aluminum nitride with silicon carbide (SiC), which, in addition to its high thermal conductivity and heat resistance, possesses substantially improved mechanical properties (hardness, fracture toughness, thermal stability, and creep resistance) [7; 8]. Silicon carbide is also attractive due to its crystal structure, which is similar to that of aluminum nitride, allowing it to form a single-phase homogeneous solid solution with AlN, enhancing flexural strength and fracture toughness, thereby reducing brittleness [9; 10]. Additionally, in a two-phase state with sintered, spatially separated powder components of AlN and SiC, AlN–SiC composites exhibit significantly better toughness and thermal stability [8; 11]. By controlling the grain size of AlN and SiC, it is possible to obtain AlN–SiC material with high thermal conductivity [12]. Notably, reducing grain size is another important approach to improving nearly all properties of AlN ceramics and AlN–SiC ceramic composites as a whole [13; 14].

AlN–SiC composite ceramics have shown promise not only for applications in metallurgy and mechanical engineering as a refractory and structural material with enhanced properties but also, as noted above, in electronics and photonics for the creation of a variety of high-performance devices [4; 5; 15].

Traditional energy-intensive methods for producing AlN–SiC ceramics include pressureless sintering of SiC and AlN ceramic powders, hot pressing, and injection molding, all of which require temperatures of around 2000 °C and prolonged holding times of several hours [16–19]. More modern and less energy-intensive methods include spark plasma sintering, microwave heating, and additive 3D-printing technologies; however, these require costly equipment [20–22].

In both methods, the starting material must be a composition (mixture) of AlN and SiC powders. To achieve the best properties of the resulting AlN–SiC ceramics, these powders should be as fine as possible: highly dispersed (submicron) with particle sizes $d < 1$ μm or even nanoscale with $d < 100$ μm (0.1 μm) [13; 23]. There are two approaches to producing AlN and SiC powder mixtures: *ex-situ* and *in-situ*. The first approach is the simplest and most common for producing composite ceramics and involves mixing ready-made AlN and SiC powders, compacting, and sintering them. However, for highly dispersed powders, especially nanopowders, two issues arise: high cost and the near impossibility of achieving uniform mechanical mixing due to the strong tendency of nanoparticles to form durable agglomerates that are challenging to break up during mixing. The *in-situ* processes for producing composite ceramics involve the chemical synthesis of AlN and SiC powder particles within the composite from a mixture of significantly cheaper starting reagents, allowing for better dispersion of the synthesized particles. These technologies are thus more favorable for obtaining mixtures of highly dispersed and nanoscale AlN and SiC powders [13; 23].

Traditional *in-situ* methods for producing mixtures of AlN and SiC powder components, or their solid solutions (furnace method, plasma-chemical synthesis, carbothermal synthesis, gas-phase deposition, etc.), are known for their high energy consumption, complex equipment requirements, and inconsistent ability to yield nanoscale powders and nanopowder compositions [10; 13; 14; 16; 24–26].

Self-propagating high-temperature synthesis (SHS), or “combustion synthesis”, presents distinct advantages over conventional technologies [16; 27–29]. The *in-situ* SHS approach is notably more cost-effective, as the AlN–SiC composite synthesis is driven by self-sustained combustion heat, requiring only simple equipment and low-cost precursor reagents, such as Al, Si, C (carbon black), Si_3N_4 powders, and gaseous N_2. This method has therefore garnered significant research interest, with various powder mixtures being examined for their combustion efficiency in producing AlN–SiC composites [27; 30–33]. A review of these studies [34] reveals that, in all cases, the synthesized AlN–SiC ceramics exhibit micron-sized particle structures.

To achieve a composition of highly dispersed ($d < 1$ μm) AlN–SiC powders, the authors investigated a variant of synthesis known as azide SHS technology, where sodium azide (NaN_3) powder serves as the nitriding agent. Additionally, various activating halide salts are introduced alongside elemental reagents, promoting relatively low combustion temperatures, the formation of significant intermediate vapor-gas reaction products, and the generation of condensed and gaseous by-products that effectively separate target powder particles, thus preventing their agglomeration into larger particles [34–37]. The main findings of these investigations are summarized as follows.

Azide SHS technology was employed to synthesize AlN–SiC powder compositions at five molar ratios of the target phases aluminum nitride and silicon carbide AlN:SiC = 4:1, 2:1, 1:1, 1:2, and 1:4, according to stoichiometric equations involving the use of halide salts $(NH_4)_2SiF_6$, AlF_3 and NH_4F [37].

xSi–yAl–NaN$_3$–(NH$_4$)$_2$SiF$_6$–(x + 1)C system

$$\begin{gathered}\mathrm{Si + 8Al + 6NaN_3 + (NH_4)_2SiF_6 + 2C =}\\ \mathrm{= 8AlN + 2SiC + 6NaF + 4H_2 + 6N_2,}\end{gathered}\tag{1}$$

$$\begin{gathered}\mathrm{Si + 4Al + 6NaN_3 + (NH_4)_2SiF_6 + 2C =}\\ \mathrm{= 4AlN + 2SiC + 6NaF + 4H_2 + 8N_2,}\end{gathered}\tag{2}$$

$$\begin{gathered}\mathrm{Si + 2Al + 6NaN_3 + (NH_4)_2SiF_6 + 2C =}\\ \mathrm{= 2AlN + 2SiC + 6NaF + 4H_2 + 9N_2,}\end{gathered}\tag{3}$$

$$\begin{gathered}\mathrm{3Si + 2Al + 6NaN_3 + (NH_4)_2SiF_6 + 4C =}\\ \mathrm{= 2AlN + 4SiC + 6NaF + 4H_2 +9N_2,}\end{gathered}\tag{4}$$

$$\begin{gathered}\mathrm{7Si + 2Al + 6NaN_3 + (NH_4)_2SiF_6 + 8C =}\\ \mathrm{= 2AlN + 8SiC + 6NaF + 4H_2 +9N_2.}\end{gathered}\tag{5}$$

xSi–yAl–NaN$_3$–AlF$_3$–xC system

$$\begin{gathered}\mathrm{2Si + 7Al + 3NaN_3 + AlF_3 + 2C =}\\ \mathrm{= 8AlN + 2SiC + 3NaF + 0.5N_2,}\end{gathered}\tag{6}$$

$$\begin{gathered}\mathrm{2Si + 3Al + 3NaN_3 + AlF_3 + 2C =}\\ \mathrm{= 4AlN + 2SiC + 3Na_F + 2.5N_2,}\end{gathered}\tag{7}$$

$$\begin{gathered}\mathrm{2Si + Al + 3NaN_3 + AlF_3 + 2C =}\\ \mathrm{= 2AlN + 2SiC + 3NaF + 3.5N_2,}\end{gathered}\tag{8}$$

$$\begin{gathered}\mathrm{4Si + Al + 3NaN_3 + AlF_3 + 4C =}\\ \mathrm{= 2AlN + 4SiC+ 3NaF + 3.5N_2,}\end{gathered}\tag{9}$$

$$\begin{gathered}\mathrm{8Si + Al + 3NaN_3 + AlF_3 + 8C =}\\ \mathrm{= 2AlN + 8SiC + 3NaF + 3.5N_2.}\end{gathered}\tag{10}$$

xSi–yAl–NaN$_3$–NH$_4$F–xC system

$$\begin{gathered}\mathrm{Si + 4Al + NaN_3 + NH_4F + C =}\\ \mathrm{= 4AlN + SiC + NaF + 2H_2,}\end{gathered}\tag{11}$$

$$\begin{gathered}\mathrm{Si + 2Al + NaN_3 + NH_4F + C =}\\ \mathrm{= 2AlN + SiC + NaF + 2H_2 + N_2,}\end{gathered}\tag{12}$$

$$\begin{gathered}\mathrm{Si + Al + NaN_3 + NH_4F + C =}\\ \mathrm{= AlN + SiC + NaF + 2H_2 + 1.5N_2,}\end{gathered}\tag{13}$$

$$\begin{gathered}\mathrm{2Si + Al + NaN_3 + NH_4F + 2C =}\\ \mathrm{= AlN + 2SiC + NaF + 2H_2 + 1.5N_2,}\end{gathered}\tag{14}$$

$$\begin{gathered}\mathrm{4Si + Al + NaN_3 + NH_4F + 4C =}\\ \mathrm{= AlN + 4SiC + NaF + 2H_2 + 1.5N_2.}\end{gathered}\tag{15}$$

The initial reagent mixtures (charges) from equations (1)–(15) were burned in bulk form with a relative density of 0.4 in a tracing paper cup with a diameter of 30 mm and a height of 45 mm inside a 4.5 L azide SHS reactor at a nitrogen gas pressure of 4 MPa. The cooled combustion product was removed from the reactor, crushed to a loose powdered state in a porcelain mortar, and washed with water to remove the by-product sodium fluoride (NaF). In most cases, the combustion product consisted of a highly dispersed powder of complex composition, appearing as equiaxed submicron particles with sizes ranging from 100 nm to 1 μm and fibers with diameters of 50–500 nm and lengths up to 5 μm, with a tendency toward an increased proportion of finer particles as the SiC content in the AlN–SiC composition increased. This is illustrated in Fig. 1 for the system with the halide salt NH_4F, and in study [34] for the system with $(NH_4)_2SiF_6$. The results comparing the phase composition of the washed solid combustion products from charges (1)–(15) (determined experimentally) with the theoretical composition of the target phases expected according to the stoichiometric equations (1)–(15) are presented in Table 1. As shown, the experimental phase composition of the azide SHS products significantly deviates from the expected theoretical composition of the AlN–SiC powder compositions. First, the content of the target phases AlN and SiC is lower than theoretically expected, particularly the SiC phase, whose quantity is on average half of the theoretical amount. Second, an undesirable side phase of silicon nitride in α- and β-modifications is present in considerable amounts (up to 22.1 and 15.2 wt. %, respectively). Third, there is a noticeable amount (from 4.1 to 9.8 wt. %) of an unwanted water-insoluble impurity, the cryolite salt Na_3AlF_6.

In this context, the aim of this study was to bring the experimental composition of the target highly dispersed AlN and SiC powder mixture closer to the theoretical composition according to the stoichiometric equations of azide SHS Technology by adjusting the composition of the initial reagents and the conditions of the azide SHS process. Primarily, it is essential to significantly increase the content of the SiC carbide phase in the azide SHS product. Several approaches are known [38] to promote the formation of SiC during the combustion of a silicon and carbon black powder mixture via the weakly exothermic reaction

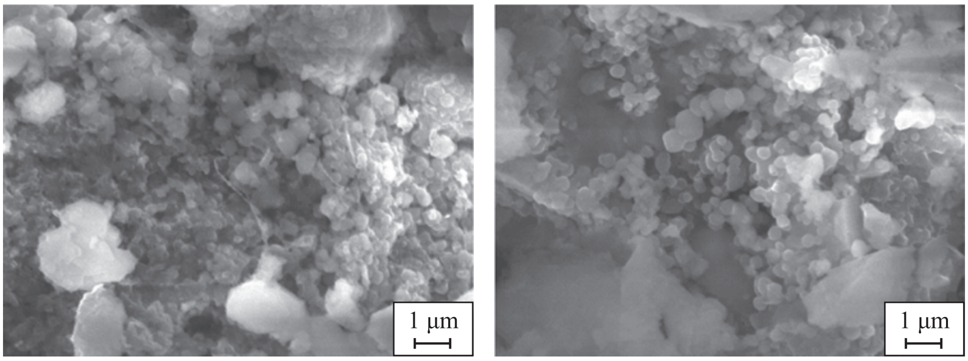

(11) $Si + 4Al + NaN_3 + NH_4F + C$ (12) $Si + 2Al + NaN_3 + NH_4F + C$

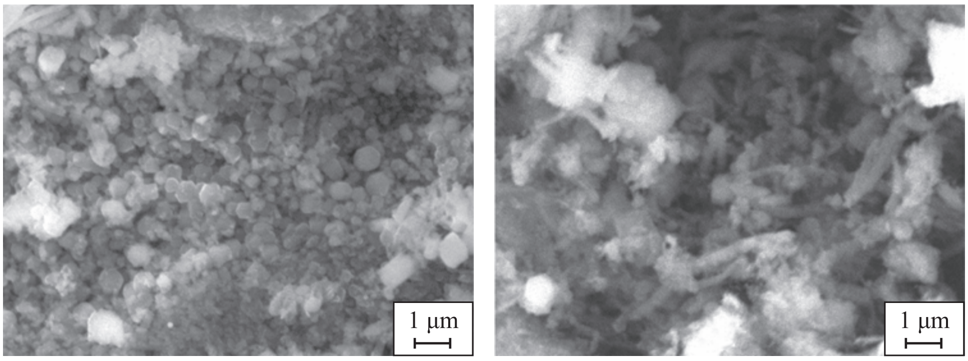

(13) $Si + Al + NaN_3 + NH_4F + C$ (14) $2Si + Al + NaN_3 + NH_4F + 2C$

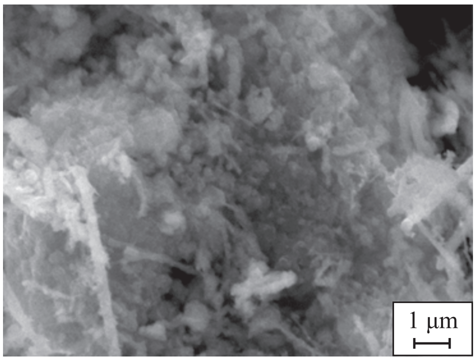

(15) $4Si + Al + NaN_3 + NH_3F + 4C$

Fig. 1. SEM images of combustion products of charges with NH4F according to equations (11)–(15)

Рис. 1. Микроструктура продуктов горения шихт с NH_4F в соответствии с уравнениями (11)–(15)

$$Si + C \rightarrow SiC: \quad (16)$$

– preheating the charge;

– applying an electric field;

– mechanical activation of the charge;

– conducting combustion in a gaseous nitrogen or air atmosphere;

– chemical activation with catalytic powder additives.

Most of these approaches can lead to submicron or even nanoscale SiC powders in the combustion mode. In this study, the simplest approach was chosen – using the most effective catalytic additive, powdered polytetrafluoroethylene (PTFE) [39; 40].

In the first study on this topic, the chemical transformation mechanism and combustion modes in the silicon–carbon–PTFE system were investigated, depending on the ratios of the starting components, the pressure of the inert atmosphere, ignition source temperature, and sample diameter [39]. Subsequently, combustion in this system was studied in a nitrogen atmosphere at varying pressures to produce SHS composite ceramic powders of Si_3N_4–SiC and silicon carbide [41]. It was found that without PTFE, the synthesized Si_3N_4–SiC composites contained between 5 and 60 wt. % SiC, whereas the use

Table 1. **Theoretical and experimental phase composition of washed solid products of azide SHS**

Таблица 1. **Теоретический и экспериментальный фазовые составы промытых твердых продуктов азидного СВС**

Reaction equation	AlN:SiC (mol)	Content, wt. %						
		Theoretical		Experimental				
		AlN	SiC	AlN	SiC	α-Si_3N_4	β-Si_3N_4	Na_3AlF_6
xSi–yAl–NaN_3–$(NH_4)_2SiF_6$–$(x + 1)$C								
(1)	4:1	80.4	19.6	69.3	8.5	8.0	7.0	7.2
(2)	2:1	67.2	32.8	54.6	10.3	13.2	12.1	9.8
(3)	1:1	50.6	49.4	38.0	19.2	22.1	13.2	7.5
(4)	1:2	33.8	66.2	29.9	28.0	21.4	14.0	6.7
(5)	1:4	20.4	79.6	18.5	42.1	19.6	15.2	4.6
xSi–yAl–NaN_3–AlF_3–xC								
(6)	4:1	80.4	19.6	73.6	8.2	5.7	8.4	4.1
(7)	2:1	67.2	32.8	58.0	17.9	11.2	7.4	5.5
(8)	1:1	50.6	49.4	47.0	24.6	13.0	9.1	6.3
(9)	1:2	33.8	66.2	23.9	34.8	19.7	15.0	6.6
(10)	1:4	20.4	79.6	13.5	47.2	21.4	12.6	5.3
xSi–yAl–NaN_3–NH_4F–xC								
(11)	4:1	80.4	19.6	72.5	7.9	8.2	7.1	4.3
(12)	2:1	67.2	32.8	64.0	12.9	9.6	8.5	5.0
(13)	1:1	50.6	49.4	39.0	25.0	18.1	11.9	6.0
(14)	1:2	33.8	66.2	25.4	33.5	21.2	13.6	6.3
(15)	1:4	20.4	79.6	14.4	46.2	21.9	12.3	5.2

of an activating additive at 5–15 wt. % increased the SiC content to 100 %. Study [42] demonstrated that partially replacing carbon with PTFE led to complete carbidizing in the reaction $Si + 0.9C + 0.05C_2F_4 = SiC + 0.1F_2$ in a nitrogen atmosphere at 3 MPa, producing SiC particles with an average size of around 200 nm. Study [43] showed that PTFE can be used not only as an activating additive but also as a carbidizing reagent when fully replacing technical carbon during combustion of a bulk Si + PTFE mixture in gaseous argon at 0.5 MPa, resulting in the synthesis of silicon carbide in the form of fibers with diameters of 100–500 nm and equiaxed particles of 0.5–3.0 µm, which aggregate into clusters. However, the yield of SiC synthesis was very low: only about 10 % of the total charge mass reacted to form fibrous SiC, with the remainder consisting of unreacted carbon and silicon [43].

The reactions for silicon carbide formation involving polytetrafluoroethylene $(–C_2F_4–)_n$ can be represented as follows [43; 44]:

$$2(–C_2F_4–)_n \rightarrow CF_4(g) + 2CF_2(g) + C(s), \qquad (17)$$

$$4Si(l) + 2CF_4(g) + 2CF_2(g) \rightarrow$$
$$\rightarrow SiF_4(g) + 2SiF_3(g) + SiF_2(g) + 4C(s), \qquad (18)$$

$$2SiF_2(g) + 2SiF_3(g) \rightarrow 2.5SiF_4(g) + 1.5Si(l), \qquad (19)$$

$$Si(l) + C(s) \rightarrow SiC(s). \qquad (20)$$

The first stage (17) involves the exothermic decomposition of PTFE in the preheating zone into gaseous fluorides and solid carbon particles. The intermediate stages (18) and (19) represent interactions between the gaseous fluorides with each other and with molten silicon particles, while the final stage (20) depicts the reaction between silicon and carbon particles (both the original carbon in the form of carbon black and the carbon generated from PTFE decomposition) to form the target silicon carbide. The completion of all stages results in the formation of highly dispersed SiC, whereas only the first stage yields gaseous fluorides and carbon black particles [43]. Combustion involving PTFE occurs at a high rate with intense gas release, which may cause dispersion of the charge components, preventing the silicon and carbon particles from reacting with each other, a reaction that is unlikely to proceed in the gas phase [43]. Therefore, a PTFE-containing charge should be in a pressed, rather than bulk, form, as a briquette with a diameter of at least 30 mm, and combusted under excess gas pressure in the SHS reactor to prevent PTFE decomposition products from escaping the reaction zone [39; 42–44].

In the present study, these findings were used to increase the SiC phase content in the target composition of highly dispersed AlN–SiC powders produced via azide SHS technology with PTFE, aiming to bring the experimental composition of the target highly dispersed AlN and SiC powders closer to the theoretical composition in accordance with the stoichiometric equations of azide SHS.

Research methodology

In the study of AlN–SiC composition synthesis processes using azide SHS technology with PTFE, the following initial charge components were used (here and throughout: wt. %):

– silicon powder, grade Kr00 (main substance content ≥ 99.9 %, average particle size $d = 40$ μm);

– aluminum powder, grade PA-4 (≥ 98.0 %, $d = 100$ μm);

– sodium azide powder, analytical grade (≥ 98.71 %, $d = 100$ μm);

– polytetrafluoroethylene (PTFE), grade PN-40 (≥ 99.0 %, $d = 40$ μm);

– technical carbon black, grade P701 (≥ 88.0 %, $d = 70$ nm, in the form of agglomerates up to 1 μm).

PTFE was used as an activating and carbidizing additive, partially replacing technical carbon black. Based on the findings from studies [39; 41; 42], a carbidizing mixture of technical carbon and PTFE of various compositions was used to carbidize silicon, equivalent to 1 mole of carbidizing carbon:

$$0.9C + 0.05C_2F_4, \qquad (A)$$

$$0.8C + 0.1C_2F_4, \qquad (B)$$

$$0.7C + 0.15C_2F_4. \qquad (C)$$

These mixtures correspond to PTFE concentrations of 5 to 15 %, necessary for obtaining pure SiC through reaction (16) and achieving an increased SiC content in composites with silicon nitride [41]. Sodium azide (NaN_3) was added to the charge in an amount sufficient to neutralize the fluorine released during the complete decomposition of PTFE, binding it into the water-soluble compound NaF, which can be easily removed from the azide SHS product by washing with water. As a result, the stoichiometric equations of the azide SHS for AlN–SiC powder compositions with 5 molar ratios of target phases AlN:SiC = 4:1, 2:1, 1:1, 1:2 and 1:4 using carbidizing mixture (*A*) with PTFE under combustion in gaseous nitrogen are as follows:

$$4Al + Si + 0.9C + 0.05C_2F_4 + 0.2NaN_3 + 1.7N_2 = 4AlN + SiC + 0.2NaF, \qquad (21)$$

$$2Al + Si + 0.9C + 0.05C_2F_4 + 0.2NaN_3 + 0.7N_2 = 2AlN + SiC + 0.2NaF, \qquad (22)$$

$$Al + Si + 0.9C + 0.05C_2F_4 + 0.2NaN_3 + 0.2N_2 = AlN + SiC + 0.2NaF, \qquad (23)$$

$$Al + 2Si + 1.8C + 0.1C_2F_4 + 0.4NaN_3 = AlN + 2SiC + 0.4NaF + 0.2N_2, \qquad (24)$$

$$Al + 4Si + 3.6C + 0.2C_2F_4 + 0.8NaN_3 = AlN + 4SiC + 0.8NaF + 0.7N_2. \qquad (25)$$

To achieve an AlN–SiC composition with the maximum silicon carbide phase content (AlN:SiC = 1:4) carbidizing mixtures (*B*) and (*C*) with an increased PTFE content were also used:

$$Al + 4Si + 3.2C + 0.4C_2F_4 + 1.6NaN_3 = AlN + 4SiC + 1.6NaF + 1.9N_2, \qquad (26)$$

$$Al + 4Si + 2.8C + 0.6C_2F_4 + 2.4NaN_3 = AlN + 4SiC + 2.4NaF + 3.1N_2. \qquad (27)$$

The initial reagent mixtures (charges) from equations (21)–(27), with an average mass of 22 g, were burned in a 4.5 L azide SHS reactor under a nitrogen gas pressure of 3 MPa, both in bulk form in a tracing paper cup with a diameter of 30 mm and height of 45 mm, and as briquettes pressed at a pressure of 7 MPa with a diameter of 30 mm and an average height of 22 mm. Combustion was initiated with an electric tungsten coil. The maximum gas pressure generated in the reactor during combustion was recorded using a manometer, and the maximum combustion temperature was measured with a tungsten-rhenium thermocouple of 200 μm in diameter, inserted into the charge. The cooled combustion product was removed from the reactor, ground to a loose powder state in a porcelain mortar and washed with water to remove the by-product sodium fluoride (NaF).

The phase composition of the synthesized products was determined using an ARL X’TRA powder *X*-ray diffractometer (Thermo Fisher Scientific, Switzerland) equipped with a copper anode *X*-ray tube. Diffraction pattern analysis and quantitative phase composition assessment were performed using the Rietveld method in the HighScore Plus software with the COD-2024 crystallographic database. The morphology and particle size of the synthesized compositions were examined using a JSM-6390A scanning electron microscope (Jeol, Japan).

Results and discussion

The results of experimental determination of the parameters for azide SHS of AlN–SiC powder compositions according to equations (21)–(25) are presented in Table 2. As the data indicate, combustion of bulk mixtures occurs more intensively than that of pressed mixtures, with higher maximum temperatures and pressure spikes, accompanied by greater dispersion of the SHS reactants and products. The higher the aluminum content in the charge, the greater the combustion parameters (temperature and pressure); however, at maximum aluminum content, the mass loss of the product due to dispersion is offset by mass gain from increased absorption of gaseous nitrogen during aluminum nitride formation. Mass loss is highest in the synthesis of AlN–SiC compositions with roughly equal molar ratios, especially in the case of bulk mixtures. However, this loss decreases as the SiC content in the combustion product increases, accompanied by a reduction in combustion parameters

The *X*-ray diffraction (XRD) patterns of phase analysis of water-washed solid combustion products from bulk and pressed mixtures are shown in Figs. 2 and 3, respectively.

The data in Fig. 2 show that the XRD patterns of water-washed combustion products from bulk charges used for synthesizing AlN–SiC composites with higher and equal molar content of the AlN phase, i.e., AlN:SiC = 4:1, 2:1 and 1:1, contain strong reflections only for the target phases AlN and SiC, along with weak reflections from free silicon impurities. For the combustion products with increased SiC phase content, i.e., AlN:SiC = 1:2 and 1:4, in addition to the AlN, SiC, and Si reflections, distinct peaks of the undesirable by-product phase Si_3N_4 appear, particularly noticeable in the sample with the maximum SiC content. The XRD patterns of combustion products from pressed charges shows only the target phases AlN and SiC for four ratios AlN:SiC = 4:1, 2:1, 1:1 and 1:2 (with a Si impurity for AlN:SiC = 2:1) and the appearance of an additional undesirable by-product phase, Si_3N_4, in one case, AlN:SiC = 1:4, with maximum SiC content (Fig. 3).

Table 3 presents the results of quantitative analysis of the XRD patterns, showing the quantitative phase content in the washed combustion products from charges (21)–(25) with carbidizing mixture (*A*) and minimal PTFE content, as well as for equations (26) and (27) to obtain an AlN–SiC composition with the maximum silicon carbide phase content (AlN:SiC = 1:4) using mixtures (*B*) and (*C*) with increased PTFE content. These experimental data are compared with the theoretical results for the target phases AlN and SiC content in the reaction products according to stoichiometric equations (21)–(27).

Table 3 shows that, compared to the azide SHS products without PTFE presented in Table 1, the use of equations (21)–(25) with the first carbidizing mixture (*A*), containing minimal PTFE ($0.9 + 0.05C_2F_4$), led to several notable changes:

Table 2. **Combustion parameters of initial powder mixtures for reactions (21)–(25)**

Таблица 2. **Параметры горения исходных порошковых смесей реакций (21)–(25)**

Reaction equation	Initial powder mixture	Maximum combustion temperature, K	Maximum pressure, MPa	Yield of solid products, g	Mass loss, %
Bulk initial powder mixtures					
(21)	$4Al + Si + 0.9C + 0.05C_2F_4 + 0.2NaN_3$	3270	4.38	26.18	0.38
(22)	$2Al + Si + 0.9C + 0.05C_2F_4 + 0.2NaN_3$	3270	4.20	25.07	0.23
(23)	$Al + Si + 0.9C + 0.05C_2F_4 + 0.2NaN_3$	2870	4.14	17.76	26.27
(24)	$Al + 2Si + 1.8C + 0.1C_2F_4 + 0.4NaN_3$	2790	4.19	14.26	38.90
(25)	$Al + 4Si + 3.6C + 0.2C_2F_4 + 0.8NaN_3$	2620	4.09	15.99	26.68
Pressed mixtures					
(21)	$4Al + Si + 0.9C + 0.05C_2F_4 + 0.2NaN_3$	3180	3.89	26.25	0.11
(22)	$2Al + Si + 0.9C + 0.05C_2F_4 + 0.2NaN_3$	3120	3.61	25.10	0.11
(23)	$Al + Si + 0.9C + 0.05C_2F_4 + 0.2NaN_3$	2720	3.51	11.41	26.27
(24)	$Al + 2Si + 1.8C + 0.1C_2F_4 + 0.4NaN_3$	2690	3.81	20.61	11.69
(25)	$Al + 4Si + 3.6C + 0.2C_2F_4 + 0.8NaN_3$	2550	3.71	20.80	4.60

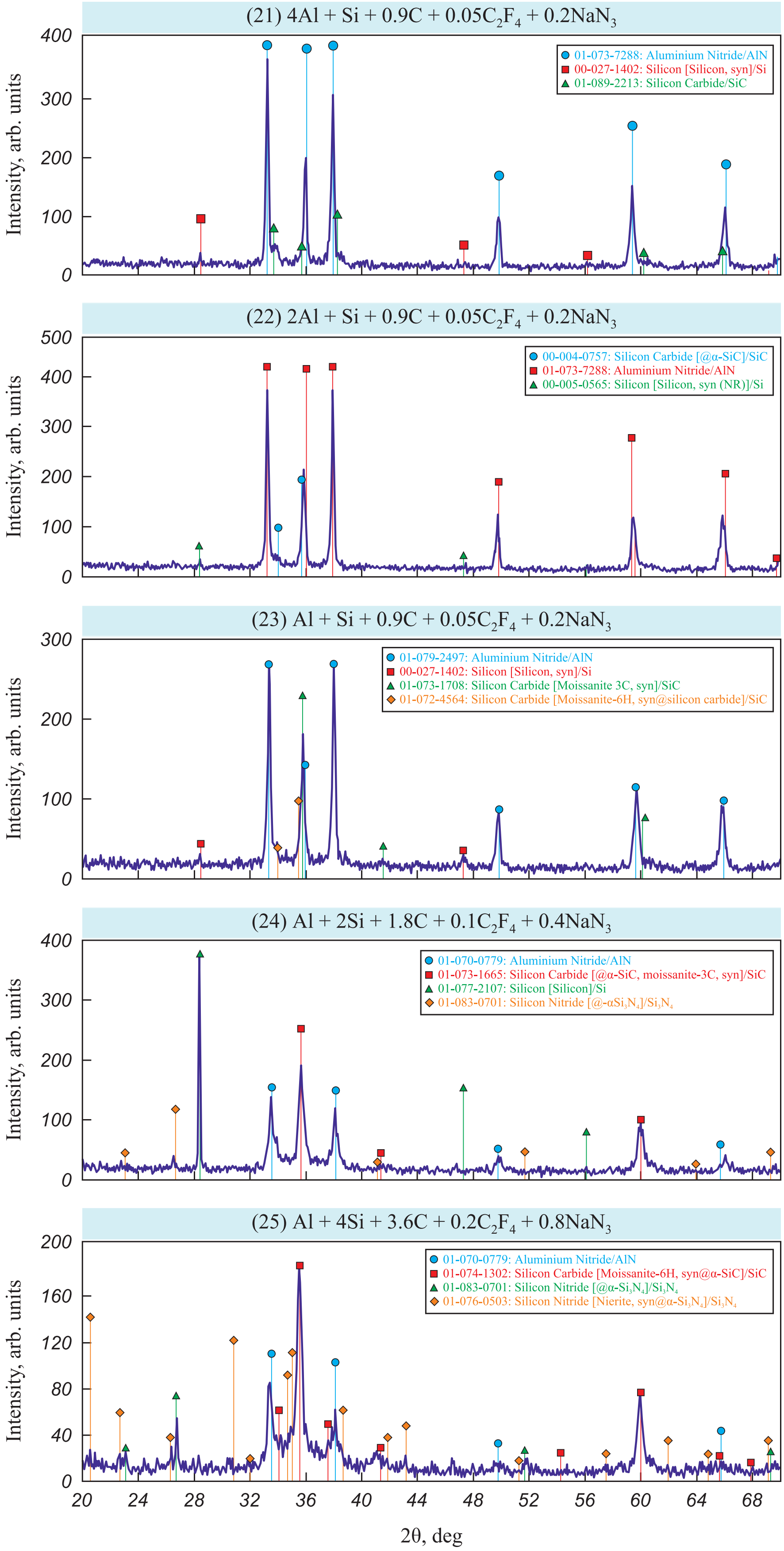

Fig. 2. XRD patterns of combustion products from bulk charges (21)–(25)

Рис. 2. Рентгеновские дифрактограммы продуктов горения насыпных шихт (21)–(25)

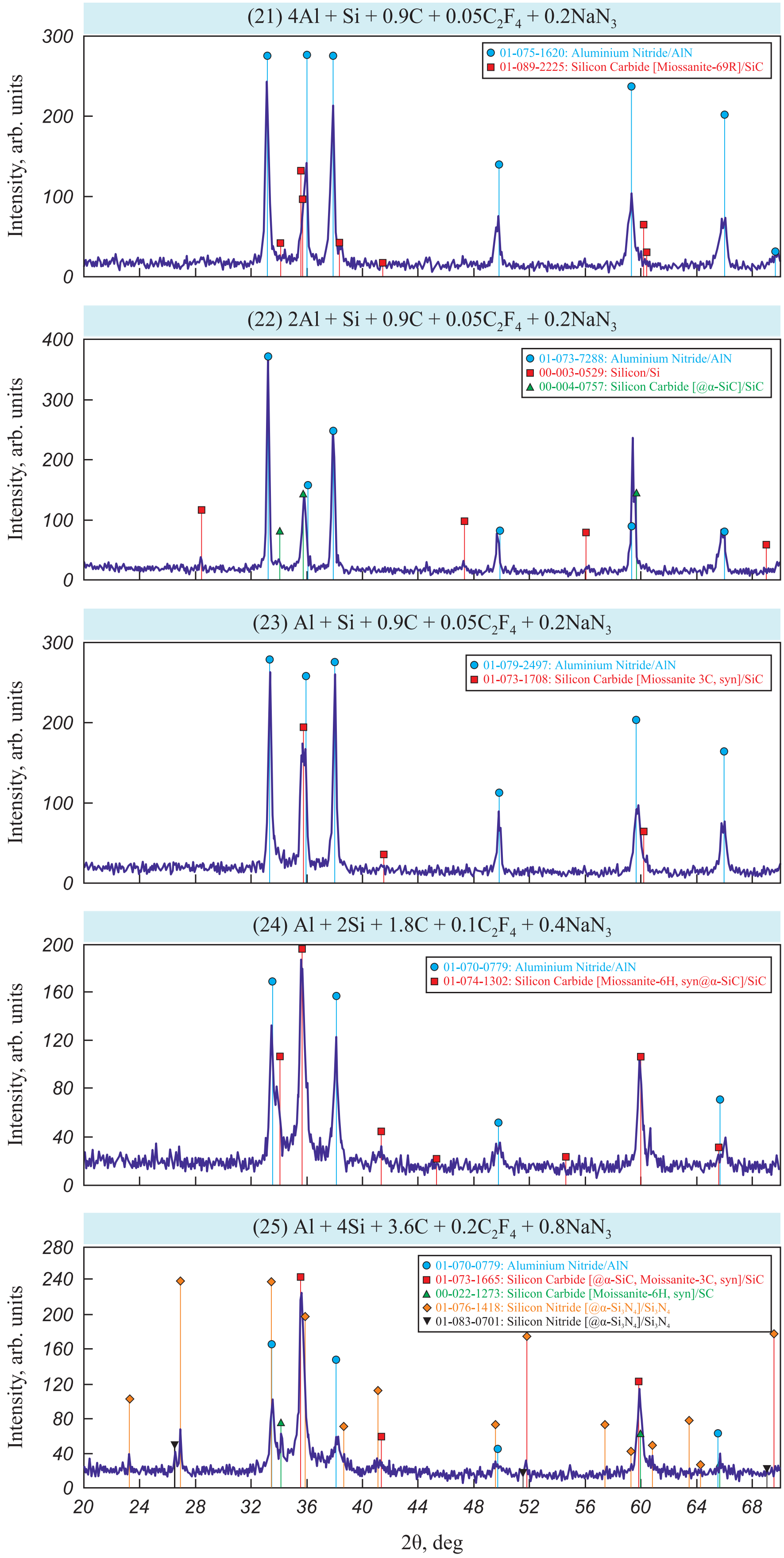

Fig. 3. XRD patterns of combustion products from pressed charges (21)–(25)

Рис. 3. Рентгеновские дифрактограммы продуктов горения прессованных шихт (21)–(25)

– the undesirable, water-insoluble impurity of cryolite salt Na_3AlF_6 completely absent from the combustion products of both bulk and pressed charges, which represents a significant improvement;

– the presence of the undesirable Si_3N_4 by-product phase is eliminated or substantially reduced to 15 % (observed in bulk charges with AlN:SiC ratios of 1:2 and 1:4, and in pressed charges with an AlN:SiC ratio of 1:4);

– impurities of free silicon and carbon are reduced or even absent, particularly in pressed charges, where only 2 % free silicon was detected at an AlN:SiC ratio of 2:1;

– the experimental content of the target phases AlN and SiC for most ratios closely aligns with the theoretical content, especially in pressed charges, with the exception of bulk charges at AlN:SiC ratios of 1:2 and 1:4 and pressed charges at an AlN:SiC ratio of 1:4.

At the same time, increasing the amount of PTFE in carbidizing mixtures (*B*) and (*C*), along with a higher proportion of sodium azide NaN_3 for fluorine neutralization in equations (26) and (27), leads to the appearance of the undesirable cryolite salt impurity Na_3AlF_6 (from 4 to 8 %) in the combustion products of both bulk and pressed charges. It also significantly increases the content of the undesirable Si_3N_4 by-product phase and, consequently, substantially reduces the proportion of the target phases AlN and SiC compared to their theoretical content.

The microstructures of the washed powder combustion products from bulk and pressed charges according to the stoichiometric reaction equations (21)–(25) are shown in Figs. 4 and 5. These figures reveal a trend of decreasing particle size in the combustion products as the SiC content increases in the AlN–SiC powder compositions, corresponding to the trend of decreasing maximum combustion temperature as the SiC content in the product rises (see Table 2). The powders are largest at an AlN:SiC ratio of 4:1, with particles up to 5 μm for bulk charges and up to 2 μm for pressed charges. In other compositions with lower AlN content, the synthesized powders are highly dispersed, consisting of submicron equiaxed particles ranging from 100 nm to 1 μm and nanofibers with diameters of 50–500 nm and lengths up to 5 μm. As the SiC content in the product increases, the proportion of the smallest equiaxed particles, measuring 100–300 nm, also increases. The AlN:SiC ratio of 1:4 composition, with the highest

Table 3. **Theoretical and experimental phase composition of water-washed solid products of azide SHS according to equations (21)–(27) for bulk and pressed charges**

Таблица 3. **Теоретический и экспериментальный фазовые составы промытых твердых продуктов азидного СВС согласно уравнениям (21)–(27) для насыпных и прессованных шихт**

Equation reaction	AlN:SiC (mol)	Content, wt. %							
		Theoretical		Experimental					
		AlN	SiC	AlN	SiC	Si_3N_4	Si	C	Na_3AlF_6
Bulk charges									
(21)	4:1	80.4	19.6	81.0	15.0	–	4.0	–	–
(22)	2:1	67.2	32.8	62.0	36.0	–	2.0	–	–
(23)	1:1	50.6	49.4	47.5	51.5	–	1.0	–	–
(24)	1:2	33.8	66.2	20.0	65.0	15.0	–	–	–
(25)	1:4	20.4	79.6	33.7	49.5	15.9	–	0.9	–
(26)	1:4	20.4	79.6	6.1	46.4	36.5	3.0	4.0	4.0
(27)	1:4	20.4	79.6	11.1	42.4	34.4	4.0	–	8.1
Pressed charges									
(21)	4:1	80.4	19.6	80.0	20.0	–	–	–	–
(22)	2:1	67.2	32.8	66.0	32.0	–	2.0	–	–
(23)	1:1	50.6	49.4	51.0	49.0	–	–	–	–
(24)	1:2	33.8	66.2	38.0	62.0	–	–	–	–
(25)	1:4	20.4	79.6	18.0	67.0	15.0	–	–	–
(26)	1:4	20.4	79.6	19.0	46.4	27.6	3.0	4.0	7.0
(27)	1:4	20.4	79.6	17.0	42.4	31.6	4.0	–	5.0

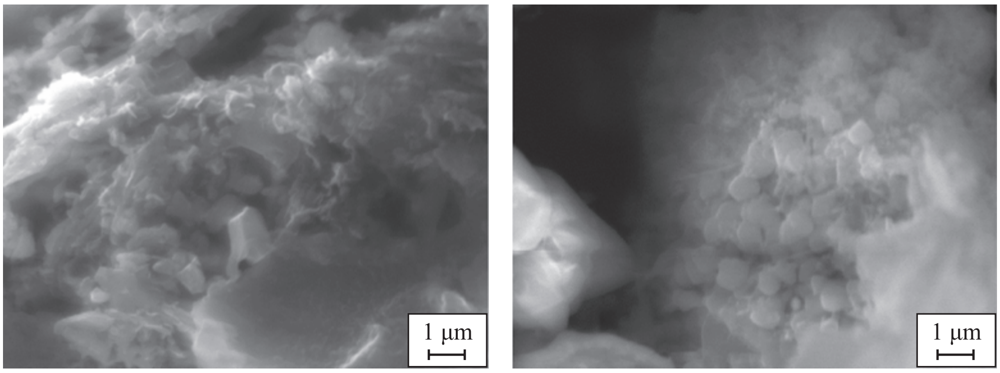

(21) $4Al + Si + 0.9C + 0.05C_2F_4 + 0.2NaN_3$ (22) $2Al + Si + 0.9C + 0.05C_2F_4 + 0.2NaN_3$

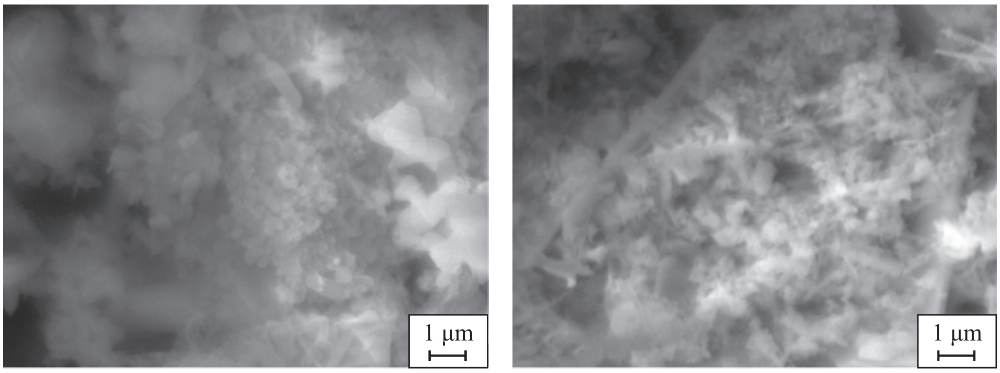

(23) $Al + Si + 0.9C + 0.05C_2F_4 + 0.2NaN_3$ (24) $Al + 2Si + 1.8C + 0.1C_2F_4 + 0.4NaN_3$

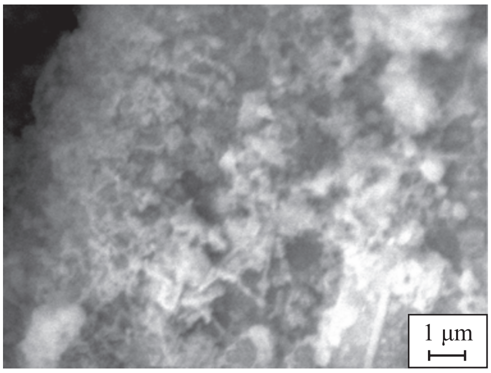

(25) $Al + 4Si + 3.6C + 0.2C_2F_4 + 0.8NaN_3$

Fig. 4. SEM images of combustion products from bulk charges (21)–(25)

Рис. 4. Микроструктура продуктов горения насыпных шихт (21)–(25)

silicon carbide content, forms agglomerates of these small particles.

Nanofibers are practically absent in compositions with a high AlN content in the combustion products of both bulk and pressed charges, as well as in compositions with a high SiC content in the combustion products of pressed charges. The highest presence of nanofibers is observed in compositions with an equal phase content of AlN and SiC in the combustion products of both types of charges, as well as in compositions with a high SiC content in the combustion products of bulk charges.

Conclusion

The results of this study indicate that incorporating polytetrafluoroethylene (PTFE) in azide SHS technology has a highly positive impact on the production of AlN–SiC ceramic powders. While the traditional approach of azide SHS using sodium azide (NaN_3) as a nitriding agent and activating halide salt additives $(NH_4)_2SiF_6$, AlF_3, and NH_4F enabled the production of highly dispersed AlN–SiC powder compositions with particle sizes below 1 μm from a mixture of elemental aluminum, silicon, and carbon pow-

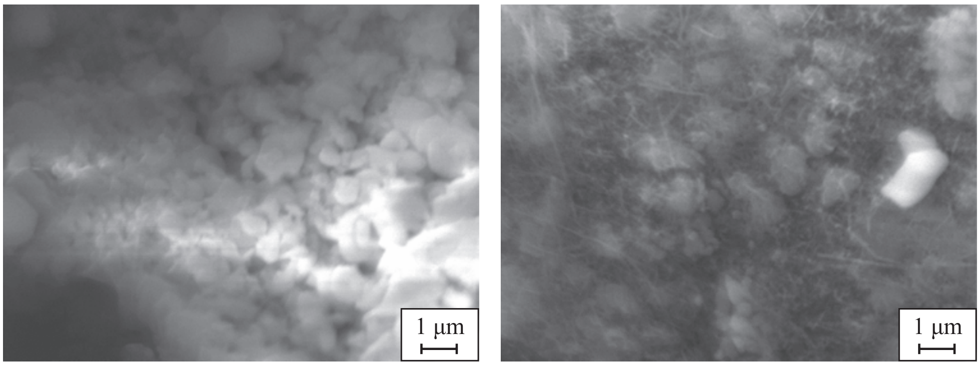

(21) $4Al + Si + 0.9C + 0.05C_2F_4 + 0.2NaN_3$ (22) $2Al + Si + 0.9C + 0.05C_2F_4 + 0.2NaN_3$

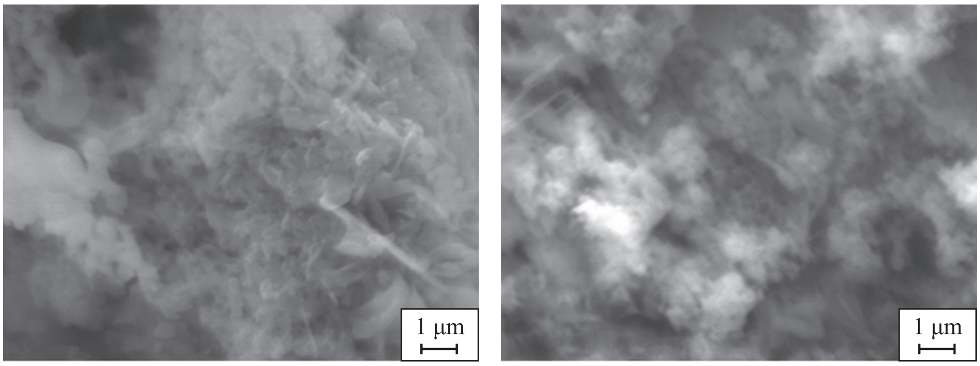

(23) $Al + Si + 0.9C + 0.05C_2F_4 + 0.2NaN_3$ (24) $Al + 2Si + 1.8C + 0.1C_2F_4 + 0.4NaN_3$

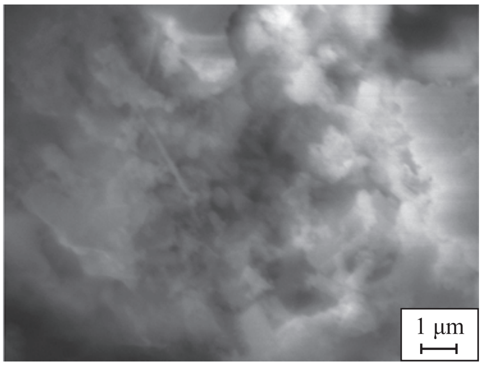

(25) $Al + 4Si + 3.6C + 0.2C_2F_4 + 0.8NaN_3$

Fig. 5. SEM images of combustion products from pressed charges (21)–(25)

Рис. 5. Микроструктура продуктов горения прессованных шихт (21)–(25)

ders – a clear advantage of this technology – the phase composition of these compositions had significant drawbacks. Ideally, the phase composition should match the various targeted theoretical ratios of aluminum nitride and silicon carbide phases in accordance with the initial stoichiometric equations. However, the experimentally obtained target phases AlN and SiC were substantially below the theoretical values, particularly for the SiC phase, whose quantity was, on average, half of the theoretical amount. Additionally, significant amounts of undesirable by-product phases, including silicon nitride and the water-insoluble cryolite salt Na_3AlF_6, were present.

Introducing PTFE as an activating and carbidizing additive, partially replacing carbon in the carbidizing mixture $0.9C + 0.05C_2F_4$ during azide SHS, resolved most of the traditional approach's limitations across various AlN and SiC target ratios.

This adjustment maintained the high dispersity of the synthesized AlN–SiC powders while bringing their phase composition – especially in pressed charges – much closer to the theoretical target. The SiC phase content also increased significantly, and the unwanted by-products of silicon nitride and the water-insoluble cryolite salt Na_3AlF_6 were eliminated. However, for AlN–SiC compositions with the highest relative SiC content, it was not possible to completely avoid the formation of the silicon nitride by-product phase.

References / Список литературы

1. Kosolapova T.Ya., Andreeva T.V., Bartnitskaya T.B., Gnesin G.G., Makarenko G.N., Osipova I.I., Prilutskii E.V. Nonmetallic refractory compounds. Moscow: Metallurgiya, 1985. 224 p. (In Russ.).

   Косолапова Т.Я., Андреева Т.В., Бартницкая Т.Б., Гнесин Г.Г., Макаренко Г.Н., Осипова И.И., Прилуцкий Э.В. Неметаллические тугоплавкие соединения. М.: Металлургия, 1985. 224 с.
2. Yaguchi H., Ozaki K., Somekawa M. Improvement of cutting tool life by AlN deposition on the tool. *The Iron and Steel Institute of Japan International*. 2004;44(3):598–602. https://doi.org/10.2355/isijinternational.44.598
3. Wang Z., Zou J., Cai S., Zou Y., Ling L., Liang H., Weimin W., Lv X., Fu Z. Aluminum nitride-based ceramics with excellent thermal shock resistances. *Journal of the American Ceramic Society*. 2024;107(8):5352–5363. https://doi.org/10.1111/jace.19829
4. Nepochatov Yu., Zemnitskaya A., Mul' P. Development of ceramics based on aluminum nitride for electronic products. *Sovremennaya elektronika*. 2011;(9):14–16. (In Russ.).

   Непочатов Ю., Земницкая А., Муль П. Разработка керамики на основе нитрида алюминия для изделий электронной техники. *Современная электроника*. 2011;(9):14–16.
5. Li N., Ho C.P., Zhu S., Fu Y.H., Zhu Y., Lee L.Y.T. Aluminium nitride integrated photonics: A review. *Nanophotonics*. 2021;10(9):2347–2387. https://doi.org/10.1515/nanoph-2021-0130
6. Unni C.K., Gordon D.E. Mechanical properties of monolithic AlN and SiC_w/AlN composites. *Journal of Materials Science*. 1995;30(5):1173–1179. https://doi.org/10.1007/BF00356116
7. Besisa D.H.A., Ewais E.M.M., Ahmed Ya.M.Z., Elhosiny F.I., Fend T., Kuznetsov D.V. Investigation of microstructure and mechanical strength of SiC/AlN composites processed under different sintering atmospheres. *Journal of Alloys and Compounds*. 2018;756:175–181. https://doi.org/10.1016/J.JALLCOM.2018.05.020
8. Besisa D.H.A., Ewais E.M.M., Ahmed Ya.M.Z., Elhosiny F.I., Fend T., Kuznetsov D.V. Thermal shock resistance of pressureless sintered SiC/AlN ceramic composites. *Materials Research Express*. 2018;5(1):015506. https://doi.org/10.1088/2053-1591/aaa2c2
9. Zangvil A., Ruh R. Phase relationship in the silicon carbide-aluminum nitride system. *Journal of the American Ceramic Society*. 1988;71(10):884–890. https://doi.org/10.1111/J.1151-2916.1988.TB07541.X
10. Han J., Li Y., Chenhong M., Zheng Q., Zhang X. Formation mechanism of AlN-SiC solid solution with multiple morphologies in Al-Si-SiC composites under flowing nitrogen at 1300 °C. *Journal of the European Ceramic Society*. 2022;42(14):6356–6363. https://doi.org/10.1016/j.jeurceramsoc.2022.07.011
11. Miura M., Yogo T., Hirano S.-I. Phase separation and toughening of SiC–AlN solid-solution ceramics. *Journal of Materials Science*. 1993;28(14):3859–3865. https://doi.org/10.1007/BF00353191
12. Lee R.-R., Wei W.-C. Chapter 39 – Fabrication, microstructure, and properties of SiC–AlN ceramic alloys. In: *A Collection of Papers Presented at the 14th Annual Conference on Composites and Advanced Ceramic Materials: Ceramic Engineering and Science Proceedings*. 1990. P. 1094–1121. https://doi.org/10.1002/9780470313008.ch39
13. Palmero P. Structural ceramic nanocomposites: A review of properties and powders' synthesis methods. *Nanomaterials*. 2015;5(2):656–696. https://doi.org/10.3390/nano5020656
14. Li G., Li B., Ren B., Chen H., Zhu B., Chen J. Synthesis of aluminum nitride using sodium aluminate as aluminum source. *Processes*. 2023;11(4):1034. https://doi.org/10.3390/pr11041034
15. Gao P., Jia Ch.-Ch., Cao W.-B., Wang C.-C., Liang D., Xu G.-L. Dielectric properties of spark plasma sintered AlN/SiC composite ceramics. *International Journal of Minerals, Metallurgy, and Materials*. 2014;21(6):589–594. https://doi.org/10.1007/s12613-014-0946-1
16. Elagin A.A., Beketov A.R., Baranov M.V., Shishkin R.A. Aluminum nitride. Preparation methods (Review). *Refractories and Industrial Ceramics*. 2013;53(6):395–403.

    Елагин А.А., Бекетов А.Р., Баранов М.В., Шишкин Р.А. Нитрид алюминия. Методы получения (обзор). *Новые огнеупоры*. 2012;(11):57–67. https://doi.org/10.1007/s11148-013-9534-6
17. Teusel I., Rüssel C. Pressureless sintering of aluminium nitride/silicon carbide ceramics. *Journal of Materials Science Letters*. 1992;11(4):205–207. https://doi.org/10.1007/bf00741422
18. Ruh R., Zangvil A. Composition and properties of hot-pressed SiC–AlN solid solution. *Journal of the American Ceramic Society*. 1982;65(5):260–265. https://doi.org/10.1111/J.1151-2916.1982.tb10429.x
19. Du X.L., Qin M.L., Sun Y., Yuan Z.H., Yang B.H., Qu X.H. Structure and thermal conductivity of powder injection molded AlN ceramic. *Advanced Powder Technology*. 2010;21(4):431–434. https://doi.org/10.1016/j.apt.2010.01.001
20. Kobayashi R., Oh-Ishi K., Tu R., Goto T. Sintering behavior, microstructure, and thermal conductivity of dense AlN ceramics processed by spark plasma sintering with Y_2O_3-CaO-B additives. *Ceramics International*. 2015;41(1B):1897–1901. https://doi.org/10.1016/j.ceramint.2014.09.040
21. Xu G.F., Olorunyolemi T., Wilson O.C., Lloyd I.K., Carmel Y. Microwave sintering of high-density, high thermal conductivity AIN. *Journal of Materials Research*. 2002;17(11):2837–2845. https://doi.org/10.1557/JMR.2002.0412
22. Tang Y., Xue Z., Zhou G., Hu S. Fabrication of high thermal conductivity aluminum nitride ceramics via digital

light processing 3D printing. *Materials*. 2024,17(9):2010. https://doi.org/10.3390/ma17092010

23. Basu B., Balani K. Advanced structural ceramics. Hoboken. New Jersey: John Wiley & Sons, Inc., 2011. 502 p.

24. Camargo P.H.C., Satyanarayana K.G., Wypych F. Nanocomposites: Synthesis, structure, properties and new application opportunities. *Materials Research*. 2009; 12(1):1–39. https://doi.org/10.1590/S1516-14392009000100002

25. Rane V., Kanny K., Abitha V.K., Thomas S. Chapter 5 – Methods for synthesis of nanoparticles and fabrication of nanocomposites. In: *Synthesis of inorganic nanomaterials: Advances and key technologies. A volume in micro and nano technologies.* (Eds. S.M. Bhagyaraj, O.S. Oluwafemi, N. Kalarikkal, S. Thomas). Woodhead Publishing, 2018. P. 121–139. https://doi.org/10.1016/B978-0-08-101975-7.00005-1

26. Wu X., Deng C., Di J., Ding J., Zhu H., Yu C. Fabrication of novel AlN–SiC–C refractories by nitrogen gas-pressure sintering of Al_4SiC_4. *Journal of the European Ceramic Society*. 2022;42(8):3634–3643. https://doi.org/10.1016/j.jeurceramsoc.2022.02.058

27. Chen K., Jin H., Zhou H., Ferreira J. Combustion synthesis of AlN–SiC solid solution particles. *Journal of The European Ceramic Society*. 2000;20(14-15):2601–2606. https://doi.org/10.1016/S0955-2219(00)00119-9

28. Rogachev A.S., Mukasyan A.S. Combustion for material synthesis. New York: CRC Press, 2014. 424 p. https://doi.org/10.1201/b17842

Рогачев А.С., Мукасьян А.С. Горение для синтеза материалов. М.: Физматлит, 2012. 400 с.

29. Levashov E.A., Mukasyan A.S., Rogachev A.S., Shtansky D.V. Self-propagating high-temperature synthesis of advanced materials and coatings. *International Materials Reviews*. 2016;62(4):1–37. https://doi.org/10.1080/09506608.2016.1243291

30. Xue H., Munir Z.A. The synthesis of composites and solid solutions of α-SiC AlN by field-activated combustion. *Scripta Materialia*. 1996;35(8):979–982. https://doi.org/10.1016/1359-6462(96)00246-1

31. Abbasi Z., Shariat M.H., Javadpour S. Microwave-assisted combustion synthesis of AlN–SiC composites using a solid source of nitrogen. *Powder Technology*. 2013;249:181–185. https://doi.org/10.1016/j.powtec.2013.08.012

32. Borovinskaya I.P., Akopdzhanyan T.G., Chemagina E.A., Sachkova N.V. Solid solution $(AlN)_x(SiC)_{1-x}$ ($x = 0.7$) by SHS under high pressure of nitrogen gas. *International Journal of Self-Propagating High-Temperature Synthesis*. 2018;27(1):33–36. https://doi.org/10.3103/S1061386218010028

33. Juang R.-C., Chen C.-C., Kuo J.-C., Huang T.-Y., Li Y.-Y. Combustion synthesis of hexagonal AlN–SiC solid solution under low nitrogen pressure. *Journal of Alloys and Compounds*. 2009;480(2):928–933. https://doi.org/10.1016/j.jallcom.2009.02.102

34. Amosov A.P., Titova Yu.V., Belova G.S., Maidan D.A., Minekhanova A.F. SHS of highly dispersed powder compositions of nitrides with silicon carbide. Review. *Powder Metallurgy and Functional Coatings*. 2022;16(4):34–57. https://doi.org/10.17073/1997-308X-2022-4-34-57

Амосов А.П., Титова Ю.В., Белова Г.С., Майдан Д.А., Минеханова А.Ф. СВС высокодисперсных порошковых композиций нитридов с карбидом кремния. Обзор. *Известия вузов. Порошковая металлургия и функциональные покрытия*. 2022;16(4):34–57. https://doi.org/10.17073/1997-308X-2022-4-34-57

35. Titova Yu.V., Amosov A.P., Maidan D.A., Belova G.S., Minekhanova A.F. Physical and chemical features of combustion synthesis of nanopowder composition AlN–SiC using sodium azide. *AIP Conference Proceedings*. 2020;2304(1):020008. https://doi.org/10.1063/5.0034318

36. Amosov A., Smetanin K., Titova Yu., Maidan D. Preparation of ceramic nitride-carbide composition AlN–SiC by SHS method using halide salt and sodium azide. In: *Proceedings of 7th International Congress on Energy Fluxes and Radiation Effects (EFRE-2020)* (Tomsk, Russia, September 14–25, 2020). IEEE Xplore. 2020:1110–1114. https://doi.org/10.1109/EFRE47760.2020.9241986

37. Belova G.S. Self-propagating high-temperature synthesis of ceramic nitride-carbide highly dispersed powder compositions Si_3N_4–SiC, AlN–SiC and TiN–SiC using sodium azide and halide salts: Diss. Cand. Sci. (Eng.). Samara: SamSTU, 2022. 209 p. (In Russ.).

Белова Г.С. Самораспространяющийся высокотемпературный синтез керамических нитридно-карбидных высокодисперсных порошковых композиций Si_3N_4–SiC, AlN–SiC и TiN–SiC с применением азида натрия и галоидных солей: дис. …канд. техн. наук. Самара: СамГТУ, 2022. 209 с.

38. Mukasyan A.S. Combustion synthesis of silicon carbide. In: *Properties and applications of silicon carbide.* (Ed. R. Gerhardt). Rijeka, Croatia: InTech, 2011. P. 361–388.

39. Nersisyan G.A., Nikogosov V.N., Kharatyan S.L., Merzhanov A.G. Chemical transformation mechanism and combustion regimes in the system silicon-carbon-fluoroplastic. *Combustion, Explosion, and Shock Waves*. 1991;27(6):720–724. https://doi.org/10.1007/BF00814517

Нерсисян Г.А., Никогосов В.Н., Харатян С.Л., Мержанов А.Г. Химический механизм превращения и режимы горения в системе кремний–углерод–фторопласт. *Физика горения и взрыва*. 1991;27(6):77–81.

40. Kharatyan S.L., Nersisyan H.H. Chemically activated SHS in synthesis of refractory carbide powders. *Key Engineering Materials*. 2002;217:83–92. https://doi.org/10.4028/www.scientific.net/KEM.217.83

41. Khachatryan G.L., Arutyunyan A.B., Kharatyan S.L. Activated combustion of a silicon–carbon mixture in nitrogen and SHS of Si_3N_4–SiC composite ceramic powders and silicon carbide. *Combustion, Explosion, and Shock Waves*. 2006;42(5):543–548. https://doi.org/10.1007/S10573-006-0086-7

Хачатрян Г.Л., Арутюнян А.Б., Харатян С.Л. Активированное горение смеси кремний–углерод в азоте и СВС композиционных керамических порошков

Si_3N_4/SiC и карбида кремния. *Физика горения и взрыва*. 2006;42(5):56–62.

42. Amirkhanyan N., Kirakosyan H., Zakaryan M., Zurnachyan A., Rodriguez M.A., Abovyan L., Aydinyan S. Sintering of silicon carbide obtained by combustion synthesis. *Ceramics International*. 2023;49(15):26129–26134. https://doi.org/10.1016/j.ceramint.2023.04.233

43. Zakorzhevsky V.V., Loryan V.E., Akopdzhanyan T.G. Self-propagating high-temperature synthesis of silicon carbide nanofibers. *Russian Journal of Non-Ferrous Metals*. 2020;61(6):675–679. https://doi.org/10.3103/S106782122006022X

Закоржевский В.В., Лорян В.Э., Акопджанян Т.Г. Самораспространяющийся высокотемпературный синтез нановолокон карбида кремния. *Известия вузов. Порошковая металлургия и функциональные покрытия*. 2020;(2):14–20. https://doi.org/10.17073/1997-308X-2020-2-14-20

44. Vorotilo S., Levashov E.A., Potanin A.Yu., Loginov P.A., Shvyndina N.V. Features of synthesizing ceramic composites discretely reinforced by carbon fibers and SiC nanowires formed in situ in the combustion wave. *Russian Journal of Non-Ferrous Metals*. 2020;61(5):559–570. https://doi.org/10.3103/S1067821220050168

Воротыло С., Левашов Е.А., Потанин А.Ю., Логинов П.А., Швындина Н.В. Особенности синтеза керамических композитов, дискретно армированных углеродными волокнами и формирующимися в волне горения in situ волокнами карбида кремния. *Известия вузов. Порошковая металлургия и функциональные покрытия*. 2020;(1):41–54. https://doi.org/10.17073/1997-308X-2020-41-54

Information about the Authors

Aleksandr P. Amosov – Dr. Sci. (Phys.-Math.), Professor, Head of the Department of Metallurgy, Powder Metallurgy, Nanomaterials (MPMN), Samara State Technical University (SamSTU)
ORCID: 0000-0003-1994-5672
E-mail: egundor@yandex.ru

Yuliya V. Titova – Cand. Sci. (Eng.), Associate Professor of the Department of MPMN, SamSTU
ORCID: 0000-0001-6292-280X
E-mail: titova600@mail.ru

Irina A. Uvarova – Junior Researcher of the Research Sector of the Department of MPMN, SamSTU
ORCID: 0000-0003-3023-3289
E-mail: mr.simple2@mail.ru

Galina S. Belova – Cand. Sci. (Eng.), Associate Professor of the Department of MPMN, SamSTU
ORCID: 0000-0002-6430-9408
E-mail: galya.belova.94@mail.ru

Сведения об авторах

Александр Петрович Амосов – д.ф.-м.н., профессор, зав. кафедрой «Металловедение, порошковая металлургия, наноматериалы» (МПМН), Самарский государственный технический университет (СамГТУ)
ORCID: 0000-0003-1994-5672
E-mail: egundor@yandex.ru

Юлия Владимировна Титова – к.т.н., доцент кафедры МПМН, СамГТУ
ORCID: 0000-0001-6292-280X
E-mail: titova600@mail.ru

Ирина Александровна Уварова – мл. науч. сотрудник научно-исследовательского сектора кафедры МПМН, СамГТУ
ORCID: 0000-0003-3023-3289
E-mail: mr.simple2@mail.ru

Галина Сергеевна Белова – к.т.н., доцент кафедры МПМН, СамГТУ
ORCID: 0000-0002-6430-9408
E-mail: galya.belova.94@mail.ru

Contribution of the Authors

A. P. Amosov – defined the purpose of the work, summarized the obtained results, wrote and edited the manuscript.
Yu. V. Titova – formulated the research objectives, planned the experiments, analyzed and discussed the results, contributed to writing the article.
I. A. Uvarova – conducted experiments, prepared and organized the experimental results, contributed to the analysis and discussion, and helped write the article.
G. S. Belova – contributed to conducting experiments, analyzing, and discussing the results.

Вклад авторов

А. П. Амосов – определение цели работы, обобщение полученных результатов, написание и редактирование текста статьи.
Ю. В. Титова – постановка задачи исследований, планирование экспериментов, анализ и обсуждение результатов, участие в написании статьи.
И. А. Уварова – проведение экспериментов, подготовка и оформление результатов экспериментов, участие в анализе и обсуждении результатов, участие в написании статьи.
Г. С. Белова – участие в проведении экспериментов, участие в анализе и обсуждении результатов.

Received 16.10.2024
Revised 25.10.2024
Accepted 11.11.2024

Статья поступила 16.10.2024 г.
Доработана 25.10.2024 г.
Принята к публикации 11.11.2024 г.

Self-Propagating High-Temperature Synthesis
Самораспространяющийся высокотемпературный синтез

UDC 544.452 + 621.762.2 + 666.3

https://doi.org/10.17073/1997-308X-2024-6-44-55

Research article
Научная статья

Self-propagating high-temperature synthesis of highly dispersed Si_3N_4–TiC composition using sodium azide and various carbon sources

Yu. V. Titova, A. F. Yakubova, G. S. Belova

Samara State Technical University
244 Molodogvardeyskaya Str., Samara 443100, Russia

titova600@mail.ru

Abstract. The main properties of the highly dispersed Si_3N_4–TiC composition are presented, demonstrating the potential for using nitride-carbide composite materials across various industries. An *in-situ* process was employed to synthesize composite ceramics by chemically producing nitride and carbide nanoparticles directly within the composite volume. The study details the development of the technology for synthesizing the highly dispersed Si_3N_4–TiC composition using the azide SHS method during the combustion of mixtures of Ti, C, and sodium azide (NaN_3) powders with polytetrafluoroethylene (PTFE, $(C_2F_4)_n$) serving as an activating and carbiding additive. Thermodynamic calculations of these reactions showed that the adiabatic temperatures were sufficiently high to sustain a self-propagating combustion mode. Experimental investigations into the microstructure and phase composition of the combustion products are also presented. The synthesized compositions consist of highly dispersed equiaxed particles, which include a mixture of nanosized (less than 100 nm) and submicron (100–500 nm) particles of titanium carbide and nitride, as well as silicon nitride fibers with diameters of 50–200 nm and lengths of up to 5 μm. The use of PTFE as a partial replacement for carbon in the mixture during azide SHS eliminated, in most cases, the limitations of traditional approaches for achieving various ratios of target phases of Si_3N_4 and TiC. This enabled the synthesis of highly dispersed Si_3N_4–TiC powder compositions with a phase composition closely aligned with theoretical calculations. Thus, the application of the azide SHS method proved effective for obtaining highly dispersed ceramic powder compositions, including Si_3N_4–TiC and Si_3N_4–TiN–TiC.

Keywords: silicon nitride, titanium carbide, composite ceramics, self-propagating high-temperature synthesis, sodium azide, polytetrafluoroethylene, halide salts, combustion, composition

Acknowledgements: This work was carried out with financial support from the Russian Science Foundation under Project No. 23-29-00680.

For citation: Titova Yu.V., Yakubova A.F., Belova G.S. Self-propagating high-temperature synthesis of highly dispersed Si_3N_4–TiC composition using sodium azide and various carbon sources. *Powder Metallurgy and Functional Coatings*. 2024;18(6):44–55. https://doi.org/10.17073/1997-308X-2024-6-44-55

Самораспространяющийся высокотемпературный синтез высокодисперсной композиции Si_3N_4–TiC с использованием азида натрия и различных источников углерода

Ю. В. Титова, А. Ф. Якубова, Г. С. Белова

Самарский государственный технический университет,
Россия, 443100, г. Самара, ул. Молодогвардейская, 244

titova600@mail.ru

Аннотация. Исследованы основные свойства композиции Si_3N_4–TiC, которые показывают перспективы использования нитридно-карбидных композиционных материалов в различных отраслях промышленности. Применен *in-situ* процесс получения композиционной керамики путем проведения химического синтеза нитридных и карбидных наночастиц в объеме композита, так как известно, что полученные заранее очень мелкие частицы различных фаз не могут быть равномерно распределены в объеме композита путем механического смешивания порошков (*ex-situ* процесс). Представлены результаты развития технологии получения композиции Si_3N_4–TiC методом азидного СВС при сжигании смесей порошков Ti, C, NaN_3 с активирующей и карбидизирующей добавкой политетрафторэтилена $(C_2F_4)_n$ (ПТФЭ). Результаты термодинамических расчетов этих реакций показали, что адиабатические температуры достаточно высоки для реализации самоподдерживающегося режима горения. Представлены экспериментальные исследования микроструктуры и фазового состава продуктов горения. Синтезированные композиции состоят из высокодисперсных частиц равноосной формы, представляющих собой смесь наноразмерных (менее 100 нм) и субмикронных (от 100 до 500 нм) частиц карбида и нитрида титана, а также волокон нитрида кремния диаметром от 50–200 нм и длиной до 5 мкм. Применение ПТФЭ с частичной заменой углерода в составе смесей в азидном СВС позволило устранить в большинстве случаев недостатки традиционного подхода для различных соотношений целевых фаз Si_3N_4 и TiC и синтезировать высокодисперсные порошковые композиции Si_3N_4–TiC с фазовым составом, значительно более близким к рассчитанному теоретическому составу. Таким образом, рассмотренное применение метода азидного СВС позволило получить высокодисперсные композиции керамических порошков Si_3N_4–TiC и Si_3N_4–TiN–TiC.

Ключевые слова: нитрид кремния, карбид титана, композиционная керамика, самораспространяющийся высокотемпературный синтез, азид натрия, политетрафторэтилен, галоидные соли, горение, состав

Благодарности: Работа выполнена при финансовой поддержке Российского научного фонда в рамках проекта № 23-29-00680.

Для цитирования: Титова Ю.В., Якубова А.Ф., Белова Г.С. Самораспространяющийся высокотемпературный синтез высокодисперсной композиции Si_3N_4–TiC с использованием азида натрия и различных источников углерода. *Известия вузов. Порошковая металлургия и функциональные покрытия*. 2024;18(6):44–55. https://doi.org/10.17073/1997-308X-2024-6-44-55

Introduction

Silicon nitride ceramics exhibit excellent mechanical and thermal properties, making them an ideal material for high-temperature applications such as aerospace structural components and turbine engines [1]. Their microstructure after sintering resembles that of composites reinforced with β-Si_3N_4 whiskers, which act as reinforcing elements [2–4]. Adequate fracture toughness, high hardness, and good wear resistance are critical characteristics for advanced ceramics, which find applications in cutting tools and automotive components such as cam rollers and ball bearings in diesel engines [5–7]. Recently, silicon nitride ceramics have attracted significant interest due to their high mechanical properties, wear resistance, and corrosion resistance [8–12]. Thermal shock resistance is a key property for their high-temperature applications. However, most studies on silicon nitride nanocomposites focus on optimizing fracture toughness and flexural strength. To expand the application areas of silicon nitride ceramics, improvements in shock resistance and high-temperature creep resistance are essential [13].

Considerable efforts have been made to improve the mechanical properties of Si_3N_4 by controlling the microstructure or creating various types of composites. During the densification process, β-Si_3N_4 fibers significantly increase fracture toughness as cracks interact with these large grains [14].

Tensile strength is widely recognized as one of the most important factors for enhancing the thermal stability of ceramics [15; 16]. Incorporating second-phase particles into a ceramic matrix can enhance the mechanical properties of ceramics. Studies have also shown that the addition of a secondary phase can improve crack initiation and propagation resistance in various ways [17–20]. For example, adding TiC particles to a silicon nitride matrix enhances mechanical performance, thermal shock behavior, and fatigue resistance, with an optimal TiC content of 10 wt. % [13]. Other researchers [21–23] have also reported the influence of TiC particles on the Si_3N_4 matrix.

Moreover, silicon nitride is extremely hard and non-conductive, making machining with conventional diamond tools challenging and costly, significantly increasing the final cost of ceramic components. Consequently, new electrically conductive composites based on silicon nitride have been developed for more cost-effective electrical discharge machining by incorporating certain amounts of electrically conductive particles such as TiC, TiN, or TiCN into the ceramic matrix [24; 25]. For instance, a Si_3N_4 + TiN composite with critical TiN content can be machined using inexpensive electrical discharge machining [26].

A Si_3N_4–TiC nanocomposite with high mechanical properties was obtained by hot pressing with the addition of 10 wt. % nanosized Si_3N_4 particles and 15 wt. % TiC to a submicron Si_3N_4 matrix, using Al_2O_3 and Y_2O_3 as sintering aids. Layered composites demonstrated high strength, fracture toughness, and wear resistance due to the presence of compressive surface stresses in the layers. A ceramic nanocomposite Si_3N_4–TiC was fabricated using a Si_3N_4 micro-matrix with nanosized Si_3N_4 and TiC particles. Cutting tools made from this ceramic exhibited better wear resistance than those made from sialon. Wear occurred mainly through abrasion and adhesion, whereas sialon cutting tools predominantly experienced abrasion, adhesion, thermal cracking, and delamination [27; 28].

The addition of secondary phases, namely the production of composites with ceramic matrices, offers many significant advantages, such as improved fracture toughness compared to unreinforced ceramics [29; 30]. Moreover, recent studies have shown that *in-situ* phase formation provides additional opportunities compared to composites produced using traditional *ex-situ* methods. The main advantages of *in-situ* manufacturing methods include enhanced mechanical properties, the ability to achieve unique microstructures, process simplicity, and inexpensive raw materials [27].

One promising *in-situ* technology is the self-propagating high-temperature synthesis (SHS) process, which enables the production of a wide range of refractory compounds, including nitrides and carbides, by utilizing the heat released during combustion in simple, compact equipment with short processing times [30].

To produce highly dispersed (d < 1 μm) Si_3N_4–TiC powder compositions, the authors of this article investigated the use of azide synthesis, a variation of SHS where sodium azide (NaN_3) powder serves as the nitriding agent, and various activating halide salts are used alongside elemental reactants. This approach results in relatively low combustion temperatures, the formation of numerous intermediate vapor-gas reaction products, and final by-products consisting of condensed and gaseous phases. These by-products separate the target powder particles and prevent their agglomeration into larger particles.

The study summarizes the results of azide SHS synthesis of Si_3N_4–TiC ceramic compositions with various nitride-to-carbide phase ratios of Si_3N_4:TiC = 4:1, 2:1, 1:1, 1:2, and 1:4, according to the following stoichiometric equations, using halide salts such as Na_2SiF_6 and $(NH_4)_2SiF_6$ [33; 34].

Si–Ti–NaN_3–Na_2SiF_6–C system

$$11Si + Ti + 4NaN_3 + Na_2SiF_6 + C = \\ = 4Si_3N_4 + TiC + 6NaF, \quad (1)$$

$$5Si + Ti + 4NaN_3 + Na_2SiF_6 + C = \\ = 2Si_3N_4 + TiC + 6NaF + 2N_2, \quad (2)$$

$$2Si + Ti + 4NaN_3 + Na_2SiF_6 + C = \\ = Si_3N_4 + TiC + 6NaF + 4N_2, \quad (3)$$

$$2Si + 2Ti + 4NaN_3 + Na_2SiF_6 + 2C = \\ = Si_3N_4 + 2TiC + 6NaF + 4N_2, \quad (4)$$

$$2Si + 4Ti + 4NaN_3 + Na_2SiF_6 + 4C = \\ = Si_3N_4 + 4TiC + 6NaF + 4N_2. \quad (5)$$

Si–Ti–NaN_3–$(NH_4)_2SiF_6$–C system

$$11Si + Ti + 6NaN_3 + (NH_4)_2SiF_6 + C = \\ = 4Si_3N_4 + TiC + 6NaF + 4H_2 + 2N_2, \quad (6)$$

$$5Si + Ti + 6NaN_3 + (NH_4)_2SiF_6 + C = \\ = 2Si_3N_4 + TiC + 6NaF + 4H_2 + 6N_2, \quad (7)$$

$$2Si + Ti + 6NaN_3 + (NH_4)_2SiF_6 + C = \\ = Si_3N_4 + TiC + 6NaF + 4H_2 + 8N_2, \quad (8)$$

$$2Si + 2Ti + 6NaN_3 + (NH_4)_2SiF_6 + 2C = \\ = Si_3N_4 + 2TiC + 6NaF + 4H_2 + 8N_2, \quad (9)$$

$$2Si + 4Ti + 6NaN_3 + (NH_4)2SiF_6 + 4C = \\ = Si_3N_4 + 4TiC + 6NaF + 4H_2 + 8N_2. \quad (10)$$

In these stoichiometric reactions, the composition of the reaction products is expressed in moles. When converted to weight percent (wt. %), the following ratios are obtained for the expected theoretical composition of the target Si_3N_4–TiC compositions after the removal of the water-soluble byproduct salt, NaF, from the condensed reaction products:

(1), (6) $4Si_3N_4 + TiC = 90.4\ \%\ Si_3N_4 + 9.6\ \%\ TiC$,

(2), (7) $2Si_3N_4 + TiC = 82.4\ \%\ Si_3N_4 + 17.6\ \%\ TiC$,

(3), (8) $Si_3N_4 + TiC = 70.1\ \%\ Si_3N_4 + 29.9\ \%\ TiC$,

(4), (9) $Si_3N_4 + 2TiC = 53.9\ \%\ Si_3N_4 + 46.1\ \%\ TiC$,

(5), (10) $Si_3N_4 + 4TiC = 36.9\ \%\ Si_3N_4 + 63.1\ \%\ TiC$.

The results of the phase composition analysis of the washed solid combustion products from reactions (1)–(10), determined experimentally, are presented in Table 1. In most cases, the products consist of a highly dispersed powder with a complex composition, appearing as submicron equiaxed particles ranging in size from 100 nm to 1 μm (Fig. 1).

From the data in Table 1, it is evident that the experimental phase composition of the products from azide SHS differs significantly from the expected theoretical composition of Si_3N_4–TiC powder compositions. The content of the target carbide phase TiC is significantly lower than its theoretical value (ranging from 2.7 to 19.9 %), the amount of Si_3N_4 is excessive, and an undesirable secondary phase, titanium nitride, is present (ranging from 1.9 to 19.2 %). These results can be attributed to the fact that very fine and lightweight particles of technical carbon may be partially or completely removed from the burning, highly porous bulk charge sample by gases released during the decomposition of sodium azide and halide salts, preventing their participation in the formation of titanium carbide. As a result, silicon nitride forms in larger quantities, and titanium nitride forms due to an excess of nitrogen (since combustion in a nitrogen atmosphere is essential for *in-situ* nitride formation in SHS compositions), while titanium carbide forms in smaller amounts than predicted by the initial stoichiometric reaction equations and thermodynamic calculations. Additionally, the synthesized compositions may contain impurities of unreacted free silicon (up to 1.9 %) or carbon (up to 1.5 %).

To address these shortcomings, several directions for further research on applying the SHS process to produce highly dispersed Si_3N_4–TiC compositions can be pursued. The simplest approach is to use polytetrafluoroethylene (PTFE $(C_2F_4)_n$) as an activating and carbon-containing additive in the charge, promoting the formation of TiC, as successfully demonstrated in previous studies [35; 36].

In this context, the aim of the present study was to maximize the convergence of the theoretical and experimental compositions of the Si_3N_4–TiC powder composition by modifying the initial reactant composition with full or partial replacement of carbon with PTFE and optimizing the conditions of the azide SHS process.

Research methodology

To synthesize the target Si_3N_4–TiC composition with phase molar ratios ranging from 2:1 to 1:4, chemical reaction equations involving full (11)–(14) and partial (15), (16) substitution of carbon with polytetrafluoroethylene (PTFE) were used:

Table 1. **Experimental phase composition of washed solid products from azide SHS**

Таблица 1. **Экспериментальный фазовый состав промытых твердых продуктов азидного СВС**

Equation	Si_3N_4:TiC (mol)	Content, wt. %					
		α-Si_3N_4	β-Si_3N_4	TiN	TiC	C	Si
Si–Ti–NaN_3–Na_2SiF_6– C system							
(1)	4:1	51.2	34.8	7.9	6.1	–	–
(2)	2:1	43.2	29.8	18.9	8.1	–	–
(3)	1:1	55.7	29.2	1.9	11.3	–	1.9
(4)	1:2	51.6	29.3	2.3	15.3	1.5	–
(5)	1:4	48.6	27.6	4.0	19.9	0.8	–
(6)	4:1	65.5	25.0	5.0	2.7	–	1.8
(7)	2:1	60.8	24.0	5.1	9.3	–	0.7
(8)	1:1	48.6	27.6	19.2	4.7	–	–
(9)	1:2	43.2	29.8	18.9	8.1	–	–
(10)	1:4	43.0	21.1	16.1	8.9	–	–

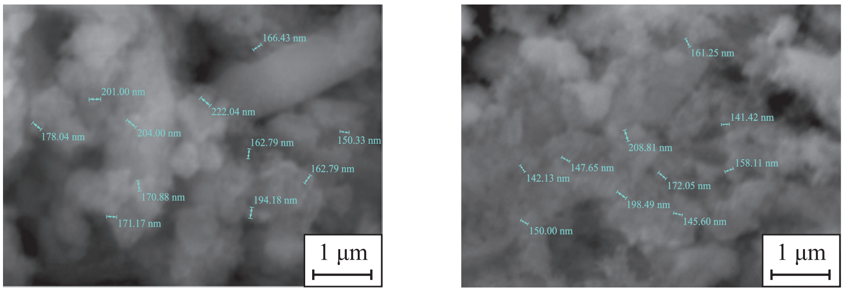

(1) $11Si + Ti + 4NaN_3 + Na_2SiF_6 + C$

(2) $5Si + Ti + 4NaN_3 + Na_2SiF_6 + C$

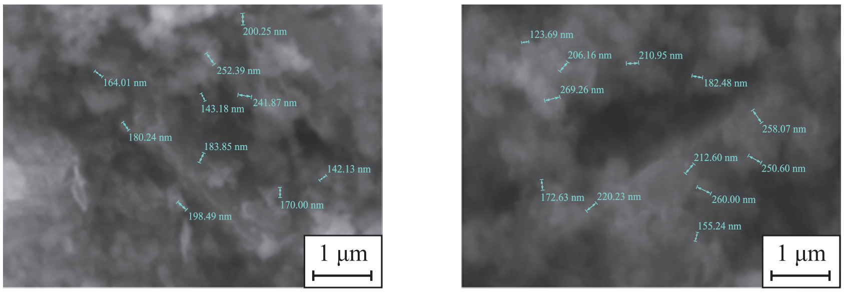

(3) $2Si + Ti + 4NaN_3 + Na_2SiF_6 + C$

(4) $2Si + 2Ti + 4NaN_3 + Na_2SiF_6 + 2C$

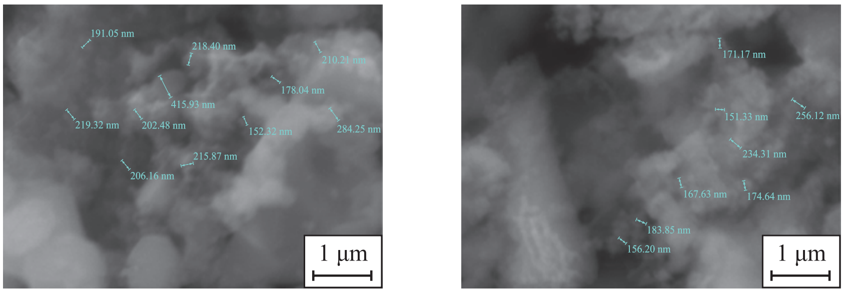

(5) $2Si + 4Ti + 4NaN_3 + Na_2SiF_6 + 4C$

(6) $11Si + Ti + 6NaN_3 + (NH_4)_2SiF_6 + C$

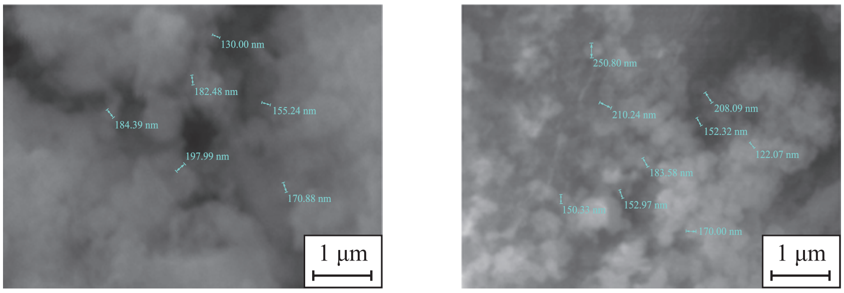

(7) $5Si + Ti + 6NaN_3 + (NH_4)_2SiF_6 + C$

(8) $2Si + Ti + 6NaN_3 + (NH_4)_2SiF_6 + C$

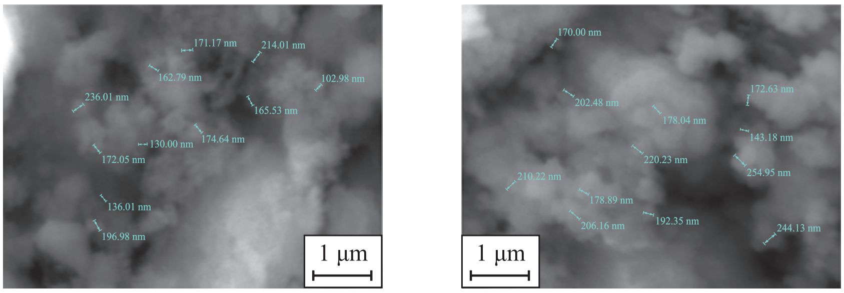

(9) $2Si + 2Ti + 6NaN_3 + (NH_4)_2SiF_6 + 2C$

(10) $2Si + 4Ti + 6NaN_3 + (NH_4)_2SiF_6 + 4C$

Fig. 1. Microstructure of combustion products from charges according to equations (1)–(10)

Рис. 1. Микроструктура продуктов горения шихт в соответствии с уравнениями (1)–(10)

$$12Si + 2Ti + 4NaN_3 + C_2F_4 + 3.25N_2 = 4Si_3N_4 + 2TiC + 4NaF + 1.25N_2, \quad (11)$$

$$6Si + 2Ti + 4NaN_3 + C_2F_4 = 2Si_3N_4 + 2TiC + 4NaF + 2N_2, \quad (12)$$

$$3Si + 2Ti + 4NaN_3 + C_2F_4 = Si_3N_4 + 2TiC + 4NaF + 4N_2, \quad (13)$$

$$3Si + 4Ti + 8NaN_3 + 2C_2F_4 = Si_3N_4 + 4TiC + 8NaF + 10N_2, \quad (14)$$

$$3Si + 2Ti + 0.32NaN_3 + 1.84C + 0.08C_2F_4 + 1.52N_2 = Si_3N_4 + 2TiC + 0.32Na, \quad (15)$$

$$3Si + 4Ti + 0.64NaN_3 + 3.68C + 0.16C_2F_4 + 1.04N_2 = Si_3N_4 + 4TiC + 0.64NaF. \quad (16)$$

To achieve the Si_3N_4–TiC composition with the maximum titanium carbide phase content (Si_3N_4:TiC = 1:4), carbiding mixtures with increased PTFE content were also used:

$$3Si + 4Ti + 0.8NaN_3 + 3.6C + 0.2C_2F_4 + 0.8N_2 = Si_3N_4 + 4TiC + 0.8NaF, \quad (17)$$

$$3Si + 4Ti + 1.6NaN_3 + 3.2C + 0.4C_2F_4 = Si_3N_4 + 4TiC + 1.6NaF + 0.4N_2, \quad (18)$$

$$3Si + 4Ti + 2.4NaN_3 + 2.8C + 0.6C_2F_4 = Si_3N_4 + 4TiC + 2.4NaF + 1.6N_2. \quad (19)$$

Thermodynamic calculations were conducted using the Thermo software [37] to predict the feasibility of combustion reactions by determining thermal effects (enthalpies), adiabatic temperatures, and the compositions of synthesis products.

The following raw materials were used in the experiments:

– silicon powder, grade Kr0 (main substance content ≥98.8 wt. %, average particle size d = 5 μm;

– titanium powder, grade PTOM-1 (98.0 wt. %, d = 30 μm);

– sodium azide powder, analytical grade (≥98.71 wt. %, d = 100 μm);

– carbon black, grade P701 (≥99.7 wt. %, d = 70 nm, agglomerates up to 1 μm);

– polytetrafluoroethylene, grade PN-40 (≥99.0 %, d = 40 μm).

Combustion of the starting reactant mixtures (charge) with a bulk relative density of 0.4 was conducted in a paper crucible with a diameter of 30 mm and a height of 45 mm. The experiments were performed in a laboratory SHS-Az reactor with a volume of 4.5 L, equipped with two thermocouples, under a nitrogen pressure of 4 MPa. The thermocouples were used to measure combustion temperatures and calculate the combustion rate. The pressure variation in the reactor during the combustion process was monitored with a pressure gauge.

The synthesized product was weighed and compared to the theoretical yield calculated from reactions (11)–(19). The combustion product was washed with water to remove water-soluble impurities, and the pH of the wash water was measured to assess the presence of free sodium in the combustion product and the completeness of the chemical reaction. The phase composition of the synthesized combustion products was determined using an automated ARL X'trA X-ray diffractometer (Thermo Scientific, Switzerland). CuK_α radiation was employed with continuous scanning over the angular range of 2θ = 20–80° at a scan rate of 2°/min. The resulting spectra were processed using the WinXRD software package. The surface topography and powder particle morphology were examined using a JSM-6390A scanning electron microscope (Jeol, Japan) equipped with a Jeol JED-2200 energy-dispersive spectroscopy attachment.

Results and discussion

The results of thermodynamic calculations for reactions (11)–(19) performed using the Thermo software are presented in Tables 2–4.

From the presented data, it is evident that all reactions exhibit high adiabatic temperatures sufficient for the realization of the SHS process in a combustion mode. The reaction products contain all the phases corresponding to the right-hand sides of equations (11)–(19), including the target phases of silicon nitride (Si_3N_4) and titanium carbide (TiC), the water-soluble byproduct salt NaF, and minor impurities of free silicon (Si) and titanium (Ti).

The results of the microstructural analysis of the combustion products of the initial powder mixtures (charges) from reactions (11)–(19) after washing with water to remove the byproduct salt NaF are shown in Fig. 2.

As shown in Fig. 2, the combustion products of charges from reactions (11)–(19) consist of highly dispersed equiaxed particles, comprising a mixture of nanosized (less than 100 nm) and submicron (100–500 nm) particles of titanium carbide and tita-

Table 2. **Thermodynamic analysis results for reactions (11)–(14)**

Таблица 2. **Результаты термодинамического анализа реакций (11)–(14)**

Reaction equation	T_{ad}, K	Combustion products composition, mol								ΔH, kJ
		F(g)	Na(g)	Si(g)	N_2(g)	NaF(g)	NaF(l)	TiC(s)	Si_3N_4(s)	
(11)	3033	0.0314	0.0314	2.0400	2.6100	3.9686	–	2.0000	3.3200	–5271
(12)	2984	0.0253	0.0253	1.0602	2.7068	3.9747	–	2.0000	1.6466	–3695
(13)	2893	0.0196	0.0196	0.3998	4.2666	3.9804	–	2.0000	0.8667	–2908
(14)	2810	0.0284	0.0284	0.3246	10.2164	7.3922	0.5794	4.0000	0.8918	–5027

Table 3. **Thermodynamic analysis results for reactions (15), (16)**

Таблица 3. **Результаты термодинамического анализа реакций (15), (16)**

Reaction equation	T_{ad}, K	Combustion products composition, mol								ΔH, kJ
		F(g)	Na(g)	N_2(g)	Si(g)	Ti(g)	NaF(g)	TiC(s)	Si_3N_4(s)	
(15)	3702	0.0117	0.0117	0.0074	0.0056	0.0002	0.3083	1.9998	0.9981	–1342
(16)	3380	0.0108	0.0108	0.0025	0.0019	0.0023	0.6292	3.9999	0.9994	–1896

Table 4. **Results of thermodynamic analysis of reactions (17)–(19)**

Таблица 4. **Результаты термодинамического анализа реакций (17)–(19)**

Reaction equation	T_{ad}, K	Combustion products composition, mol								ΔH, kJ
		F(g)	Na(g)	N_2(g)	Si(g)	NaF(g)	TiC(l)	TiC(s)	Si_3N_4(s)	
(17)	3426	0.0199	0.0199	–	0.6002	0.7801	3.9999	–	0.7999	–1964
(18)	2271	0.0114	0.0114	0.8959	0.7438	1.5886	–	4.0000	0.7521	–2304
(19)	2937	0.0157	0.0157	2.0485	0.6728	2.3843	–	4.0000	0.7757	–2645

nium nitride, as well as silicon nitride fibers with diameters of 50–200 nm and lengths of up to 5 μm.

The results of *X*-ray phase analysis for the washed combustion products of systems with the maximum titanium carbide phase content (Si_3N_4:TiC = 1:4) are presented in Fig. 3.

The results of quantitative processing of the XRD spectra presented in Fig. 3 are summarized in Table 5. These results show the phase content in the washed combustion products of charges with the maximum titanium carbide phase fraction (Si_3N_4:TiC = 1:4) under various conditions: full replacement of carbon black with PTFE (reaction 14), carbiding mixtures with minimal PTFE content (reaction 16), and carbiding mixtures based on reactions (17)–(19) to synthesize the Si_3N_4–TiC composition. The experimental data are compared with theoretical phase compositions of target products Si_3N_4 and TiC based on the stoichiometric equations (11)–(19).

From the data in Table 5, it is evident that using PTFE as a carbon source for synthesizing nitride-carbide compositions via azide SHS is a promising research direction. A comparison of the experimental phase compositions of combustion products from charges (11)–(14) with theoretical values indicates that full replacement of carbon black with PTFE is not advisable, although the titanium carbide phase content increases compared to azide SHS without PTFE. For example, the titanium carbide content in the combustion products of charge (5): $2Si + 4Ti + 4NaN_3 + Na_2SiF_6 + 4C$ with the maximum TiC content (Si_3N_4:TiC = 1:4), is 19.9 wt. %. With full replacement of carbon black by PTFE in charge: $3Si + 4Ti + 8NaN_3 + 2C_2F_4$) the titanium carbide content increases to 31.0 wt. %. However, partial replacement of carbon black and its combined use with PTFE as a carbon source allows the titanium carbide content to reach 52.3 wt. % in the combustion products of charge (16): $3Si + 4Ti + 0.64NaN_3 + 3.68C + 0.16C_2F_4 + 1.04N_2$.

The best results were obtained using carbiding mixtures with increased PTFE content according to equations (17)–(19), where the TiC content in the experimental products ranged from 58.6 to 61.7 wt. %. Furthermore, the use of PTFE reduced the content of the secondary phase, titanium nitride, to 2.0–4.0 wt. % in the products of carbiding mixtures (17)–(19).

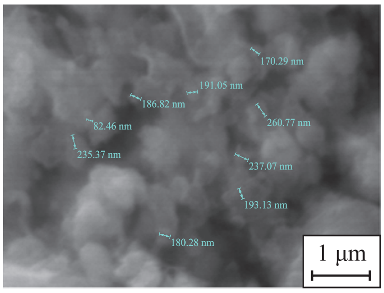

(11) $12Si + 2Ti + 4NaN_3 + C_2F_4 + 3,25N_2$

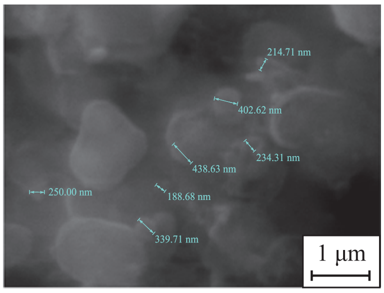

(12) $6Si + 2Ti + 4NaN_3 + C_2F_4$

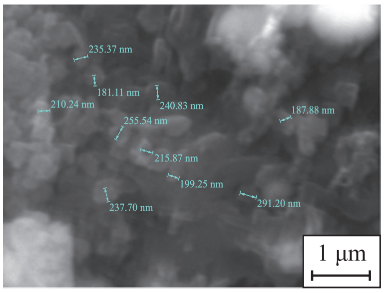

(13) $3Si + 2Ti + 4NaN_3 + C_2F_4$

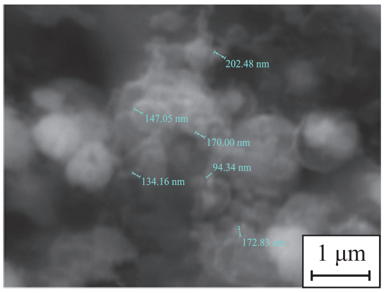

(14) $3Si + 4Ti + 8NaN_3 + 2C_2F_4$

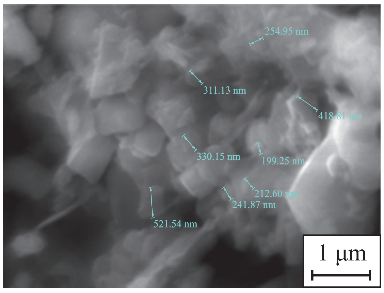

(15) $3Si + 2Ti + 0.32NaN_3 + 1.84C + 0.08C_2F_4 + 1.52N_2$

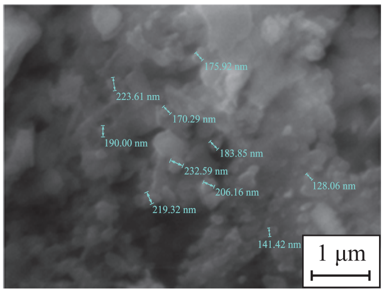

(16) $3Si + 4Ti + 0.64NaN_3 + 3.68C + 0.16C_2F_4 + 1.04N_2$

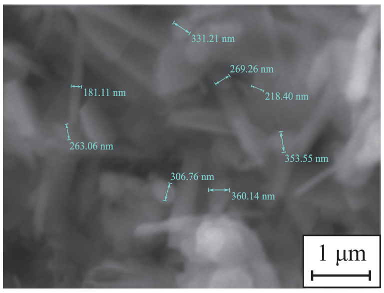

(17) $3Si + 4Ti + 0.8NaN_3 + 3.6C + 0.2C_2F_4 + 0.8N_2$

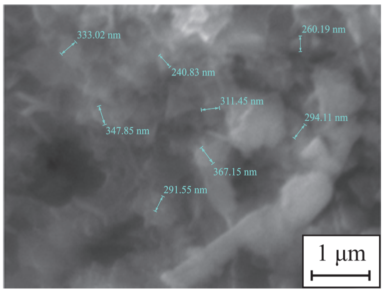

(18) $3Si + 4Ti + 1.6NaN_3 + 3.2C + 0.4C_2F_4$

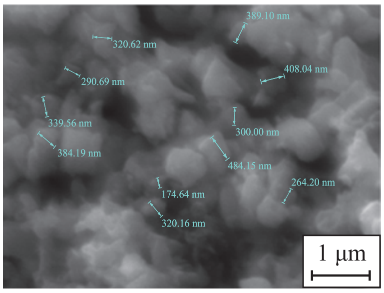

(19) $3Si + 4Ti + 2.4NaN_3 + 2.8C + 0.6C_2F_4$

Fig. 2. Microstructure of combustion products from charges according to equations (11)–(19)

Рис. 2. Микроструктура продуктов горения шихт в соответствии с уравнениями (11)–(19)

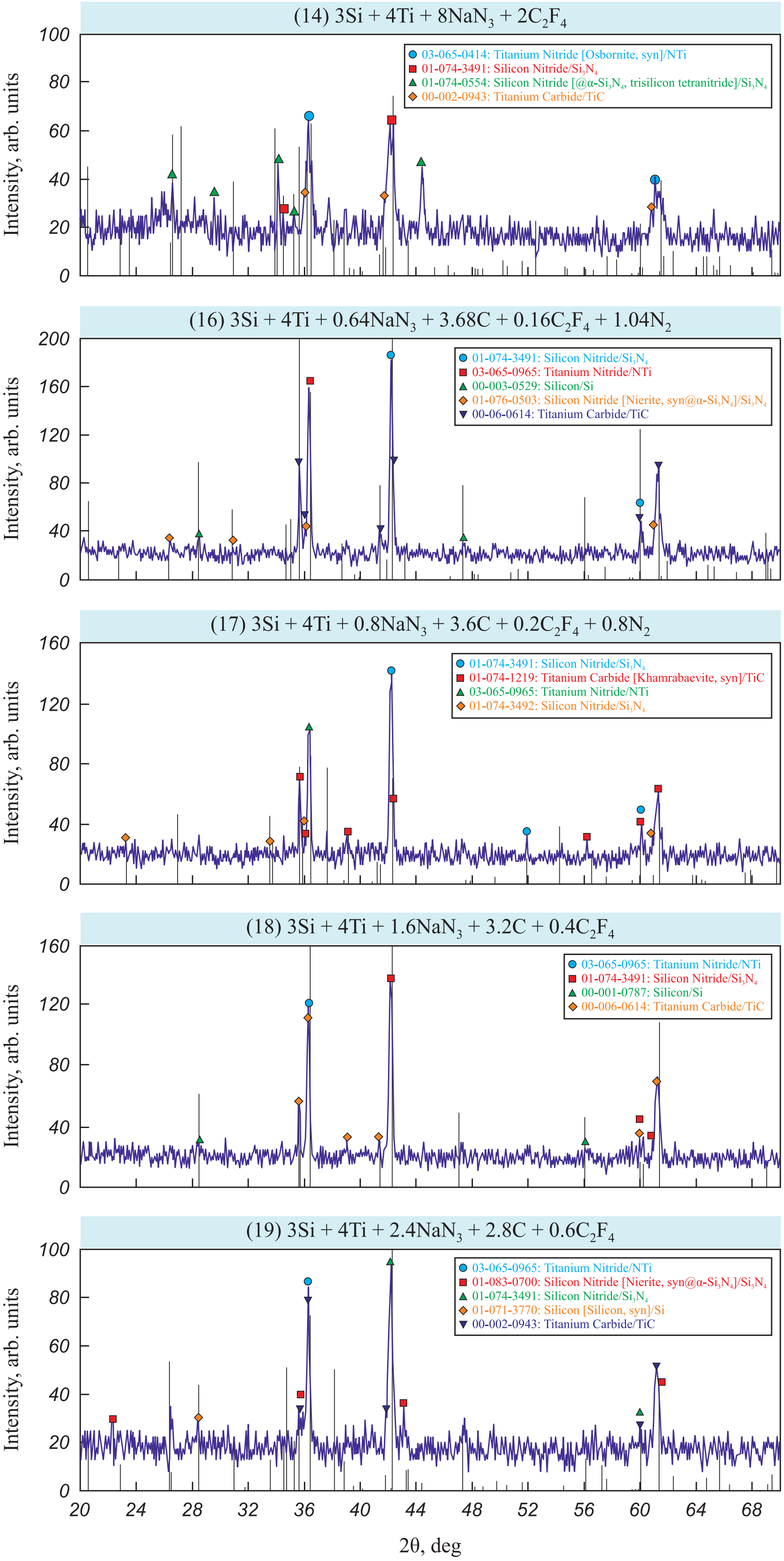

Fig. 3. *X*-ray diffraction patterns of combustion products from charges (14), (16)–(19)

Рис. 3. Рентгеновские дифрактограммы продуктов горения шихт (14), (16)–(19)

Table 5. **Theoretical and experimental phase compositions of washed products from azide SHS according to equations (11)–(19)**

Таблица 5. **Теоретический и экспериментальный фазовые составы промытых продуктов азидного СВС согласно уравнениям (11)–(19)**

Reaction equation	Si_3N_4:TiC (mol)	Content, wt. %						
		Theoretical		Experimental				
		Si_3N_4	TiC	α-Si_3N_4	β-Si_3N_4	TiC	TiN	Si
(11)	2:1	82.4	17.6	62.0	17.0	12.0	9.0	–
(12)	1:1	70.1	29.9	52.0	20.0	23.0	5.0	–
(13)	1:2	53.9	46.1	53.0	14.0	27.0	6.0	–
(14)	1:4	36.9	63.1	42.0	7.0	31.0	10.0	–
(15)	1:2	53.9	46.1	26.6	14.1	44.1	5.2	–
(16)	1:4	36.9	63.1	27.8	10.0	52.3	9.9	–
(17)	1:4	36.9	63.1	29.7	7.7	58.6	2.0	2.0
(18)	1:4	36.9	63.1	28.0	9.0	59.0	4.0	–
(19)	1:4	36.9	63.1	28.7	3.0	61.7	3.6	3.0

Conclusion

The presented results demonstrate that the SHS technology can make a significant contribution to the development of methods for producing highly dispersed Si_3N_4–TiC nitride-carbide compositions. The SHS process is attractive for its simplicity and cost-effectiveness and is one of the promising *in-situ* chemical methods for the direct synthesis of ceramic powders within the desired composition from a mixture of inexpensive starting reagents.

Traditional azide SHS using NaN_3 and gasifying halide fluorides, such as Na_2SiF_6 and $(NH_4)_2SiF_6$, is characterized by comparatively low combustion temperatures, the formation of large amounts of intermediate vapor and gaseous reaction products, as well as final byproduct condensed and gaseous products that separate the target powder particles. This enabled the synthesis of a highly dispersed (<1 μm) Si_3N_4–TiC powder composition, with Si_3N_4 predominantly in the α-modification phase during the combustion of all studied mixtures.

However, in all cases of traditional azide SHS application, the amount of TiC phase synthesized in the experiments was significantly lower than expected. Additionally, all synthesized compositions contained the TiN phase, with its content exceeding that of titanium carbide in mixtures without PTFE additives. Furthermore, the synthesized compositions may include impurities of unreacted free silicon (up to 3.0 wt. %).

The use of PTFE as an activating and carbiding additive with partial replacement of carbon in the mixtures (15)–(19) in azide SHS eliminated, in most cases, the shortcomings of the traditional approach for various ratios of target phases Si_3N_4 and TiC. This allowed for the synthesis of highly dispersed Si_3N_4–TiC powder compositions with a phase composition significantly closer to the calculated theoretical composition.

References / Список литературы

1. Schioler L.J. Heat engine ceramics. *American Ceramic Society Bulletin*. 1985;64(2):268–294.
2. Ding S., Zeng Y.P., Jiang D. Oxidation bonding if porous silicon nitride ceramics with high strength and low dielectric constant. *Materials Letters*. 2007;6(11-12):2277–2280. https://doi.org/10.1016/j.matlet.2006.08.067
3. Huang Zh., Chen F., Su R., Wang Zh., Li J., Shen Q., Zhang L. Electronic and optical properties of Y-doped Si_3N_4, by density functional theory. *Journal of Alloys and Compounds*. 2015;637(15):376–381. https://doi.org/10.1016/j.jallcom.2015.02.213
4. Kim S., Park B.G. Tuning tunnel barrier in Si_3N_4-based resistive memory embedding SiO_2, for low-power and high-density cross-point array applications. *Journal of Alloys and Compounds*. 2016;663:256–261. https://doi.org/10.1016/j.jallcom.2015.12.107
5. Qi G., Zhang C., Hu H. High strength three-dimensional silica fiber reinforced silicon nitride-based composites via poly hydridomethylsilazane pyrolysis. *Ceramics International*. 2007;33(5):891–894. https://doi.org/10.1016/j.ceramint.2006.01.018
6. Barta J., Manela M., Fischer R. Si_3N_4 and Si_2N_2O for high performance randomes. *Materials Science and Engineering*. 1985;71:265–272. https://doi.org/10.1016/0025-5416(85)90236-8
7. Riley F.L. Silicon nitride and related materials. *Journal of the American Ceramic Society*. 2000;83(2):245–265. https://doi.org/10.1111/j.1151-2916.2000.tb01182.x
8. Niihara K. New design concept of structural ceramic–ceramic nanocomposites. *Journal of the Ceramic Society of Japan*. 1991;99(10):974–982.

https://doi.org/10.2109/jcersj.99.974

9. Hirai H., Hondo K. Shock-compacted Si_3N_4 nano-crystalline ceramic. *Journal of the American Ceramic Society*. 1994;77(2):487–492. https://doi.org/10.1111/j.1151-2916.1994.tb07018.x
10. Vaben R., Stover D. Processing and properties of nanophase nonoxide ceramics. *Materials Science and Engineering: A*. 2001;301(1):59–68. https://doi.org/10.1016/S0921-5093(00)01389-7
11. Steritzke M. Review: Structural ceramic nanocomposites. *Journal of the European Ceramic Society*. 1997; 17(9):1061–1082. https://doi.org/10.1016/S0955-2219(96)00222-1
12. Gasch M.J., Wan J., Mukherjee A.K. Preparation of a Si_3N_4/SiC nanocomposite by high-pressure sintering of polymer precursor derived powders. *Scripta Materialia*. 2001;45(9):1063–1068. https://doi.org/10.1016/S1359-6462(01)01140-X
13. Tian Ch., Liu N., Lu M. Thermal shock and thermal fatigue behavior of Si_3N_4–TiC nano-composites. *International Journal of Refractory Metals & Hard Materials*. 2008;26(5):478–484. https://doi.org/10.1016/j.ijrmhm.2007.11.004
14. Ziegler G. Thermal properties and thermal shock resistance of silicon nitride. In: *Progress in nitrogen ceramics*. F.L. Riley Ed. Boston: Martinus Nihoff Publ., 1983. P. 565–588. https://doi.org/10.1007/978-94-009-6851-6
15. Hirosaki N., Okamoto Y., Akimune Y., Mitomo M. Sintering of Y_2O_3–Al_2O_3 doped β-Si_3N_4 powder and mechanical properties of sintered materials. *Journal of the American Ceramic Society*. 1978;61(3-4):114–118. https://doi.org/10.2109/JCERSJ.102.790
16. Clarke D.R., Thomas G. Microstructure of Y_2O_3 fluxed hot-pressed silicon nitride. *Acta Metallurgica et Materialia*. 1995;43(3):923–930. https://doi.org/10.1111/j.1151-2916.1978.tb09251.x
17. Hirano T., Niihara K. Thermal shock resistance of Si_3N_4/SiC nanocomposites fabricated from amorphous Si–C–N precursor powders. *Materials Letters*. 1996; 26(6):285–289. https://doi.org/10.1016/0167-577X(96)80001-2
18. Pettersson P., Johnsson M. Thermal shock properties of alumina reinforced with Ti(C,N) whiskers. *Journal of the European Ceramic Society*. 2003;23(2):309–313. https://doi.org/10.1016/S0955-2219(02)00177-2
19. Ebrabimi M.E., Chevalier J., Fantozzi G. Slow crack growth behavior of alumina ceramics. *Journal of Materials Research*. 2000;15(1):142–147. https://doi.org/10.1557/JMR.2000.0024
20. Hirata T., Katsunori A., Yamamotto H. Sintering behavior of Cr_2O_3–Al_2O_3 ceramics. *Journal of the European Ceramic Society*. 2000;20(2):195–199. https://doi.org/10.1016/S0955-2219(99)00161-2
21. Szafran M., Bobryk E., Kukla D., Olszyna A. Si_3N_4–Al_2O_3–TiC–Y_2O_3 composites intended for the edges of cutting tools. *Ceramics International*. 2000;26(6):579–582. https://doi.org/10.1016/S0272-8842(99)00098-X
22. Ling B., Ge Ch., Shen W., Mao X., Zhang K. Densification, microstructure, and fracture behavior of Si_3N_4–TiC composites by spark plasma sintering. *Rare Metals*. 2008;27(3):315–319. https://doi.org/10.1016/S1001-0521(08)60136-9
23. Buljan S.T., Zilberstein G. Effect of impurities on microstructure and mechanical properties of Si_3N_4–TiC composites. In: *Tailoring Multiphase and Composite Ceramics*. US. Springer, 1986. P. 305–316. https://doi.org/10.1007/978-1-4613-2233-7_23
24. Martin C., Cales B., Vivier P., Mathieu P. Electrical discharge machinable ceramic composites. *Materials Science and Engineering: A*. 1989;109:351–356. https://doi.org/10.1016/0921-5093(89)90614-X
25. Gogotsi G. Particulate silicon nitride-based composites. *Journal of Materials Science*. 1994;29(10):2541–2556. https://doi.org/10.1007/BF00356803
26. Wang C.M. Microstructure development of Si_3N_4-TiN composite prepared by in situ compositing. *Journal of Materials Science*. 1995;30(12):3222–3230. https://doi.org/10.1007/BF01209241
27. Singh V., Bansal A., Jindal M., Sharma P., Singla A.K. Slurry erosion resistance, morphology, and machine learning modeling of plasma-sprayed Si_3N_4 + TiC + VC and CrNi based ceramic coatings. *Ceramics International*. 2024;50(16):27961–27973. https://doi.org/10.1016/j.ceramint.2024.05.092
28. Ye Ch., Yue X., Ru H., Long H., Gong X. Effect of addition of micron-sized TiC particles on mechanical properties of Si_3N_4 matrix composites. *Journal of Alloys and Compounds*. 2017;709:165–171. https://doi.org/10.1016/j.jallcom.2017.03.124
29. Xing Y., Deng J., Feng X., Yu Sh. Effect of laser surface texturing on Si_3N_4/TiC ceramic sliding against steel under dry friction. *Materials and Design*. 2013;52:234–245. https://doi.org/10.1016/j.matdes.2013.05.077
30. Han J.-C., Chen G.-Q., Du Sh.-Y., Wood J.V. Synthesis of Si_3N_4–TiN–SiC composites by combustion reaction under high nitrogen pressures. *Journal of the European Ceramic Society*. 2000;20(7):927–932. https://doi.org/10.1016/S0955-2219(99)00230-7
31. Bichurov G.V. Halides in SHS azide technology of nitrides obtaining. In: *Nitride Ceramics: Combustion synthesis, properties, and applications*. Weinheim: Wiley, 2015. P. 229–263. https://doi.org/10.1002/9783527684533.ch8
32. Amosov A.P., Titova Yu.V., Belova G.S., Maidan D.A., Minekhanova A.F. SHS of highly dispersed powder compositions of nitrides with silicon carbide. Review. *Powder Metallurgy and Functional Coatings*. 2022;16(4):34–57. https://doi.org/10.17073/1997-308X-2022-4-34-57

    Амосов А.П., Титова Ю.В., Белова Г.С., Майдан Д.А., Минеханова А.Ф. СВС высокодисперсных порошковых композиций нитридов с карбидом кремния: Обзор. *Известия вузов. Порошковая металлургия и функциональные покрытия*. 2022;16(4):34–57. https://doi.org/10.17073/1997-308X-2022-4-34-57
33. Titova Yu.V., Belova G.S., Yakubova A.F. Application of combustion of Ti–Si–NaN_3–Na_2SiF_6–C powder mixture for the synthesis of highly dispersed Si_3N_4–TiC ceramic composition. In: *Proceeding of the International Conference on Physics and Chemistry of Combustion and Processes in Extreme Environments* (Samara, Russia, 2–6 July

2024). Samara: Publishing OOO “Insoma-Press”. 2024. P. 60.

34. Titova Y.V., Belova G.S., Yukubova A.F. Self-propagating high-temperature synthesis of Si_3N_4–TiC composition using sodium azide. In: *Proceeding of 9th International Congress on Energy Fluxes and Radiation Effects* (EFRE-2024). Tomsk: Academizdat, 2024. P. 583.

35. Nersisyan G.A., Nikogosov V.N., Kharatyan S.L. Thermal regimes for carbidizing wave propagation in the system titanium-halogen-containing polymer. *Combustion Explosion and Shock Waves*. 1992;28(3):251–254. https://doi.org/10.1007/BF00749638

Нерсисян Г.А., Никогосов В.Н., Харатян С.Л. Тепловые режимы распространения волны карбидизации в системе титан – галогенсодержащий полимер. *Физика горения и взрыва*. 1992;28(3):46–49.

36. Kharatyan S.L., Nersisyan H.H. Chemically activated SHS in synthesis of refractory carbide powders. *Key Engineering Materials*. 2002;217:83–92. https://doi.org/10.4028/www.scientific.net/KEM.217.83

37. Rogachev A.S., Mukasyan A.S. Combustion for material synthesis. New York: CRC Press., 2014. 422 p.

Рогачев А.С., Мукасьян А.С. Горение для синтеза материалов. М.: Физматлит, 2012. 400 с.

Information about the Authors

Yuliya V. Titova – Cand. Sci. (Eng.), Associate Professor at the Department of Metallurgy, Powder Metallurgy, Nanomaterials (MPMN), Samara State Technical University (SamSTU)
ORCID: 0000-0001-6292-280X
E-mail: titova600@mail.ru

Alsu F. Yakubova – Postgraduate Student, Department of MPMN, SamSTU
ORCID: 0000-0002-6081-8264
E-mail: minekhanovaaf@mail.ru

Galina S. Belova – Cand. Sci. (Eng.), Associate Professor at the Department of MPMN, SamSTU
ORCID: 0000-0002-6430-9408
E-mail: galya.belova.94@mail.ru

Сведения об авторах

Юлия Владимировна Титова – к.т.н., доцент кафедры «Металловедение, порошковая металлургия, наноматериалы» (МПМН), Самарский государственный технический университет (СамГТУ)
ORCID: 0000-0001-6292-280X
E-mail: titova600@mail.ru

Алсу Фаридовна Якубова – аспирант кафедры МПМН, СамГТУ
ORCID: 0000-0002-6081-8264
E-mail: minekhanovaaf@mail.ru

Галина Сергеевна Белова – к.т.н., доцент кафедры МПМН, СамГТУ
ORCID: 0000-0002-6430-9408
E-mail: galya.belova.94@mail.ru

Contribution of the Authors

Yu. V. Titova – defined the study’s objective, summarized the results, and contributed to writing and editing the manuscript.
A. F. Yakubova – conducted the experiments, prepared and presented the experimental results, participated in the analysis and discussion, and contributed to the writing of the article.
G. S. Belova – formulated the research objectives, planned the experiments, analyzed and discussed the results, and contributed to the writing of the article.

Вклад авторов

Ю. В. Титова – определение цели работы, обобщение полученных результатов, написание и редактирование текста статьи.
А. Ф. Якубова – проведение экспериментов, подготовка и оформление результатов экспериментов, участие в анализе и обсуждении результатов, участие в написании статьи.
Г. С. Белова – постановка задачи исследований, планирование экспериментов, анализ и обсуждение результатов, участие в написании статьи.

Received 18.10.2024
Revised 26.10.2024
Accepted 30.10.2024

Статья поступила 18.10.2024 г.
Доработана 26.10.2024 г.
Принята к публикации 30.10.2024 г.

Porous Materials and Biomaterials
Пористые материалы и биоматериалы

UDC 539.217

https://doi.org/10.17073/1997-308X-2024-6-56-64

Research article
Научная статья

The influence of porogen dispersion on the structure and permeability of highly porous material from nickel nanopowder

V. S. Shustov, V. A. Zelensky, M. I. Alymov,
A. B. Ankudinov, A. S. Ustyukhin

A.A. Baikov Institute of Metallurgy and Materials Science of the Russian Academy of Sciences
49 Leninskiy Prosp., Moscow 119334, Russia

✉ vshscience@mail.ru

Abstract. The study investigates the structure, porosity, and permeability of highly porous materials based on nickel nanopowders, which were synthesized using ammonium carbonate as a porogen. The process of sample fabrication involves three technological steps: preparation of the initial mixtures of metal nanopowder with a porogen, compaction of the green samples, and subsequent sintering. The average particle size of the nickel powder was less than 100 nm. Ammonium carbonate powders with particle sizes of 40–63, 100–160, 200–250, and 315–400 µm, obtained by sieving, were selected for the experiments. The porogen's volume fraction in the initial mixtures with nickel nanopowder was 60, 80, 85, and 88 %, with a compaction pressure of 300 MPa. The stages of sintering the nickel nanopowder were preceded by the removal of ammonium carbonate from the green sample by heating it in an argon flow to 100 °C at a rate not exceeding 1 °C/min. The optimal sintering temperature and time for the nickel nanopowder were determined to be 550 °C for 120 min. The research aimed to establish the influence of the porogen's particle size, its size distribution, and volume fraction on the material's porosity and permeability. The results showed that increasing the particle size and volume fraction of the porogen leads to higher porosity and permeability of the material. The maximum permeability value achieved was $8.4 \cdot 10^{-12}$ m^2 from a sample with 88.5 % porosity, produced using a porogen with a particle size of 315–400 µm. When using porogen powders with two different particle size ranges: 40–50 µm and 315–400 µm (or 100–125 µm and 315–400 µm), the permeability was limited to values obtained from samples using only one of these fractions. In this case, the permeability changed nonlinearly depending on the ratio of each fraction component.

Keywords: permeability, porous material, nanopowder, nickel, ammonium carbonate

Acknowledgements: The work was completed according to state order № 075-00320-24-00.

For citation: Shustov V.S., Zelensky V.A., Alymov M.I., Ankudinov A.B., Ustyukhin A.S. The influence of porogen dispersion on the structure and permeability of highly porous material from nickel nanopowder. *Powder Metallurgy and Functional Coatings*. 2024;18(6):56–64. https://doi.org/10.17073/1997-308X-2024-6-56-64

Влияние дисперсности порообразователя на структуру и проницаемость высокопористого материала из нанопорошка никеля

В. С. Шустов ✉, В. А. Зеленский, М. И. Алымов,
А. Б. Анкудинов, А. С. Устюхин

Институт металлургии и материаловедения им. А.А. Байкова Российской академии наук
Россия, 119334, г. Москва, Ленинский пр-т, 49

✉ vshscience@mail.ru

Аннотация. В работе исследованы структура, пористость и проницаемость высокопористых материалов на основе нанопорошков никеля, полученных с использованием карбоната аммония в качестве порообразователя. Процесс изготовления образцов включает три технологические операции: приготовление исходных смесей нанопорошка металла с порообразователем, прессование заготовок и их спекание. Средний размер частиц порошка никеля составлял менее 100 нм. Для исследований выбраны порошки карбоната аммония с частицами размером 40–63, 100–160, 200–250 и 315–400 мкм, полученные методом ситового просева. Объемная доля порообразователя в исходных смесях с нанопорошком никеля составляла 60, 80, 85 и 88 %, давление прессования – 300 МПа. Стадии спекания нанопорошка никеля предшествовала стадия удаления карбоната аммония из прессовки путем ее нагревания в потоке аргона до температуры 100 °C со скоростью, не превышающей 1 °C/мин. Для нанопорошка никеля установлены рациональные значения температуры и времени спекания – 550 °C, 120 мин. Исследование направлено на установление влияния размера частиц порообразователя, их распределения по размеру и его объемной доли на пористость и проницаемость материала. Полученные результаты показали, что увеличение размера частиц порообразователя и его объемной доли приводит к повышению пористости и проницаемости материала. Максимальное значение достигнутой проницаемости составило $8{,}4\cdot 10^{-12}$ м^2 у образца с пористостью 88,5 %, полученного с применением порообразователя с размером частиц 315–400 мкм. При использовании порошков порообразователя с частицами сразу двух размерных диапазонов: 40–50 и 315–400 мкм (либо 100–125 и 315–400 мкм), проницаемость ограничивается значениями, полученными на образцах с применением порошка только одной из указанных фракций. При этом проницаемость меняется нелинейно в зависимости от соотношения каждой составляющей фракции.

Ключевые слова: проницаемость, пористый материал, нанопорошок, никель, карбонат аммония

Благодарности: Работа выполнена в рамках госзадания № 075-00320-24-00.

Для цитирования: Шустов В.С., Зеленский В.А., Алымов М.И., Анкудинов А.Б., Устюхин А.С. Влияние дисперсности порообразователя на структуру и проницаемость высокопористого материала из нанопорошка никеля. *Известия вузов. Порошковая металлургия и функциональные покрытия*. 2024;18(6):56–64. https://doi.org/10.17073/1997-308X-2024-6-56-64

Introduction

Porous materials are used in many industries. The porous structure, typically regarded as a defect in structural materials, provides unique properties that can be utilized for specific purposes [1]. Highly porous materials can be effectively used as electrodes [2], filters that separate impurity particles larger than the pore size [3–5], and are often employed as thermal insulators [6; 7]. Another application of porous materials is in biocompatible implants [8]. The relatively high internal surface area makes highly porous materials excellent catalysts [9; 10].

Depending on the specific application and the required porous structure, various fabrication methods can be employed to produce such materials, including partial sintering, the use of temporary porogens, direct foaming, and others. In the first case, the powder material is sintered in such a way that pores remain between the particles [11; 12]. This is due either to too low temperature and duration of sintering or to the low density of the initial green sample. In the second method, the added porogens decompose into volatile components or are washed out of the material during its production. The porous structure is controlled by appropriately selecting the porogenic substances. For porous materials produced using dispersed porogens, the shape and size of the pores depend on the shape and size of the porogen particles, while porosity is controlled by the quantitative content of the porogen [13]. This methodology allows for higher porosity values compared to the partial sintering technique. The approaches applied to the fabrication of highly porous materials from powders of various natures with the addition of temporary porogens are seen by the authors as promising, as they enable wide-ranging control over porosity and pore size in the resulting material.

It is important to note that simply having a highly porous structure is insufficient for certain applications. For filters and catalysts, it is necessary to create a porous material with a high proportion of open interconnected pores. This ensures good permeability, an important property for ensuring the reliable operation of the products in which they are used. Permeability is defined as the coefficient that relates the pressure gradient to the flow rate of the medium passing through the sample. It depends on the porous structure and can vary sharply with changes in the pore size distribution or the spatial arrangement and shape of the pore channels [10; 14–17]. It should be noted that a high porosity value does not always indicate good permeability.

In many studies where the authors create a porous material and investigate its structure, insufficient attention is paid to this parameter. However, some researchers provide permeability data without a thorough analysis of their relationship with the morphology of the porous space. Most studies focusing on permeability examine the flow of media through porous structures governed by Darcy's law or Forchheimer's law [18–25]. These laws are phenomenological and do not contain any condition describing the influence of the material's microstructure. Therefore, researchers face the pressing task of finding ways to accurately assess permeability based on models developed considering the material's microstructure parameters and allowing for predictions of permeability levels [26; 27]. Existing models do not fully account for all the features of the porous structures of modern materials, and creating new models requires a significant amount of experimental data on the relationship between permeability and various structural characteristics. Consequently, to better understand the processes, experimental studies are necessary to identify the connection between the structural features of the porous material and its permeability.

The aim of this work was to establish the influence of the porogen particle size and its volume fraction on the porosity and permeability of the nickel nanopowder material produced through pressing and sintering.

Research methodology

Nickel nanopowder with an average particle size of less than 100 nm, produced by wire explosion technology, was used as the starting material for the production of porous samples. This powder contained a small amount of larger spherical particles, up to 3 μm in size, which is a characteristic and drawback of this method for obtaining nanopowders. Ammonium carbonate $(NH_4)_2CO_3$ powders were used as the porogen. To study the influence of the volume fraction and dispersion of the porogen on the structure and permeability, ammonium carbonate powders with particle sizes of $d = 40 \div 63$, $100 \div 160$, $200 \div 250$, and $315 \div 400$ μm were selected.

To determine the effect of the particle size distribution of the porogen on the structure and permeability, additional mixtures of the porogen were prepared, using particles from two size ranges: 40–50 and 315–400 μm, as well as 100–125 and 315–400 μm. For simplicity, these porogen powders will hereafter be referred to as "bidisperse". In each mixture, the amounts of both fractions of the powders were varied in steps of 25 % – from 100 % content of the powder with $d = 40 \div 50$ μm (or $100 \div 125$ μm) to 100 % content of the powder with $d = 315 \div 400$ μm.

The production of porous nickel materials consisted of three technological operations: preparing the initial mixtures of nickel nanopowder with the porogen, compacting the green samples, and sintering them. The volume fraction of the porogen in the initial mixtures was 60, 80, 85, and 88 %, with a compaction pressure of 300 MPa. The samples were produced by uniaxial compaction on a hydraulic press (Knuth, Germany) in a split mold with a diameter of 13.6 mm. The height of the compacts before sintering was 10 mm. To remove ammonium carbonate, the compacts were heated in an argon flow to a temperature of 100 °C at a rate not exceeding 1 °C/min. The optimal sintering temperature for the nickel nanopowder was determined to be 550 °C, with a sintering time of 120 min. The heating rate to the sintering temperature did not exceed 2 °C/min, which was necessary for the slow removal of the decomposition products of the porogen. Higher heating rates resulted in structural defects in the samples, such as microcracks. The thermal treatment of the samples was conducted in a tube furnace (MTI GSL1500X, USA).

Porosity was measured using the hydrostatic weighing method, with a relative error not exceeding 0.6 %. The permeability of the obtained porous nickel samples was determined using a method based on Darcy's law. For this, while a liquid flowed through the sample, the pressure drop across its ends and the flow rate of the liquid – determined by the known volume of liquid passing through the sample over a fixed period – were recorded. The study was conducted by passing distilled water under pressure at room temperature. The pressure drop across the tested samples varied from 0 to 0.02 MPa, with the value recorded using a digital manometer (DM5002M, Manotomy JSC, Russia) with an allowable measurement error of $2 \cdot 10^{-5}$ MPa. The relative error in the permeability measurement did not exceed 10 %.

Results and discussion

Fig. 1 presents the microstructure of the fracture surfaces of samples with porosities of 79.3 and 88.5 %, sintered in a hydrogen atmosphere at a temperature of 550 °C. The volume fraction of the porogen in the mixture from which these samples were pressed was 80 and 88 %, respectively. Scanning electron microscopy revealed that, due to the thermal decomposition of the porogen, a pore structure was formed, which can be considered a replica of the removed porogen, with some modification in their shape and size as a result of compaction and sintering. Due to the high activity of the nanopowders, sintering was conducted at a relatively low temperature, resulting in samples with sufficient strength necessary for further investigation of their permeability.

In samples with an initial porogen content of 88 %, a significant number of thin walls, with a thickness of no more than 1–3 µm, were observed, featuring "windows" formed at the points of contact between porogen particles as well as from the escape of decomposition products. The small amount of nickel powder present in the framework of the highly porous material apparently defined a "lace-like" structure in these walls, characterized by numerous smaller holes or voids compared to the windows. Moreover, the smaller the porogen used, the more pronounced this structure became.

The influence of the volume fraction of the porogen and its dispersion on the porosity (P) and permeability (K) of the sintered material was investigated. Fig. 2 presents the dependencies of the porosity of the sintered material on the particle size (d) of the porogen for samples in which the volume fraction of the porogen was 65, 80, 85, and 88 %. It is evident that the value of P increases with increasing values of d. When using a porogen with $d > 100$ µm, the porosity of the sintered material equals or exceeds the expected value, which is equal to the volume fraction of the porogen in the initial mixture. For $d = 40{\div}63$ µm, the value of P was lower than expected, except for samples with a porogen volume fraction of 65 %. The closed porosity of all materials did not exceed 1 %. The porogen $(NH_4)_2CO_3$ decomposes during sintering at temperatures below 100 °C. This leads to the release of pore space and

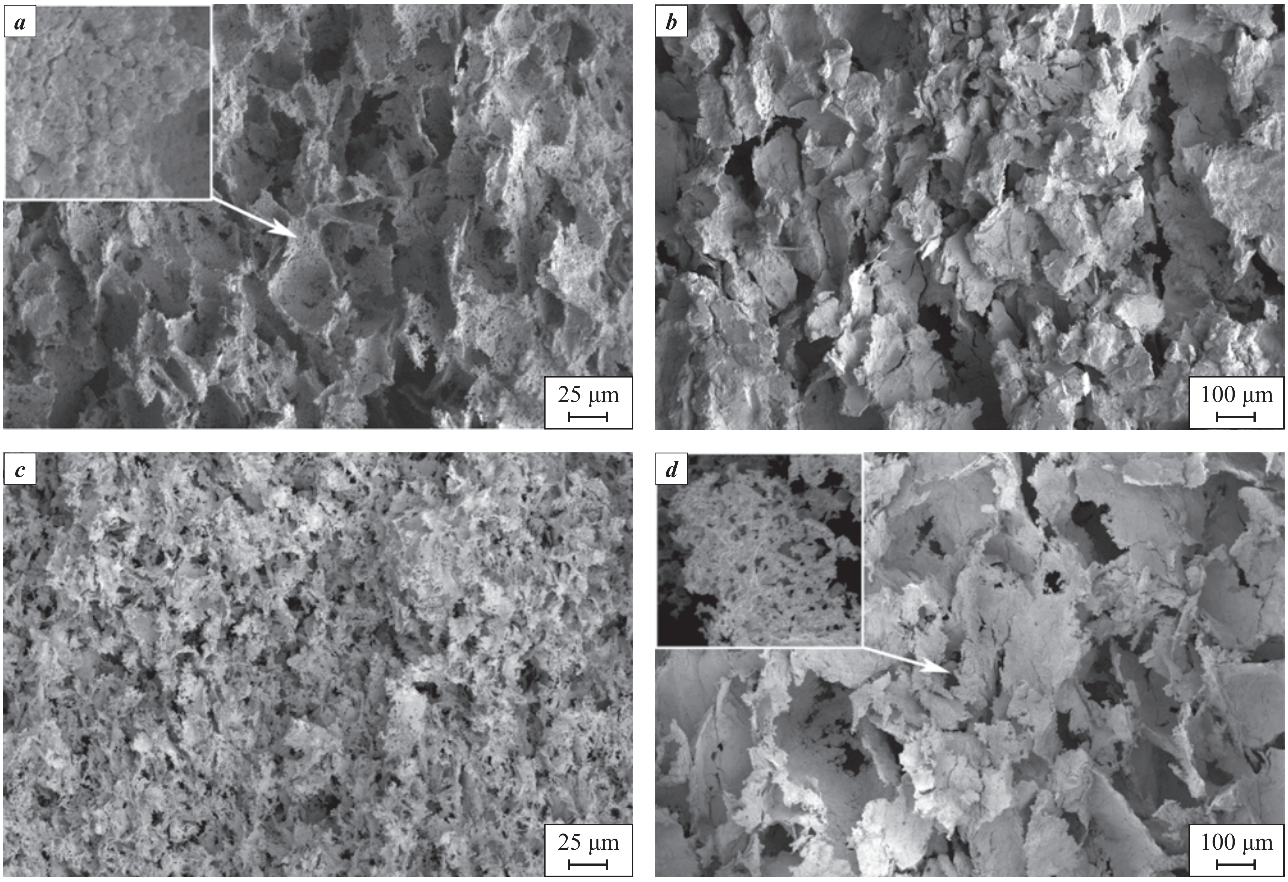

Fig. 1. SEM images of the fracture of nickel nanopowder samples obtained using a porogen of 80 vol. % (***a***, ***b***) and 88 vol. % (***c***, ***d***), and particle sizes of 40–63 µm (***a***, ***c***) and 315–400 µm (***b***, ***d***)

Рис. 1. РЭМ-изображения излома образцов из нанопорошка никеля, полученных с применением порообразователя объемной долей 80 % (***a***, ***b***) и 88 % (***c***, ***d***) и размером частиц 40–63 мкм (***a***, ***c***) и 315–400 мкм (***b***, ***d***) the formation of channels that connect the pores to the free surface of the sample. The interconnection of pores in such materials determines the high proportion of open porosity and their permeability.

The dependence of permeability on the volume fraction of the porogen and its dispersion was investigated (Fig. 3). It was found that as the volume fraction of the porogen increases, the permeability also rises. Additionally, this increase is achieved through the enlargement of the porogen particle size while maintaining a constant volume fraction in the initial powder mixture. For example, with a porogen content of 65 vol. %, the permeability (K, 10^{-12}) increases from 0.1 to 0.4 m^2, at 80 vol. %, it rises from 1 to 2.9 m^2, at 85 vol. %, from 1.8 to 4.6 m^2, and at 88 vol. %, from 3.9 to 8.4 m^2.

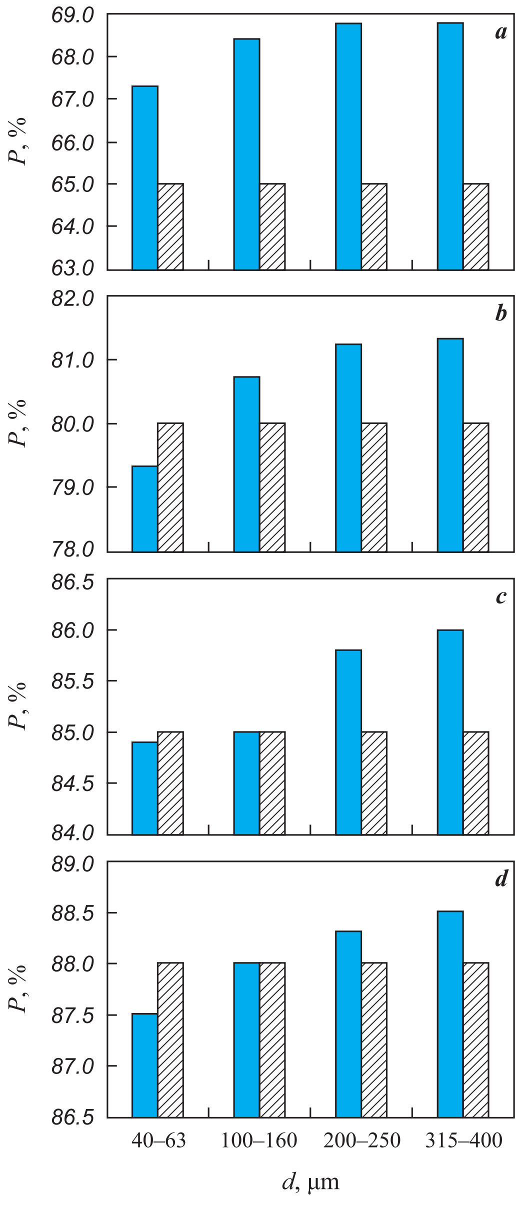

Fig. 2. Diagrams showing the dependence of the porosity of the sintered material on the particle size of the porogen for samples with volume fractions of 65 (***a***), 80 (***b***), 85 (***c***), and 88 % (***d***)

The hatching indicates the volume fraction of the porogen in the initial mixture

Рис. 2. Диаграммы зависимости пористости спеченного материала от размера частиц порообразователя для образцов, в которых объемная доля последнего составляла 65 (***a***), 80 (***b***), 85 (***c***) и 88 % (***d***)

Штриховкой указана объемная доля порообразователя в исходной смеси

Fig. 4 illustrates the dependence of permeability on the porosity of the material for samples obtained using porogen powder with particles of a specified size range.

Using the compaction and sintering regimes described above, samples were obtained from mixtures of nickel nanopowder and bidisperse porogen, with the latter fixed at 85 vol. %. Data from Fig. 5 show that the samples contain pores corresponding to the sizes of the particles of the porogen used – large pores from particles with diameters of 315–400 μm and small pores from particles with diameters of 40–50 μm or 100–125 μm (Fig. 5, *a*, *b*). No inhomogeneity in the pore distribution within the volume of the samples was detected.

It is noteworthy that in samples containing the porogen with smaller particle sizes (40–50 μm), there was a greater number of windows on the surfaces of the larger pores. These windows are comparable in size to the smaller porogen particles and were likely formed due to their contact with the larger ones. It can be hypothesized that a greater number of windows will provide better permeability in this series of samples, along with the high permeability achieved

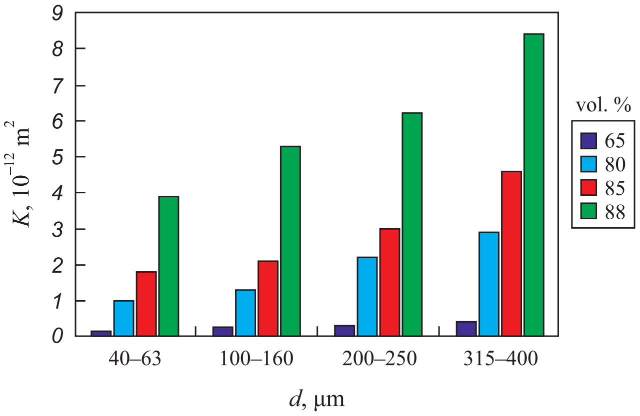

Fig. 3. Diagram showing the dependence of the permeability of the nickel nanopowder material on the volume fraction of the porogen and its dispersion

Рис. 3. Диаграмма зависимости проницаемости материала из нанопорошка никеля от объемной доли порообразователя и его дисперсности

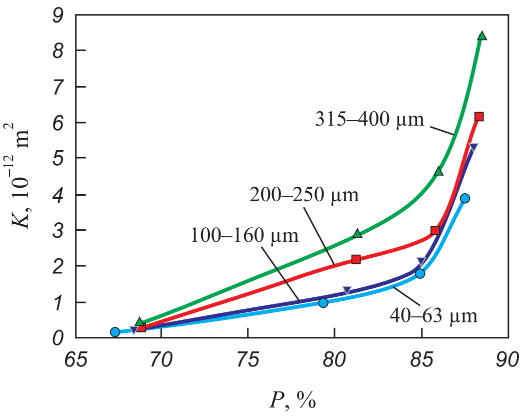

Fig. 4. Graph showing the dependence of the material's permeability on the total porosity for samples obtained using porogens of varying dispersion

Рис. 4. График зависимости проницаемости материала от общей пористости для образцов, полученных с применением порообразователей разной дисперсности

by using porogen with particle sizes of 315–400 μm. However, according to the results of the study (Fig. 6), the samples obtained from mixtures with smaller porogen particles (40–50 μm) exhibited lower permeability compared to those using powders with diameters of 100–125 μm. The content of larger porogen particles (315–400 μm) ranging from 0 to 50 % did not lead to a significant change in the value of K: for samples made with porogen of 40–50 μm, the permeability was $(1.3\pm0.1)\cdot10^{-12}$ m^2, while with 100–125 μm it was $(2.2\pm0.2)\cdot10^{-12}$ m^2. Further increasing the proportion of 315–400 μm particles in the porogen resulted in an increase in K to $4.6\cdot10^{-12}$ m^2.

Conclusions

As a result of the conducted studies on the structure and permeability of the obtained porous materials, the following conclusions were established.

1. The permeability of highly porous materials made from nickel nanopowders increases with both the volume fraction of the porogen, ranging from 60 to 88 %, and the particle size of the porogen. The maximum permeability achieved was $8.4\cdot10^{-12}$ m^2 in a sample with a porosity of 88.5 %.

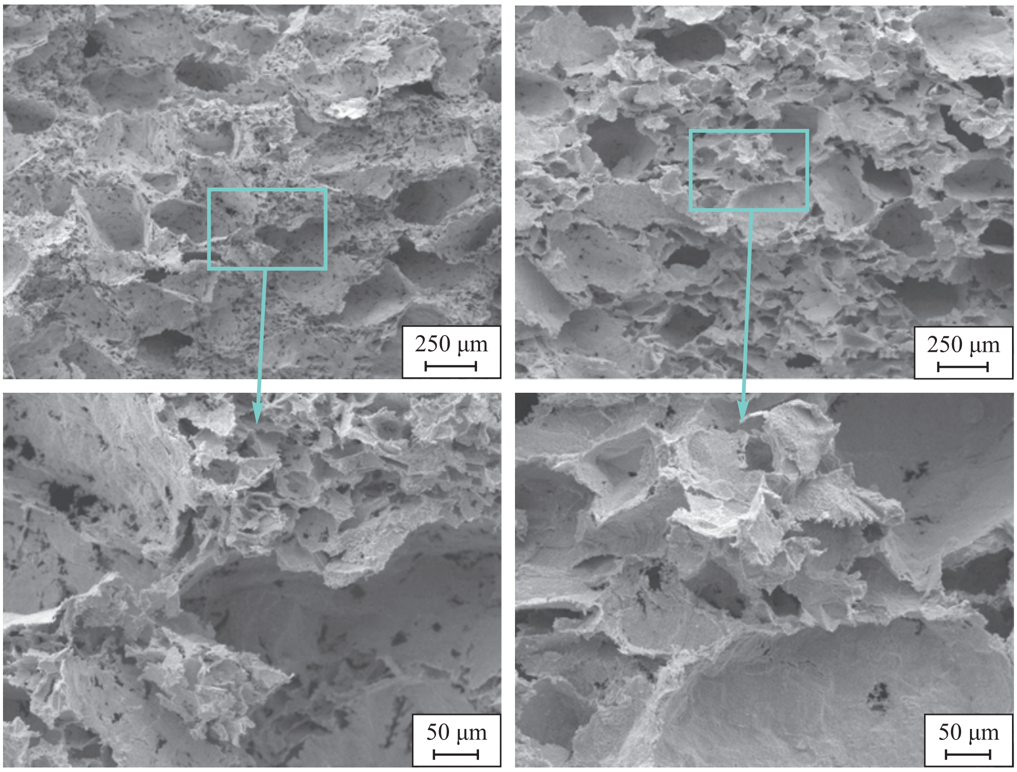

a ***b***

Fig. 5. SEM images of the fracture of porous nickel nanopowder samples obtained using a bidisperse porogen with particle sizes of 40–50 and 315–400 μm (***a***), and 100–125 and 315–400 μm (***b***)

The volume ratio of porogen particles of both sizes in the samples was 50:50

Рис. 5. РЭМ-изображения излома пористых образцов из нанопорошка никеля, полученных с применением бидисперсного порообразователя с размером частиц 40–50 и 315–400 мкм (***a***) и 100–125 и 315–400 мкм (***b***)

Объемное соотношение частиц порообразователя обоих размеров в образцах составляло 50:50

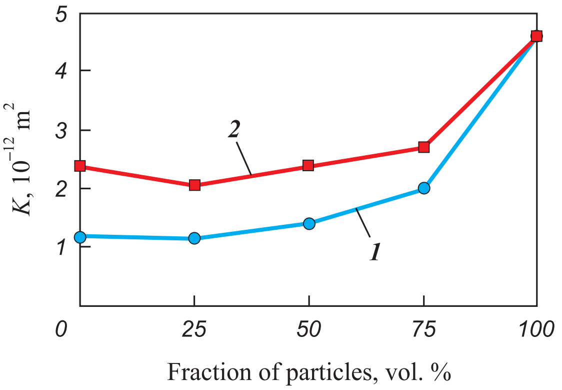

Fig. 6. Dependence of the permeability of samples obtained using a bidisperse porogen on the volume fraction of particles sized 315–400 μm in the initial mixture containing particles sized 40–50 μm (*1*) and 100–125 μm (*2*)

Рис. 6. Зависимость проницаемости образцов, полученных с применением бидисперсного порообразователя, от объемной доли его частиц размером 315–400 мкм в исходной смеси дисперсностью 40–50 мкм (*1*) и 100–125 мкм (*2*)

2. Using a bidisperse porogen facilitates smoother regulation of the permeability in nickel nanopowder materials. As the proportion of larger particles (315–400 μm) in the porogen powder increases, the samples exhibit enhanced permeability. The lowest permeability was recorded when only fine porogen was used (e.g., with particle sizes of 40–50 μm or 100–125 μm). When up to 50 vol. % of larger particles is added, the permeability varies by approximately 10 %. A notable increase in permeability, reaching $4.6 \cdot 10^{-12}$ m^2, is observed at a 100 % volume fraction of porogen particles sized 315–400 μm in the initial mixture.

References / Список литературы

1. Lefebvre L., Banhart J., Dunand D.C. Porous metals and metallic foams: Current status and recent developments. *Advanced Engineering Materials*. 2008;10(9):775–787. https://doi.org/10.1002/adem.200800241
2. Chen H., Hu L., Chen M., Yan Y., Wu L. Nickel-cobalt layered double hydroxide nanosheets for high – performance supercapacitor electrode materials. *Advanced Functional Materials*. 2014;24(7):934–942. https://doi.org/10.1002/adfm.201301747
3. Maggay I.V., Chang Y., Venault A., Dizon G.V., Wu C.J. Functionalized porous filtration media for gravity-driven filtration: Reviewing a new emerging approach for oil and water emulsions separation. *Separation and Purification Technology*. 2021;259:117983. https://doi.org/10.1016/j.seppur.2020.117983
4. Mazurkow J.M., Yüzbasi N.S., Domagala K.W., Pfeiffer S., Kata D., Graule T. Nano-sized copper (oxide) on alumina granules for water filtration: effect of copper oxidation state on virus removal performance. *Environmental Science & Technology*. 2019;54(2):1214–1222. https://doi.org/10.1021/acs.est.9b05211
5. Hellmann A., Pitz M., Schmidt K., Haller F., Ripperger S. Characterization of an open-pored nickel foam with respect to aerosol filtration efficiency by means of measurement and simulation. *Aerosol Science and Technology*. 2015;49(1):16–23. https://doi.org/10.1080/02786826.2014.990555
6. Qiu L., Zou H., Tang D., Wen D., Feng Y., Zhang X. Inhomogeneity in pore size appreciably lowering thermal conductivity for porous thermal insulators. *Applied Thermal Engineering*. 2018;130:1004–1011. https://doi.org/10.1016/J.APPLTHERMALENG.2017.11.066
7. Jia C., Li L., Liu Y., Fang B., Ding H., Song J., Liu Y., Xiang K., Lin S., Li Z., Si W., Li B., Sheng X., Wang D., Wei X., Wu H. Highly compressible and anisotropic lamellar ceramic sponges with superior thermal insulation and acoustic absorption performances. *Nature Communications*. 2020;11(1):1–13. https://doi.org/10.1038/s41467-020-17533-6
8. Szlązak K., Jaroszewicz J., Ostrowska B., Jaroszewicz T., Nabiałek M., Szota M., Swieszkowski W. Characterization of three-dimensional printed composite scaffolds prepared with different fabrication methods. *Archives of Metallurgy and Materials*. 2016;61(2A):645–650. https://doi.org/10.1515/amm-2016-0110
9. Yang C., Zhang C., Chen Z. J., Li Y., Yan W.Y., Yu H.B., Liu L. Three-dimensional hierarchical porous structures of metallic glass/copper composite catalysts by 3D printing for efficient wastewater treatments. *ACS Applied Materials & Interfaces*. 2021;13(6):7227–7237. https://doi.org/10.1021/acsami.0c20832
10. Ibrahim S.H., Skibinski J., Oliver G.J., Wejrzanowski T. Microstructure effect on the permeability of the tape-cast open-porous materials. *Materials and Design*. 2019;167:1–7. https://doi.org/10.1016/j.matdes.2019.107639
11. Ohji T., Fukushima M. Macro-porous ceramics: processing and properties macro-porous ceramics: processing and properties. *International Materials Reviews*. 2013;57(2):115–131. https://doi.org/10.1179/1743280411Y.0000000006
12. Lyckfeldt O., Ferreira J.M.F. Processing of porous ceramics by ‘starch consolidation’. *Journal of the European Ceramic Society*. 1998;18(2):131–140. https://doi.org/10.1016/S0955-2219(97)00101-5
13. Li Y., Yang X., Liu D., Chen J., Zhang D., Wu Z. Permeability of the porous Al_2O_3 ceramic with bimodal pore size distribution. *Ceramics International*. 2019;45(5):5952–5957. https://doi.org/10.1016/j.ceramint.2018.12.064
14. Lv C., Li W., Du J., Liang J., Yang H., Zhu Y., Ma B. Experimental investigation of permeability and Darcy-Forchheimer flow transition in metal foam with high pore density. *Experimental Thermal and Fluid Science*. 2024;154:111149. https://doi.org/10.1016/j.expthermflusci.2024.111149
15. Afsharpoor A., Javadpour F. Liquid slip flow in a network of shale noncircular nanopores. *Fuel*. 2016;180:580–590. https://doi.org/10.1016/j.fuel.2016.04.078
16. Xu X., Liu X., Wu J., Zhang C., Tian K., Yu J. Effect of preparation conditions on gas permeability parameters

of porous SiC ceramics. *Journal of the European Ceramic Society*. 2021;41(6):3252–3263.
https://doi.org/10.1016/j.jeurceramsoc.2021.01.015

17. Dai Q., Wang G., Zhao X., Han Z., Lu K., Lai J., Wang S., Li D., Li Y., Wu K. Fractal model for permeability estimation in low-permeable porous media with variable pore sizes and unevenly adsorbed water lay. *Marine and Petroleum Geology*. 2021;130:105135.
https://doi.org/10.1016/j.marpetgeo.2021.105135

18. Dukhan N., Bağcı Ö., Özdemir M. Metal foam hydrodynamics: Flow regimes from pre-Darcy to turbulent. *International Journal of Heat and Mass Transfer*. 2014;77:114–123.
https://doi.org/10.1016/j.ijheatmasstransfer.2014.05.017

19. Belyaev E.S., Khlybov A.A., Matsulevich Z.V., Titov E.Y., Getmanovsky Y.A., Belyaeva S. S., Bystrov E.O., Ryabov D.A., Kovylin R.S., Tchesnokov S.A., Bazanov A.V., Mezhevoi I.N., Baykov V.E., Yunin V.V. Micromechanics of porosity of various degrees in porous permeable Ti–V30 getter made of powder. *Vacuum*. 2023;211:111934.
https://doi.org/10.1016/j.vacuum.2023.111934

20. Tang H.P., Wang J., Qian M. 28-Porous titanium structures and applications. In: *Titanium Powder Metallurgy.* Ed. Ma Qian, Francis H. (Sam) Froes, Butterworth-Heinemann, 2015. P. 533–554.
https://doi.org/10.1016/B978-0-12-800054-0.00028-9

21. Xie D., Dittmeyer R. Correlations of laser scanning parameters and porous structure properties of permeable materials made by laser-beam powder-bed fusion. *Additive Manufacturing*. 2021;47:102261.
https://doi.org/10.1016/j.addma.2021.102261

22. Lupo M., Neveu A., Gemine T., Francqui F., Lumay G. Measuring permeability and flowability of powders at various packing fractions. *Particuology*. 2024.
https://doi.org/10.1016/j.partic.2024.03.008

23. Xu Y., Zhang S., Ding W., Du H., Li M., Li Z., Chen M. Additively-manufactured gradient porous bio-scaffolds: Permeability, cytocompatibility and mechanical properties. *Composite Structures*. 2024;336:118021.
https://doi.org/10.1016/j.compstruct.2024.118021

24. Li C., Zhou Z. Preparation and characterization of permeability and mechanical properties of three-dimensional porous stainless steel. *RSC Advances*. 2022;12(43): 28079–28087. https://doi.org/10.1039/D2RA03893E

25. Sauermoser-Yri M., Veldurthi N., Wölfle C.H., Svartvatn P.J., Hoem S.O.F., Lid M.J., Bock R., Palko J.W., Torgersen J. On the porosity-dependent permeability and conductivity of triply periodic minimal surface based porous media. *Journal of Materials Research and Technology*. 2023;27:585–599.
https://doi.org/10.1016/j.jmrt.2023.09.242

26. Otaru A.J., Auta M. Machine learning backpropagation network analysis of permeability, Forchheimer coefficient, and effective thermal conductivity of macroporous foam–fluid systems. *International Journal of Thermal Sciences*. 2024;201:109039.
https://doi.org/10.1016/j.ijthermalsci.2024.109039

27. Song S., Rong L., Dong K., Liu X., Le-Clech P., Shen Y. Pore-scale numerical study of intrinsic permeability for fluid flow through asymmetric ceramic microfiltration membranes. *Journal of Membrane Science*. 2022;642: 119920. https://doi.org/10.1016/j.memsci.2021.119920

Information about the Authors

Vadim S. Shustov – Cand. Sci. (Eng.), Senior Research Scientist at the Laboratory of Physical Chemistry of Surfaces and Ultrafine Powder Materials, Baykov Institute of Metallurgy and Materials Science of the Russian Academy of Sciences (IMET RAS)
ORCID: 0000-0001-6395-3747
E-mail: vshscience@mail.ru

Viktor A. Zelensky – Cand. Sci. (Phys.-Math.), Leading Researcher at the Laboratory of Physical Chemistry of Surfaces and Ultrafine Powder Materials, IMET RAS
ORCID: 0000-0002-4441-9132
E-mail: zelensky55@bk.ru

Mikhail I. Alymov – Dr. Sci. (Eng.), Corresponding Member of RAS, Head of the Laboratory of Physical Chemistry of Surfaces and Ultrafine Powder Materials, IMET RAS
ORCID: 0000-0001-6147-5753
E-mail: alymov@ism.ac.ru

Alexey B. Ankudinov – Senior Research Scientist at the Laboratory of Physical Chemistry of Surfaces and Ultrafine Powder Materials, IMET RAS
ORCID: 0009-0002-1150-8515
E-mail: a-58@bk.ru

Alexey S. Ustyukhin – Cand. Sci. (Eng.), Junior Research Scientist at the Laboratory of Physical Chemistry of Surfaces and Ultrafine Powder Materials, IMET RAS
ORCID: 0000-0003-1578-4883
E-mail: fcbneo@yandex.ru

Сведения об авторах

Вадим Сергеевич Шустов – к.т.н., науч. сотрудник лаборатории физикохимии поверхности и ультрадисперсных порошковых материалов, Институт металлургии и материаловедения им. А.А. Байкова Российской академии наук (ИМЕТ РАН)
ORCID: 0000-0001-6395-3747
E-mail: vshscience@mail.ru

Виктор Александрович Зеленский – к.ф.-м.н., вед. науч. сотрудник лаборатории физикохимии поверхности и ультрадисперсных порошковых материалов, ИМЕТ РАН
ORCID: 0000-0002-4441-9132
E-mail: zelensky55@bk.ru

Михаил Иванович Алымов – д.т.н., чл.-корр. РАН, зав. лабораторией физикохимии поверхности и ультрадисперсных порошковых материалов, ИМЕТ РАН
ORCID: 0000-0001-6147-5753
E-mail: alymov@ism.ac.ru

Алексей Борисович Анкудинов – ст. науч. сотрудник лаборатории физикохимии поверхности и ультрадисперсных порошковых материалов, ИМЕТ РАН
ORCID: 0009-0002-1150-8515
E-mail: a-58@bk.ru

Алексей Сергеевич Устюхин – к.т.н., мл. науч. сотрудник лаборатории физикохимии поверхности и ультрадисперсных порошковых материалов, ИМЕТ РАН
ORCID: 0000-0003-1578-4883
E-mail: fcbneo@yandex.ru

Contribution of the Authors

V. S. Shustov – defined the purpose of the work, conducted experiments to determine permeability, participated in the discussion of the results, and wrote the article.
V. A. Zelensky – prepared mixtures and initial samples, participated in the discussion of the results, and editing the article.
M. I. Alymov – defined the purpose of the work and participated in the discussion of the results.
A. B. Ankudinov – determined the porosity of the samples and participated in the discussion of the results.
A. S. Ustyukhin – conducted electron microscopy of the samples' structure.

Вклад авторов

В. С. Шустов – определение цели работы, проведение экспериментов по определению проницаемости, участие в обсуждении результатов, написание текста статьи.
В. А. Зеленский – подготовка смесей и исходных образцов, участие в обсуждении результатов и редактировании статьи.
М. И. Алымов – определение цели работы, участие в обсуждении результатов.
А. Б. Анкудинов – определение пористости образцов, участие в обсуждении результатов.
А. С. Устюхин – проведение электронной микроскопии структуры образцов.

Received 05.08.2024
Revised 11.09.2024
Accepted 13.09.2024

Статья поступила 05.08.2024 г.
Доработана 11.09.2024 г.
Принята к публикации 13.09.2024 г.

Porous Materials and Biomaterials
Пористые материалы и биоматериалы

UDC 67.017

https://doi.org/10.17073/1997-308X-2024-6-65-76

Research article
Научная статья

Influence of composition and surface roughness of titanium alloys on vital activity of mesenchymal stem cells

M. A. Sudarchikova[1] ✉, E. O. Nasakina[1], G. A. Davydova[2], L. R. Valiullin[3], Ya. A. Morozova[1], S. Yu. Kottsov[4], P. A. Prokofiev[1], S. V. Konushkin[1], K. V. Sergienko[1], M. A.Sevostyanov[1], A. G. Kolmakov[1]

[1] **Baykov Institute of Metallurgy and Materials Science, Russian Academy of Sciences**
49 Leninskiy Prosp., Moscow 119334, Russia
[2] **Institute of Theoretical and Experimental Biophysics, Russian Academy of Sciences**
3 Institutskaya Str., Pushchino, Moscow region 142290, Russia
[3] **Federal Center for Toxicological, Radiation and Biological Safety**
2 Nauchny Town, Kazan, Republic of Tatarstan 420075, Russia
[4] **Kurnakov Institute of General and Inorganic Chemistry, Russian Academy of Sciences**
31 Leninskiy Prosp., Moscow 119071, Russia

✉ mariahsudar@yandex.ru

Abstract. The study focused on titanium-based alloys for medical applications, including commercially available grades VT1-0 and VT6, and a newly developed alloy with the composition (wt. %): Ti–23Nb–5Zr. The surfaces of all samples underwent sandblasting using six different sand fractions, mechanical grinding, polishing by tumbling, tumbling polishing, and, in the case of the Ti–Nb–Zr alloy, electrolytic plasma polishing. The effects of surface treatment methods and the chemical composition of medical-grade titanium alloys on surface roughness, microhardness, wettability, and interaction with mesenchymal stem cells (MSCs) was investigated. Surface microhardness was measured using the micro-Vickers method with a diamond indenter under varying loads, while surface roughness was determined using a contact profilometer. It was found that electrolytic plasma polishing enhanced both the microhardness and roughness of the alloy compared to tumbling polishing. Wettability was characterized by the contact angle of deionized water, measured using a specialized setup, with the droplet shape described by a 5-point ellipse model. All treated surfaces exhibited wettability; the contact angle increased as surface roughness decreased. However, sandblasting with mixtures containing a wide particle size distribution increased the contact angle due to the more complex surface relief. To evaluate the biological properties of implants made from VT6, VT1-0, and Ti–23Nb–5Zr alloys after the described surface treatments, their effects on cell viability and the adhesive characteristics of the materials were studied using a direct contact method with two types of mesenchymal stem cells. The newly developed alloy, which potentially offers superior biomechanical compatibility compared to commercial materials, demonstrated no compromise in surface characteristics or adverse effects on cell viability.

Keywords: titanium alloys, medical-grade alloys, surface microhardness, surface roughness, surface wettability, mesenchymal stem cells (MSCs)

Acknowledgements: The research was carried out at the expense of a grant from the Russian Science Foundation No. 21-79-10256, https://rscf.ru/project/21-79-10256/.

For citation: Sudarchikova M.A., Nasakina E.O., Davydova G.A., Valiullin L.R., Morozova Ya.A., Kottsov S.Yu., Prokofiev P.A., Konushkin S.V., Sergienko K.V., Sevostyanov M.A., Kolmakov A.G. Influence of composition and surface roughness of titanium alloys on vital activity of mesenchymal stem cells. *Powder Metallurgy and Functional Coatings*. 2024;18(6):65–76. https://doi.org/10.17073/1997-308X-2024-6-65-76

Влияние состава и шероховатости поверхности титановых сплавов на жизнедеятельность мезенхимальных стволовых клеток

М. А. Сударчикова[1], Е. О. Насакина[1], Г. А. Давыдова[2], Л. Р. Валиуллин[3],
Я. А. Морозова[1], С. Ю. Котцов[4], П. А. Прокофьев[1], С. В. Конушкин[1],
К. В. Сергиенко[1], М. А. Севостьянов[1], А. Г. Колмаков[1]

[1] **Институт металлургии и материаловедения им. А. А. Байкова Российской академии наук**
Россия, 119334, г. Москва, Ленинский пр-т, 49
[2] **Институт теоретической и экспериментальной биофизики Российской академии наук**
Россия, 142290, Московская обл., г. Пущино, ул. Институтская, 3
[3] **Федеральный центр токсикологической, радиационной и биологической безопасности**
Россия, 420075, Республика Татарстан, г. Казань, г-к Научный, 2
[4] **Институт общей и неорганической химии имени Н.С. Курнакова Российской академии наук**
Россия, 119071, г. Москва, Ленинский пр-т, 31

mariahsudar@yandex.ru

Аннотация. В работе исследовались сплавы на основе титана медицинского назначения: коммерческие марки ВТ1-0, ВТ6 и разрабатываемый сплав, мас. %: Ti–23Nb–5Zr. Поверхности всех образцов подвергались струйной обработке с применением 6 видов различных фракций песка, механической шлифовке и полировке методом галтовки, а также, дополнительно, электролитно-плазменной полировке (для сплава системы Ti–Nb–Zr). Исследовалось влияние метода поверхностной обработки титановых сплавов медицинского назначения и их химического состава на шероховатость, микротвердость, смачиваемость поверхности и ее взаимодействие с мезенхимальными стволовыми клетками. Микротвердость поверхности определялась по схеме «микро-Виккерс» с применением алмазного индентора при различной нагрузке. Измерения шероховатости поверхности проводились с помощью контактного профилометра. Отмечено, что электролитно-плазменная полировка повышает микротвердость и шероховатость поверхности сплава по сравнению с галтовкой. Краевой угол смачивания образцов деионизированной водой измерялся при помощи специальной установки. При этом форма капли описывалась моделью эллипса по 5 точкам. Установлено, что все созданные поверхности смачиваемы, угол смачивания возрастает с понижением шероховатости поверхности, однако струйная обработка смесями с широким разбросом частиц по размеру приводит к его повышению за счет усложнения рельефа поверхности. Для изучения биологических свойств имплантатов из сплавов ВТ6, ВТ1-0 и Ti–23Nb–5Zr после указанных видов поверхностной обработки, а также их влияния на выживаемость клеток и адгезивные характеристики материалов использовался метод прямого контакта с двумя типами мезенхимальных стволовых клеток. Разрабатываемый сплав, потенциально обладающий лучшей биомеханической совместимостью, чем коммерческие, не вызвал ухудшения поверхностных характеристик и отрицательно не повлиял на жизнедеятельность клеток.

Ключевые слова: титановые сплавы, сплавы медицинского назначения, микротвердость поверхности, шероховатость поверхности, смачиваемость поверхности, мезенхимальные стволовые клетки (МСК)

Благодарности: Исследование выполнено за счет гранта Российского научного фонда № 21-79-10256, https://rscf.ru/project/21-79-10256/.

Для цитирования: Сударчикова М.А., Насакина Е.О., Давыдова Г.А., Валиуллин Л.Р., Морозова Я.А., Котцов С.Ю., Прокофьев П.А., Конушкин С.В., Сергиенко К.В., Севостьянов М.А., Колмаков А.Г. Влияние состава и шероховатости поверхности титановых сплавов на жизнедеятельность мезенхимальных стволовых клеток. *Известия вузов. Порошковая металлургия и функциональные покрытия*. 2024;18(6):65–76. https://doi.org/10.17073/1997-308X-2024-6-65-76

Introduction

Biomaterials, designed for contact with the living organism's environment, are commonly used for manufacturing implants. These materials ensure compatibility with medical devices through a combination of properties such as superelasticity, low Young's modulus, high corrosion resistance, and either bioinertness or adhesiveness [1–3]. Typically, these include metallic alloys (titanium, cobalt, stainless steels), polymers, and ceramics. However, they exhibit certain drawbacks, such as low strength and/or high elastic modulus, which ultimately lead to the degradation of both the implants and surrounding tissues [4–8]. Besides organizational factors (e.g., small-scale production), the manufacturing of titanium-based products is constrained by technological challenges. One such issue is the mechanical strength and fatigue properties of titanium alloy blanks, which, however, can be addressed by developing methods for surface structure modification and optimizing alloy composition.

Shape memory alloys, particularly those in the Ti–Ni system, exhibit low Young's modulus and superelastic behavior, akin to that of living tissues [9–11]. However, the toxic properties of nickel and the potential for corrosion-related damage (material degradation in operating environments) limit their application [12–14].

At the same time, modern research indicates that shape memory and superelastic effects can also be observed in alloys composed exclusively of non-toxic metals [15–23]. For instance, tantalum [24] and niobium [17; 25–27], which exhibit high corrosion resistance and biocompatibility, can be employed as β-stabilizers in titanium alloys, thereby contributing to a reduction in the elastic modulus. In particular, research [23] has demonstrated that the Ti–Nb–Ta alloy has a lower elastic modulus and higher corrosion resistance compared to the Ti–6Al–4V alloy. Zirconium is typically used as a neutral strengthening element [28–31]; however, as reported by the authors of [20], it may also exhibit β-stabilizing effects in β-titanium alloys. Furthermore, titanium and niobium have similar atomic radii (0.145–0.146 nm), whereas zirconium has a slightly larger atomic radius (0.160 nm). Thus, alloying titanium with zirconium is expected to increase the interatomic distance in the alloy, reduce the bonding force between atoms, and consequently lower the Young's modulus. Conversely, alloying titanium with niobium is expected to at least maintain the lattice parameter of the β-phase.

Therefore, Ti–Nb–Zr alloys can be considered excellent candidates for biomedical applications involving implantation.

Mesenchymal stem cells (MSCs) are an optimal test system for analyzing the biological activity of materials intended for implant fabrication, as they possess a high potential for differentiation into cellular elements of various mesenchymal-derived tissues [32].

The interaction of any material with cells is largely influenced by the quality of its surface. Therefore, the aim of this study was to investigate the interaction of the Ti–Nb–Zr alloy, following various surface treatments, with mesenchymal stem cells in comparison with materials already used in medical applications.

Materials and methods

Samples for the study were fabricated from the following titanium-based biomedical materials:

– commercially available material VT1-0 (pure titanium), as per GOST 19807-91;

– commercially available alloy VT6 (titanium alloy with aluminum and vanadium), as per GOST 19807-91;

– a newly developed titanium-based alloy with the composition (at. %): Ti–23Nb–5Zr.

The starting materials used included iodide titanium, niobium grade Nb-1, and iodide zirconium. Alloy ingots were melted in an argon-arc melting furnace with a non-consumable tungsten electrode. To produce sheets, the ingots underwent homogenizing annealing in a vacuum, followed by warm rolling with intermediate annealing and subsequent quenching.

The Young's modulus of the Ti–23Nb–5Zr alloy sheet samples was determined using a universal testing machine, INSTRON 3382 (USA), at room temperature.

The interaction of any material with cells depends significantly on the quality of its surface; hence, several surface treatment options were selected for evaluation. Samples of the VT1-0, VT6, and Ti–23Nb–5Zr alloys, with a diameter of 20 mm and thickness of 4 mm, were cut from sheets using a DK 7745 ME11 electrical discharge machine by Meatec (China). Before sandblasting, the samples were pre-ground using abrasive papers with grit sizes ranging from 240 to 600 and treated by tumbling in a KT-100 electromagnetic tumbling machine (CARLO de GIORGI, Italy) with a metallic needle abrasive. Additionally, some samples were subjected to electrolytic plasma polishing (EPP) in a 5 % aqueous solution of a 20 % NH_4F + 80 % KF mixture at a voltage of 300 V and a temperature of 85–88 °C for 10 min. The sandblasting of sample surfaces was conducted in a 90 L chamber under 12 atm of high-purity argon pressure using copper slag (particle sizes ≤0.63 mm) and sand fractions of 0.63–1.0 mm, 1.0–1.5 mm, and 0.63–1.5 mm, as well as their 1:1 mixture (0.63–1.5 mm). For the treated surfaces, characteristics such as roughness and wettability were determined.

Surface roughness was evaluated according to GOST 25142-82 using a Proton profilometer model 130 (Russia). Prior to measurement, all samples were cleaned in an ultrasonic bath with a specialized soap solution, bidistilled water, and alcohol, then carefully dried.

Surface microhardness (*HV*) was determined using the micro-Vickers method as per GOST 9450-76 with a 401/402-MVD device (Wolpert Group, Germany) equipped with an optical microscope. A diamond indenter with a tip size of 10 μm and test loads of 25, 100, 300, and 500 g were used.

The wettability of the samples was characterized by the contact angle of deionized water, measured using a Lonroy SDC-350 setup (Dongguan Lonroy

Equipment Co., LTD, China) at a tilt angle of 0°. A droplet with a volume of 6 μL was deposited on the sample, and an image of the droplet was taken 60 s later. When measuring the contact angle, the droplet shape was analyzed after a delay following its contact with the substrate. This delay helps eliminate dynamic effects that could distort the shape of the elastic droplet immediately upon impact with the sample. Typically, the waiting time before droplet shape analysis is 30–60 s after the start of the measurement [33–35]. When calculating the contact angle, the droplet shape was described using a 5-point ellipse model.

To evaluate the biological properties of implants made from VT6, VT1-0, and Ti–23Nb–5Zr alloys following the described surface treatments, as well as the effect of the samples on cell viability and the adhesive characteristics of the materials, a direct contact method was employed using two types of mesenchymal stem cells (MSCs): dental pulp stem cells (DPSCs) from human dental pulp (clone Th44), and immortalized fibroblast-like cells (embryonic connective tissue cells involved in regeneration and synthesis of proteins critical for dermal rejuvenation [36], skin MSCs [37]).

For cell viability assessment, the samples were sterilized with 70 % ethanol and placed in wells of a 24-well plate. DPSC cells at the 5th passage were seeded into the plate wells at a density of 30,000 cells/cm^2 in DMEM/F12 medium containing 10 % FBS and supplemented with 100 U/mL penicillin/streptomycin. The cells were cultured for 24 h at 37 °C in a humidified atmosphere with 5 % CO_2. Following the culture period, the morphology of the cells in direct contact with the samples was assessed on the surface of the culture plastic.

As a negative control, DMEM/F12 medium without cells was added to the wells. At the end of the cultivation period, the morphology of the cells on the surfaces of the tested materials was evaluated, and cell viability was assessed using fluorescent staining with SYTO 9, propidium iodide (PI), and Hoechst 33342 reagents. The fluorescent dye SYTO 9, at an excitation wavelength (λ_{exc}) of 450÷490 nm and an emission wavelength (λ_{em}) of 515÷565 nm, stains the DNA and RNA of both live and dead cells green. The intercalating reagent propidium iodide (PI), with λ_{exc} = 546 nm and λ_{em} = 575÷640 nm, stains the nuclei of dead cells red. The fluorescent dye Hoechst 33342, with λ_{exc} = 343 nm and λ_{em} = 483 nm, stains the DNA of both live and dead cells blue.

The effect of the tested materials on fibroblast cells was evaluated by culturing the cells directly in the presence of the samples. After 24 h, the cell layer was evaluated using an inverted microscope based on the following parameters: surface coverage area, cell shape, the number of cellular aggregates, and the number of floating cells. Cell counting was performed using a Goryaev chamber, and the number of viable and dead cells was determined using trypan blue staining (0.1 % solution) [38]. The influence of the Ti-based samples on the culture morphology of the cells was determined based on the following metrics:

– viability coefficient: the ratio of live cells to the total number of cells, %;

– proliferation index: the ratio of the number of grown cells to the number of seeded cells [39];

– cell death percentage: the ratio of the number of dead cells remaining after exposure to the compound to the total number of cells after exposure, %.

Statistical analysis of the obtained data was conducted using the methods of variation statistics with Student's *t*-test to assess significance.

The isolation of dental pulp stem cells (DPSCs) was performed as follows: after opening the crown, the pulp was extracted, washed with Hank's solution, minced, and incubated in a 0.1 % type I collagenase solution for 30 min at 37 °C. The resulting cell suspension was centrifuged at 1000 rpm for 5 min. The pellet was resuspended in growth medium (DMEM/F12) supplemented with 10 % fetal calf serum (FCS), 100 U/mL penicillin, 100 U/mL streptomycin, and 2 mM glutamine, and then transferred into culture flasks. After 3 days, non-adherent cells were removed, and the fraction of adherent cells was cultured until 80–90 % confluence was reached. The cells were then suspended using a mixture of 0.25 % trypsin solution and Versene solution (1:1) and reseeded at a 1:3 ratio. Passaging of cells *in-vitro* was performed using standard methods in culture flasks within a CO_2 incubator (37 °C, 5 % CO_2, 80 % humidity) with the growth medium changed every 3 days.

Results and discussion

The Young's modulus of the Ti–23Nb–5Zr alloy surface in its initial state was $E = 56\pm5$ GPa, which is significantly lower than that of the commercially available alloys VT1-0 and VT6 ($E > 90$ GPa) [40; 41] and is closer to the values of bone [42].

Six types of samples were prepared for each alloy, differing in the method of sandblasting and the presence of electrolytic plasma polishing (EPP). The results of roughness (R_a) and microhardness (*HV*) measurements for the samples are presented in Tables 1 and 2, while microphotographs of the polished samples (tumbling and EPP) are shown in Fig. 1. High surface heterogeneity after sandblasting prevented reliable results due to indenter slippage. The R_a values for the samples after tumbling were lower than those after

EPP. This can be explained by the fact that, in the first case, a kind of "smoothing" of the surface relief occurs, while in the latter, preferential etching of certain structural components and segregation zones may take place. No correlation was observed between the roughness and microhardness of the samples.

At the same time, electrolytic plasma polishing contributes to an increase in the hardness of the surface layer (see Tables 1 and 2). This is presumably due to structural changes in the surface layer of the metallic materials, which influence their mechanical properties [43]. Notably, as the load decreases, microhardness increases, since the contribution of the surface itself becomes more significant compared to the bulk material (Table 2). No correlation was observed between surface roughness and microhardness of the samples.

The effect of treatment on surface roughness is consistent with the results of contact angle measurements (see Table 1, Fig. 2). A typical trend observed for solid materials wetted by liquid is that the contact angle increases (wettability decreases) as surface roughness decreases [44]. Minimum wettability was observed

Table 1. **Results of roughness and Vickers microhardness at 500 g load, and wettability depending on material surface treatment**

Таблица 1. **Результаты исследования шероховатости, микротвердости по Виккерсу при нагрузке 500 г и смачиваемости в зависимости от обработки материалов**

Material	Sample No.	Surface treatment	R_a, μm	Microhardness, HV	Contact angle, deg
VT1-0	*1*	Copper slag	1.90 ± 0.10	–	46 ± 2
	2	Sand (1.0–1.5 mm)	5.40 ± 0.20	–	31 ± 2
	3	Sand (<1.0 mm)	3.10 ± 0.20	–	43 ± 2
	4	Original sand	5.10 ± 0.20	–	49 ± 2
	5	Copper slag + original sand	4.30 ± 0.20	–	53 ± 2
	6	Tumbling	0.46 ± 0.04	245 ± 28	72 ± 2
VT6	*1*	Copper slag	2.50 ± 0.20	–	41 ± 2
	2	Sand (1.0–1.5 mm)	5.70 ± 0.20	–	35 ± 2
	3	Sand (<1.0 mm)	3.30 ± 0.20	–	43 ± 2
	4	Original sand	5.10 ± 0.20	–	48 ± 2
	5	Copper slag + original sand	4.20 ± 0.20	–	54 ± 2
	6	Tumbling	0.27 ± 0.02	219 ± 19	73 ± 2
Ti–23Nb–5Zr	*1*	Copper slag	2.60 ± 0.20	–	43 ± 2
	2	Sand (1.0–1.5 mm)	5.50 ± 0.20	–	32 ± 2
	3	Sand (<1.0 mm)	3.70 ± 0.30	–	44 ± 2
	4	Original sand	5.10 ± 0.20	–	49 ± 2
	5	Copper slag + original sand	4.10 ± 0.30	–	55 ± 2
	6	Tumbling	0.17 ± 0.01	269 ± 15	74 ± 2
	7	Electrolytic plasma polishing	0.75 ± 0.06	297 ± 17	57 ± 2

Table 2. **Results of studies of microhardness of polished samples depending on the load**

Таблица 2. **Результаты исследования микротвердости полированных образцов в зависимости от нагрузки**

Sample No.	Material	Treatment	Microhardness, HV, at load		
			25 g	100 g	300 g
6	Ti–23Nb–5Zr	Tumbling	306 ± 61	271 ± 45	276 ± 21
7	Ti–23Nb–5Zr	EPP	363 ± 42	313 ± 35	301 ± 13
6	VT1-0	Tumbling	313 ± 64	269 ± 32	238 ± 31
6	VT6	Tumbling	358 ± 158	282 ± 74	232 ± 26

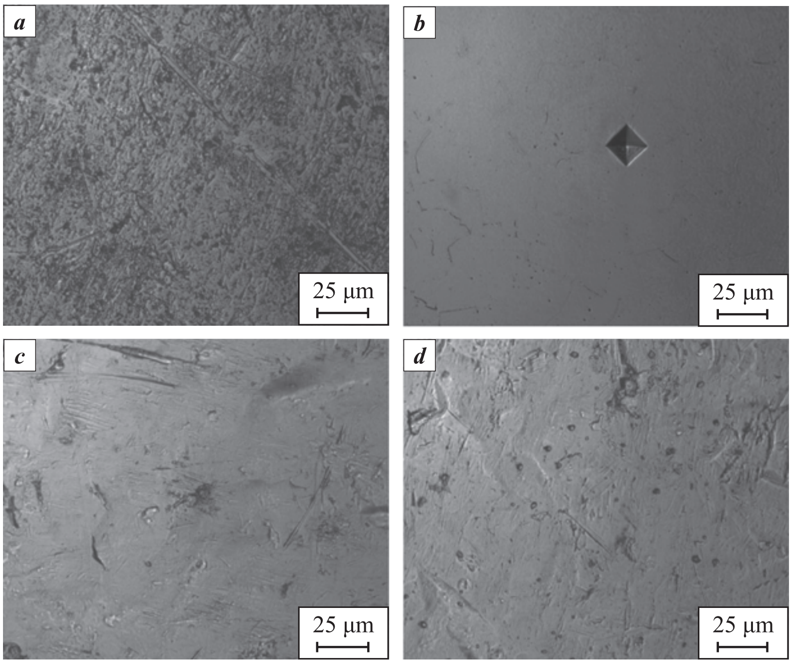

Fig. 1. Microphotographs of samples with smooth surfaces
a – Ti–23Nb–5Zr after tumbling, ***b*** – Ti–23Nb–5Zr after EPP, ***c*** – VT1-0, ***d*** – VT6

Рис. 1. Микрофотографии образцов с гладкой поверхностью
a – Ti–23Nb–5Zr после галтовки, ***b*** – Ti–23Nb–5Zr после ЭПП, ***c*** – ВТ1-0, ***d*** – ВТ6

after tumbling. However, a deviation from the direct relationship occurred for all materials treated with a mixture of copper slag and original (non-fractionated) sand. This is likely due to the wide range of particle sizes impacting the surface, resulting in many small cavities among the larger ones, which locally increased the contact angle. For a similar reason, albeit to a lesser extent, the contact angle for samples treated with original sand also deviates from the trend, as the range of particle sizes is narrower. All three alloys demonstrated similar surface characteristics after each type of treatment.

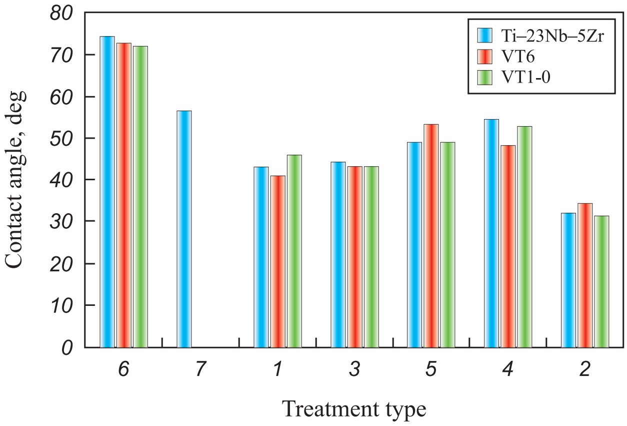

Fig. 2. Dependence of wettability on surface treatment (see Table 1)
1 – cooper slag, ***2*** – sand (1.0–1.5 mm), ***3*** – sand (<1.0 mm), ***4*** – original sand (0.63–1.5 mm), ***5*** – cooper slag + original sand, ***6*** – tumbling, ***7*** – EPP

Рис. 2. Зависимость смачиваемости от обработки поверхности (см. табл. 1)
1 – купершлак, ***2*** – песок (1,0–1,5 мм), ***3*** – песок (<1,0 мм), ***4*** – песок исходный (0,63–1,5 мм), ***5*** – купершлак + песок исходный, ***6*** – галтовка, ***7*** – ЭПП

The images in Fig. 3 show the appearance of DPSC cells at the contact area with the tested materials after 24 h of cultivation. It is evident that none of the materials inhibit cell growth, demonstrating their biocompatibility[1]. No differences were observed depending on the alloy composition or treatment type.

Characteristic microphotographs from the first day of cultivation for samples treated with copper slag and sand (1.0–1.5 mm) are shown in Fig. 4 and 5, respectively. The surfaces displayed a large number of “spread-out” cells, evenly distributed with only a few non-viable ones. This demonstrates that all sample types were adhesive to cells.

Table 3 presents the culture-morphological properties of fibroblast cells in contact with the alloys after sandblasting treatments. All materials showed low cytotoxicity, highlighting their suitability for medical applications. No correlation was found between the cytotoxic properties of the alloys and their composition or surface treatment methods.

---

[1] The study of extracts from these materials is deemed impractical.

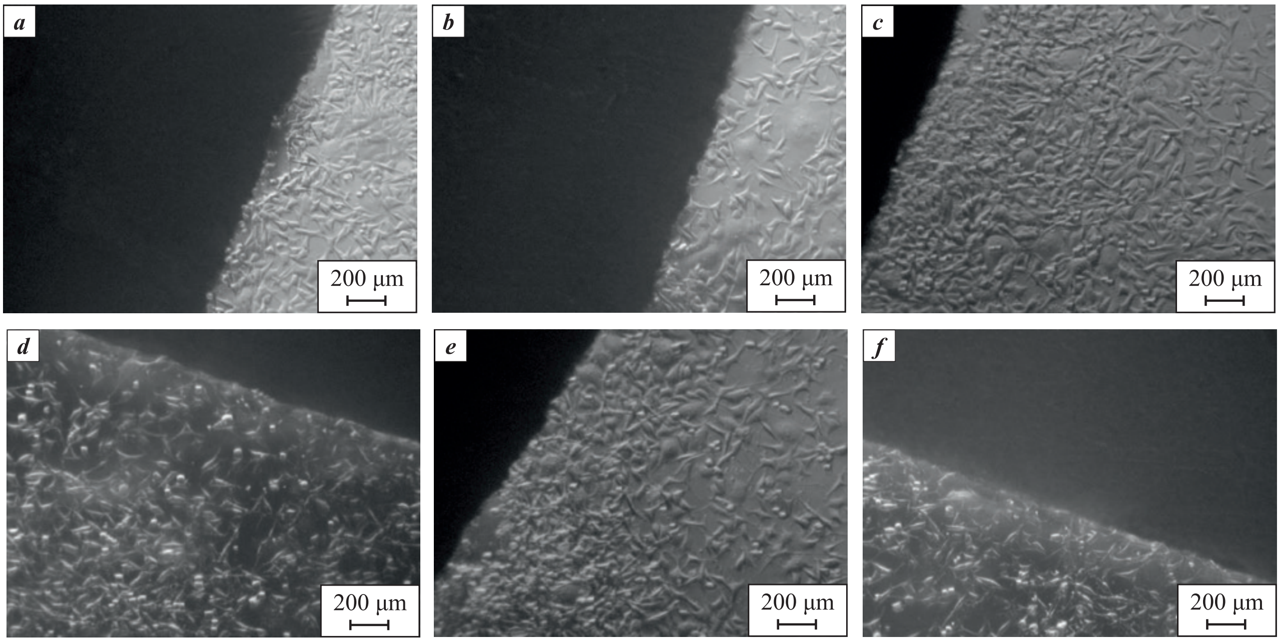

Fig. 3. Appearance of DPSC cells at the contact area with tested materials 24 h after seeding

a–c: Ti–23Nb–5Zr after EPP (***a***), treatment with original sand (non-fractionated) (***b***), and sand with a grain size of 1.0–1.5 mm (***c***);
d and ***f***: VT1-0 after tumbling (***d***) and treatment with sand (<1.0 mm) (***f***);
e – VT6 after treatment with sand (1.0–1.5 mm)

Рис. 3. Внешний вид клеток DPSC в месте контакта с исследуемыми материалами через 24 ч после посева

а–с: Ti–23Nb–5Zr после ЭПП (***а***), обработки песком – исходным (не разделенным на фракции) (***b***) и зернистостью 1,0–1,5 мм (***с***);
d и ***f***: ВТ1-0 после галтовки (***d***) и обработки песком зернистостью до 1,0 мм (***f***);
е – ВТ6 после обработки песком (1,0–1,5 мм)

Table 3. **Cytotoxic properties of alloys depending on surface treatment**

Таблица 3. **Цитотоксические свойства сплавов в зависимости от обработки поверхности**

Material	Sample No.	Surface treatment	Proliferative activity, %	Viability, %	Cytotoxicity index IC_{50}
VT1-0	*1*	Copper slag	80	83	0,90 ± 0,04
	2	Sand (1.0–1.5 mm)	82	84	0,90 ± 0,02
	3	Sand (<1.0 mm)	82	82	0,90 ± 0,04
	4	Original sand	49	74	0,80 ± 0,03
	5	Copper slag + original sand	82	85	0,90 ± 0,03
	6	Tumbling	83	86	0,90 ± 0,02
VT6	*1*	Copper slag	60	80	0,90 ± 0,04
	2	Sand (1.0–1.5 mm)	65	74	0,80 ± 0,03
	3	Sand (<1.0 mm)	51	62	0,70 ± 0,01
	4	Original sand	81	85	0,90 ± 0,02
	5	Copper slag + original sand	79	80	0,90 ± 0,03
	6	Tumbling	68	72	0,60 ± 0,02
Ti–23Nb–5Zr	*1*	Copper slag	79	80	0,90 ± 0,02
	2	Sand (1.0–1.5 mm)	49	56	0,50 ± 0,01
	3	Sand (<1.0 mm)	81	76	0,90 ± 0,04
	4	Original sand	75	80	0,80 ± 0,03
	5	Copper slag + original sand	53	67	0,60 ± 0,01
	6	Tumbling	80	76	0,80 ± 0,03

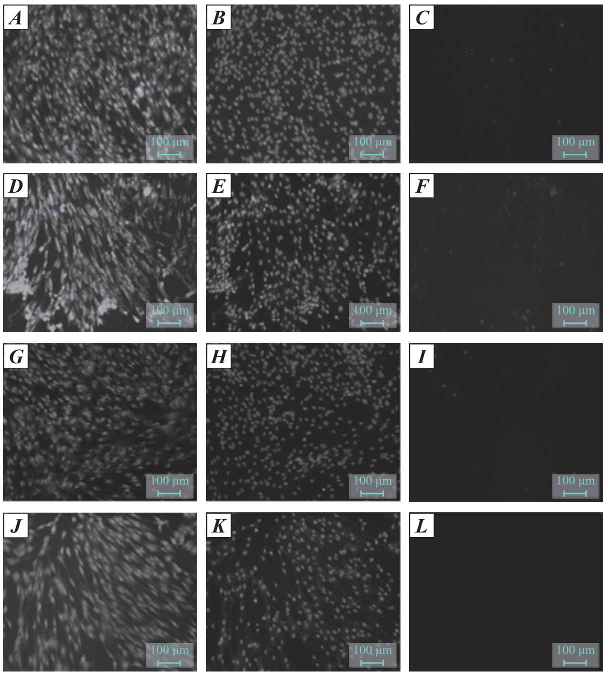

a ***б*** ***c***

Fig. 4. Appearance of DPSC cells incubated on the surface of titanium alloy samples: TiNbZr (***A***–***C***), VT1-0 (***D***–***F***), VT6 (***G***–***I***), and control (***J***–***L***), after sandblasting with cooper slag 24 h post-seeding

a – Staining with SYTO 9, ***b*** – staining with Hoechst 33342, ***c*** – staining with PI

Рис. 4. Внешний вид клеток DPSC при инкубации на поверхности образцов титановых сплавов: TiNbZr (***A***–***C***), ВТ1-0 (***D***–***F***), ВТ6 (***G***–***I***) и контрольного (***J***–***L***), после струйной обработки купершлаком через 24 ч после посева

a – окраска SYTO 9, ***b*** – Hoechst 33342, ***c*** – PI

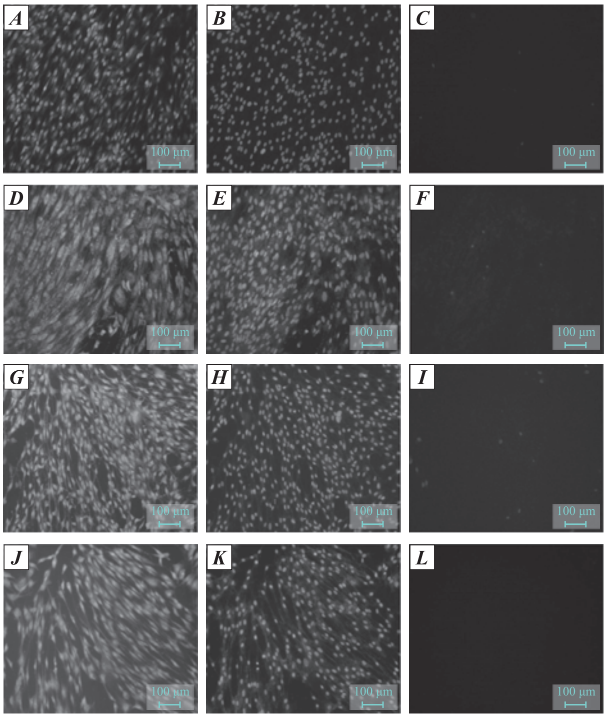

a ***b*** ***c***

Fig. 5. Appearance of DPSC cells incubated on the surface of titanium alloy samples: Ti–Nb–Zr (***A***–***C***), VT1-0 (***D***–***F***), VT6 (***G***–***I***), and control (***J***–***L***), after sandblasting with coarse sand (1.0–1.5 mm) 24 h post-seeding

a – Staining with SYTO 9, ***b*** – staining with Hoechst 33342, ***c*** – staining with PI

Рис. 5. Внешний вид клеток DPSC при инкубации на поверхности образцов титановых сплавов: TiNbZr (***A***–***C***), ВТ1-0 (***D***–***F***), ВТ6 (***G***–***I***) и контрольного (***J***–***L***), после струйной обработки крупным песком (1,0–1,5 мм) через 24 ч после посева

a – окраска SYTO 9, ***b*** – Hoechst 33342, ***c*** – PI

Conclusion

The study examined the effects of six sandblasting techniques and electrolytic plasma polishing (EPP) on the surface properties and interaction with mesenchymal stem cells of two commercially available titanium-based alloys – VT1-0 (pure titanium) and VT6 (a titanium-aluminum-vanadium alloy) – as well as a newly developed Ti–Nb–Zr alloy.

EPP was found to enhance microhardness but reduce surface roughness compared to tumbling.

All treated surfaces exhibited wettability, with the contact angle increasing as surface roughness decreased. However, sandblasting with mixtures containing a wide range of particle sizes increased the contact angle, likely due to the creation of a more complex surface texture. Tumbling produced the highest contact angle among all alloys, resulting in the most “developed” surface relief.

All three materials exhibited low cytotoxicity, high proliferative activity, and excellent cell viability. A significant number of viable cells were evenly distributed on the sample surfaces. No definitive relationship was observed between cytotoxicity parameters and either the material composition or the surface treatment method.

The newly developed alloy Ti–23Nb–5Zr, which shows promise for improved biomechanical compatibility compared to the commercial alloys, demonstrated stable surface properties and had no adverse effects on cell viability.

References / Список литературы

1. Park J.B., Lakes R.S. Metallic implant materials. *Biomaterials*. 2007;5:99–137. https://doi.org/10.1007/978-0-387-37880-0_5
2. Amirtharaj Mosas K.K., Chandrasekar A.R., Dasan A., Pakseresht A., Galusek D. Recent advancements in materials and coatings for biomedical implants. *Gels*. 2022;8(5):323. https://doi.org/10.3390/gels8050323

3. Pandey A., Awasthi A., Saxena K.K. Metallic implants with properties and latest production techniques: A review. *Advances in Materials and Processing Technologies*. 2020;6(2):405–440.
https://doi.org/10.1080/2374068X.2020.1731236

4. Biesiekierski A., Wang J., Gepreel M. A.-H., Wen C. A new look at biomedical Ti-based shape memory alloys. *Acta Bio-Materialia*. 2012;8(5):1661–1669.
https://doi.org/10.1016/j.actbio.2012.01.018

5. Zhao X., Zhang J., Song X., Guo W. Investigation on mechanical properties of laser welded joints for Ti–6Al–4V titanium alloy. *Materials Science and Technology*. 2013;29(12):1405–1413.
https://doi.org/10.1179/1743284713Y.00000003

6. Nune K.C., Misra R., Gai X., Li S.J., Hao Y.L. Surface nanotopography-induced favorable modulation of bioactivity and osteoconductive potential of anodized 3D printed Ti–6Al–4V alloy mesh structure. *Journal of Biomaterials Applications*. 2018;32(8):1032–1048.
https://doi.org/10.1177/0885328217748860

7. Navarro M., Michiardi A., Castaño O., Planell J.A. Biomaterials in orthopaedics. *Journal of the Royal Society Interface*. 2008;5(27):1137–1158.
https://doi.org/10.1098/rsif.2008.0151

8. Renganathan G., Tanneru N., Madurai S. L. Orthopedical and biomedical applications of titanium and zirconium metals. *Fundamental Biomaterials: Metals*. 2018:211–241.
https://doi.org/10.1016/B978-0-08-102205-4.00010-6

9. Alferi D., Fojt J., Kristianova E., Edwards D.W., Laasch H.-U. Influence of the manufacturing process on the corrosion and mechanical behavior of Esophageal stents. *Metals*. 2023;13(9):1542.
https://doi.org/10.3390/met13091542

10. Elsisy M., Chun Y. Materials properties and manufacturing processes of nitinol endovascular devices. In: *Bártolo, P.J., Bidanda, B. (eds) Bio-materials and prototyping applications in medicine*. Springer, Cham. 2021. P. 59–79.
https://doi.org/10.1007/978-3-030-35876-1_4

11. Stoeckel D., Bonsignore C., Duda S. A survey of stent designs. *Minimally Invasive Therapy & Allied Technologies*. 2002;11(4):137–147.
https://doi.org/10.1080/136457002760273340

12. Nasakina E.O., Sudarchikova M.A., Sergienko K.V., Konushkin S.V., Sevost'yanov M.A. Ion release and surface characterization of nanostructured nitinol during long-term testing. *Nanomaterials*. 2019;9(11):1569.
https://doi.org/10.3390/nano9111569

13. Zhang Y., Zhang Z.W., Xie Y.M., Wang S.S., Qiu Q.H., Zhou Y.L., Zeng G.H. Toxicity of nickel ions and comprehensive analysis of nickel ion-associated gene expression profiles in THP-1 cells. *Molecular Medicine Reports*. 2015;12(3):3273–3278.
https://doi.org/10.3892/mmr.2015.3878

14. Lü X., Bao X., Huang Y., Qu Y., Lu H., Lu Z. Mechanisms of cytotoxicity of nickel ions based on gene expression profiles. *Biomaterials*. 2009;30(2):141–148.
https://doi.org/10.1016/j.biomaterials.2008.09.011

15. Chen L.Y., Cui Y.W., Zhang L.C. Recent development in beta titanium alloys for biomedical applications. *Metals*. 2020;10(9):1139.
https://doi.org/10.3390/met10091139

16. Dobromyslov A.V., Elkin V.A. Martensitic transformation and metastable β-phase in binary titanium alloys with d-metals of 4–6 periods. *Scripta Materialia*. 2001;44(6):905–910.
https://doi.org/10.1016/S1359-6462(00)00694-1

17. Kim H.Y., Hashimoto S., Kim J.I., Inamura T., Hosoda H., Miyazaki S. Effect of Ta addition on shape memory behavior of Ti–22Nb alloy. *Materials Science and Engineering: A*. 2006;417(1-2):120–128.
https://doi.org/10.1016/j.msea.2005.10.065

18. Weinmann M., Schnitter C., Stenzel M., Markhoff J., Schulze C., Bader R. Development of bio-compatible refractory Ti/Nb(/Ta) alloys for application in patient-specific orthopaedic implants. *International Journal of Refractory Metals and Hard Materials*. 2018;75:126–136.
https://doi.org/10.1016/j.ijrmhm.2018.03.018

19. Miyazaki S., Kim H. Y., Hosoda H. Development and characterization of Ni-free Ti-base shape memory and superelastic alloys. *Materials Science and Engineering: A*. 2006;438–440:18–24.
https://doi.org/10.1016/j.msea.2006.02.054

20. Guehennec L. Surface treatments of titanium dental implants for rapid osseointegration. *Dental Materials*. 2007;23(7):844–854.
https://doi.org/10.4012/dmj.2012-015

21. Dubinskiy S.M., Prokoshkin S.D., Brailovski V., Inaekyan K.E., Korotitskiy A.V., Filonov M.R., Petrzhik M.I. Structure formation during thermomechanical processing of Ti-Nb-(Zr, Ta) alloys and the manifestation of the shape-memory effect. *The Physics of Metals and Metallography*. 2011;112(5):503–516.
https://doi.org/10.1134/S0031918X11050206

22. Liu J., Chang L., Liu H., Li Y., Yang H., Ruan J. Microstructure, mechanical behavior and biocompatibility of powder metallurgy Nb–Ti–Ta alloys as biomedical material. *Materials Science and Engineering: C*. 2017;71:512–519.
https://doi.org/10.1016/j.msec.2016.10.043

23. Hussein A.H., Gepreel M.A.H., Gouda M.K., Hefnawy A.M., Kandil S.H. Biocompatibility of new Ti–Nb–Ta base alloys. *Materials Science and Engineering: C*. 2016;61: 574–578. https://doi.org/10.1016/j.msec.2015.12.071

24. Zhou Y.L., Niinomi M., Akahori T. Effects of Ta content on Young's modulus and tensile properties of binary Ti–Ta alloys for biomedical applications. *Materials Science and Engineering: A*. 2004;371(1-2):283–290.
https://doi.org/10.1016/j.msea.2003.12.011

25. Cheng X., Liu S., Chen C., Chen W., Liu M., Li R., Zhang X., Zhou K. Microstructure and mechanical properties of additive manufactured porous Ti–33Nb–4Sn scaffolds for orthopaedic applications. *Journal of Materials Science: Materials in Medicine*. 2019;30:1–12.
https://doi.org/10.1007/s10856-019-6292-0

26. Li Y.H., Shang X.Y. Recent progress in porous TiNb-based alloys for biomedical implant applications. *Materials Science and Technology*. 2020;36(4):385–392.
https://doi.org/10.1080/02670836.2020.1724415

27. Zhao D., Chang K., Ebel T., Qian M., Willumeit R., Yan M., Pyczak F. Microstructure and mechanical behavior of metal injection molded Ti–Nb binary alloys as biomedical material. *Journal of the Mechanical Behavior*

of Biomedical Materials. 2013;28:171–182.
https://doi.org/10.1016/j.jmbbm.2013.08.013

28. Munir K., Lin J., Wright P. F., Ozan S., Li Y., Wen C. Mechanical, corrosion, nanotribological, and biocompatibility properties of equal channel angular pressed Ti–28Nb–35.4 Zr alloys for biomedical applications. *Acta Biomaterialia*. 2022;149:387–398.
https://doi.org/10.1016/j.actbio.2022.07.005

29. Li S., Choi M., Nam T. Effect of thermo-mechanical treatment on microstructural evolution and mechanical properties of a superelastic Ti–Zr-based shape memory alloy. *Materials Science and Engineering: A*. 2020;789:139664.
https://doi.org/10.1016/j.msea.2020.139664

30. Hussein M. A., Kumar M., Drew R., Al-Aqeeli N. Electrochemical corrosion and in vitro bioactivity of nanograined biomedical Ti–20Nb–13Zr alloy in a simulated body fluid. *Materials*. 2017;11(1):26.
https://doi.org/10.3390/ma11010026

31. Kim J. I., Kim H. Y., Inamura T., Hosoda H., Miyazaki S. Shape memory characteristics of Ti–22Nb–(2–8) Zr (at.%) biomedical alloys. *Materials Science and Engineering: A*. 2005;403(1-2):334–339.
https://doi.org/10.1016/j.msea.2005.05.050

32. Lykov A.P. Mesenchymal stem cells: properties and clinical application. *Sibirskiy nauchnyi meditsinskiy zhurnal*. 2023;43(2):40–53. (In Russ.).
https://doi.org/10.18699/SSMJ20230204

Лыков А.П. Мезенхимные стволовые клетки: свойства и клиническое применение. *Сибирский научный медицинский журнал*. 2023;43(2):40–53.
https://doi.org/10.18699/SSMJ20230204

33. Lanning B.R. Method for predicting wettability and interfacial bond strengths at metal/ceramic interfaces. Mines Theses & Dissertations. Ann Arbor: ProQuest LLC, 1990. 180 p.

34. Hebbar R.S., Isloor A.M., Ismail A.F. Chapter 12 – Contact angle measurements. In: *Membrane characterization.* Massachusetts: Elsevier Inc., 2019. P. 219–255.
https://doi.org/10.1016/B978-0-444-63776-5.00012-7

35. Decker E.L., Frank B., Suo Y., Garoff S. Physics of contact angle measurement. *Colloids and Surfaces A: Physicochemical and Engineering Aspects*. 1999;156(1-3):177–189.
https://doi.org/10.1016/S0927-7757(99)00069-2

36. Shurygina I.A., Shurygin M.G., Ayushinova N.I., Kanya O.V. Fibroblasts and their role in the development of connective tissue. *Baykal'skiy meditsinskiy zhurnal*. 2012;110(3):8–12. (In Russ.).

Шурыгина И.А., Шурыгин М.Г., Аюшинова Н.И., Каня О.В. Фибробласты и их роль в развитии соединительной ткани. *Байкальский медицинский журнал*. 2012;110(3):8–12.

37. Pavlova S.V., Sergeyevichev D.S., Chepeleva Ye.V., Kozyreva V.S., Malakhova A.A., Zakharova I.S., Zakiyan S.M. Comparison of mesenchymal stromal cells of the bone marrow and regional stem cells of the heart and human skin fibroblasts. *Patologiya krovoobrashcheniya i kardiokhirurgiya*. 2015;19(S4-2):12–19. (In Russ.).

Павлова С.В., Сергеевичев Д.С., Чепелева Е.В., Козырева В.С., Малахова А.А., Захарова И.С., Закиян С.М. Сравнение мезенхимальных стромальных клеток костного мозга и региональных стволовых клеток сердца и фибробластов кожи человека. *Патология кровообращения и кардиохирургия*. 2015;19(S4-2):12–19.

38. Nabatov A.A., Raginov I.S. The DC-SIGN-CD56 interaction inhibits the anti-dendritic cell cytotoxicity of CD56 expressing cells. *Infectious Agents and Cancer*. 2015(10):1–11.
https://doi.org/10.1186/s13027-015-0043-8

39. Dyakonov L.P., Akinshina G.T., Bilko N.M., Galnbek T.V. Animal cell in culture. Ed. 2nd updated. Moscow: Companiya Sputnik, 2009. 652 p. (In Russ.).

Дьяконов Л.П., Акиншина Г.Т., Билько Н.М., Гальнбек Т.В. Животная клетка в культуре. Изд. 2-е доп. М.: Компания Спутник, 2009. 652 с.

40. Lutfullin R.Ya., Trofimova Ye.A. Young's modulus of titanium alloy VT6S and its structural sensitivity. *Letters on Materials*. 2017;7(1):12–16. (In Russ.).
https://doi.org/10.22226/2410-3535-2017-1-12-16

Лутфуллин Р.Я., Трофимова Е.А. Нормальный модуль упругости титанового сплава ВТ6С и его чувствительность к изменению структуры. *Письма о материалах*. 2017;7(1):12–16.
https://doi.org/10.22226/2410-3535-2017-1-12-16

41. GOST R 8.982-2019. Titanium alloys grade VT. Sound velocity, relative thermal expansion, density and Young's modulus in the temperature range from 20 °C to 800 °C. Moscow: Standartinform, 2019. 20 p. (In Russ.).

ГОСТ Р 8.982-2019. Титановые сплавы марки ВТ. Скорость звука, относительное температурное расширение, плотность и модуль Юнга в диапазоне температур от 20 °C до 800 °C. М.: Стандартинформ, 2019. 20 с.

42. Wu D., Isaksson P., Ferguson S.J., Persson C. Young's modulus of trabecular bone at the tissue level: A review. *Acta Biomaterialia*. 2018;78:1–12.
https://doi.org/10.1016/j.actbio.2018.08.001

43. Terent'yev V.F., Slizov A.K., Smyslov A.M., Tamidarov D.R., Prosvirnin D.V., Penkin A.G., Shiryayev L.P., Sirotinkin V.P. Effect of electrolytic-plasma polishing on the mechanical properties of austenitic–martensitic VNS9-Sh TRIP steel. *Russian Metallurgy (Metally)*. 2020;2020(10):1199–1206.
https://doi.org/10.1134/S0036029520100286

Терентьев В.Ф., Слизов А.К., Смыслов А.М., Тамидаров Д.Р., Просвирнин Д.В., Пенкин А.Г., Ширяев Л.П., Сиротинкин В.П. Влияние электролитно-плазменной полировки на механические свойства аустенитно-мартенситной трип-стали ВНС9-Ш. *Деформация и разрушение материалов*. 2020;2:21–28.

44. Grodsky A.S., Kienskaya K.I., Gavrilova N.N., Nazarov V.V. Basic concepts and equations of colloidal chemistry. Moscow: RCTU named after D.I. Mendeleeva, 2013. 40 p. (In Russ.).

Гродский А.С., Киенская К.И., Гаврилова Н.Н., Назаров В.В. Основные понятия и уравнения коллоидной химии. М.: РХТУ им. Д.И. Менделеева, 2013. 40 с.

Information about the Authors

Maria A. Sudarchikova – Junior Research Scientist, Laboratory of Strength and Plasticity of Metal and Composite Materials and Nanomaterials, A.A. Baykov Institute of Metallurgy and Materials Science, Russian Academy of Sciences (IMET RAS)
ORCID: 0000-0001-9708-3284
E-mail: mariahsudar@yandex.ru

Elena O. Nasakina – Cand. Sci. (Eng.), Senior Research Scientist, Laboratory of Strength and Plasticity of Metal and Composite Materials and Nanomaterials, IMET RAS
ORCID: 0000-0002-0783-1558
E-mail: nacakina@mail.ru

Galina A. Davydova – Cand. Sci. (Phys.-Math.), Leading Research Scientist, Laboratory of Cell and Tissue Growth, Institute of Theoretical and Experimental Biophysics, Russian Academy of Sciences (ITEB RAS)
ORCID: 0000-0003-4215-7084
E-mail: davidova_g@mail.ru

Lenar R. Valiullin – Cand. Sci. (Biolog.), Head of the Laboratory of Probiotic Preparations and Enzymes, Federal Center for Toxicological, Radiation, and Biological Safety
ORCID: 0000-0002-8277-3941
E-mail: mariahsudar@yandex.ru

Yaroslava A. Morozova – Research Engineer, Laboratory of Strength and Plasticity of Metal and Composite Materials and Nanomaterials, IMET RAS
ORCID: 0000-0003-3526-5474
E-mail: yasya12987@gmail.com

Sergey Yu. Kottsov – Junior Research Scientist, Laboratory of Synthesis of Functional Materials and Processing of Mineral Raw Materials, N.S. Kurnakov Institute of General and Inorganic Chemistry, Russian Academy of Sciences
ORCID: 0000-0001-8263-889X
E-mail: mariahsudar@yandex.ru

Pavel A. Prokofiev – Cand. Sci. (Eng.), Junior Research Scientist, Laboratory of Physicochemistry of Refractory and Rare Metals and Alloys, IMET RAS
ORCID: 0000-0003-0477-0822
E-mail: nacakina@mail.ru

Sergey V. Konushkin – Cand. Sci. (Eng.), Research Scientist of the Laboratory of Strength and Plasticity of metal and composite materials and Nanomaterials, IMET RAS
ORCID: 0000-0002-4363-3604
E-mail: venev.55@mail.ru

Konstantin V. Sergienko – Junior Research Scientist, Laboratory of Strength and Plasticity of Metal and Composite Materials and Nanomaterials, IMET RAS
ORCID: 0000-0003-4018-4599
E-mail: shulf@yandex.ru

Mikhail A. Sevostyanov – Cand. Sci. (Eng.), Leading Research Scientist, Laboratory of Strength and Plasticity of Metal and Composite Materials and Nanomaterials, IMET RAS
ORCID: 0000-0003-2652-8711
E-mail: cmakp@mail.ru

Сведения об авторах

Мария Андреевна Сударчикова – мл. науч. сотрудник лаборатории прочности и пластичности металлических и композиционных материалов и наноматериалов, Институт металлургии и материаловедения им. А.А. Байкова Российской академии наук (ИМЕТ РАН)
ORCID: 0000-0001-9708-3284
E-mail: mariahsudar@yandex.ru

Елена Олеговна Насакина – к.т.н., ст. науч. сотрудник лаборатории прочности и пластичности металлических и композиционных материалов и наноматериалов, ИМЕТ РАН
ORCID: 0000-0002-0783-1558
E-mail: nacakina@mail.ru

Галина Анатольевна Давыдова – к.ф.-м.н., вед. науч. сотрудник лаборатории роста клеток и тканей, Институт теоретической и экспериментальной биофизики Российской академии наук (ИТЭБ РАН)
ORCID: 0000-0003-4215-7084
E-mail: davidova_g@mail.ru

Ленар Рашитович Валиуллин – к.б.н., заведующий лабораторией пробиотических препаратов и ферментов, Федеральный центр токсикологической, радиационной и биологической безопасности
ORCID: 0000-0002-8277-3941
E-mail: mariahsudar@yandex.ru

Ярослава Анатольевна Морозова – инженер-исследователь лаборатории прочности и пластичности металлических и композиционных материалов и наноматериалов, ИМЕТ РАН
ORCID: 0000-0003-3526-5474
E-mail: yasya12987@gmail.com

Сергей Юрьевич Котцов – мл. науч. сотрудник лаборатории синтеза функциональных материалов и переработки минерального сырья, Институт общей и неорганической химии имени Н.С. Курнакова Российской академии наук
ORCID: 0000-0001-8263-889X
E-mail: mariahsudar@yandex.ru

Павел Александрович Прокофьев – к.т.н., мл. науч. сотрудник лаборатории физикохимии тугоплавких и редких металлов и сплавов, ИМЕТ РАН
ORCID: 0000-0003-0477-0822
E-mail: nacakina@mail.ru

Сергей Викторович Конушкин – к.т.н., науч. сотрудник лаборатории прочности и пластичности металлических и композиционных материалов и наноматериалов, ИМЕТ РАН
ORCID: 0000-0002-4363-3604
E-mail: venev.55@mail.ru

Константин Владимирович Сергиенко – мл. науч. сотрудник лаборатории прочности и пластичности металлических и композиционных материалов и наноматериалов, ИМЕТ РАН
ORCID: 0000-0003-4018-4599
E-mail: shulf@yandex.ru

Михаил Анатольевич Севостьянов – к.т.н., вед. науч. сотрудник лаборатории прочности и пластичности металлических и композиционных материалов и наноматериалов, ИМЕТ РАН
ORCID: 0000-0003-2652-8711
E-mail: cmakp@mail.ru

Alexey G. Kolmakov – Dr. Sci. (Eng.), Corresponding Member of the Russian Academy of Sciences, Head of the Laboratory of Strength and Plasticity of Metal and Composite Materials and Nanomaterials, IMET RAS
ORCID: 0000-0002-4907-951X
E-mail: imetranlab10@mail.ru

Алексей Георгиевич Колмаков – д.т.н., чл.-корр. РАН, зав. лабораторией прочности и пластичности металлических и композиционных материалов и наноматериалов, ИМЕТ РАН
ORCID: 0000-0002-4907-951X
E-mail: imetranlab10@mail.ru

Contribution of the Authors

M. A. Sudarchikova – conducted surface roughness measurements, contributed to result discussions, and prepared documentation.
E. O. Nasakina – secured project financing, defined the study objectives, and processed research results.
G. A. Davydova – conducting research on mesenchymal stem cell cultures derived from human tooth pulp (DPSC) (clone Th44) and participated in result discussions.
L. R. Valiullin – conducting research on immortalized fibroblast cell cultures and skin mesenchymal stem cells, and contributed to result discussions.
Ya. A. Morozova – performed a literature review and prepared the article layout.
S. Yu. Kottsov – studied the contact angle of wettability of surfaces and participated in result discussions.
P. A. Prokofiev – prepared samples for research and contributed to result discussions.
S. V. Konushkin – performed smelting, rolling, and heat treatment of the alloys.
K. V. Sergienko – prepared sheets and cut samples using an electric discharge machine.
M. A. Sevostyanov – selected research methodologies and equipment.
A. G. Kolmakov – participated in result discussions.

Вклад авторов

М. А. Сударчикова – измерения шероховатости поверхности, обсуждение результатов, подготовка документации.
Е. О. Насакина – привлечение финансирования проекта, определение цели работы, обработка результатов исследований.
Г. А. Давыдова – проведение исследований на культурах МСК из пульпы зуба человека (DPSC) (клон Th44), обсуждение результатов.
Л. Р. Валиуллин – проведение исследований на иммортализованных культурах клеток фибробластов, МСК кожи, обсуждение результатов.
Я. А. Морозова – обзор литературы, оформление статьи.
С. Ю. Котцов – исследование краевого угла смачивания поверхностей, обсуждение результатов.
П. А. Прокофьев – подготовка образцов к исследованиям, обсуждение результатов.
С. В. Конушкин – выплавка, прокатка и термическая обработка сплавов.
К. В. Сергиенко – подготовка листов и резка образцов на электроэрозионном станке.
М. А. Севостьянов – выбор методики исследований и подбор оборудования.
А. Г. Колмаков – обсуждение результатов.

Received 29.05.2024
Revised 04.09.2024
Accepted 12.09.2024

Статья поступила 29.05.2024 г.
Доработана 04.09.2024 г.
Принята к публикации 12.09.2024 г.

Materials and Coatings Fabricated Using the Additive Manufacturing Technologies
Материалы и покрытия, получаемые методами аддитивных технологий

UDC 621.763
https://doi.org/10.17073/1997-308X-2024-6-77-88

Review article
Обзорная статья

Additive manufacturing of polymer-ceramic materials using fused deposition modeling (FDM) technology: A review

A. I. Zaytsev, A. V. Sotov, A. E. Abdrahmanova, A. A. Popovich

Peter the Great St.Petersburg Polytechnic University
29 Polytechnicheskaya Str., St.Petersburg 195251, Russia

zajtsev_ai2@spbstu.ru

Abstract. Additive manufacturing technologies, also known as 3D printing, are currently undergoing rapid development and gaining wide popularity, complementing and, in some cases, replacing traditional manufacturing methods. Particular attention is being paid to the fabrication of products from metallic, ceramic, polymeric, and composite materials. Among the seven commonly recognized methods of additive manufacturing, material extrusion stands out, which includes the Fused Deposition Modeling (FDM) technology. The heightened interest in FDM is due to the accessibility of equipment and the wide range of starting materials available, ranging from classic polymers such as PLA and PETG to composite materials, including metal- and ceramic-filled filaments. The objective of this study was to systematize and summarize the existing knowledge on the fabrication process of polymer-ceramic products using ceramic-filled filaments. The paper provides an analysis of the main stages of production, including material selection, filament fabrication, and the 3D printing process. Areas of research and potential applications are also examined.

Keywords: additive manufacturing, 3D-printing, FDM technology, polymer-ceramic materials, filled filament

Acknowledgements: This research was supported by a grant from the St. Petersburg Science Foundation, Agreement No 23-RB-0939.

For citation: Zaytsev A.I., Sotov A.V., Abdrahmanova A.E., Popovich A.A. Additive manufacturing of polymer-ceramic materials using fused deposition modeling (FDM) technology: A review. *Powder Metallurgy and Functional Coatings*. 2024;18(6):77–88. https://doi.org/10.17073/1997-308X-2024-6-77-88

Аддитивное производство полимер-керамических материалов методом послойного наплавления материала (FDM-технология): Обзор

А. И. Зайцев, А. В. Сотов, А. Э. Абдрахманова, А. А. Попович

Санкт-Петербургский политехнический университет Петра Великого
Россия, 195251, г. Санкт-Петербург, ул. Политехническая, 29

zajtsev_ai2@spbstu.ru

Аннотация. Технологии аддитивного производства, также известные как 3D-печать, находятся в фазе активного развития и набирают широкую популярность, заменяя и дополняя при этом традиционные способы производства. Особое внимание уделяется получению изделий из металлических, керамических, полимерных и композиционных материалов. Среди 7 общепринятых методов аддитивного производства отдельно выделяют экструзию материала (*material extrusion* – MEX), которая включает в себя технологию послойного наплавления материала (FDM). Повышенное внимание к ней объясняется доступностью оборудования и возможностью использования широкого спектра исходных материалов (от ставших классическими полимеров PLA, PETG и др. до композиционных материалов, в том числе метало- и керамонаполненных нитей). Цель настоящей работы заключалась в систематизации и обобщении существующих знаний о процессе изготовления полимер-керамических изделий с использованием керамонапо243ненных филаментов. Представлен анализ основных этапов производства, выбора исходных материалов, получения филамента и процесса 3D-печати. Рассмотрены области исследований и потенциальные сферы применения.

Ключевые слова: аддитивное производство, 3D-печать, FDM-технология, полимер-керамические материалы, наполненный филамент

Благодарности: Исследование выполнено за счет гранта Санкт-Петербургского научного фонда, договор № 23-РБ-0939.

Для цитирования: Зайцев А.И., Сотов А.В., Абдрахманова А.Э., Попович А.А. Аддитивное производство полимер-керамических материалов методом послойного наплавления материала (FDM-технология): Обзор. *Известия вузов. Порошковая металлургия и функциональные покрытия*. 2024;18(6):77–88. https://doi.org/10.17073/1997-308X-2024-6-77-88

Introduction

In recent decades, there has been significant growth in the development of new materials and manufacturing methods, driving the advancement of additive manufacturing (AM) technologies, also known as 3D printing. These are considered innovative fabrication processes capable of partially replacing or optimizing traditional manufacturing methods [1–4]. An advantage of AM is its ability to reduce material waste during production by building products with diverse geometries layer by layer. This approach allows for creating complex shapes in a single technological process. AM technologies enable scientists and engineers to drive unique innovations through the use of advanced materials and cutting-edge solutions [5–9]. One of these innovations is the implementation of AM processes for producing polymer-ceramic materials [10]. Interest in these materials is driven by the combined benefits of polymers and ceramics: the manufacturing flexibility of polymers and the unique properties of ceramics, such as high strength, hardness, and electrical characteristics.

This review provides a detailed examination of the process for fabricating polymer-ceramic composites (PCC) using FDM (Fused Deposition Modeling) technology (see Fig. 1). An overview of the 3D printing method for polymer-ceramic materials is presented, along with an analysis of the process for obtaining ceramic-filled filament. The specifics of FDM printing with these materials are described, current trends in research and manufacturing of PCCs by 3D printing are highlighted, and conclusions are drawn on the current state of FDM printing with polymer-ceramic materials.

3D printing with polymer-ceramic materials

The production of polymer-ceramic products is advancing, driven by developments in new materials, designs, and components for functional applications. A well-established traditional manufacturing method for these materials is injection molding [11–13]. Among the AM methods used for producing PCC, FDM and stereolithography (SLA) [14–17] are widely applied, along with other technologies [18; 19].

The FDM method has been in use since the late 20th century when the U.S. company Stratasys patented it as “Fused Deposition Modeling” [20; 21]. This method works by sequentially depositing layers of filament, heated to a viscoelastic state, through a nozzle to build up the product layer by layer [22]. Today, many commercially available machines are based on this technology, commonly as desktop systems that

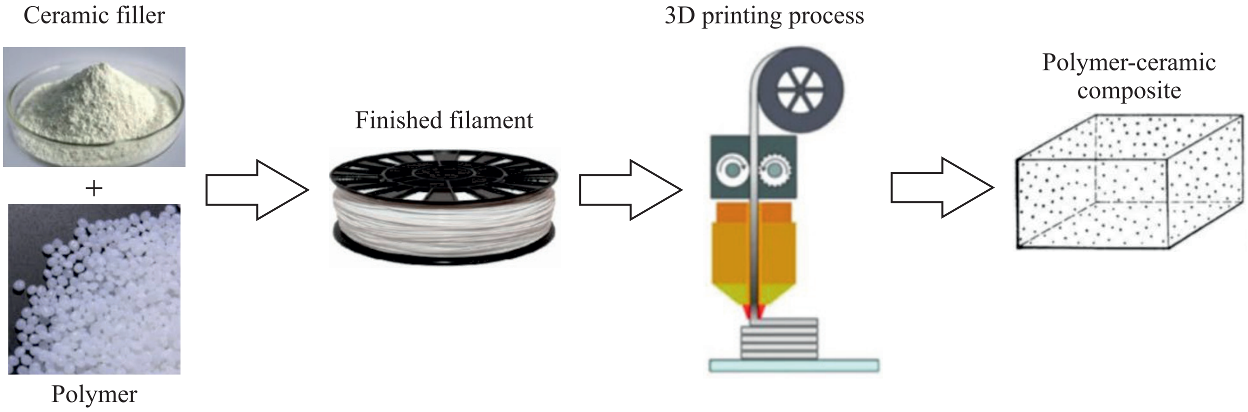

Fig. 1. Key stages in ceramic-filled filament production, from raw material selection to final product

Рис. 1. Основные стадии производства керамонаполненного филамента: от выбора сырья до конечного изделия construct products within the build platform's plane. FDM printers are classified by their material feeding systems, which vary by feeder placement:

– direct extruder, where the feeder is attached directly to the print head;

– bowden extruder, where the feeder is mounted on the printer's frame, and the material is channeled to the print head via a tube [23–25].

Direct extruders are preferred for flexible, brittle, and composite materials as they reduce the risk of nozzle clogging and polymer deformation in the feeding channel during printing.

In FDM technology, polymer filaments of varying diameters, tailored to equipment specifications, are used as feedstock. Currently, many manufacturers offer both standard 3D printing polymers and advanced materials with improved compositions that provide better mechanical strength, wear resistance, shape memory, and higher operating temperatures. Research continues to enhance existing thermoplastic filaments for FDM printing and develop new formulations with improved properties based on various material types [26–28].

Key aspects of producing ceramic-filled filament

Filament production is a crucial step in the fabrication of PCC, as it significantly influences the properties of the final products and affects the entire production cycle – from 3D printing to the finished item.

In the initial stage, the matrix material and functional filler are selected according to the desired characteristics of the final product. The polymer matrix is typically made from common thermoplastic materials used in FDM printing, such as polylactic acid (PLA) [29; 30], acrylonitrile butadiene styrene (ABS) [31; 32], and, less frequently, polyethylene terephthalate glycol (PETG) [33; 34] and polyamide-12 (PA12) [35; 36]. Ceramic fillers often include technical ceramics, such as aluminum oxide (Al_2O_3), silicon dioxide (SiO_2), zirconium oxide (ZrO_2), titanium oxide (TiO_2), and silicon carbide (SiC) [12; 37]. These materials are widely used due to their unique physical, mechanical, electrical, and thermal properties. In addition, piezoceramic powders – such as barium titanate ($BaTiO_3$) and barium strontium titanate ($BaSrTiO_3$) – are used to enhance electrical properties. During material selection, the particle size of the ceramic powder is also determined, as it affects both the properties of the PCC and the quality of 3D printing. Table 1 presents different combinations of ceramic-filled filament materials, including commercially available options and those developed in research studies.

Following the selection of the raw material composition, the next steps are PCC preparation and filament production. The primary stages of this process include creating the composite mixture and manufacturing the ceramic-filled filament for 3D printing. Preparation and intermediate steps often involve moisture removal from the initial materials. Additionally, various additives such as acetone, stearic acid, and others are used to enhance the adhesion of ceramic particles to the polymer and to improve dispersion (see Table 1).

This filament production process is detailed in numerous studies by various research teams. For example, in [40], researchers from the Institute of Nanoscience and Nanotechnology, N.C.S.R. Demokritos (Greece) produced composite filament from PLA granules (Gorinchem, Netherlands) as the matrix, combined with SiC powder (particle size 8.3 μm) (Struers, Denmark). The polymer granules were pre-dried and then mixed with the ceramic powder. Acetone was added to enhance adhesion between the granules and ceramic particles. The prepared mixture was then dried (100 °C for 24 h). The resulting raw material was processed through a single-screw extruder (Felfil Evo, Italy) at 185–195 °C, yielding five types of composite filaments with a diameter of 1.75 mm and varying SiC content (from 1 to 3 wt. %).

A similar combination of materials was chosen by a team of researchers from the Department of Mechanical Engineering at Stevens Institute of Technology, New Jersey, USA [39]. However, instead of polymer granules, PLA (74 μm) and SiC (15 μm) powders were used as the starting materials. Before further processing, the materials were pre-dried at 70 °C for 4 h. Mixing was conducted in a rotary tumbler using chromium steel balls. Filament production was carried out on a single-screw extruder. To further study the dispersion of SiC in PLA, filament samples containing 50 wt. % SiC were analyzed. Based on image analysis (Fig. 2), it was concluded that SiC particles were adequately dispersed within the PLA matrix. This is supported by scanning electron microscopy (SEM) images showing a substantial reduction in ceramic powder particle size from the initial 15 μm to approximately 5 μm during mixing.

A similar filament fabrication method was used in [45], where researchers from the Czech Technical University in Prague (Department of Electrotechnology, Faculty of Electrical Engineering) employed PETG granules and TiO_2 powder (50–300 μm) as starting materials. Filaments with varying TiO_2 content were produced for the study. In two cases, PETG was filled with titanium dioxide (10 and 20 wt. %) to increase

Table 1. **Results of analyzing the process of producing ceramic-filled filament**

Таблица 1. **Результаты анализа процесса получения керамонаполненного филамента**

Polymer	Ceramic	Brief description of filament extrusion technology	Source
PLA	ZrO_2	Material by Zetamix, France	[38]
	SiC	*Starting materials*: PLA powder (74 µm) and SiC powder (15 µm). The powders were dried at 70 °C for 4 h, then mixed in a rotary tumbler at 64 rpm with steel balls for better dispersion. A single-screw extruder was used to produce filament. Melt temperature was 180 °C, and screw speed was 35 rpm. Various filaments were produced with SiC contents of 10, 20, 30, and 40 wt. %. Comparison was made with pure PLA and PLA with added graphite (C) or a SiC + C mix	[39]
		Starting materials: PLA granules and SiC powder (8.3 µm). PLA granules were dried at 100 °C for 24 h, then mixed at 75 °C with added acetone. The resulting mixture was dried at 100 °C for 24 h. Filament was produced using a single-screw extruder. Extrusion temperature was 185–195 °C, and extrusion speed was 50 cm/min. Five composite types were obtained with SiC contents of 1.0, 1.5, 2.0, 2.5, and 3.0 wt. %	[40]
	Si_3N_4	Ceramic-filled filament made of PLA/Si_3N_4 in a mass ratio of 95/5 using a twin-screw extruder	[12]
ABS	$BaSrTiO_3$	*Starting materials:* ABS granules and $BaSrTiO_3$ ceramic powder. ABS granules were dissolved in acetone at a 1:1.5 mass ratio. The mixture was blended with the ceramic powder, poured into molds, and dried at room temperature for 48 h. The resulting composites were granulated and dried at 80 °C for 48 h. Filament production was carried out using an extruder at 220 °C and 60 rpm. The maximum ceramic powder content reached 50.27 wt. %	[41]
	$BaTiO_3$	*Starting materials:* ABS granules and $BaTiO_3$ ceramic powder (3 µm). ABS granules were mixed with $BaTiO_3$ particles in volume ratios of 10, 20, 30, 35, 40, 45, and 50 %, with 1.1 wt. % stearic acid added as a surfactant. The raw material was dried for 24 h at 130 °C. Filament was produced using a Noztek Pro single-screw extruder (UK) at temperatures between 185 and 210 °C	[42]
		Starting materials: ABS granules and $BaTiO_3$ microparticles (<3 µm). ABS granules were dissolved in acetone, then barium titanate was added. The resulting suspension was placed in molds to allow acetone evaporation. Solidified composite sheets were ground and dried at 70 °C. Filament production was carried out using a Noztek Pro single-screw extruder at 190÷210 °C	[43]
		Starting materials: ABS granules and $BaTiO_3$ microparticles. Octyl gallate and dibutyl phthalate were used as surfactants and plasticizers. Filament production was based on the previous work of Castles F. et al. [43].	[44]
PETG	TiO_2	Ceramic-filled filament prepared in collaboration with Prusa Polymers, Czech Republic. *Starting materials*: PETG granules and TiO_2 particles (50–300 µm). PETG granules were mixed with ceramic particles and melted for homogenization. Composite filaments with TiO_2 contents of 10 and 20 wt. % were produced using a screw extruder	[45]
PA12	ZrO_2 Al_2O_3	*Starting materials*: PA12 granules, Al_2O_3, and ZrO_2 powders. A two-step surface modification of the ceramic powders was conducted: etching and chemical treatment. Preliminary drying: PA12 at 50 °C for 10 h, ceramic powders at 150 °C. Compounding was done with a twin-screw extruder, and filament production used a single-screw extruder (Dr. Collin GmbH, Germany)	[46]
PMMA	ZrO_2	*Starting materials:* PMMA and ZrO_2 nanoparticles (20–80 nm). Preliminary drying was conducted at 100 °C for 2 h. Filament production was performed using a Haake Rheomix 252p single-screw extruder (Thermo Fisher Scientific, USA)	[47]

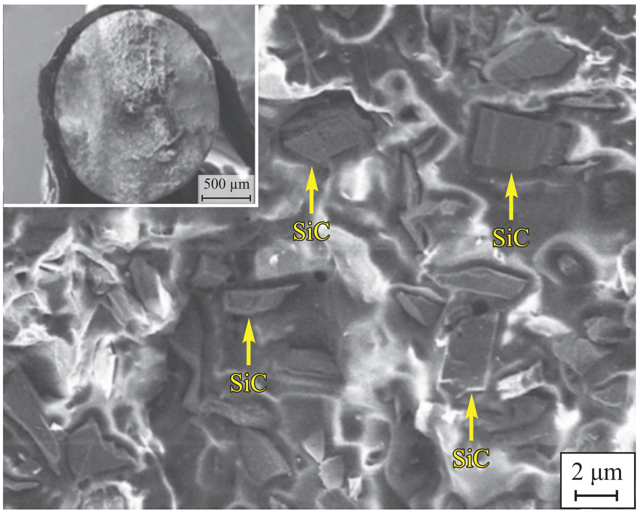

Fig. 2. SEM image of the cross-section of PLA-based ceramic filament containing 50 wt. % SiC [39]

Рис. 2. СЭМ-изображение поперечного сечения керамического филамента на основе PLA с содержанием SiC 50 мас. % [39]

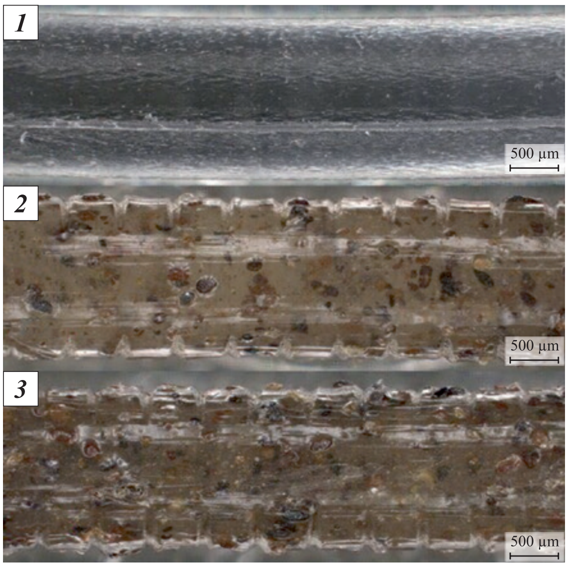

Fig. 3. Microscope images of filaments produced [45]

1 – pure PETG; *2* – PETG + 10 wt. % TiO_2;
3 – PETG + 20 wt. % TiO_2

Рис. 3. Изображения филаментов, полученные с помощью микроскопа [45]

1 – чистый PETG; *2* – PETG + 10 мас. % TiO_2;
3 – PETG + 20 мас. % TiO_2

dielectric permittivity, while a third filament was composed of pure PETG (Fig. 3).

The specifics of the process can depend on the methods used to prepare the composite mixture based on the starting components. For instance, study [41] describes a method of producing a polymer-ceramic composite that differs from previous approaches. Researchers in the United Kingdom mixed ABS granules with acetone, dissolving the polymer to create a viscous mixture. To this solution, they added piezoceramic $BaSrTiO_3$ powder (particle size <0.5 μm) and mixed for 10 min. The resulting composite mixtures were poured into specialized molds, where complete solidification occurred over 48 h. The composites were then subjected to mechanical granulation, additional drying, and extrusion to produce filament.

Thus, the analysis presented in this section reflects the essence of producing ceramic-filled filament using various technological methods and materials. This approach is adaptable for working with different combinations of polymer and ceramic compositions, making it one of the most versatile and widely used methods.

3D printing process features

The process of 3D printing with ceramic-filled filaments involves several technological considerations, linked both to equipment specifics and the challenges of working with filled, particularly high-filled, polymers. The particles in the filament increase its brittleness, which can lead to nozzle clogging and filament breakage during printing [48; 49]. Addressing these and other issues in PCC 3D printing is feasible by maintaining optimal conditions, including print temperature, speed, layer height, and feed rate, among others [50–53] (Table 2).

Study [54] explores key FDM printing parameters, including printing speed, track width, layer height, and infill structure (Fig. 4), and examines their effects on the dielectric properties and quality of printed items. The findings indicate that printing speed significantly influences interlayer adhesion and bonding to the build platform. As shown in Fig. 4, *a*, printing speed has a notable impact on surface quality and pore formation, both of which directly affect the final properties of the printed products. A speed range of 10–20 mm/s provided the best print quality, with no visible defects.

Samples were prepared using the specified parameters to measure dielectric characteristics. Results indicated a significant decrease in dielectric permittivity ($\varepsilon_r = 7.38$) compared to a sample produced by injection molding ($\varepsilon_r = 10$). To identify the cause of this discrepancy, surface analysis was conducted using an optical microscope, which revealed air gaps between the print tracks. The solution involved reducing the extrusion width from 0.5 to 0.45 mm (Fig. 4, *c*), which helped increase relative dielectric permittivity and reduce the dielectric loss tangent. Additionally, the influence of layer height on dielectric

Table 2. **Key parameters of FDM printing with ceramic filaments**

Таблица 2. **Основные параметры FDM-печати керамонаполненными филаментами**

Material	Ceramic content, wt. %	Print temperature, °C	Print speed, mm/s	Nozzle diameter, mm	Layer height, mm	Source
PLA/ZrO_2	86	190	40	0.60	0.20	[38]
ABS/$BaSrTiO_3$	50	250	40	0.55	0.10	[41]
PETG/TiO_2	10 and 20	250	–	0.40	0.15	[45]
PLA/Si_3N_4	5, 10 and 15	200	40	0.40	0.15	[12]
PLA/SiC	1–3	200–210	50	1.00	–	[40]
ABS/Ceramic (Premix Oy)	–	260	10–20	0.50	0.30	[54]

characteristics was studied (Fig. 4, *d*), showing that dielectric properties improve as layer height increases. It was also found that adjusting the material infill allows effective control over the dielectric properties of 3D-printed structures (Fig. 4, *e*).

Many studies use commercially available desktop FDM printers. For example, in [45], samples of PETG polymer filled with TiO_2 particles (10 and 20 wt. %) were produced using the I3 MK3S 3D printer by PRUSA Research (Czech Republic), which is equipped with a direct extruder. A 0.4 mm nozzle was used to print samples with a 0.15 mm layer thickness and 100 % infill rate, ensuring high density and minimizing porosity. In study [38], equipment from the same company was selected for fabricating samples from various materials, including PLA with 50 % ZrO_2 particles and polyolefin with different levels of TiO. In this case, a 0.6 mm nozzle was used, with a layer height of 0.2 mm.

An analysis of published studies shows that larger-diameter nozzles are frequently used due to the specific challenges of printing with filled polymers, which can

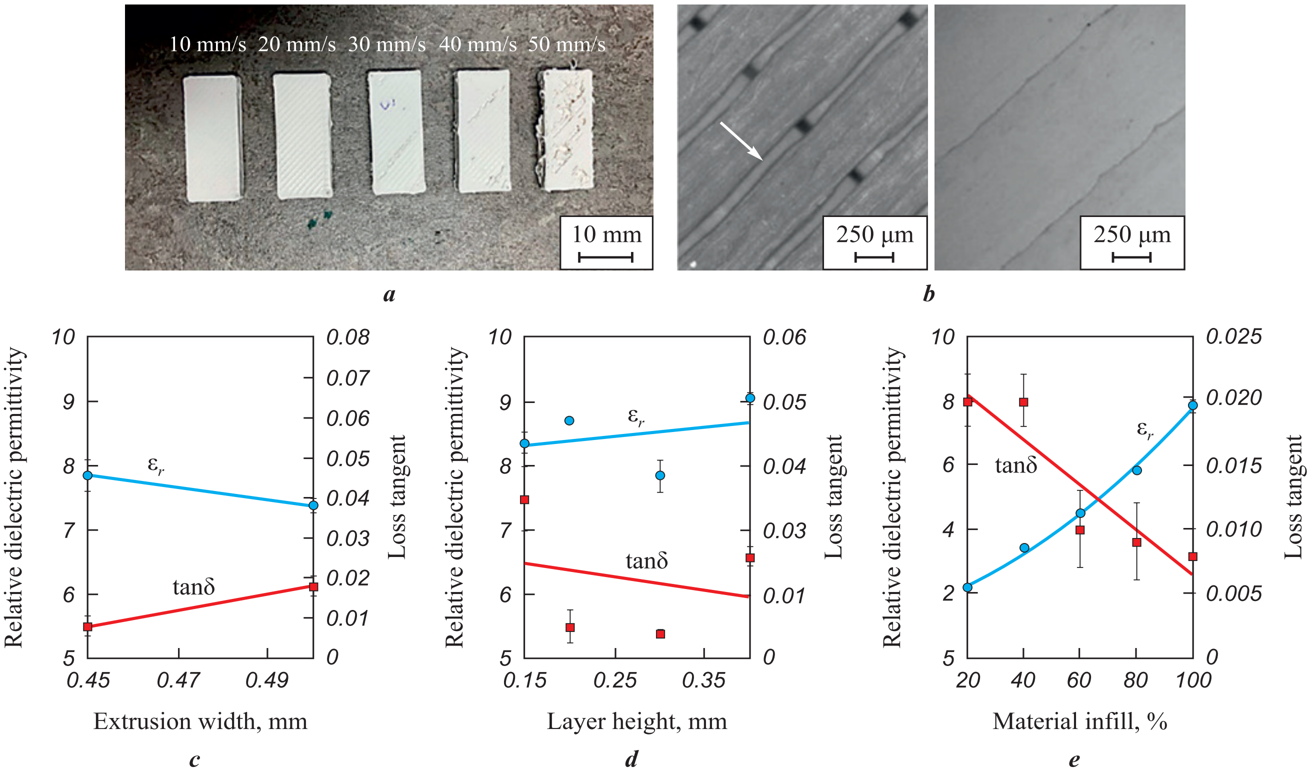

Fig. 4. Research results on the influence of printing parameters on sample quality and dielectric properties [54]

a – influence of printing speed on sample quality; ***b*** and ***c*** – influence of extrusion width on track spacing and dielectric properties; ***d*** and ***e*** – layer height and material infill on dielectric properties

Рис. 4. Результаты исследования влияния параметров печати на качество образцов и диэлектрические свойства [54]

a – влияние скорости печати на качество образцов; ***b*** и ***c*** – влияние ширины экструзии на расстояние между треками и диэлектрические свойства; ***d*** и ***e*** – влияние высоты слоя и коэффициента заполнения на диэлектрические свойства gradually clog the nozzle. Brass nozzles, commonly used in FDM printing, are prone to rapid wear when exposed to ceramic particles, prompting researchers to opt for wear-resistant nozzles. Additionally, nozzle diameter affects the uniformity of material extrusion; increasing the diameter can help reduce the risk of defects (such as pores and cracks) caused by material inconsistencies.

Applications

Research on products made from polymer-ceramic filaments can be grouped into three main areas:

– improving dielectric properties;

– investigating the impact of ceramic fillers on mechanical properties;

– producing ceramic components from high-filled polymer-ceramic filaments.

A significant portion of research on PCC development using FDM printers focuses on dielectric properties, driven by the ease of fabrication, the broad range of applications, and the growth of 3D-printed electronics. Polymers produced by 3D printing are commonly used as insulators [55]. However, adding conductive carbon fibers or metal particles enables the production of functional parts that conduct electricity [56; 57], while incorporating ceramic powder into the polymer matrix improves dielectric properties. Studies have investigated the effects of TiO_2, ZrO_2, $BaSrTiO_3$ and other ceramic fillers on the dielectric properties of polymer-ceramic samples for application in capacitors, dielectric antennas, and other components that require dielectric materials.

As mentioned in [45], researchers in the Czech Republic investigated PCC made with PETG polymer and TiO_2 ceramic powder. The study involved testing cylindrical samples of different diameters (19.1 and 9.5 mm) and thicknesses (2.8 and 3.0 mm) to assess the dielectric properties of PCC. The sample with 20 wt. % TiO_2 yielded the best results, showing a 50 % increase in dielectric permittivity compared to pure PETG, reaching a maximum value of 4.4. The study found that temperature and frequency had no significant effect on dielectric permittivity or dielectric losses.

In addition to examining the dielectric properties of printed samples, research also explores the potential applications of 3D-printed polymer-ceramic dielectrics in electronic and radio equipment. A team of researchers from the United Kingdom studied PCC properties in [41], using a material based on ABS and $BaSrTiO_3$ powder in a 50/50 weight ratio, which achieved a maximum relative dielectric permittivity ε_r of 6,05. The study also developed a prototype patch antenna (Fig. 5) incorporating a semi-spherical polymer-ceramic dielectric lens. This lens increased the antenna gain by 3.86 dB, with minimal impact on efficiency.

In addition to studies on the dielectric properties of PLA-based polymer-ceramic composites, research is also focused on the impact of ceramic additives on the mechanical strength of the material. In [12], the results of mechanical testing on PLA samples reinforced with Si_3N_4 powder are presented. The researchers compared samples produced by injection molding with those printed on an FDM printer. For the injection-molded samples, three series were prepared with different polymer/ceramic weight ratios (85/15, 90/10, 95/05). Based on mechanical testing results, a 95/05 ratio was chosen for further studies. These samples showed better adhesion and fewer defects, resulting in higher strength values. Using this selected ratio, the mechanical properties of samples produced by both methods were compared. The results indicated that printed samples exhibited reductions in tensile strength, flexural strength, and impact toughness by 12,0, 15.5, and 13.5 %, respectively.

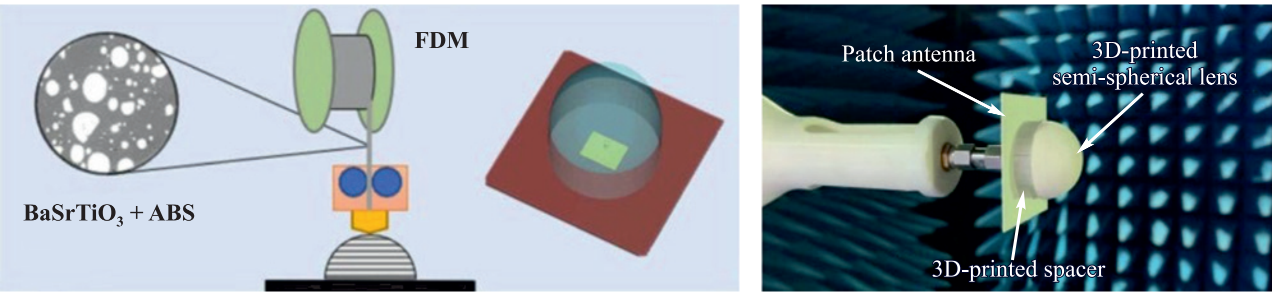

a *b*

Fig. 5. Prototype of the patch antenna

a – process diagram for producing epy polymer-ceramic dielectric lens; ***b*** – appearance of the finished antenna [41]

Рис. 5. Прототип патч-антенны

a – схема получения полимер-керамической диэлектрической линзы; ***b*** – внешний вид готовой антенны [41]

One of the less explored but promising areas in PCC research is the investigation of how ceramic particles affect shape memory effect (SME). It is known that many polymers used in FDM printing can exhibit SME, generally triggered by thermal stimulation [58–61]. Study [39] examined the influence of SiC additives in a PLA matrix on shape recovery characteristics. Results showed that recovery time could be influenced by the thermal conductivity of the material. Tests were conducted on extruded filaments (Fig. 6) and printed samples, revealing that SiC-filled composites recovered shape faster than pure PLA material.

Thus, producing polymer-ceramic composites using FDM technology is an emerging field with several challenges and limitations. Key strategies to address issues such as defect formation (pores, cracks) involve a comprehensive approach that includes achieving an optimal filament composition and selecting appropriate printing parameters.

However, not all issues regarding material homogeneity and defect formation during printing have been resolved. Aspects like the effects of heat treatment and mechanical stresses that occur during printing on product quality and final properties remain insufficiently studied and require further research. These challenges provide a scientific basis for continued study of PCCs and their potential applications in future products.

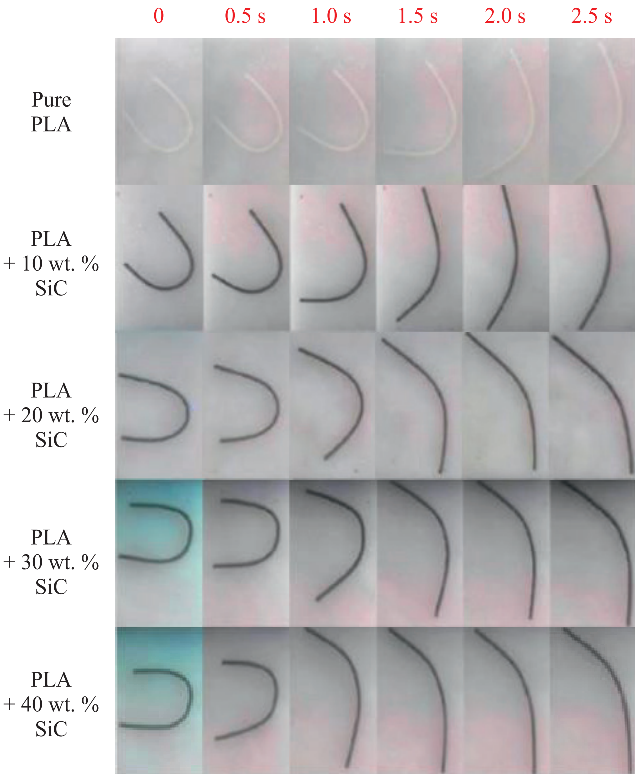

Fig. 6. Images of ceramic-filled filaments showing shape recovery [39]

Рис. 6. Изображения, полученные для керамонаполненных филаментов, показывающие восстановление формы [39]

Conclusion

A detailed analysis of the production of polymer-ceramic composites using FDM printing has been presented, covering key technological stages – from raw material selection to final product creation. A review of scientific publications highlights the most commonly used ceramic additives, such as SiC, ZrO_2, $BaTiO_3$ and others. The use of these fillers improves dielectric permittivity, mechanical strength, and affects the activation time of the shape memory effect. This makes ceramic filaments suitable for creating dielectric components in electronic and radio-frequency systems, sensors, structural elements, and shape-memory products.

The review provides a foundation for further research in the development and study of 3D-printed PCCs. Future work will focus on producing 3D-printed volumetric PCC items with enhanced dielectric permittivity.

References / Список литературы

1. Bhatia A., Sehgal A.K. Additive manufacturing materials, methods and applications: A review. *Materials Today: Proceedings*. 2023;81:1060–1067. https://doi.org/10.1016/j.matpr.2021.04.379
2. Pereira T., Kennedy J.V., Potgieter J. A comparison of traditional manufacturing vs additive manufacturing, the best method for the job. *Procedia Manufacturing*. 2019; 30:11–18. https://doi.org/10.1016/j.promfg.2019.02.003
3. Attaran M. The rise of 3-D printing: The advantages of additive manufacturing over traditional manufacturing. *Business Horizons*. 2017;60(5):677–688. https://doi.org/10.1016/j.bushor.2017.05.011
4. Kanishka K., Acherjee B. Revolutionizing manufacturing: A comprehensive overview of additive manufacturing processes, materials, developments, and challenges. *Journal of Manufacturing Processes*. 2023;107:574–619. https://doi.org/10.1016/j.jmapro.2023.10.024
5. Hajare D.M., Gajbhiye T.S. Additive manufacturing (3D printing): Recent progress on advancement of materials and challenges. *Materials Today: Proceedings*. 2022;58: 736–743. https://doi.org/10.1016/j.matpr.2022.02.391
6. Hasanov S., Alkunte S., Rajeshirke M., Gupta A., Huseynov O., Fidan I., Alifui-Segbaya F., Rennie A. Review on additive manufacturing of multi-material parts: progress and challenges. *Journal of Manufacturing and Materials Processing*. 2022;6(1):4. https://doi.org/10.3390/jmmp6010004
7. Mehrpouya M., Dehghanghadikolaei A., Fotovvati B., Vosooghnia A., Emamian S.S., Gisario A. The potential of additive manufacturing in the smart factory industrial

4.0: A review. *Applied Sciences*. 2019;9(18):3865.
https://doi.org/10.3390/app9183865

8. Martinelli A., Mina A., Moggi M. The enabling technologies of industry 4.0: examining the seeds of the fourth industrial revolution. *Industrial and Corporate Change*. 2021;30(1):161–188. https://doi.org/10.1093/icc/dtaa060

9. Sotov A.V., Zaytsev A.I., Abdrahmanova A.E., Popovich A.A. Additive manufacturing of continuous fibre reinforced polymer composites using industrial robots: A review. *Powder Metallurgy and Functional Coatings*. 2024;18(1):20–30.
https://doi.org/10.17073/1997-308X-2024-1-20-30

Сотов А.В., Зайцев А.И., Абдрахманова А.Э., Попович А.А. Аддитивное производство непрерывно армированных полимерных композитов с использованием промышленных роботов: Обзор. Известия вузов. *Порошковая металлургия и функциональные покрытия*. 2024;18(1):20–30.
https://doi.org/10.17073/1997-308X-2024-1-20-30

10. Kumar R., Singh R., Hashmi M.S. J. Polymer-ceramic composites: A state of art review and future applications. *Advances in Materials and Processing Technologies*. 2022;8(1):895–908.
https://doi.org/10.1080/2374068X.2020.1835013

11. Czepiel M., Bańkosz M., Sobczak-Kupiec A. Advanced injection molding methods. *Materials*. 2023;16(17):5802.
https://doi.org/10.3390/ma16175802

12. John L.K., Ramu M., Singamneni S., Binudas N. Strength evaluation of polymer ceramic composites: a comparative study between injection molding and fused filament fabrication techniques. *Progress in Additive Manufacturing*. 2024;1–9. https://doi.org/10.1007/s40964-024-00626-9

13. Fu H., Xu H., Liu Y., Yang,Z., Kormakov S., Wu D., Sun J. Overview of injection molding technology for processing polymers and their composites. *ES Materials & Manufacturing*. 2020;8(20):3–23.
http://dx.doi.org/10.30919/esmm5f713

14. Li W.D., Wang C., Yin H.Y., Deng J.B., Mu H.B., Zhang G.J., Chen Y., Song F.L., Chen Y.L. Additive manufacturing of polymer-matrix composite dielectric materials using stereolithography technique. In: *International Conference on Electrical Materials and Power Equipment (ICEMPE). IEEE*. 2021. P. 1–4.
https://doi.org/10.1109/ICEMPE51623.2021.9509221

15. Colella R., Chietera F. P., Montagna F., Greco A., Catarinucci L. Customizing 3D-printing for electromagnetics to design enhanced RFID antennas. *IEEE Journal of Radio Frequency Identification*. 2020;4(4):452–460.
https://doi.org/10.1109/JRFID.2020.3001043

16. Colella R., Chietera F.P., Catarinucci L. Analysis of FDM and DLP 3D-printing technologies to prototype electromagnetic devices for RFID applications. *Sensors*. 2021; 21(3):897. https://doi.org/10.3390/s21030897

17. Edhere E.S. 3D-printing of dielectric antennas through digital light processing. Master’s thesis. North Carolina Agricultural and Technical State University, 2022.

18. Chueh Y.H., Zhang X., Wei C., Sun Z., Li L. Additive manufacturing of polymer-metal/ceramic functionally graded composite components via multiple material laser powder bed fusion. *Journal of Manufacturing Science and Engineering*. 2020;142(5):051003.
https://doi.org/10.1115/1.4046594

19. Chaudhary R.P., Parameswaran C., Idrees M., Rasaki A.S., Liu C., Chen Z., Colombo P. Additive manufacturing of polymer-derived ceramics: Materials, technologies, properties and potential applications. *Progress in Materials Science*. 2022;128:100969.
https://doi.org/10.1016/j.pmatsci.2022.100969

20. Lalegani Dezaki M., Mohd Ariffin M.K.A., Hatami S. An overview of fused deposition modelling (FDM): Research, development and process optimization. *Rapid Prototyping Journal*. 2021;27(3):562–582.
https://doi.org/10.1108/RPJ-08-2019-0230

21. Gibson I., Rosen D.W., Stucker B., Khorasani M., Rosen D., Stucker B., Khorasani M. Additive manufacturing technologies. Cham, Switzerland: Springer, 2021.
https://doi.org/10.1007/978-3-030-56127-7

22. GOST 59100-2020. Plastics. Filaments for additive technologies. Moscow: Standartinform, 2020.

ГОСТ Р 59100-2020 Пластмассы. Филаменты для аддитивных технологий. Общие технические требования. М.: Стандартинформ, 2020.

23. Patel A., Taufik M. Extrusion-based technology in additive manufacturing: a comprehensive review. *Arabian Journal for Science and Engineering*. 2024;49(2):1309–1342.
https://doi.org/10.1007/s13369-022-07539-1

24. Moetazedian A., Budisuharto A.S., Silberschmidt V.V., Gleadall A. CONVEX (CONtinuously Varied EXtrusion): a new scale of design for additive manufacturing. *Additive Manufacturing*. 2021;37:101576.
https://doi.org/10.1016/j.addma.2020.101576

25. Azhar M.A.M., Sukindar N.A., Ani M.H., Anuar H.B., Kamaruddin S.B., Shaharuddin S.I.S., Mustafa M.Y., Adesta E.Y.T., Arief R.K., Sulaiman M.H. Review on fused deposition modelling extruder types with their specialities in filament extrusion process. In: *Advances in Manufacturing and Materials Engineering: ICAMME 2022* (5th Intern. Conf. on Mechanical Engineering, Kuala Lumpur, Malaysia 9–10 August). Singapore: Springer, 2023. P. 407–413.
https://doi.org/10.1007/978-981-19-9509-5_54

26. Krajangsawasdi N., Blok L.G,. Hamerton I., Longana M.L., Woods B.K.S., Ivanov D.S. Fused deposition modelling of fibre reinforced polymer composites: A parametric review. *Journal of Composites Science*. 2021; 5(1):29. https://doi.org/10.3390/jcs5010029

27. Kantaros A., Soulis E., Petrescu F.I.T., Ganetsos T. Advanced composite materials utilized in FDM/FFF 3D printing manufacturing processes: The case of filled filaments. *Materials*. 2023;16(18):6210.
https://doi.org/10.3390/ma16186210

28. Wickramasinghe S., Do T., Tran P. FDM-based 3D printing of polymer and associated composite: A review on mechanical properties, defects and treatments. *Polymers*. 2020;12(7):1529.
https://doi.org/10.3390/polym12071529

29. Yang L., Li S., Li Y., Yang M., Yuan Q. Experimental investigations for optimizing the extrusion parameters on FDM PLA printed parts. *Journal of Materials Engineering and Performance*. 2019;28:169–182.
https://doi.org/10.1007/s11665-018-3784-x

30. Valerga A.P., Batista M., Salguero J., Girot F. Influence of PLA filament conditions on characteristics of FDM parts. *Materials*. 2018;11(8):1322.
http://dx.doi.org/10.3390/ma11081322

31. Samykano M., Selvamani S.K., Kadirgama K., Ngui W.K., Kanagaraj G., Sudhakar K. Mechanical property of FDM printed ABS: Influence of printing parameters. *The International Journal of Advanced Manufacturing Technology*. 2019;102:2779–2796.
https://doi.org/10.1007/s00170-019-03313-0

32. Rodríguez-Panes A., Claver J., Camacho A.M. The influence of manufacturing parameters on the mechanical behaviour of PLA and ABS pieces manufactured by FDM: A comparative analysis. *Materials*. 2018;11(8):1333.
http://dx.doi.org/10.3390/ma11081333

33. Özen A., Auhl D., Völlmecke C., Kiendl J., Abali B.E. Optimization of manufacturing parameters and tensile specimen geometry for fused deposition modeling (FDM) 3D-printed PETG. *Materials*. 2021;14(10):2556.
http://dx.doi.org/10.3390/ma14102556

34. Sehhat M.H., Mahdianikhotbesara A., Yadegari F. Impact of temperature and material variation on mechanical properties of parts fabricated with fused deposition modeling (FDM) additive manufacturing. *The International Journal of Advanced Manufacturing Technology*. 2022;120(7):4791–4801.
https://doi.org/10.1007/s00170-022-09043-0

35. Rahim T.T., Abdullah A.M., Akil H.M., Mohamad D., Rajion Z.A. The improvement of mechanical and thermal properties of polyamide 12 3D printed parts by fused deposition modelling. *Express Polymer Letters*. 2017;11(12):963–982.
https://doi.org/10.3144/expresspolymlett.2017.92

36. Jafferson J.M., Chatterjee D. A review on polymeric materials in additive manufacturing. *Materials Today: Proceedings*. 2021;46:1349–1365.
https://doi.org/10.1016/j.matpr.2021.02.485

37. Romero G.F., Maldonado S.R., Arciniaga L.F., Gonzales D.A., Villalobos E.B., Potter B.G., Muralidharan K., Loy D.A., Szivek J.A., Margolis D.S. Polymer-ceramic composites for fused deposition modeling of biomimetic bone scaffolds. *Results in Engineering*. 2024;102407.
https://doi.org/10.1016/j.rineng.2024.102407

38. Sofokleous P., Paz E., Herraiz-Martínez F.J. Design and Manufacturing of Dielectric Resonators via 3D Printing of Composite Polymer/Ceramic Filaments. *Polymers*. 2024; 16(18):2589. https://doi.org/10.3390/polym16182589

39. Liu W., Wu N., Pochiraju K. Shape recovery characteristics of SiC/C/PLA composite filaments and 3D printed parts. *Composites Part A: Applied Science and Manufacturing*. 2018;108:1–11.
https://doi.org/10.1016/j.compositesa.2018.02.017

40. Skorda S., Bardakas A., Segkos A., Chouchoumi N., Hourdakis E., Vekinis G., Tsamis C. Influence of SiC doping on the mechanical, electrical, and optical properties of 3D-printed PLA. *Journal of Composites Science*. 2024;8(3):79. https://doi.org/10.3390/jcs8030079

41. Goulas A., McGhee J.R., Whittaker T., Ossai D., MistryE., Whittow W., Vaidhyanathan B., Reaney I.M., Vardaxoglou J.C., Engstrøm, D. S. Synthesis and dielectric characterisation of a low loss $BaSrTiO_3$/ABS ceramic/polymer composite for fused filament fabrication additive manufacturing. *Additive Manufacturing*. 2022;55:102844.
http://dx.doi.org/10.1016/j.addma.2022.102844

42. Khatri B., Lappe K., Habedank M., Mueller T., Megnin C., Hanemann T. Fused deposition modeling of ABS-Barium Titanate composites: A simple route towards tailored dielectric devices. *Polymers*. 2018;10(6):666.
https://doi.org/10.3390/polym10060666

43. Castles F., Isakov D., Lui A., Lei Q., Dancer C.E., Wang Y., Janurudin J.M., Speller S.C., Grovenor C.R.M., Grant P.S. Microwave dielectric characterisation of 3D-printed $BaTiO_3$/ABS polymer composites. *Scientific Reports*. 2016;6(1):1–8. http://dx.doi.org/10.1038/srep22714

44. Wu Y., Isakov D., Grant P.S. Fabrication of composite filaments with high dielectric permittivity for fused deposition 3D printing. *Materials*. 2017;10(10):1218.
https://doi.org/10.3390/ma10101218

45. Veselý P., Froš D., Hudec T., Sedláček J., Ctibor P., Dušek K. Dielectric spectroscopy of PETG/TiO_2 composite intended for 3D printing. *Virtual and Physical Prototyping*. 2023;18(1):e2170253.
https://doi.org/10.1080/17452759.2023.2170253

46. Nakonieczny D.S., Kern F., Dufner L., Antonowicz M., Matus K. Alumina and zirconia-reinforced polyamide PA-12 composites for biomedical additive manufacturing. *Materials*. 2021;14(20):6201.
https://doi.org/10.3390/ma14206201

47. Linh N.T.D., Huy K.D., Dung N.T.K., Luong N.X., Hoang T., Tham D.Q. Fabrication and characterization of PMMA/ZrO_2 nanocomposite 3D printing filaments. *Vietnam Journal of Chemistry*. 2023;61(4):461–469.
https://doi.org/10.1002/vjch.202200185

48. Kuznetsova E., Pristinskiy Y.O., Bentseva E., Pinargote N.S., Smirnov A. Rheological behavior and 3D printing of highly filled alumina-polyamide filaments during fused deposition modeling. *High Temperature Material Processes: An International Quarterly of High-Technology Plasma Processes*. 2024;28(3):9–24.
https://doi.org/10.1615/HighTempMatProc.2023051057

49. Angelopoulos P.M., Samouhos M., Taxiarchou M. Functional fillers in composite filaments for fused filament fabrication: A review. *Materials Today: Proceedings*. 2021;37:4031–4043.
https://doi.org/10.1016/j.matpr.2020.07.069

50. Solomon I.J., Sevvel P., Gunasekaran J. A review on the various processing parameters in FDM. *Materials Today: Proceedings*. 2021;37:509–514.
https://doi.org/10.1016/j.matpr.2020.05.484

51. Dey A., Yodo N. A Systematic Survey of FDM process parameter optimization and their influence on part characteristics. *Journal of Manufacturing and Materials Processing*. 2019;3(3):64. https://doi.org/10.3390/jmmp3030064

52. Portoacă A.I., Ripeanu R.G., Diniță A., Tănase M. Optimization of 3D printing parameters for enhanced surface quality and wear resistance. *Polymers*. 2023;15(16):3419. https://doi.org/10.3390/polym15163419

53. Syrlybayev D., Zharylkassyn B., Seisekulova A., Akhmetov M., Perveen A., Talamona D. Optimisation of strength properties of FDM printed parts: A critical review. *Polymers*. 2021;13(10):1587. https://doi.org/10.3390/polym13101587

54. Goulas A., Zhang S., Cadman D.A., Järveläinen J., Mylläri V., Whittow W.G., Vardaxoglou J.C., Engstrøm D.S. The impact of 3D printing process parameters on the dielectric properties of high permittivity composites. *Designs*. 2019;3(4):50. https://doi.org/10.3390/designs3040050v

55. Zhang Y., Li W., Wang C., Xue H., Yuan A., Li D., Zhang G. 3D printed polycarbonate support insulator for quick repair: Insulation and mechanical performance. In: *International Conferebce on High Voltage Engineering and Applications (ICHVE). IEEE*. 2022. P. 1–5. https://doi.org/10.1109/ICHVE53725.2022.9961392

56. Nabipour M., Akhoundi B., Bagheri Saed A. Manufacturing of polymer/metal composites by fused deposition modeling process with polyethylene. *Journal of Applied Polymer Science*. 2020;137(21):48717. https://doi.org/10.1002/app.48717

57. Galos J., Hu Y., Ravindran A.R., Ladani R.B., Mouritz A.P. Electrical properties of 3D printed continuous carbon fibre composites made using the FDM process. *Composites Part A: Applied Science and Manufacturing*. 2021;151:106661. https://doi.org/10.1016/j.compositesa.2021.106661

58. Valvez S., Reis P.N.B., Susmel L., Berto F. Fused filament fabrication-4D-printed shape memory polymers: A review. *Polymers*. 2021;13(5):701. https://doi.org/10.3390/polym13050701

59. Ehrmann G., Ehrmann A. 3D printing of shape memory polymers. *Journal of Applied Polymer Science*. 2021; 138(34):50847. https://doi.org/10.1002/app.50847

60. Barletta M., Gisario A., Mehrpouya M. 4D printing of shape memory polylactic acid (PLA) components: Investigating the role of the operational parameters in fused deposition modelling (FDM). *Journal of Manufacturing Processes*. 2021;61:473–480. https://doi.org/10.1016/j.jmapro.2020.11.036

61. Kong D., Guo A., Wu H., Li X., Wu J., Hu Y., Qu P., Wang S., Guo S. Four-dimensional printing of polymer-derived ceramics with high-resolution, reconfigurability, and shape memory effects. *Additive Manufacturing*. 2024;83:104050. https://doi.org/10.1016/j.addma.2024.104050

Information about the Authors

Alexander I. Zaytsev – Engineer at the Russian-Chinese Research Laboratory “Functional materials”, Peter the Great St.Petersburg Polytechnic University (SPbPU)
ORCID: 0000-0002-3138-8365
E-mail: zajtsev_ai2@spbstu.ru

Anton V. Sotov – Cand. Sci. (Eng.), Leading Researcher of the Laboratory “Material Design and Additive Manufacturing”, SPbPU
ORCID: 0000-0002-7303-5912
E-mail: sotov_av@spbstu.ru

Anna E. Abdrahmanova – Engineer of the Laboratory “Material Design and Additive Manufacturing”, SPbPU
ORCID: 0009-0003-4494-7300
E-mail: abdrahm_ae@spbstu.ru

Anatoliy A. Popovich – Dr. Sci. (Eng.), Professor, Scientific and Educational Center “Structural and Functional Materials”, SPbPU
ORCID: 0000-0002-5974-6654
E-mail: director@immet.spbstu.ru

Сведения об авторах

Александр Ильич Зайцев – инженер российско-китайской научно-исследовательской лаборатории «Функциональные материалы», Санкт-Петербургский политехнический университет Петра Великого (СПбПУ)
ORCID: 0000-0002-3138-8365
E-mail: zajtsev_ai2@spbstu.ru

Антон Владимирович Сотов – к.т.н., вед. науч. сотрудник лаборатории «Дизайн материалов и аддитивного производства», СПбПУ
ORCID: 0000-0002-7303-5912
E-mail: sotov_av@spbstu.ru

Анна Эдуардовна Абдрахманова – инженер лаборатории «Дизайн материалов и аддитивного производства», СПбПУ
ORCID: 0009-0003-4494-7300
E-mail: abdrahm_ae@spbstu.ru

Анатолий Анатольевич Попович – д.т.н., профессор Научно-образовательного центра «Конструкционные и функциональные материалы», СПбПУ
ORCID: 0000-0002-5974-6654
E-mail: director@immet.spbstu.ru

Contribution of the Authors

A. I. Zaytsev – literature search and analysis, writing the manuscript.
A. V. Sotov – development of the main concept, literature search and analysis, conclusion formulation.

Вклад авторов

А. И. Зайцев – поиск и анализ литературы, подготовка текста статьи.
А. В. Сотов – формирование основной концепции, поиск и анализ литературы, формулировка выводов.

A. E. Abdrahmanova – manuscript revision, conclusion formulation.
A. A. Popovich – scientific supervision, problem formalization, development of the main concept.

А. Э. Абдрахманова – корректировка текста, формулировка выводов.
А. А. Попович – научное руководство, формализация задачи, формирование основной концепции.

Received 05.08.2024
Revised 11.09.2024
Accepted 13.09.2024

Статья поступила 05.08.2024 г.
Доработана 11.09.2024 г.
Принята к публикации 13.09.2024 г.

Зарегистрирован Федеральной службой по надзору
в сфере связи, информационных технологий
и массовых коммуникаций.
Свидетельство о регистрации **ПИ № ФС77-79230**

Журнал распространяется агентством «Урал-Пресс»
Подписной индекс: 80752 (печатная версия)
05108 (электронная версия)